NUMERICAL MODELING OF FAILURE IN COMPOSITE L-BEAM AND T-JOINT STRUCTURES

A THESIS SUBMITTED TO
THE GRADUATE SCHOOL OF NATURAL AND APPLIED SCIENCES
OF
MIDDLE EAST TECHNICAL UNIVERSITY

BY

PAKİZE TEMİZ

IN PARTIAL FULFILLMENT OF THE REQUIREMENTS
FOR
THE DEGREE OF MASTER OF SCIENCE
IN
AEROSPACE ENGINEERING

DECEMBER 2022

Approval of the thesis:

NUMERICAL MODELING OF FAILURE IN COMPOSITE L-BEAM AND T-JOINT STRUCTURES

submitted by **PAKİZE TEMİZ** in partial fulfillment of the requirements for the degree of **Master of Science in Aerospace Engineering, Middle East Technical University** by,

Prof. Dr. Halil Kalıpçılar
Dean, Graduate School of **Natural and Applied Sciences**

Prof. Dr. Serkan Özgen
Head of the Department, **Aerospace Engineering, METU**

Prof. Dr. Demirkan Çöker
Supervisor, **Aerospace Engineering, METU**

Examining Committee Members:

Prof. Dr. Altan Kayran
Aerospace Engineering Dept., METU

Prof. Dr. Demirkan Çöker
Aerospace Engineering, METU

Assoc. Prof. Dr. Ercan Gürses
Aerospace Engineering Dept., METU

Asst. Prof. Dr. Görkem Eğemen Güloğlu
Aerospace Engineering Dept., METU

Prof. Dr. Kemal Levend Parnas
Mechanical Engineering Dept., TEDU

Date: 02.12.2022

I hereby declare that all information in this document has been obtained and presented in accordance with academic rules and ethical conduct. I also declare that, as required by these rules and conduct, I have fully cited and referenced all material and results that are not original to this work.

Name Last name : Pakize Temiz

Signature :

ABSTRACT

NUMERICAL MODELING OF FAILURE IN COMPOSITE L-BEAM AND T-JOINT STRUCTURES

TEMİZ, PAKİZE
Master of Science, Aerospace Engineering
Supervisor : Prof. Dr. Demirkan Çöker

December 2022, 183 pages

Laminated curved-shape composite structures which are used as stiffening components in aerospace, wind, automotive and marine industries are subjected to high radial and tangential stresses. For the scope of this thesis, different modelling strategies are investigated to simulate interlaminar and intralaminar failure in composite L-beam and T-joint structures using commercial finite element (FE) code ABAQUS/Standard 2020. In the first part, $[0_{30}]$ and $[0_3/90_3/0_3/90_3/0_3]$s laminated L-beams are evaluated using implicit finite element analysis. 3D and 3D-slice FE models are generated, and XFEM in conjunction with LaRC05 criteria and CZM in conjunction with QUADS initiation criteria and Benzeggagh-Kenane (BK) propagation criterion are used separately. The implicit FE results are validated in terms of load-displacement behavior, stress fields, and failure location with both explicit analysis results and experimental results for $[0_{30}]$ laminates. For $[0_3/90_3/0_3/90_3/0_3]$s laminates, the results were compared to the experimental results in the literature. For cross-ply L-beam specimens, failure load is overestimated compared to the experiments in literature. Additional FE analyses are carried out with reduced strengths considering the observed defects and ply mismatch angle at the interface which results in comparable failure load with experiments. To the authors’ best knowledge, this is the first study implementing LaRC05 failure criteria to analysis of L-beam structures.

In the second part, 2D implicit FE models with CZM is used to model T-joints under axial loading and compared with 3D implicit FE results in terms of the load-displacement curves, stress fields and failure locations to address the 3D effects. 3D model revealed that the debonding initiates at the middle-width of the filler/stringer interface and extends towards the free edges. Furthermore, 2D implicit FE models with CZM is used to model T-joints under oblique and transverse loadings and compared to axial loading. T-joint under 45° loading resulted in higher load bearing than the others due to opposing mechanisms of vertical and horizontal components of the loading. The results of this thesis contribute to the understanding of failure mechanisms of L-beam and T-joint structures.

Keywords: Composite, L-Beam, T-Joint, Delamination, Matrix Cracking

ÖZ

KOMPOZİT L-KİRİŞ VE T-BAĞLANTI YAPILARINDA HASARIN NÜMERİK MODELLEMESİ

TEMİZ, PAKİZE
Yüksek Lisans, Havacılık ve Uzay Mühendisliği
Tez Yöneticisi: Prof. Dr. Demirkan Çöker

Aralık 2022, 183 sayfa

Havacılık, rüzgar, otomotiv ve denizcilik endüstrilerinde takviye elemanı olarak kullanılan kavisli kompozit lamine yapılar, yüksek radyal ve teğet gerilmelere maruz kalmaktadır. Bu tez kapsamında, ticari sonlu eleman (FE) kodu ABAQUS/Standard 2020 kullanılarak kompozit L-kiriş ve T-bağlantı yapılarında tabaka içi ve tabakalar arası hasarı simüle etmek için farklı modelleme stratejileri araştırılmıştır. İlk bölümde, $[0_{30}]$ ve $[0_3/90_3/0_3/90_3/0_3]$ katmanlı L-kirişler örtük sonlu eleman analizi kullanılarak değerlendirilir. 3B ve 3B-dilim FE modelleri oluşturulur ve LaRC05 kriterleri ile bağlantılı olarak XFEM ve QUADS başlatma kriterleri ve Benzeggagh-Kenan (BK) yayılma kriteri ile bağlantılı olarak CZM ayrı ayrı kullanılır. Örtük FE sonuçları, $[0_{30}]$ laminatlar için literatürdeki hem analiz sonuçları hem de deneysel sonuçlar ile yük-yer değiştirme davranışı, gerilim alanları ve hasar konumu açısından doğrulandı. $[0_3/90_3/0_3/90_3/0_3]$ laminatları için sonuçlar literatürdeki deneysel sonuçlarla karşılaştırıldı. Çapraz katlı L-kiriş numuneleri için, literatürdeki deneylere kıyasla kırılma yükü fazla hesaplanmıştır. Ek FE analizleri, arayüzde gözlenen kusurlar ve kat uyuşmazlığı açısı göz önünde bulundurularak azaltılmış dayanımlarla gerçekleştirilir, bu da deneylerle karşılaştırılabilir arıza yükü ile sonuçlanır. Yazarların en iyi bilgisine göre bu, L kiriş yapılarının analizinde LaRC05 hasar kriterlerini uygulayan ilk çalışmadır.

İkinci bölümde, eksenel yük altında T bağlantılarını modellemek için CZM'li 2B örtülü FE modeli kullanılır ve 3B etkileri ele almak için yük-yer değiştirme eğrileri, gerilim alanları ve hasar konumları açısından 3B örtülü FE sonuçlarıyla karşılaştırılır. 3B model, ayrılmanın dolgu/stringer arayüzünün orta genişliğinde başladığını ve serbest kenarlara doğru uzandığını ortaya çıkardı. Ayrıca, CZM'li 2B örtülü FE modelleri, eğik ve yanal yükler altında T bağlantılarını modellemek için kullanılır ve eksenel yükleme ile karşılaştırılır. 45° yükleme altındaki T-bağlantısı, yükün dikey ve yatay bileşenlerinin zıt mekanizmaları nedeniyle diğerlerinden daha yüksek yük taşıma ile sonuçlanmıştır. Bu tezin sonuçları, L-kiriş ve T-bağlantı yapılarının hasar mekanizmalarının anlaşılmasına katkıda bulunur.

Anahtar Kelimeler: Kompozit, L-Kiriş, T-Bağlantı, Delaminasyon, Matris Çatlaması

To my family

ACKNOWLEDGMENTS

In the first place, I would like to express my sincere appreciation to my supervisor Prof. Dr. Demirkan Çöker for his inspiring motivation and guidance during this study.

I also would like to thank Prof. Dr. Altan Kayran, Prof. Dr. Kemal Levend Parnas, Assoc. Prof. Dr. Ercan Gürses and Asst. Prof. Dr. Görkem Eğemen Güloğlu for their precious comments and suggestions in my thesis committee.

I dedicate this thesis to my family. I wish to thank my husband Hakan Temiz and my son Birkan Murat Temiz for their love, endless support, and encouragement which greatly helped me to finish this work.

I would like to thank my friends Onur Ali Batmaz, Can Muyan, Aydın Amireghbali, Ahmet Çevik, Umut Altuntaş and Tutku Ilgın Özcan from RUZGEM for their friendship and research partnership.

I am thankful to all my former colleagues at Turkish Aerospace Industries (TAI), especially Tamer Tahir Ata and Mustafa Ekren for their guidance over the course of this study.

I also would like to thank RUZGEM for giving me the opportunity to use the computational capabilities.

TABLE OF CONTENTS

CHAPTERS

LIST OF TABLES

TABLES

LIST OF FIGURES

FIGURES

LIST OF ABBREVIATIONS

ABBREVIATIONS

2D	Two Dimensional
3D	Three Dimensional
4-ENF	4 Point End Notched Flexure
ALLAE	Artificial Strain Energy
ALLIE	Internal Energy
BK	Benzeggagh-Kenane
CFRP	Carbon Fiber Reinforced Plastics
CZM	Cohesive Zone Method
DCB	Double Cantilever Beam
DDM	Discrete Damage Modeling
DoE	Design of Experiment
ECDM	Extended Cohesive Damage Model
ENF	End Notch Flexure
KE	Kinetic Energy
LaRC	Langley Research Center
MMB	Mixed Mode Bending
PHILSM	Phi Level Set Method
QUADS	Quadratic Stress
RxFEM	Regularized Extended Finite Element Method
SDV8	Matrix Failure Index
SERR	Strain Energy Release Rate
SQRTM	Same Qualified Resin Transfer Molding
UD	Unidirectional Ply
UMAT	User Material Subroutine
VCE	Virtual Crack Extension
VCCT	Virtual Crack Closure Technique

VUMAT	User Material Subroutine for ABAQUS/Explicit
WWFE	World Wide Failure Exercise
XFEM	eXtended Finite Element Method

LIST OF SYMBOLS

SYMBOLS

$\boldsymbol{a}_I$	Nodal enriched degree of freedom vector
$\boldsymbol{b}_I$	Nodal enriched degree of freedom vector
D	Damage variable
E_1	Elastic moduli in direction 1
E_{22}, E_2	Elastic moduli in direction 2
E_{int}	Interaction energy
$f_\alpha(x)$	Signed distance function for an arbitrary point x
$F_\alpha(x)$	Asymptotic crack tip singularity function
f	Failure index
$FI_{KINK}, f_{kinking}$	Fiber kinking failure index
FI_M, f_{matrix}	Matrix failure index
$FI_{SPLIT}, f_{splitting}$	Fiber splitting failure index
$FI_{FT}, f_{tension}$	Fiber tension failure index
f_{tol}	Tolerance
G_{12}	Shear modulus in longitudinal direction
G_{IC}	Fracture toughness under mode I
G_{IIC}	Fracture toughness under mode II
G_{IIIC}	Fracture toughness under mode III
$G_I(T)$	Fracture toughness under mode-I in transverse direction
$G_{II}(T)$	Fracture toughness under mode-II in transverse direction
$G_I(L)$	Fracture toughness under mode-I in longitudinal direction
$G_{II}(L)$	Fracture toughness under mode-I in longitudinal direction
G_n, G_s, G_t	Strain energy release rates in Mode-I, II and III

$H(x)$	Heaviside jump function
K_{nn}, K_{ss}, K_{tt}	Penalty stiffness of cohesive elements
$L_{CZ_I}, L_{CZ_{II}}, L_{CZ_{III}}$	Cohesive zone lengths
N	Set of nodes enriched by Heaviside function
$N_I(x)$	Shape function
$\boldsymbol{n}(\overline{\boldsymbol{x}})$	Unit normal vector to the crack
S_T^{is}	Transverse in-situ shear strength
S_L^{is}	In-plane in-situ shear strength
S_L^{UD}	Unidirectional in-plane shear strength
T_0	Initial thickness
$\langle t_n \rangle$	Nominal traction in n direction
t_I^0	Interlaminar strength under mode I
t_{II}^0	Interlaminar strength under mode II
t_{III}^0	Interlaminar strength under mode III
t_n	Nominal traction in n direction
t_s	Nominal traction in s direction
t_t	Nominal traction in t direction
$\overline{t_n}$	Stress component without damage in n direction
$\overline{t_s}$	Stress component without damage in s direction
$\overline{t_t}$	Stress component without damage in t direction
$\boldsymbol{u}_I$	Nodal displacement vector
ν_{21}	Poisson’s ratio in 21 plane
$\bar{x}$	Closest point to x on crack surface
X_C	Compressive strength in fiber direction
γ_{12}	In-plane shear strain
Y_C	Transverse compressive strength
Y_C^{is}	Transverse in-situ compressive strength
Y_T^{UD}	Unidirectional transverse tensile strength
α_0	Matrix fracture angle under pure compression

β	Shear response factor
σ_N	Normal stress
τ_T	Transverse shear stress
τ_L	Longitudinal shear stress
φ	Fiber misalignment angle
ε_n	Nominal strain in n direction
ε_s	Nominal strain in s direction
ε_t	Nominal strain in t direction
δ_m	Displacement in mixed mode
δ_n	Displacement in n direction
δ_s	Displacement in s direction
δ_t	Displacement in t direction
η	Material parameter for in-situ strength

CHAPTER 1

INTRODUCTION

1.1 Overview

Material science and technology is growing day to day by the increasing need to tailor properties for specific usage of different industries. Composite materials are the most favorable ones in most of the industries such as aerospace, wind, automobile, marine etc. in recent decades. The reason behind this choice is their qualitative characteristics and immense advantageous features from manufacturing to service. To clarify the qualitative characteristics, composite materials are corrosion resistant, electrically non-conductive and thermally low conductive together with better fatigue performance compared to isotropic materials besides their high strength/stiffness to weight ratio.

Fiber orientations are selected and stacked carefully to generate fabulous in-plane properties, but laminated composites are weak through the thickness or out-of-plane directions. Although fibers have significant tensile properties in their primary direction, their laterally weak properties result in the matrix-driven properties in out-of-plane direction of the lamina. Stiffening components are used to enhance the composite panels' out-of-plane strength. Stiffener, spar, rib and stringer are the main types of panel stiffening components. The section of the stiffening component can be one of these; I, T, Z, Ω, C, J, L. Most stiffening components have curved regions to transfer load from panels to the webs by approximately 90° angle. This induces high out-of-plane and shear stresses at the curved region. That’s why this thesis is devoted to understand behavior of such structures.

Out-of-plane load transfer is achieved also by joints in composite structures. In past applications, riveted or fastened joints are seen in a great majority however, weaker alternatives have been preferred recently, especially in the aerospace industry. The airliners look for the cheapest option throughout the service life, ensuring fuel saving by fulfilling the strength and damage tolerance requirements while selecting an aircraft. This choice pushes aircraft manufacturers to compete with each other to produce lightweight structures with less maintenance and operational cost by ensuring safety. Therefore, joints and components exposed to out-of-plane load transfer such as L-beam and T-joint structures require special attention from the designer. Understanding and predicting failure mechanisms of such structures and joints are of vital importance.

T-joint structure is widespread in the industry as seen in Figure 1-1. Some examples are given below;

Wind turbine industry----Spar/shear web joints

Aerospace industry----Spar/stiffener joints with a panel, engine blade-hub joints

Marine industry----Bulkhead-hull joints

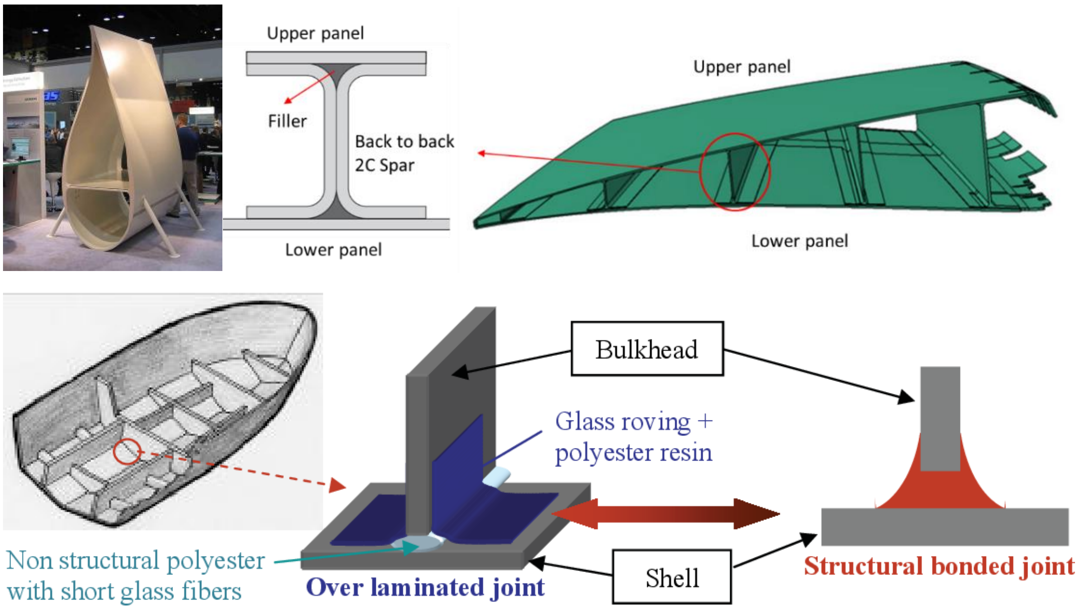

Figure 1-1 Examples of T-Joint usage in wind, aerospace and marine industries respectively [49] , [54]

T-joint, generally, is composed of over laminate, sub-laminate, and a filler. Because of the complexity of the geometry, 3D stress state is generated around the filler. For this reason, accurate analytical failure prediction method is not yet available. Since testing such complex structures in each loading condition is also costly and time-consuming, simulations come into the forefront as a virtual testing opportunity. ABAQUS is one of the most popular simulation tools in the literature for nonlinear materials and complex geometries, which are used in this research. ABAQUS contains several continuum mechanics, and fracture mechanics approaches already coded. ABAQUS version 2020 is utilized for the simulations in this thesis.

Since T-joint geometry consists of two symmetrical curved composite beams that use L-beam geometry, unidirectional and cross ply curved beams were investigated in terms of interlaminar and intralaminar failure with the approaches XFEM combined with LaRC05 failure criteria and CZM in Chapter 4. The limitations and conformance of XFEM, LaRC05 and CZM approaches were determined. The methods were validated using experimental and numerical results conducted in Çöker's research group. Then Chapter 5 deals with the failure investigation of co-bonded composite skin-stringer joints, namely "T-joints", using the geometry of Gülaşık and Çöker [1]. In this work, 2D analysis of axial (0°), transverse (90°) and oblique (45°) loadings were investigated in terms of stress fields, damage sequences, and failure load. Also, a 3D model is generated to see through the width variations under tensile loading.

1.2 Motivation

Composite materials are widely used in most industries such as aerospace, marine, wind energy, automotive, etc. This increase in demand gives rise to the development of manufacturing techniques and joining processes. Manufacturing techniques of carbon fiber composites are evolving with the industry needs, such as high production rate, low weight, reducing tools, and assembly steps assuring strength. Moreover, traditional joints such as fastening are replaced by other techniques due to the low weight requirements, especially in the aerospace industry. Co-cured, bonded, co-consolidated, and welded (resistance, induction, ultrasonic, etc.) composite joints are preferred to fulfill the weight requirements besides strength in aerospace structures.

In recent years, one-shot manufacturing of structural components made of thermoset materials gained importance. SQRTM process enables the manufacturing of structures composed of different components at a time by placing mandrels to empty spaces and laying out the fibers into them. After curing the whole structure together, there is no need to use fasteners or any other agent for joining. The joints of this type are named “co-cured”.

Thus, understanding of such components and complex joint structures’ failure mechanism have gained importance. Designers should optimize these structures in terms of weight, strength, manufacturability, and damage tolerance. This study aims to give guidance to designers about failure mechanisms, stress distributions, and failure loads for both curved L-beam and T-joint structures.

Simulation of progressive failure of curved cross-ply laminates under intralaminar damage is not covered as much in the literature to the best knowledge of the author, while delamination simulations are extensive. Moreover, CZM is the generally utilized method among counterparts. Therefore, Chapter 4 of this thesis is based on the interface and intralaminar failure prediction by using XFEM coupled with LaRC05 failure criteria compared to CZM for unidirectional and cross-ply L-beam structures.

Despite the complexity of the failure behavior under oblique and transverse loadings, most of the studies in the literature on the failure of T-joints are focused on the failure mechanism under axial tensile loading. Therefore, Chapter 5 aims to investigate the failure mechanism under oblique and transverse loadings. Moreover, 3D effects were analyzed and discussed in detail for the tensile loading case.

1.3 Objective

The overall objective of this thesis is to investigate modelling strategies to simulate the failure in composite L-beam and T-joints.

For L-Beam

Objective

- To validate 3D and 3D-Slice modeling techniques combined with CZM and XFEM on [030] laminate
- To investigate failure mechanisms of angle ply laminate

Approach

- Comparison of numerical results using implicit solver with experimental studies of Taşdemir & Çöker and explicit numerical results of Ata & Çöker.
- CZM and XFEM in conjunction with LaRC05 failure criteria are used for prediction of interlaminar and intralaminar failures.

For T-Joint

Objective

- To investigate 3D effects under axial loading
- To investigate failure mechanisms under oblique and transverse loadings

Approach

- Numerical analysis of 3D implicit model is performed using CZM and compared with 2D implicit CZM numerical results of Gülaşık & Çöker [1] under axial loading.
- Numerical analysis of 2D implicit models under oblique and transverse loadings are performed using CZM.

1.4 Outline

The outline of the thesis is the following:

- Chapter 1 is the introduction to the thesis topics.
- Chapter 2 presents the literature review on L-beam and T-joint structures separately.
- Chapter 3 explains the methods utilized throughout the thesis and failure behavior of composite materials. Specifically, the details of the CZM, XFEM, and LaRC05 failure criteria are given under damage modeling.
- Chapter 4 gives a detailed numerical investigation of the failure mechanisms involved in UD and cross-ply L-beams based on experimental results of Taşdemir [106]. 3D and 3D-slice models are compared. Also, interlaminar and intralaminar failure predictions are carried out. A strength study is performed to capture failure mode in the experiments for cross-ply laminate.
- Chapter 5 presents a T-joint failure analysis under different loading conditions. Firstly, 3D CZM is analyzed under axial loading to see free edge effects and failure propagation compared to 2D plane strain results shared by [2]. Then oblique and transverse loadings are analyzed using a 2D plane strain case.

CHAPTER 2

LITERATURE REVIEW

This chapter focuses on the uderstanding of the background in the topics of L-beam and T-joint structures. Firstly, review of L-beam studies is given and then T-joint structure is explained in detail and experimental and numerical studies are discussed.

2.1 Composite L-Beams

Developments in the composite manufacturing techniques resulted more complex structures. Some of these complex structures are L-beam and T-joints due to their high curvatures. Although the failure mechanisms and stress states of flat composites are well-known, researchers made great effort to understand new failure mechanism faced by curved structures which is called as unfolding. The unfolding failure is a special type of delamination seen in the curved parts. The reason behind this mechanism is that the high transverse stresses due to curvature despite low transverse tensile strength of the composite materials. There are two types of unfolding failure mechanisms reported in the literature; traditional unfolding as a result of purely transverse tensile stress and induced unfolding caused by intralaminar matrix cracks which is due to high transverse tensile and tangential stresses [15]. The failure location is different for these mechanisms. Traditional unfolding takes place at the location of maximum radial stress generally close to the mid-thickness while, induced unfolding is seen close to the inner radius under mixed mode of tangential and transverse tensile stresses. The matrix crack formed under mixed mode of stresses continues as a sudden delamination because radial stresses try to open this crack.

There are valuable studies to find out stress state in this type of structures analytically. First effort to calculate interlaminar stresses is shown by Lekhnitskii et al. [3] in 1968 using the classical elasticity theory. Assuming plane stress assumption, radial, tangential and shear stresses were derived for the anisotropic homogeneous curved beam under bending and end load at the edges. Kedward [4] proposed a formula for the maximum radial stress at the curved region based on Lekhnitskii's work. Although using of homogenized anisotropic material approximation is practical and used by many, the distribution of interlaminar stresses and the maximum value strictly affected by stacking sequences. That's why Ko and Jackson developed new stress expressions taking account the non-homogeneous nature of layered composite curved beams [5]. Non-homogeneity is considered by boundary conditions at the layer interfaces in Airy stress function. These studies are the bases for analytical calculation of stresses in the curved beams. Lately, Gonzalez-Cantero et al. [6] proposed model accounting curvature effect on the distribution of loads and corresponding stresses called as regularized stresses. He declared that curvature changes between the junctions of the arms and affects stress state which is crucial for better prediction of the failure.

There are analytical delamination prediction methods in literature using above mentioned stress formula. Kim and Soni [7] is the mostly used failure criterion. It is defined as an ellipsoid in radial and shear stress space. Also, Brewer and Lagace [8] proposed a criterion which has a distinction between tensile and compressive zones with two ellipsoids. Wisnom et al. [9] developed a delamination criterion taking into account matrix principal stress which is a combination of matrix stresses in all directions. By comparing this stress to the strength in the in-plane direction, delamination is predicted. Matrix stresses were determined by using modulus fractions of matrix to fiber in the direction of each stress component.

There are vast of numerical and experimental studies based on delamination failure of these structures. Firstly Chang [12] performed finite element analysis using 2D plane strain assumption considering both in-plane failure criterion of Tsai-Hill and out-of-plane criterion quadratic stress interaction. Moreover, Sun and Kelly examined the different failure modes in different stacking sequences utilizing both intralaminar and interlaminar failure prediction in [13] and [14]. They suggested to use 3D stress state due to high out-of-plane stresses for better prediction of ultimate load. Besides, they performed experiments and reported that failure is an interaction of transverse matrix cracking and delamination. In 1992, Martin [10] studied UD curved laminates under quasi-static loading both experimentally and numerically. He observed mode-I dominated crack initiation. For cross-ply laminates, Martin and Jackson [11] carried out experimental, numerical and analytical studies based on failure investigation under cyclic and static loading. Experiments showed induced unfolding mechanism with the layup $[0_4/90_3/0_5]_s$. By using VCCT in the 2D and 3D finite element models after initiation of failure, they found out SERR results were in agreement with each other. The anticlastic bending effect is analyzed by Wisnom [107] both in 2D and 3D models. He concluded that anticlastic bending caused significant stress variation through the width.

Recently, Çöker’s research group have series of studies on failure of curved beams under static and fatigue loading conditions. Gözlüklü et al. [16], [17] reported that delamination of curved beams or L-shaped beams is dynamic even under static loading. They performed explicit numerical analyses using cohesive elements under quasi-static loading and compared to the high-speed camera findings from experiments. Based on both numerical and experimental results, they declared that the complete delamination takes place in only 20μs. Moreover Taşdemir et al. performed experiments on unidirectional, cross-ply and fabric curved laminates [105] and [106]. They found out different failure mechanisms of thick cross-ply laminates under static and fatigue loading. They also realized that radial stresses grows the small defects in the structure at the maximum radial stress location under fatigue loading however failure initiates according to combined-stress criterion at inner plies rather than the maximum stress location under static loading. This finding is similar to Gonzalez-Cantera’s theory [15] about induced unfolding mechanism. Lately, Ata and Çöker [103], [104] reported 2D-3D explicit simulations of both unidirectional and fabric L-shaped laminates. It is the first study modeling the dynamic delamination of composite curved laminates using 3D simulations.

It is concluded from previously mentioned studies that failure mechanism in curved cross-ply composite laminates is a combination of both interlaminar and intralaminar failures. Also, increasing thickness changes failure mechanism from traditional unfolding into induced unfolding. Since failure behavior seen in Taşdemir et al.'s experimental work in thick cross-ply laminate under static loading is also promotes induced unfolding mechanism, Chapter 4 of this thesis deals with the numerical simulation of both unidirectional and cross-ply curved laminates. LaRC05 failure criteria is used to predict matrix cracks and CZM is utilized for the interface failures. Propagation of intralaminar failure is implemented by XFEM in ABAQUS. To the author's knowledge, this study is the first study implementing LaRC05 failure criteria to curved thick composite laminate for intralaminar failure prediction.

2.2 Composite T-Joint Structures

2.2.1 Types of T-Joint Structures

T-joints' history goes back to, butt-welded triple connections [72]. Since this study covers the composite T-joint structures, only these structures are dwelled on. Even in 1992, T-joint structures were used in ships made of fiber-reinforced plastics [42]. The geometry changes by application type and over time, as seen in Figure 2-1. The first geometry Figure 2-1 a) is a typical T-joint used mainly in the marine industry as seen in the studies of Shenoi et al. [42], [43], Dharmawan et al. [44], [48] and recently Bella et al. [45]. The second geometry is a particular type of T-joint named pi-joint due to its complicated geometry [70]. To strengthen the out-of-plane joints under bending loading, pi-joints have U-preform except for over-laminates on both sides of the filler, as seen in Figure 2-1 b). While some studies are available using triangular deltoids due to manufacturing easiness, Panigrahi and Pradhan do not recommend using of this type of structure in their parametric study about filler geometries [74]. The reason behind this investigation is that sharp corners in the over-laminate led to stress concentrations due to non-smoothness of the plies.

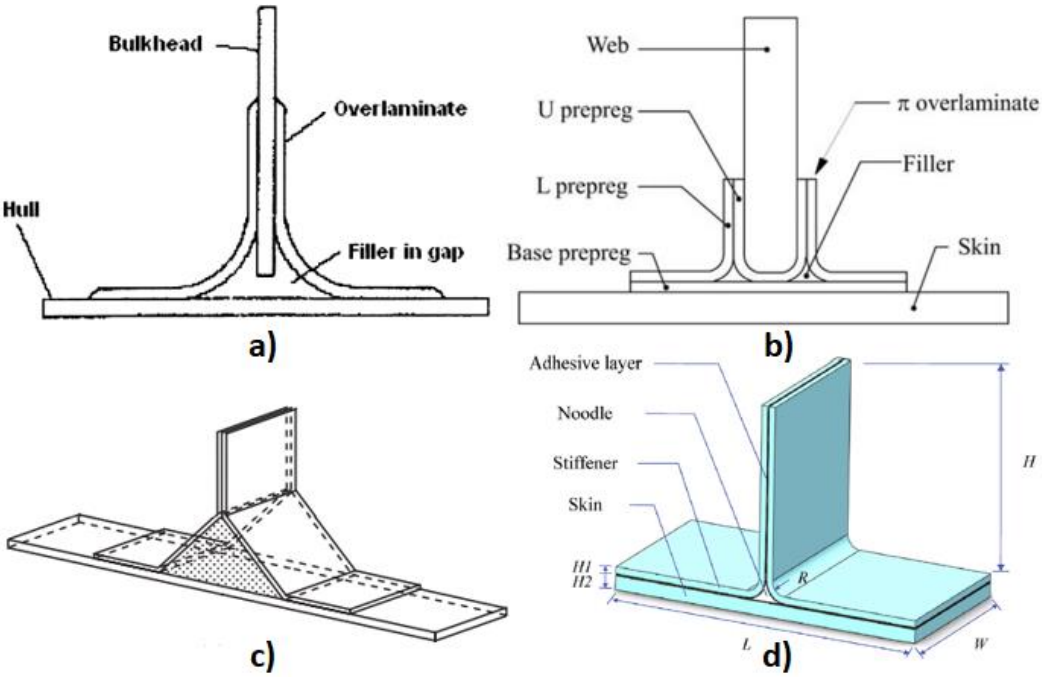

Figure 2-1 Types of T-joints investigated in most of the studies are respectively a) for marine industry [44] b) pi-joint type [70] c) with triangular deltoid [74] d) recently used T-joint type [73]

2.2.2 Composite T-Joint Manufacturing

Manufacturing a composite T-joint structure is a detailed process. Either each composite laminate can be manufactured individually and assembled with filler by secondary bonding/curing process, or one-shot manufacturing can be utilized by SQRTM process with the help of molds. However, the traditional manufacturing process involves 3 stages, shown in Figure 2-2. Firstly, skin is manufactured separately, and then the stiffening component is assembled by deltoid in Stage 2. Final assembly is done using tools to satisfy dimensional requirements at stage 3, and curing of complete assembly is performed. In the end, the T-joint structure is ready for testing.

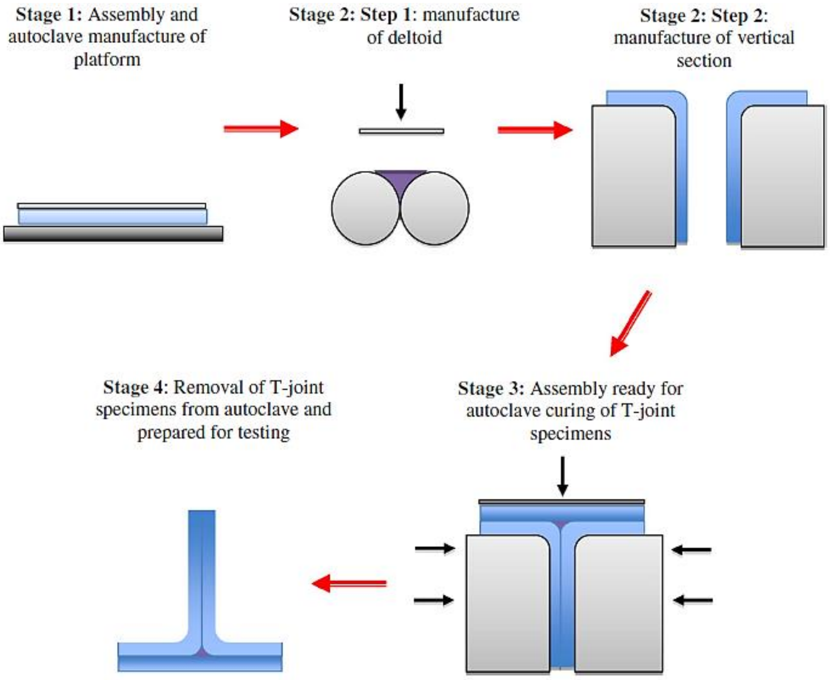

Figure 2-2 Manufacturing process of typical composite T-joint structure [46]

Stage 2 showing manufacturing of deltoid is an important process because many studies demonstrated that deltoid integrity is one of the critical points of load-carrying capacity in T-joint structures. Therefore, filler materials, geometries, and strengthening methods have gained importance, and there are many studies on this topic.

Recently, there have been many filler configurations for out-of-plane joints such as matrix, adhesive, foam, rolled UD, braided filler, etc. Sapi et al. reviewed the literature in detail and conducted several test campaigns to understand the failure behavior of T-joints manufactured by different filler types in studies [65] and [66]. Sapi declared that rolled UD type is the mainly used noodle type in similar joints [66]. However, manufacturing rolled UD filler is complex, as shown in Figure 2-3. It requires special attention to avoid manufacturing defects because Trask et al. proved the detrimental effect of defects on filler region on the structural strength of the joint in their study [46].

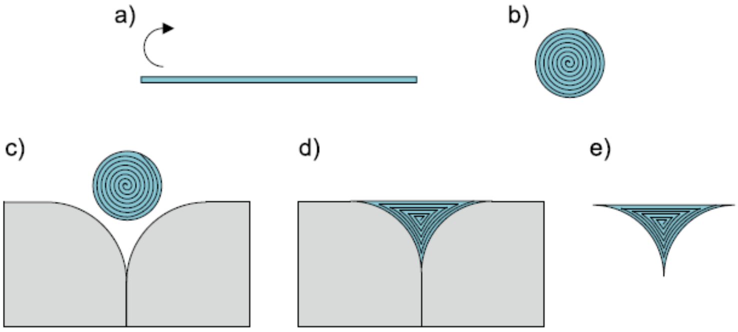

Figure 2-3 Rolled UD filler manufacturing process a) UD prepreg b) rolled UD c) tool d) noodle formed into tool e) rolled UD filler [65]

2.2.3 Failure Mechanisms

Failure mechanisms of T-joints vary with the loading and environmental conditions of use. Failures of T-joints can be categorized into failure in filler, bonding interfaces and composite laminates.

- Filler Cracking
    - Horizontal
    - Vertical
- Debonding between laminate and filler interfaces
- Delamination
    - Over-laminate plies
    - Skin/over-laminate, skin/filler interfaces

Filler failures are generally cracks in vertical or horizontal directions and delamination between adjacent laminates. Simulation of filler cracks is challenging and needs a mesh-independent method since initiation location is not predictable and inserting cohesive layers is not easy as ply interfaces due to the triangular geometry of the deltoid. Cui et al. put a cohesive element to every edge of a bulk element in the filler region to capture filler cracking. At the same time, Li and Chen developed the Extended Cohesive Damage Model as a combination of XFEM and CZM which predict more effectively multi delamination paths without previously defined mesh [33].

Horizontal cracks near the top corner of the filler, similar to Figure 2-4 a), are mainly based on thermal shrinkage. Chen et al. conducted several studies under tensile, bending, and mixed loading cases by considering initial thermal crack and concluded that it has more effect on the ultimate strength of the joint under bending and mixed loadings. At the same time, even no reduction in the load-carrying capacity is seen under tensile loading in [30], [31], and [32]. Vertical cracks are primarily initiated in the filler/stringer interface on the radius and propagate to the skin filler interface and cause complete failure, as seen in Figure 2-4 b). This mechanism is general in the lots of studies in literature, and some examples belong to Sapi et al. [46], Cui et al. [38], and Zhao et al. [76].

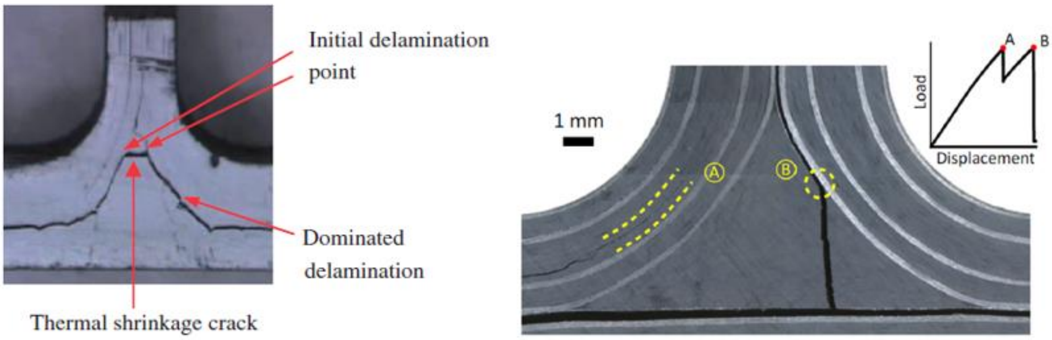

a) b)

Figure 2-4 Filler cracks a) horizontal [15] b) vertical [46]

Debonding of filler from adjacent laminates is the typical form of failure under tensile loading, as seen in Figure 2-5 a). Crack initiates at the bend region due to a combination of high interlaminar shear and peel stresses. After that it propagates through the upper and lower corners. Lastly, the final debonding of filler occurs, and load-carrying capacity is almost lost for the structure. Therefore, delamination of the filler interface is a critical mechanism for T-joint structures.

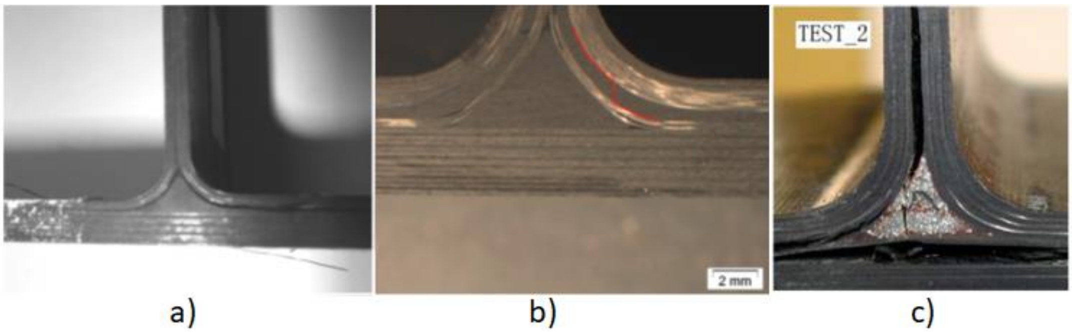

Figure 2-5 a) Delamination between bonding interfaces [39] b) delamination between over-laminate plies [26] c) delamination between filler/base plate interface [38]

Delamination in composite laminates generally occurs in the over-laminate plies on curved regions and skin plies near the flange ends or under the filler, as seen in Figure 2-5 b) and c). This mechanism extensively reduces load-bearing because of the reduced bending stiffness of the structure. As shown in Figure 2-5 b), intralaminar failures also occur during the delamination of the plies. Although Wu et al. [39] declare that intralaminar failures occur at late stages of T-joint failure due to the low interlaminar strength of the interfaces, the use of failure criteria in the simulation is vital to capture this mechanism. Sapi et al. conducted a study [29] on high-fidelity simulation of T-joint structure under tensile loading using physically based failure criterion LaRC05 and cohesive interfaces together to accurately capture failure behavior. The results were in good agreement with the tests predicting failure location and ultimate load.

2.2.4 T-Joint Testing

The structural strength of aircrafts must be validated by several tests, as represented in Figure 2-6. Tests on this pyramid should be performed to meet the requirements of aviation authorities. Virtual testing of structural components gets more comprehensive over time, especially for complex structures similar to composite T-joint components. After validating the numerical model with more straightforward testing procedures, complex loadings and parametric studies can be done numerically for cost savings.

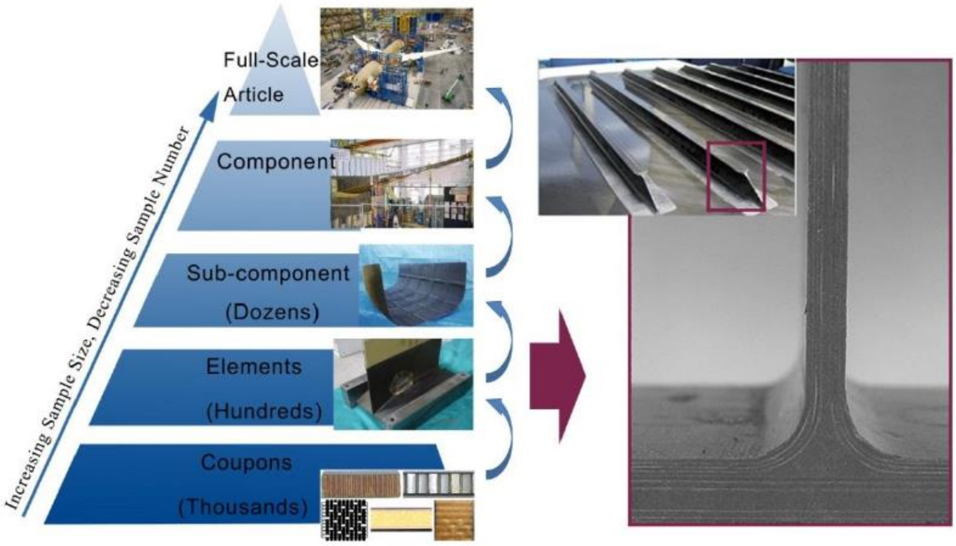

Figure 2-6 Aircraft testing pyramid [77]

T-joint testing is a typical element-level test for aircraft structures. Common testing mechanisms for T-joints under transverse, axial, and oblique loadings are represented in Figure 2-7 a), b), and c), respectively. As seen in Figure 2-7 c), oblique testing is challenging to implement. Due to its complexity, there is less research dealing with the testing of oblique loaded components.

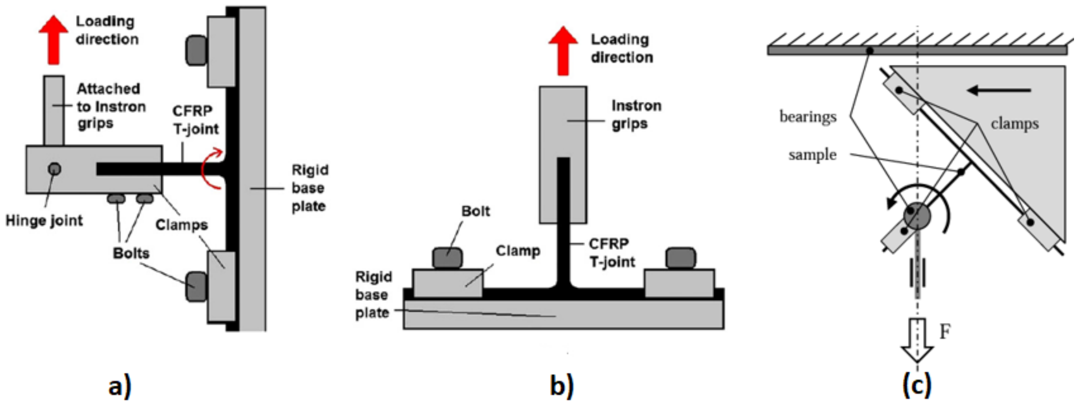

Figure 2-7 Typical testing fixtures for a) bending, b) tensile and c) mixed loadings [50], [75]

In addition to standard static tests of different loading conditions, three-point bending and fatigue tests are utilized for T-joint structures. Figure 2-8 a) stands for three-point bending, while b) is for fatigue testing under cyclic pull-out and push-in loadings.

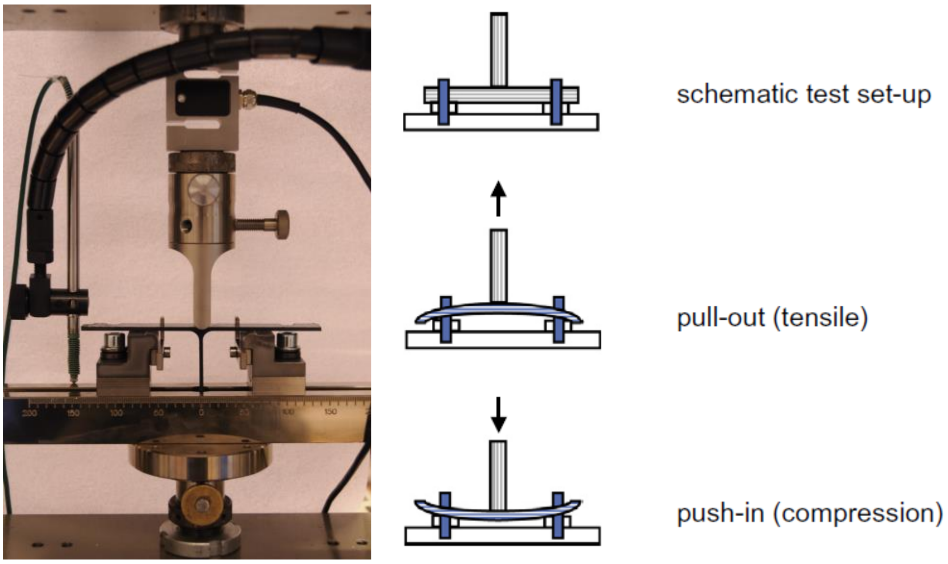

Figure 2-8 Other mostly used tests a) Three point bending setup [71] b) fatigue setup [47]

According to [25], clamp distance significantly affects the failure load. Yao et al. conducted several parametric studies on T-joint failure modeling using CZM and found that as clamp distance increased, the failure load also raised, and the failure mechanism changed. Therefore, selecting appropriate boundary conditions and clamp distance have an essential role in accurate predictions.

2.2.5 Experimental and Numerical Studies on T-Joint Structures

A thick composite shell finite element was developed to investigate the typical T-joint in wing structure subjected to pull-out loading by Kumari and Sinha [36]. A parametric study on the length of the joint, radius of the fillet region, and the endpoints of the fillet arc were performed to understand the behavior of such joints.

It was concluded by Kumari and Sinha [36] that raising the radius to a certain point increased the joint strength because of a reduction in stress concentration. However, for varying end points of arc length for different radii, strength decreased as the radius increased. Since no interlaminar failure prediction method was implemented in this work, failure loads and locations calculated from the in-plane Tsai-Wu failure criterion were same for all parameters.

The authors utilized the implementation of cohesive elements into a single delamination path in a 2D finite element model for T-joint failure prediction [30]. Failure is dominated by the mixed mode propagation rather than initiation. The ultimate load of the numerical simulations agreed with the test samples. Similar to [26], 50 % reduced strength values also gave very close results to initial ones without further refining the mesh as proposed by [19]. Although a deltoid crack due to thermal shrinkage was observed in the test specimen, it was not added to the simulation. Further studies on thermal cracking and multi-delamination modeling were done in recent articles by the authors [32] and [33].

Bruyneel et al. used Virtual Crack Extension (VCE) and CZM techniques in a 3D model to simulate an industrial multi-delamination T-joint case [40]. Both methods predicted similar crack propagation regions: noddle-stiffener interfaces and loads. However, VCE was unable to predict the ultimate load and final failure, which was the de-cohesion between the cap and the stiffener, according to CZM.

Cui et al. performed broad studies on T-joints subjected to pull-off loading to understand the effects of geometry and material properties on strength and failure mechanisms [38]. The authors obtained remarkable findings. Similar to [36], Cui et al. found a relation between the radius of the flange, filler stiffness, and overall stiffness. That is, if the stiffness of the filler is more than a certain threshold, strength increases as the radius gets larger; however, if filler stiffness is less than the threshold, then the strength of the joint decreases with increasing radius. The stiffness of the filler had a significant effect on the overall behavior of the load transfer and failure mechanism. Also, the strength and energy release rates of the adhesive, matrix, and filler affected the joint’s failure mechanism and load-carrying capacity. CZM was used as delamination debond modeling of the interfaces, and remarkably close results were obtained compared to experiments.

Chen et al. [32] considered the 45° mixed loading case (pulling + bending) together with the bending-only case. Comparing the failure loads in different loading cases revealed that T-piece specimens had much more pulling resistance than bending resistance. According to the authors' observations, the bending component leads to the opposite deformation of the pulling component in the radius. This interaction increased pulling resistance while bending resistance decreased compared to the pure bending case. This work also revealed that the initial thermal crack in the deltoid region under bending and mixed-mode loading significantly affected load-bearing capacity. Reduced percentages of failure load due to thermal cracks were 1.5 [31], 10.5 [32], and 22 [32], respectively, for pulling, bending, and mixed loading cases.

Maximum transverse stresses (perpendicular max principle stress) were used to determine the damage initiation locations with linear elastic analyses in 2D and 3D T-joint models under tensile loading by Hélénon et al. [26]. They placed the cohesive elements according to pre-analyses and investigated further propagation of the damage in the quarter and slice 3D models. The free edge effect was found to be critical in 3D modeling. Rather than refining the mesh, reducing strength values to a certain extent worked better in predicting maximum load even with coarse mesh. The primary failure mechanism was found to be the propagation of the crack, not the initiation.

The investigation of the T-joint in [26] was extended to three different bending conditions; 0°, 45°, and 90° in [27]. While 0° bending is a general case, others are unique in the literature. The High-Stress Concentration method was used to predict failure load unlikely to past study [26] with cohesive zone modeling. The linear elastic analysis resulted in conservative failure load values, but the location agreed with the experiments. This method is helpful for stress engineers in the industry where the computation time of nonlinear solutions is an issue for large models.

Gülaşık & Çöker [1] investigated both de-bond and delamination failure mechanisms in co-bonded T-joint structures under tensile loading using the CZM approach. 2D plane strain modeling combined with zero-thickness cohesive interface elements was used to model the co-bonded stiffened panel. Cohesive bilinear law was utilized for interface elements, coupled with quadratic stress interaction for initiation and Benzeggagh-Kenane law for propagation. Mixed mode behavior was observed in both the initiation and propagation of the de-bonding of curved laminates from the filler. The typical failure mode of T-joint structures 'stringer-filler de-bonding' was achieved. The primary load-carrying capacity loss was due to the complete de-bonding of the stiffener from the filler. It was found that a 30% increase in the interface strength of adhesive almost doubled the load-carrying capacity, besides changing failure mechanism.

Although most failure investigations of T-joint cover only the interlaminar damages, Wu et al. incorporated both interlaminar and in-plane damage behaviors using Tsai-Wu criterion coupled with the CZM in 3D [39]. In-plane failure is not likely to occur in the early stages for this type of joint under tensile loading since interlaminar strength is much weaker. However, it would be beneficial in bending cases since compressive stresses exist on the bent side. It is the first time in literature measuring strains at the critical regions of the joint during experiments to validate the finite element model. The maximum tensile load of the simulation and stiffness of the structure were almost the same as the tested specimens. Besides, measured strains were also in agreement. It was shown that a crack in filler does not reduce load-carrying capacity, but a crack in interfaces does.

Chen et al. developed a user element to accurately model the arbitrary crack propagation without prior knowledge of the crack path called Extended Cohesive Damage Model (ECDM) [33]. The ECDM is a combination of XFEM and CZM. Enriched user elements accounting for cohesive forces to eliminate crack tip singularity were used in XFEM, resulting in no more extended usage of path-dependent meshing for cohesive elements. As mentioned before, the crack propagation path was defined as perpendicular to the maximum principal stress. The past studies on T-joint failure under pulling [30], [31], and bending [32] loadings were used as an example to verify this newly developed modeling. Even in the vicinity of predefined interface elements, the crack path was highly correlated to the experiments. Therefore, it was proven by this work that the crack propagation direction can be determined as a perpendicular direction to the max principal stress vector. The results were agreed upon with reasonable accuracy on the multiple crack locations and failure loads. ECDM is an efficient modeling approach for arbitrary and multi-crack cases of composite T-joint structures.

Yao et al. [25] found a correlation between the thicknesses of skin and stiffener with the energy release rates at the center and edges of the flanges by deriving deflections from Timoshenko beam theory. According to [25], if the thickness of the skin is larger than the stiffener thickness, $G_{edge} > G_{center}$; delamination initiates at the stiffener radius. If the stiffener thickness is more significant than the skin, Gedge<Gcenter; initiation occurs at the flange end. Apart from analytical predictions, different numerical models with different cohesive laws and criteria were conducted and compared with the experimental results. Bilinear law was better than exponential for predicting failure behavior when test results were taken as a reference.

An adhesively bonded T-joint under tensile loading was modeled using 2D, 3D-slice, and half-width 3D techniques by Xu et al. [37]. The 2D model did not have cohesive interfaces, so it was used to predict the high stress locations. The 3D-slice model showed that a thermal crack initiated near the top of the deltoid and runouts of the stiffener, but did not propagate due to adjacent laminate constraints. The thermal crack did not cause any load drop in the load-displacement curve, in line with the previous literature on tensile loading. Although 3D-slice modeling predicted the failure mechanism, it could not predict through the width variations of stresses and failure locations. The 3D half-width model revealed that failure initiates from the middle of the width, not in the free edge of the joint. This was the natural outcome of the non-uniform stress distributions across the width since vertical stresses were less in the free edges. According to the examination of these models' stress distributions and failure mechanisms, 3D-slice modeling was found to be the most effective considering the computational cost of the half-width model.

A progressive damage model with CZM was used to simulate the failure behavior of the T-joint under tensile loading. As in the [26], it was observed that filler crack did not reduce joint stiffness and load-bearing capability, but delamination triggered by it determined the ultimate strength. The study offered discrete crack modeling to be utilized in the filler to predict crack propagation in this zone.

High-fidelity numerical studies were performed on the tensile T-joints and verified by experimental observations by Sápi et al. [29]. In-situ vs. UD strengths, manufacturing defects, residual thermal stresses and mesh size effects were accounted for in the simulations. As in [10], the 3D-slice model was used with plane strain assumptions and the free edge effect was eliminated. While physically based failure initiation criterion LaRC05 accounted for intralaminar failure criteria of fiber kinking, splitting, tensile and matrix failure, CZM was utilized for the interlaminar failure initiation and propagation in the simulations. The linear elastic numerical solutions predicted initiation location exactly and failure load with 3 % accuracy with the experiments. Without the thermal stage, the failure location changed and failure loads became 18 % higher than in the experiment, meaning that the thermal stage is essential for the realistic behavior. It was also shown that simulations using in-situ properties gave better accuracy than UD strength-based ones. According to the authors’ mesh convergence study, at least four elements are needed to capture the realistic failure locations and stress states. To conclude, the authors conducted high-fidelity T-joint numerical analysis method applicable to the industry using computationally cheap linear elastic analysis with very performant physically based composite failure criteria.

The comparison of the two high-fidelity methods to predict failure initiation and progression in composite T-joints subjected to pull-off loading was incorporated in this study [41]. The first method is based on the advanced continuum damage model combining physically-based failure criterion LaRC05 for matrix and fiber failure combined with the Cohesive Zone Method (CZM) for delamination prediction. The latter is the Discrete Damage Modeling (DDM) method utilizing Regularized Extended Finite Element Method (RxFEM) for crack formation, which also uses LaRC04 failure criteria for initiation and CZM for delamination. The experimental data were taken from the study of Sapi et al. [29] to verify these methods and they were consistently agreed in failure initiation and propagation locations with both approaches. The authors compared 2D and 3D half-width plain strain models of DDM and emphasized no significant differences between them. As a result, the DDM approach is better than the continuum damage model for predicting discrete damages in the filler region because the LaRC05 matrix crack criterion is applicable to UD fibers only. However, for the intralaminar matrix cracks in the laminate, LaRC05 gives very performant results about initiation and propagation behaviors together with the loads.

Thawre et al. conducted an experimental investigation on the fatigue behavior of composite T-joint under standard aircraft load sequence [47]. It was the first time in literature simulating the service loads for T-joints and predicting the spectrum fatigue life. Pull-out and push-in tests revealed that T-joint has less (nearly half) tensile strength compared with the compression case. Predicted fatigue life agreed to the measured data.

Trask et al. investigated the effects of process-induced defects on the failure load and the T-joint mechanism [46]. The authors deduced that while a 25% loss in the deltoid area resulted in almost no loss in the load-bearing capacity, a 50% reduction yielded a 33% reduction of the overall strength.

There were similar studies to Trask et al. figuring out the effects of defects on the joint structure and failure characteristics, mainly for marine applications.

Shenoi conducted several studies to figure out failure behavior and damage tolerance of tee joints in naval applications [42] and [43]. Shenoi and Hawkins studied 45° loading with material and geometric variations and noted that the imperfections significantly impact the load-carrying capability.

Li and Dharmawan also investigated the fracture mechanism and defects on tee joints in the marine industry [44] and [48]. Bonding defects in critical regions were examined both with the FEM and experiments. The strain distribution throughout the structure was analyzed before and after the debond modeling, and it is noted that strain distribution changes with the material discontinuities.

Burns and his colleagues conducted range of studies to improve structural properties and damage tolerance of T-joint using alternative bio-inspired optimization features [50], [51], [52], and [53]. In the study [50], Burns et al. used the embedded plies approach based on tree branch joints and tested both conventional and embedded designs under tensile loading. The experimental study indicated that while the failure of the T-joint with conventional design is more brittle and has higher fracture toughness than the embedded design, the initiation load is reduced due to higher interlaminar stresses in the embedded zones. The embedded design was not sufficient to improve all the mechanical properties including strength, stiffness and toughness by oneself, further studies should be incorporated to achieve desired properties.

The latter study about T-joint, carried out by Burns et al. [51], concentrated on tailoring the plies by mimicking the tree micro fibril orientation growth under bending loading. Both experimental and numerical observations were made to compare the tailored approach with the conventional quasi-isotropic sequence. Comparisons of the interlaminar shear and tensile stresses showed that peak stress values around the bend region reduced significantly (19%, 15% respectively). Unlike the results of the embedded case under tensile loading [50], failure onset load and toughness improved, while stiffness was nearly the same (7%) for tailored ply optimization under bending loading. The authors recommended the usage of nonstandard ply orientations by automatized manufacturing in the industry.

The above studies of Burns et al. exhibit different optimization feature investigated individually in composite T-joint design. Therefore, the combination of embedded plies with optimized ply orientations was tested and simulated under tensile and bending loadings separately in another study [52]. The results were promising about using nature to maximize the structural properties of the composite joints by reducing stress concentrations. The critical joint area was reduced by 25 % by embedded design without any increase in the interlaminar stress concentrations caused by this embedment with the help of ply angle optimization. The strain energy of the complete failure, damage onset loads, and ultimate strength values were all evolved for tensile and bending loads.

The latest study by Burns and his colleagues [53] on T-joints is about the optimization and Design of Experiment (DoE) cases of the ply angles under both tensile and bending loadings. The study covered the comparison of baseline quasi-isotropic configuration with the quasi-isotropic reduced factorial DoE design, hygrothermally stable reduced factorial DoE design, and numerical optimization design. All optimized configurations worked better than the baseline in different aspects, which are the more uniform distribution of the stresses, increase in failure initiation load, ultimate strength and evolution of strain energy absorption without compromising the stiffness and weight.

Li et al. conducted several tests to investigate geometric effects on Z-pinned T-joint failure under tensile loading [35]. As skin thickness increased, the rigidity of the joint improved, leading to significantly higher failure loads for pinned and unpinned configurations. Unlike the skin thickness effect, pins did not contribute to the rigidity of the joint but increased the failure load proportional to the skin thickness.

Wang and Soutis showed the effect of radius on the stress levels around the fillet region [18]. Since out-of-plane stresses in fillet region were higher than the others, out-of-plane reinforcement methods of the interlaminar veil and 3D woven were implemented into the finite element model and tested under both static and fatigue loading. Simulations had similar behavior to the experiments. The results showed that reinforcement methods increased the load-bearing capacity of the T-joint under static and fatigue loading, but 3D woven joint showed the best improvement. An increase in interlaminar fracture properties or a decrease in opening force by utilizing out-of-plane reinforcements will enhance the mechanical load-bearing of such joints.

2.2.6 Concluding Remarks from Literature

Interpretations drawn from the literature can be listed below;

- XFEM and its developed versions are practical modeling techniques to predict matrix cracks in discrete material zones.
- CZM is used as a predictive tool of interlaminar damages in the T-joint structure. However, it needs a pre-defined mesh to predict intralaminar damages, whose exact location is challenging to predict before an analysis.
- Mainly used cohesive law is the cohesive bilinear law combined with quadratic stress interaction for initiation and BK or Power Law for propagation.
- Most studies show that T-joint structures' primary failure mechanisms are the delamination of plies in the radius region, interface debonding, and filler cracking growing to the filler interface.
- The filler region requires special attention during design and manufacturing since geometrical features and imperfections during manufacture significantly effect on joint stiffness.
- Skin thickness significantly affects the failure mechanism and failure load since it serves as bending resistance to the structure. Also, the ratio of skin thickness to overall thickness determines the weak area in terms of energy needed to initiate the crack [25].
- Interface toughness has a significant effect on the failure load and mechanism. Interface material selection should be made carefully.
- The driving failure mode of T-joints is found to be the mixed mode failure propagation rather than the initiation of the damage.
- Mixed loading around the radius region causes failure initiation under different loading scenarios.

- In order to simulate the stress discontinuities and failure propagation through the ply, a mesh convergence study should be done. At least 3 or 4 elements across one ply are recommended by most of the authors.
- There are wide range of reinforcement methods available for this kind of joints. All of them have increasing effects on joint strength and some change the failure mechanisms of structure from brittle to ductile with increasing displacements but, they add different failure mechanisms due to additional components in the structure, such as fiber bridging mechanism due to pins.
- Thermal initial crack is investigated by many researchers, but a conclusion drawn at the end is that this initial crack does not cause any load drop if it does not reach to an interface and causes delamination-debonding under tensile loading. For bending cases, it reduces load-carrying capacity, but the effect is not significant.
- It is seen from most of the sources that perpendicular direction to maximum transverse stress is the easy and performant method to determine crack propagation direction.
- Using more realistic strength values for the plies and thick materials gives more realistic strength predictions. Because the strength of the fiber varies with its surrounding material, according to [55], [56] and [57]. Usage of these strengths called in-situ strength in the analyses, will result in better predictions.
- Stacking preference also has importance for the overall strength of the out-of-plane joints. The effect of ply directions of the joining components is not covered in past studies, but it deserves to be.
- The fatigue behavior of the T-joints should need more attention. Very few studies are available in the literature.

- Although lots of studies are available to understand the behavior of such out-of-plane joints under tensile loading, there are not enough work done for transverse bending and oblique loading cases. Since loading and geometry are symmetrical for the tensile loading, there should be more attention needed for the investigation of unsymmetrical loading cases, which are also prone to intralaminar failures rather than interlaminar.

- Utilizing the failure criterion for matrix cracks for such complex joints is a suitable method for predicting initiation and evolution of the crack in the laminate. It may be needed to utilize this kind of criteria to predict fiber and matrix failures in the compression side of the T-joints under bending loading.

- LaRC criteria are well-fitted to determine the out-of-plane structures' initiation and propagation of intralaminar failure.
- Discrete damage modeling technique should be utilized for the filler region to predict crack initiation and propagation independent of the mesh.

CHAPTER 3

METHOD

3.1 Brief Introduction to Failure of Composite Materials

Continuous fiber-reinforced composites are composed of laminates arraying of a combination of fibers with varying angles in a matrix. Matrix ensures the integrity of fibers, while fibers are the main load-carrying component. Due to its non-homogeneous nature, there are different kinds of composite material failure mechanisms, unlike isotropic materials. Although fiber and matrix can fail individually, the interaction of fiber-matrix failures is also typical in laminated composites, as seen in Figure 3-1.

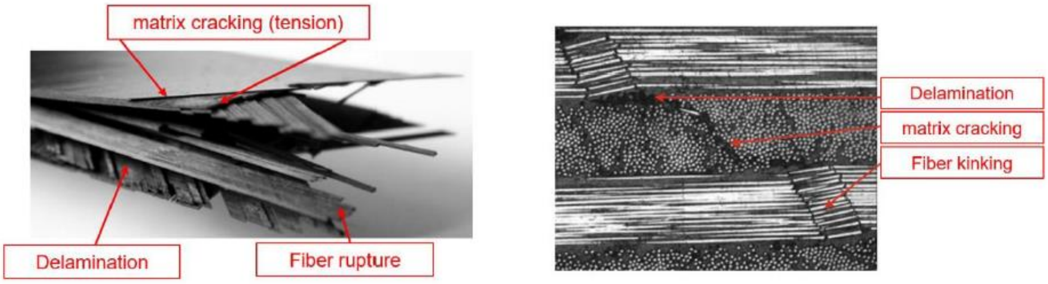

Figure 3-1 Composite laminate failure under tension and compression [68].

The main failure types of composite laminates are matrix failure, fiber failure, and delamination as stated in the [67]. The kinds of failure diversify under tension and compression. The left-hand side of Figure 3-1 represents typical failure of matrix, fiber, and delamination under typical tensile loading and the right-hand side is for compression loading. Matrix failure due to tension leads to cracking perpendicular to the loading direction. In contrast, compressive matrix failure is seen at an angle of nearly 45° by loading direction, indicating shear dominance under compression in Figure 3-2. Fiber rupture under tension requires high energy for fibers to break in their main load-carrying direction. Fiber kinking happens under compressive loading due to fiber buckling. Fiber buckling occurs due to the fiber misalignment during manufacturing or due to voids in the matrix causing matrix cracks that lead to fiber buckling.

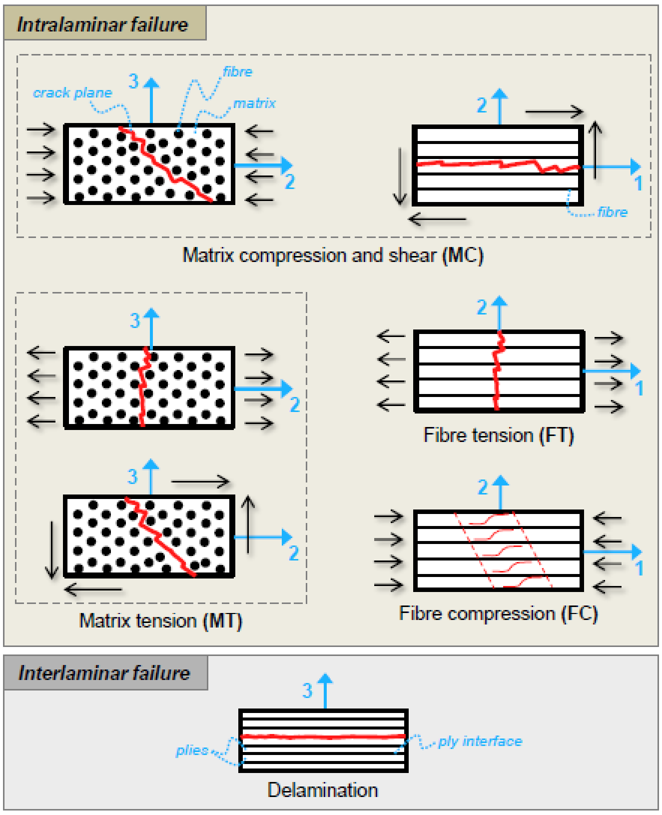

Figure 3-2 Composite material failure types [69]

As a third failure type, delamination is the separation of the ply interfaces in a laminate. Delamination detection is essential because integrity and load transfer between layers will be corrupted, and bending stiffness will decrease substantially. High transverse stresses through the thickness direction or matrix cracks can lead to delamination formation. Unlike in-plane failures of fiber and matrix, delamination is mainly triggered by out-of-plane forces, as seen in Figure 3-2. Similar to the separation of plies, debonding the laminate from adjacent laminates is also a type of delamination.

While the former failures, which are matrix, fiber, and fiber/matrix debonding, are intralaminar failures (failure in a ply), delamination/debond is an interlaminar failure (failure between plies) as clearly expressed in Figure 3-2.

The initiation of damage as a matrix crack will lead to a sequence of damages in fiber and layer interfaces. High-fidelity analytical and numerical structural analysis methods are needed to accurately capture failure initiation and progression in a composite laminate. Due to the complex geometries and large scales of most engineering cases, there are fewer analytical methods for estimating composite failures. As a result of this, numerical tools are in the foreground.

3.2 Damage Modeling in Composites

In the past few decades, strength-based methods have been generally used for numerical delamination predictions. Recently, fracture mechanics-based techniques such as Virtual Crack Closure Technique-VCCT, eXtended Finite Element Method-XFEM, and especially the Cohesive Zone Method-CZM are increasingly being used and validated by experimental results in most of the studies. Among these, XFEM and CZM are used in this thesis to simulate intralaminar and interlaminar failures, respectively. The prediction capability of failure onset and propagation without a predefined crack is the primary reason behind the selection of XFEM. While CZM is capable only of interlaminar damage initiation and propagation, XFEM has the capability of intralaminar failure onset and propagation when coupled with one of composite failure initiation and propagation criteria. For propagating cracks, enrichment regions of XFEM must be utilized for regions of interests.

In this thesis, two different methods are used to simulate the progressive failure of composite L-beam, while only CZM is utilized for T-joints. The first numerical method consists of XFEM coupled with LaRC05 failure initiation criteria as suggested by the ABAQUS [22]. The underlying features of this method are illustrated in Figure 3-3. Consisting of failure initiation criteria LaRC05 combined with cohesive segments in XFEM and the underlying theory is explained in detail in upcoming sections.

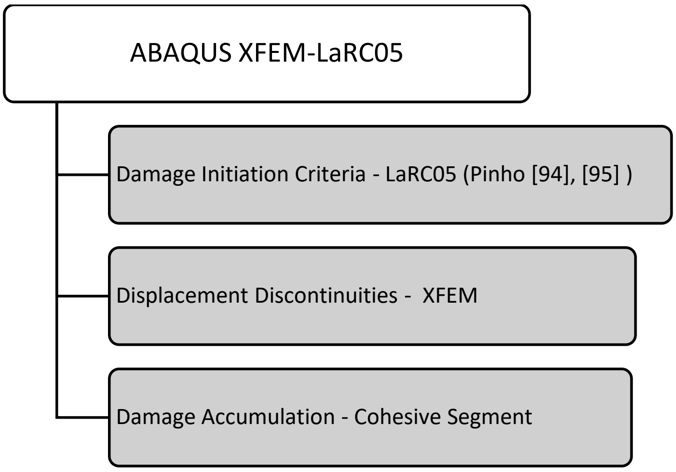

Figure 3-3 ABAQUS implementation of LaRC05 failure criteria combined with XFEM and cohesive segments

For the cohesive model, a bilinear traction-separation law together with quadratic stress interaction QUADS for damage initiation and BK law with mixed mode behavior for damage propagation are used in this study to simulate the progressive failure of bonding interfaces and ply interfaces. The CZM for modeling delamination-debond mechanisms is tabulated in Figure 3-4 are described briefly in the section.

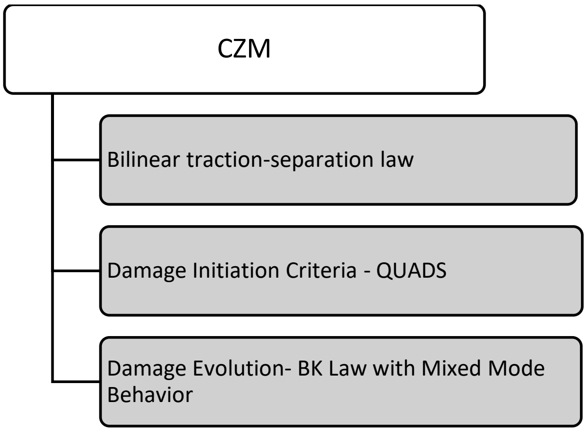

Figure 3-4 Characteristics of CZM employed throughout the thesis

3.2.1 Cohesive Zone Model-CZM

CZM is a damage mechanics approach combining strength-based initiation and fracture-based propagation rules to calculate damage within a cohesive damage zone ahead of the crack tip, as represented in Figure 3-5.

There are various cohesive laws for damage modeling in the cohesive zone, such as bilinear, linear-parabolic, exponential and trapezoidal Figure 3-6. Bilinear law is preferred for this study due to its accuracy throughout most of the literature on the topic of delamination modeling.

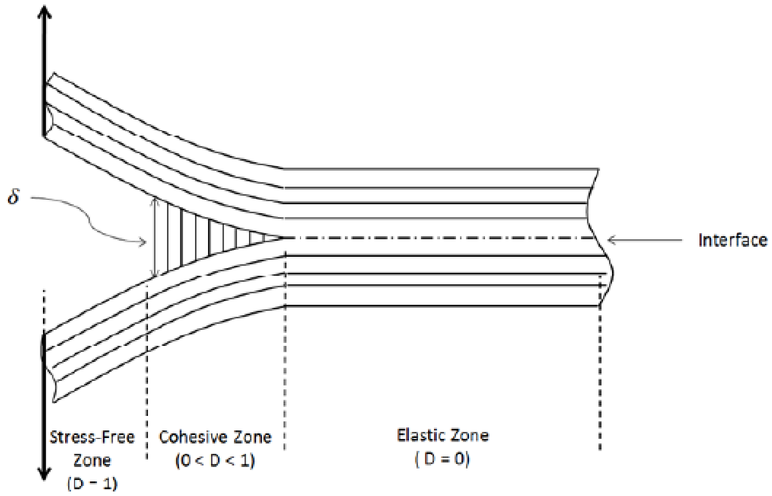

Figure 3-5 Cohesive zone definition

A relation between tractions and displacements across material discontinuity is used by CZM to model delamination. To initiate damage on the interface elements at cohesive damage zone, the traction value should reach the criteria set according to the delamination type. The energy needed to open a new crack surface, namely the critical energy release rate, should be achieved for the propagation.

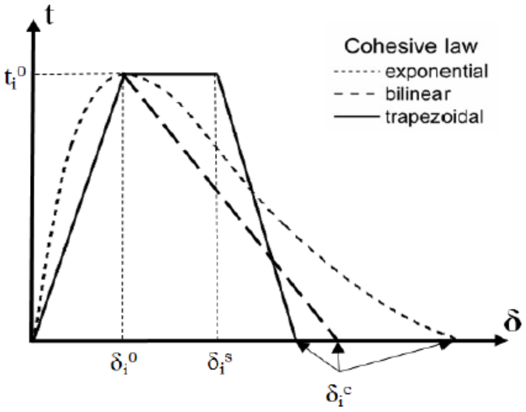

Figure 3-6 Cohesive laws

There are several types of constitutive relations for interface elements in ABAQUS [58]. However, two of them apply to model delamination: continuum and traction-separation behaviors. Continuum-based response is preferable for interfaces having finite thickness such as paste adhesives. In contrast, in the cases of negligibly small interface material thicknesses, the traction-separation response is more suitable for the constitutive response of cohesive elements [58]. In the same reference, debonding of skin-stringer interfaces is mentioned as an example case for traction-separation. Traction separation response is utilized for the cohesive element sections of bonding and ply interfaces throughout this thesis since there is a thin interface between the laminates.

3.2.1.1 Constitutive Response of CZM

Bilinear traction separation law in ABAQUS assumes a linear elastic behavior prior to damage initiation and stiffness degradation. An elastic constitutive matrix relates nominal stresses and strains through the interface.

$$\begin{Bmatrix} t_n \\ t_s \\ t_t \end{Bmatrix} = \begin{bmatrix} E_{nn} & & \\ & E_{ss} & \\ & & E_{tt} \end{bmatrix} \begin{Bmatrix} \varepsilon_n \\ \varepsilon_s \\ \varepsilon_t \end{Bmatrix} \tag{3.1}$$

where t_n, t_s, t_t are the nominal tractions in the normal and the two local shear directions, while the quantities $\varepsilon_n, \varepsilon_s, \varepsilon_t$ are the corresponding nominal strains, respectively.

$$\varepsilon_n = \frac{\delta_n}{T_0} \, , \varepsilon_s = \frac{\delta_s}{T_0} \, , \varepsilon_t = \frac{\delta_t}{T_0} \tag{3.2}$$

T_0 is the initial thickness of the cohesive element. For zero-thickness cohesive elements default value is used as 1, which means that separations are directly related to the tractions.

There are different forms of relations depending on the delamination type. Since mixed mode delamination is the main form of damage for T-joint structures as in many engineering applications, it is explained in detail in the upcoming section.

Mixed Mode Delamination

Even the pure loadings induce mixed mode loading on different T-joint sections due to their complex geometry. Damage initiation takes place before any single mode allowable traction or displacement. Therefore, initiation and propagation mechanisms under mixed mode should be analyzed carefully.

Initiation and propagation of the damage in cohesive elements under mixed mode loading are predicted by the law assigned to interface elements which are shown in Figure 3-7. The graph at the right, taken from the left mixed-mode cube, shows the mixed-mode triangle. Points A, B, and C are the initiation, arbitrary evolution, and final failure points respectively for mixed-mode delamination. Linear elastic behavior applies to the interface elements up to point A as bulk materials. The slope of this linear part defines the penalty stiffness of the elements, K.

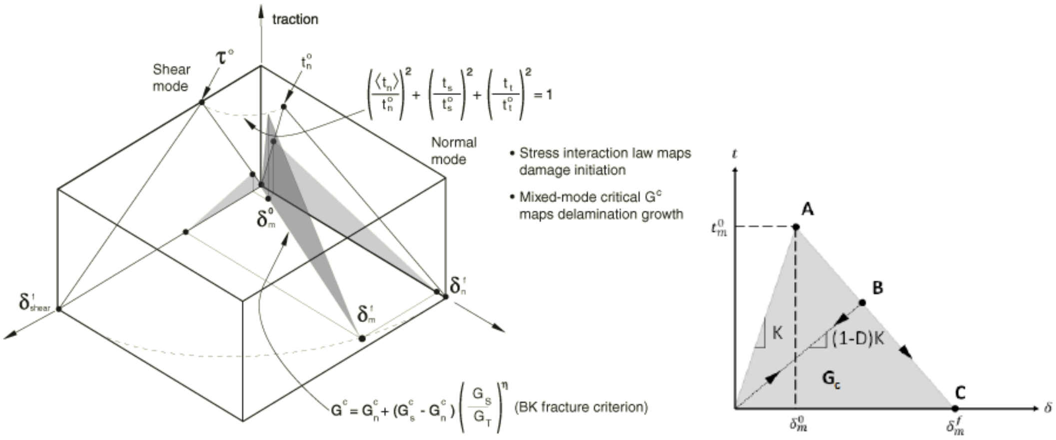

Figure 3-7 Bilinear law for mixed mode delamination [58]

The separations under mixed mode are the combination of the normal and shear modes named equivalent displacement by Camanho et al. [59] .

$$\delta_m = \sqrt{\langle \delta_n \rangle^2 + \delta_s^2 + \delta_t^2} = \sqrt{\langle \delta_n \rangle^2 + \delta_{shear}^2} \tag{3.3}$$

δ_{shear} represents the norm of the tangential relative displacements. The equivalent displacement at the initiation point can be defined as [59];

$$\delta_m^0 = \begin{cases} \delta_n^0 \delta_t^0 \sqrt{\frac{1+\beta^2}{(\delta_t^0)^2 + (\beta \delta_n^0)^2}} & , \delta_n > 0 \\ \delta_{shear}^0 & , \delta_n \leq 0 \end{cases} \tag{3.4}$$

with a mixed mode ratio formed as $\beta = \frac{\delta_{shear}}{\delta_n}$, provided that $\delta_n > 0$.

For the initiation of damage, stress based quadratic nominal stress criterion (QUADS) is employed.

$$\left\{\frac{\langle t_n \rangle}{t_n^0}\right\}^2 + \left\{\frac{t_s}{t_s^0}\right\}^2 + \left\{\frac{t_t}{t_t^0}\right\}^2 = 1 \tag{3.5}$$

$$\langle t_n \rangle = \frac{t_n + |t_n|}{2} \tag{3.6}$$

The normal stress inside the Macaulay bracket implies that compressive tractions do not cause damage onset on cohesive elements. The stress components are updated after the damage onset according to;

$$t_n = \begin{cases} (1-D)\overline{t_n} & , \ t_n \geq 0 \\ \overline{t_n} & , otherwise \end{cases} \quad (3.7)$$

$$t_s = (1-D)\overline{t_s} \quad (3.8)$$

$$t_t = (1-D)\overline{t_t} \quad (3.9)$$

where $\overline{t_n}, \overline{t_s}$ and $\overline{t_t}$ are the stress components without damage.

After damage initiation, linear softening behavior is assumed and according to that damage variable takes the form of;

$$D = \frac{\delta_m^f\,(\delta_m - \delta_m^0)}{\delta_m(\delta_m^f - \delta_m^0)} \quad (3.10)$$

where the effective displacement at complete failure, δ_m^f relative to the effective displacement at damage initiation, δ_m^0 and δ_m refers to the arbitrary point on evolution zone such as B.

Damage variable D is calculated in the line of A-C, which is the damage propagation zone in Figure 3-7 of mixed mode bilinear law. At point A, D=0, and at point C damage variable becomes unity. If unloading occurs between these two points, new loading follows a new path with reduced stiffness which is (1-D)K. Once the area under the traction separation curve equals damage evolution criterion G_C, failure is achieved in the elements, and complete stiffness degradation occurs. For the scope of this thesis, Benzeggagh-Kenane (BK) criterion is used as the propagation criterion assuming $G_s^C = G_t^C$ [60].

$$G^C = G_n^C + (G_s^C - G_n^C)\left\{\frac{G_S}{G_T}\right\}^{\eta} \quad (3.11)$$

where $G_S = G_s + G_t$, $G_T = G_s + G_n$, and η is a material parameter.

The failure displacement under mixed mode with BK criterion can be calculated [59] as;

$$\delta_m^f = \begin{cases} \frac{2}{K\delta_m^0}\left[G_n^C + (G_s^C - G_n^C)\left(\frac{\beta^2}{1+\beta^2}\right)^{\eta}\right] & , \delta_n > 0 \\ \sqrt{(\delta_s^f)^2 + (\delta_t^f)^2} & , \delta_n \leq 0 \end{cases} \tag{3.12}$$

Using initiation and failure displacements at an arbitrary point on traction separation curve after damage onset, the damage variable is defined using (3.10).

3.2.1.2 Cohesive Zone Length and Element Size

Element size strongly affects the load-displacement behavior, failure initiation, and propagation in numerical simulations. Since the CZM applies to the crack tip cohesive zone, the mesh density in this region is an important parameter. Accurate modeling of the problem requires sufficiently refined mesh in this region as the crack propagates. It is recommended by many authors [19], [20] to use at least five elements within cohesive zone length. The cohesive zone length, which is the distance between the crack tip and maximum traction as shown in Figure 3-5, can be calculated for different modes proposed by Turon [19] as;

$$L_{CZ_I} = \frac{ME_{22}G_{IC}}{\left(t_I^0\right)^2} \tag{3.13}$$

$$L_{CZ_{II}} = \frac{ME_{22}G_{IIC}}{\left(t_{II}^0\right)^2} \tag{3.14}$$

$$L_{CZ_{III}} = \frac{ME_{22}G_{IIIC}}{\left(t_{III}^0\right)^2} \tag{3.15}$$

where M is the parameter changes according to the model, but it is taken as 1, similar to Hillerborg as stated in [19]. E_{22} is modulus of the matrix and usually transverse modulus of composite ply. G_{IC}, G_{IIC} and G_{IIIC} are the fracture toughness values while t_I^0, t_{II}^0 and t_{III}^0 are the interlaminar strength values under mode I, II and III. For mixed mode case, taking minimum result of the above equations is preferred.

3.2.1.3 Finite Element Implementation of Cohesive Interfaces

ABAQUS offers two options to model the interface’s cohesive behavior: surface-based interaction and cohesive elements [22]. Both modeling techniques are used to compare their effectiveness for the T-joint model under tensile loading conditions only. Then cohesive elements were utilized for the primary failure investigation. A brief explanation is given in below for surface and element-based cohesive behaviors.

Although traction separation responses are similar in both ways of modeling, surface-based interaction is more accessible to implement than cohesive elements. Surface-to-surface contact is utilized to apply surface-based cohesive properties to the interface.

For element-based modeling, the thickness can be defined by specifying or using geometric thickness. However, there is no way to define thickness for the surface-based behavior. Therefore, cohesive elements are more appropriate for the cases of finite-thickness interfaces.

Moreover, surface-based interaction serves different interaction properties in addition to traction separation. Mostly “Hard Contact” property for normal direction and “Frictionless” property for tangential are used to prevent penetration of plies at layer interfaces. Therefore, surface-based cohesive behavior is advantageous if large deformation and compression exist on interfaces to prevent layer penetration. For the element-based implementation, additional contact definition should be attained to the interface surfaces to eliminate interpenetration.

Cohesive elements can be created in several ways for the element-based cohesive behavior, and the most preferred ones are as follows,

- Creating geometry and meshing with sweep path in the direction of thickness for finite thickness elements

- Using surrounding materials nodes by offset or project tools to create zero-thickness elements
- Using features of ABAQUS, such as inserting cohesive seams

Although implementing cohesive elements is challenging, ABAQUS offers an easy way in the latest versions from 2016 [22]. ABAQUS/CAE inserts cohesive pore pressure elements into the crack expected regions by making edge or surface selection according to 2D or 3D models. ABAQUS creates sets of these elements, their corresponding nodes, top and bottom surfaces. After insertion of these zero-thickness cohesive pore pressure elements, element type is changeable to the conventional cohesive interface type using sets created. Also, a cohesive section assignment is needed for desired constitutive response. Using this feature of ABAQUS version 2020, modeling difficulty of the zero-thickness cohesive elements is eliminated.

3.2.2 Extended Finite Element Method (XFEM)

Although modeling inter-laminar damage is straightforward with the CZM, existing of intra-laminar damages and their interactions requires accurate prediction of the crack growth without a predefined path or mesh update near the crack tip. Unlike the classical finite element method, XFEM can capture discontinuities in an element thanks to enriched degrees of freedom with displacement functions. Further, it does not require the mesh to align with the discontinuities. That is why it is called a meshless method.

The extended finite element method is introduced firstly by Belytschko and Black [61] based on the extension of the classical finite element method using enrichment near the crack tip proposed by Benzley [62] combined with the partition of unity concept proposed by Melenk and Babuska [63]. Although great effort has been made to development various versions of XFEM since 1999, the following sections will cover the implemented version in ABAQUS 2020 [22] for propagating crack cases.

3.2.2.1 Modeling Displacement Discontinuities

The XFEM implementation in ABAQUS/Standard is based on the phantom nodes with cohesive segments method for moving cracks coupled with initiation and evolution criteria [22].

Partition of Unity

By considering displacement jumps across the cracked element, propagation takes place across elements simultaneously, eliminating stress singularity inside an element. The elements inside the XFEM domain are duplicated, and phantom nodes are formed as superposed on the original nodes for the intact case. Once a crack cuts the element, the element is divided into two parts, each containing real and phantom nodes, as represented in Figure 3-8. Prior to cracking, phantom and real nodes are not tied any longer, but there exists a traction separation relation between the newly created part and the corresponding node on the other part, as shown in Figure 3-13.

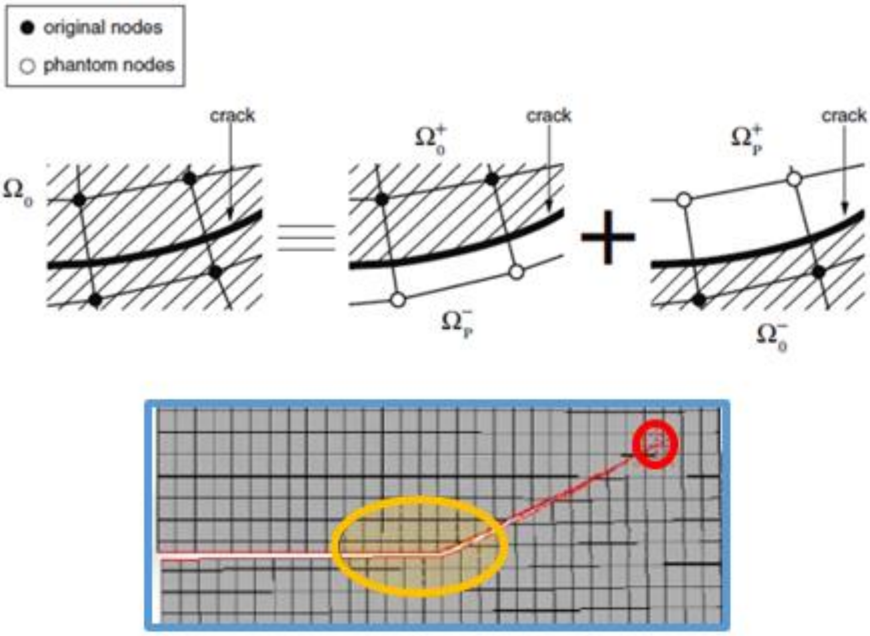

Figure 3-8 XFEM a) phantom nodes approach b) applicable regions of displacement vector components taken from [22]

The displacement vector function using partition of unity approach is as follows;

$$\boldsymbol{u} = \sum_{I=1}^{N} \boxed{N_I(x)[\boldsymbol{u}_I} + \boxed{H(x)\boldsymbol{a}_I} + \boxed{\sum_{\alpha=1}^{4} F_\alpha(x)\boldsymbol{b}_I^{\alpha}]} \tag{3.16}$$

where N is the set of nodes enriched by Heaviside function, $N_I(x)$ is shape function, $\boldsymbol{u}_I$ is nodal displacement vector, $H(x)$ is Heaviside jump function, $\boldsymbol{a}_I$ and $\boldsymbol{b}_I$ are nodal enriched degree of freedom vectors and $F_\alpha(x)$ is asymptotic crack tip singularity function. The blue part applies to all nodes in the model, while the yellow part is for the nodes whose shape function is cut by the crack that is the partition of shape function unity. Lastly, the red rectangle represents the asymptotic enriched singularity function for the crack tip. For propagating cracks, asymptotic singularity functions around the crack tip are not used in ABAQUS. Instead, a cohesive segment approach is used in the fracture process zone, and the element is cut completely to overcome discontinuity in an element.

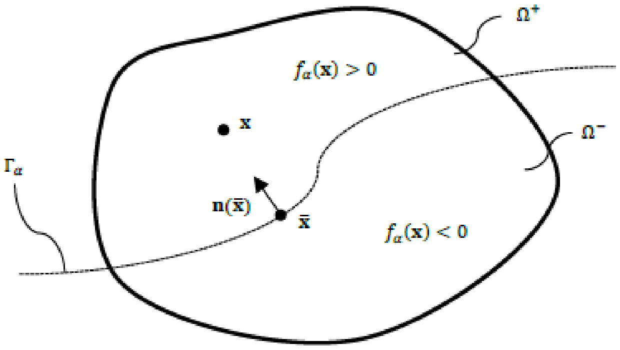

Figure 3-9 Crack representation using signed distance function [68]

$\Gamma_\alpha$representing a crack surface, signed distance function $f_\alpha(x)$ for an arbitrary point x is then;

$$f_\alpha(\boldsymbol{x}) = \min_{\bar{x}\epsilon\Gamma\_\alpha} \|\boldsymbol{x} - \bar{\boldsymbol{x}}\| \; sign(\boldsymbol{n}(\bar{\boldsymbol{x}}).(\boldsymbol{x} - \bar{\boldsymbol{x}})) \tag{3.17}$$

where $\bar{x}$ is the closest point to x on crack surface, $\boldsymbol{n}(\bar{\boldsymbol{x}})$ is the unit normal vector to the crack. The Heaviside function to capture displacement jump across the crack is then;

$$H(\boldsymbol{x}) = \begin{cases} 1 & if\ x > 0 \\ 0 & otherwise \end{cases} \quad (3.18)$$

Revising by signed distance function results in;

$$H\big(f_\alpha(\boldsymbol{x})\big) = \begin{cases} 1 & \boldsymbol{x} \epsilon \Omega^+ \\ 0 & \boldsymbol{x} \epsilon \Omega^- \end{cases} \quad (3.19)$$

Therefore, displacement field in discontinuous domain can be calculated by combining domains as;

$$u(\boldsymbol{x})|_{\boldsymbol{x}\epsilon\Omega} = H\big(f_\alpha(\boldsymbol{x})\big)u(\boldsymbol{x})|_{\boldsymbol{x}\epsilon\Omega^+} + \big(1 - H\big(f_\alpha(\boldsymbol{x})\big)\big)u(\boldsymbol{x})|_{\boldsymbol{x}\epsilon\Omega^-} \quad (3.20)$$

Level Set Method

The level set method is a numerical technique that defines the crack geometry and tracks its motion thanks to signed distance functions without remeshing. It requires only nodal displacement data without any need for explicit representation.

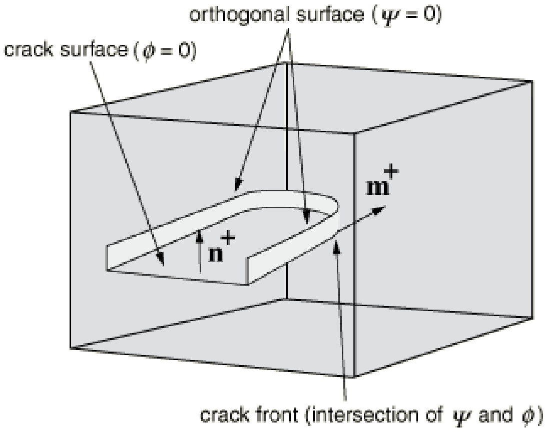

Figure 3-10 Nonplanar crack geometry by signed distance functions [22]

The first set is Φ (phi) describing crack surface and the second is Ψ (psi) used to determine the crack front with the intersection with Φ=0. For propagating cracks, only phi function is enough to determine the crack tip.

For propagating cracks Phi Level Set Method (PHILSM in ABAQUS) function is calculated for only the cracked elements to represent the signed distance. At the crack surface, it has a value of zero, while one side of the crack has positive values and on the other side it has negative values. Suppose, nodes of an element correspond to both sides, than by linear fit crack location where PHILSM=0 is determined. Knowing the coordinates of the nodes and corresponding PHILSM values, the crack tip can be easily determined.

3.2.2.2 Constitutive Response of XFEM

Damage Initiation

Built-in criteria LaRC05 is used for damage initiation for matrix and fiber failures. The details of the criteria are explained in detail in section 3.2.4. Degradation of cohesive response begins when the initiation criterion is met in that stress state. For initiation of failure, failure criterion is checked whether it is in tolerance;

$$1.0 \leq f \leq 1.0 + f_{tol} \tag{3.21}$$

f_{tol} is 0.05 as default. If $1.0 + f_{tol} < f$ than time increment is reduced to satisfy initiation criterion.

LaRC05 criteria are composed of four different criteria for different damage mechanisms observed in fiber-reinforced composites which are matrix failure, fiber kinking, fiber splitting, and fiber tension. The most severe failure index governs the initiation of an enriched element.

$$f = max\{f_{matrix}, f_{kinking}, f_{splitting}, f_{tension}\} \tag{3.22}$$

The stress values to calculate failure indices are taken locally from the neighboring element centroid to the crack tip, as shown in Figure 3-11 a). For the case of coarse meshes, nonlocal averaging of the stresses within a radius can be used to improve the accuracy of the both the crack initiation index and crack propagation direction. Crack propagation direction is set by LaRC05 built-in subroutine as fracture plane and misalignment angles.

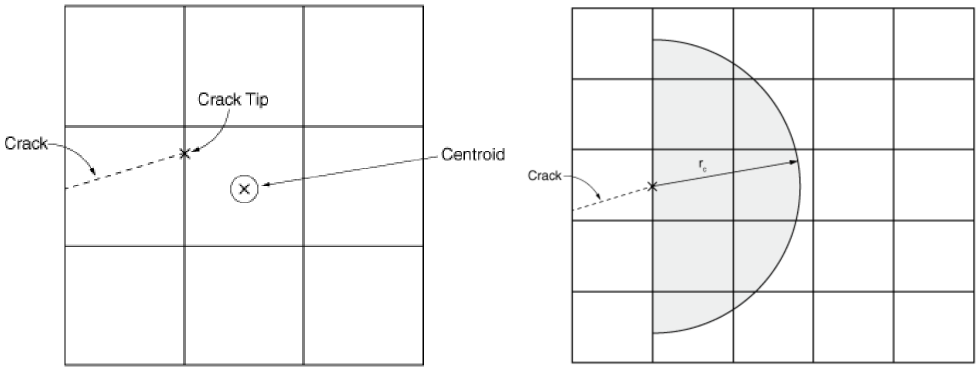

Figure 3-11 Crack tip stress calculation from a) element centroid b) nonlocal averaging taken from [22]

Cohesive Segment Approach

The cohesive segment approach allows the contribution of cohesive behavior to the contact normal stresses for opened crack. When the crack is closed, pressure-overclosure relations are applied. XFEM-based cohesive segment method uses linear elastic traction separation behavior before initiation as in CZM, explained in detail in Section 3.2.1.1. The only difference is that the XFEM-based cohesive segment method does not require material properties (K_{nn}, K_{ss}, K_{tt}) to be defined. They are calculated using the elastic properties of bulk material.

$$\begin{Bmatrix} t_n \\ t_s \\ t_t \end{Bmatrix} = \begin{bmatrix} K_{nn} & & \\ & K_{ss} & \\ & & K_{tt} \end{bmatrix} \begin{Bmatrix} \delta_n \\ \delta_s \\ \delta_t \end{Bmatrix} \tag{3.23}$$

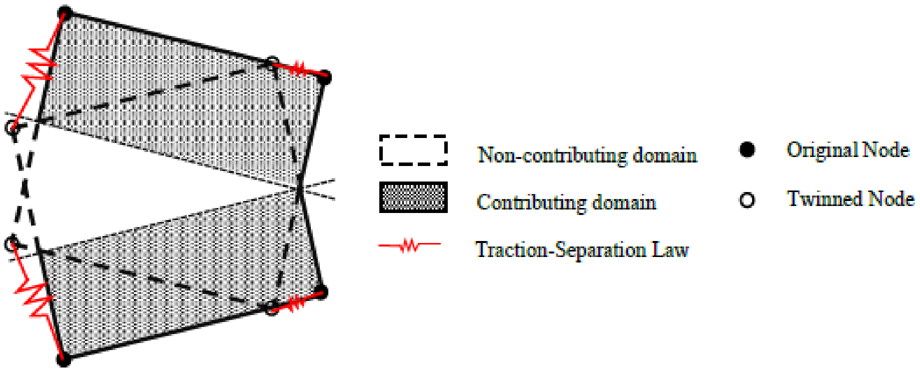

Figure 3-12 Representation of XFEM-based traction separation taken from [68]

Damage Evolution

The damage evolution of cohesive behavior is similar to that described in Section 3.2.1.1. The cohesive stiffness is degraded when initiation takes place in an element. The proportionality of the reduction of tractions is in the way that meets the fracture toughness or displacement for that specific failure criterion. The damage variable is, in this case, calculated for the intersection between the crack surface and edges of the element, as represented in Figure 3-12. As the damage variable evolves, the traction components are updated according to the way explained in Section 3.2.1.1.

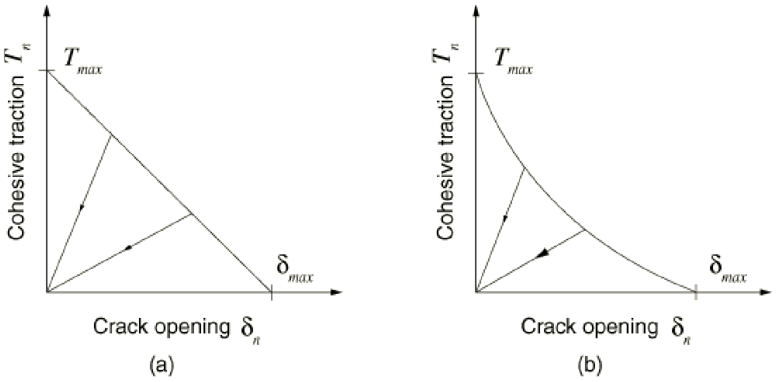

Figure 3-13 XFEM-based linear and nonlinear traction-separation response taken from [22]

Energy or displacement-based damage evolution laws compatible with traction separation law can be used with the XFEM-enriched elements. The evolution of damage is defined separately for each failure mode which are matrix cracking, fiber kinking, fiber splitting and fiber tension. For matrix crack criterion, mixed mode BK law is utilized, while for other modes of failures, single mode fracture energies are used. Fracture energies are determined from the material tests which are Double Cantilever Beam (DCB) for mode-I toughness, Four Point End Notched Flexure (4-ENF) Test for mode-II toughness, Compact Compression Test for kinking and splitting fracture energies and finally Compact Tension Test for the fiber tension fracture toughness. For matrix crack propagation, if delamination is predicted according to the shear lag model, tractions are reduced to zero directly according to Pinho et al. [95].

3.2.2.3 Limitations

Although significant developments have been achieved over time since first implemented into ABAQUS 6.9 version, the XFEM feature still has limitations. Some important ones are listed as follows;

- Allows multiple crack initiation in a single XFEM region only if they initiate in the same step. Otherwise, new crack initiations are not allowed by the program until the first crack reaches any boundary of the region. Therefore defining enrichment regions separately to expected crack initiation sites is essential.
- Although mesh size is not so important for the stationary cracks due to asymptotic crack tip singularity functions, for propagating cracks, the asymptotic near-tip singularity functions are not included in the enrichment scheme, as shown in Figure 3-14, and mesh size should be small enough to encounter correct stress values.

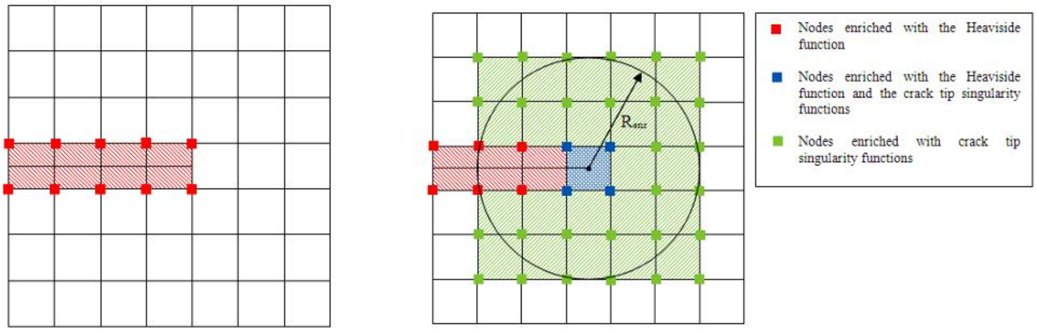

(a) Propagating cracks.

(b) Stationary cracks.

Figure 3-14 Enrichment scheme differences between (a) propagating cracks and (b) stationary cracks taken from [64].

- An enriched element cannot be intersected by more than one crack.
- The turning angle of a crack is limited by 90° in an increment.
- Available only in ABAQUS/Standard
- Supports limited element types

3.2.3 In-Situ Strength

Transverse matrix cracks due to in-plane shear and transverse stresses in composite laminates lead to the ultimate failure. Therefore, many authors focused on composite materials' matrix crack-driven failure. The matrix-dominated failure estimation relies on structural properties instead of material properties. Structural properties depending on the ply thickness, the orientation of the adjoining plies, and the location of the ply change the boundary condition of the fracture mechanics for matrix crack. Therefore, criteria accounting physics associated with micromechanical level matrix failure proposed by Puck [83] [84], Davila and Camanho [93], Pinho [94], and Catalanotti [98] use in-situ strengths. Prediction of matrix-dominated failure of composites can be made accurately using in-situ strengths instead of UD ply strengths emphasized by Davila, Camanho [93], and Pinho [94].

The effect of in-situ transverse strength was first observed by Parvizi et al. [85]. Parvizi investigated the cracking constraint in a thin 90° ply embedded with 0° plies compared to the thick ply in a cross-ply laminate. They also found the thickness of the inner ply affected the transverse matrix cracking. Therefore, the number of plies stacked together affects the strength.

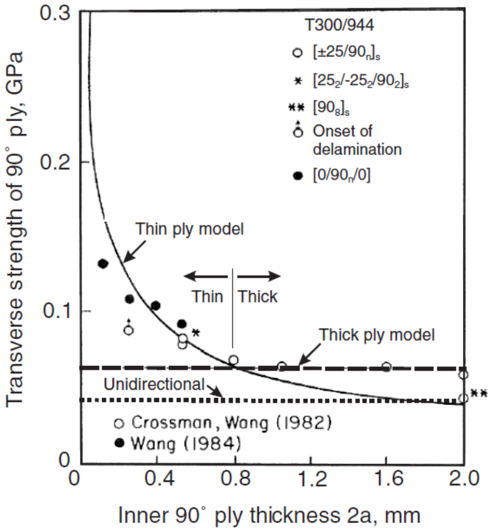

Figure 3-15 Comparison of theoretical results by Dvorak [90] and experimental data by Crossman [86] and Wang [89] (modified figure taken from [93])

After Parvizi’s findings, in-situ effects are investigated experimentally [86] - [89] and analytically [90] - [92] by several authors. Dvorak [90] proposed an analytical approach for in-situ transverse tensile strength calculation and compared it to the experimental data of Crossman [86] and Wang [89], as seen in Figure 3-15. Dvorak's transverse tensile in-situ strength calculation shows a good correlation with the experiments.

To account for the effect of in-plane shear stress in the in-situ strength, Laws [91] used combined law but overestimated the in-situ shear strength due to the shear linearity assumption. Then Camanho et al. [96] improved Dvorak and Law’s approach by accounting for nonlinear shear behavior. It is obvious in Figure 3-16 that in-situ strength assuming linear behavior of thin ply with thickness 0.2 mm is nearly two times that of assuming nonlinear behavior.

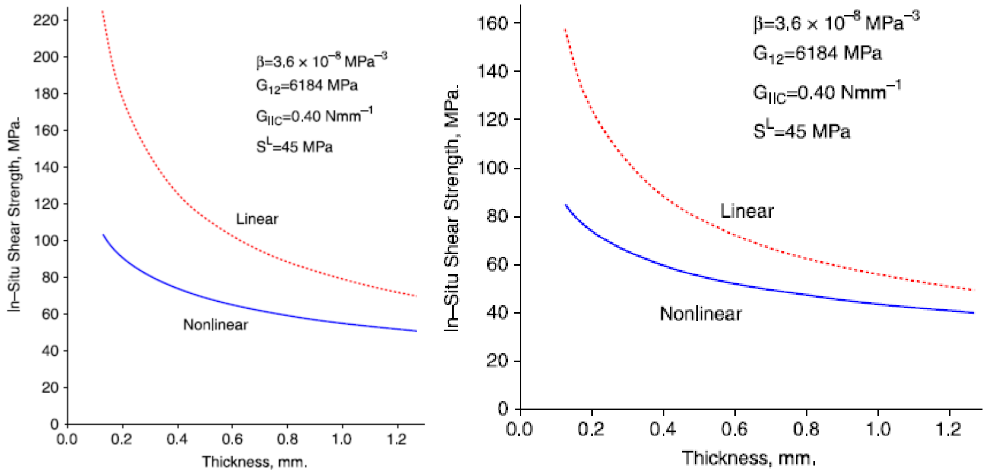

Figure 3-16 Linear and nonlinear in-situ shear strengths of thin embedded and thin outer plies respectively [96]

In this study, in-situ strengths are calculated using analytical expressions published by Camanho et al. [96] based on Dvorak and Law’s proposed method using fracture mechanics approach considering a slit crack within a ply. Slit crack represents the macroscopic effect of micromechanical conditions: matrix-fiber de-bond, manufacturing defects, voids, fiber misplacements, residual thermal stresses etc.

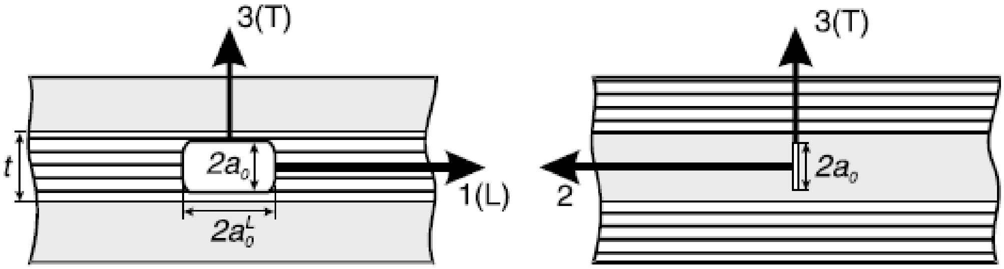

Figure 3-17 Slit crack geometry by Dvorak [90]

The slit crack is lying on the 1-3 plane, as shown in Figure 3-17 in a general form. This crack can grow in longitudinal-1, transverse-3, or in both directions. The interaction energy is expressed as follows, considering nonlinear shear behavior and neglecting the effects of neighboring plies;

$$E_{int} = \frac{1}{2}\pi a_0^2[\Lambda_{22}^0 \sigma_{22}^0 + \chi(\gamma_{12})] \tag{3.24}$$

Where $\chi(\gamma_{12}) = 2\int_0^{\gamma_{12}} \sigma_{12} d\gamma_{12}$ and $\overset{\circ}{\Lambda}_{22} = 2\left(\frac{1}{E_2} - \frac{\upsilon_{21}^2}{E_1}\right)$

Assuming plane stress conditions and mixed mode loading, energy release rates G(T) and G(L) are expressed in [90] as;

$$G(T) = \frac{1}{2}\frac{\partial E_{int}}{\partial a_0} \tag{3.25}$$

$$G(L) = \frac{E_{int}}{2a_0} \tag{3.26}$$

Then, mode I and mode II components for transverse and longitudinal propagations are obtained as follows;

$$G_I(T) = \frac{\pi a_0}{2}\Lambda_{22}^0 \sigma_{22}^0 \tag{3.27}$$

$$G_{II}(T) = \frac{\pi a_0}{2}\chi(\gamma_{12}) \tag{3.28}$$

$$G_I(L) = \frac{\pi a_0}{4}\Lambda_{22}^0 \sigma_{22}^0 \tag{3.29}$$

$$G_{II}(L) = \frac{\pi a_0}{4}\chi(\gamma_{12}) \tag{3.30}$$

According to boundary conditions and expected crack propagation, the energy release rate equation is selected from above, and obtaining corresponding fracture toughness equations, in situ strengths are derived accordingly as described in [96]. Derived versions are provided in the following sections.

Thick Embedded Ply

A slit crack in a thick embedded ply is shown in Figure 3-18. This crack is likely to grow in the transverse direction due to the significant energy release rate in this direction. Therefore, $G_I(T)$ and $G_{II}(T)$ forms of the energy release rates are used for the calculations.

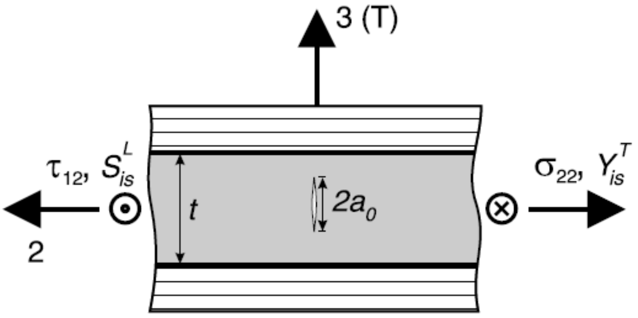

Figure 3-18 Thick embedded ply [96]

As Y_T^{UD} is unidirectional transverse tensile strength, the transverse tensile in-situ strength is in the form of;

$$Y_T^{is,thick} = 1.12\sqrt{2}Y_T^{UD} \tag{3.31}$$

The in-situ shear strength is given by;

$$S_L^{is,thick} = \sqrt{\frac{\left(1+\beta\phi G_{12}^2\right)^{\frac{1}{2}}-1}{3\beta G_{12}}} \tag{3.32}$$

where, β is shear response factor, G_{12}, in plane shear modulus, and ϕ is the expression as below for thick plies;

$$\phi = \frac{12\left(S_L^{UD}\right)^2}{G_{12}} + 18\beta\left(S_L^{UD}\right)^4 \tag{3.33}$$

where, S_L^{UD} is the unidirectional in-plane shear strength.

The β shear response factor defines the nonlinearity of the shear stress according to Hahn and Tsai [97]. For the linear behavior, it is taken as 0. Equation (3.34) is fitted to material shear stress-shear strain curve and value of β is determined.

$$\gamma_{12} = \frac{1}{G_{12}}\,\sigma_{12} + \beta\sigma_{12}^3 \tag{3.34}$$

For the in-situ strength of out-of-plane shear and transverse compression, Catalanotti proposed Equation (3.35) and (3.36) relating to in-plane shear strength as;

$$S_T^{is} = \frac{(2\sin^2\alpha_0 - 1)}{\eta_L sin2\alpha_0} S_L^{is} \tag{3.35}$$

$$Y_C^{is} = \frac{(1 - 2\cos^2\alpha_0)}{\eta_L \cos^2\alpha_0} S_L^{is} \tag{3.36}$$

where η_L is the longitudinal friction coefficient which is the slope in $\sigma_{22} - \tau_{12}$ diagram at $\sigma_{22} = 0$;

$$\eta_L = -\frac{\partial\tau_{12}}{\sigma_{22}}\bigg|_{\sigma_{22}=0} \tag{3.37}$$

Although it is a material property that needs to be measured, if test data is not available, then it can be calculated as follows as in the LaRC03-LaRC04 criteria [93],

$$\eta_L = -\frac{S_L^{UD} cos2\alpha_0}{\mathrm{Y_C^{UD}} \cos^2\alpha_0} \tag{3.38}$$

$\mathrm{Y_C}$ is transverse compressive strength and α_0 is the matrix fracture angle under pure compression which can be taken from test data but used as 53° according to [93].

Thin Embedded Ply

A slit crack in a thin embedded ply is shown in Figure 3-19. This crack is likely to grow in the longitudinal direction because it envelops the ply thickness. Therefore, $G_I(L)$ and $G_{II}(L)$ forms of the energy release rates are used for the calculations.

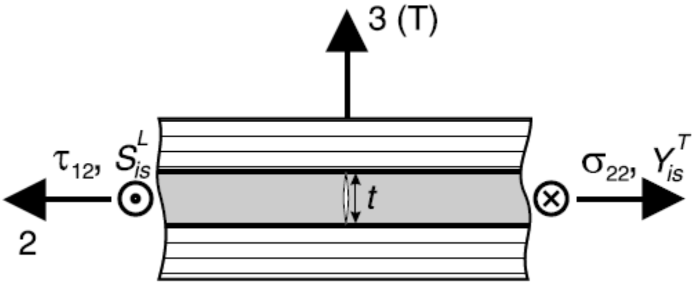

Figure 3-19 Thin embedded ply [96]

As G_{IC} is the mode I fracture toughness, t is the ply thickness, then the transverse tensile in-situ strength is in the form of;

$$Y_T^{is,thin,e} = \sqrt{\frac{8G_{IC}}{\pi t \overset{\circ}{\Lambda}_{22}}} \tag{3.39}$$

where $\overset{\circ}{\Lambda}_{22}$ is the expression defined by the E_1 and E_2 elastic moduli in 1 and 2 directions and ν_{21} is Poisson's ratio in 21 plane as follows;

$$\overset{\circ}{\Lambda}_{22} = 2\left(\frac{1}{E_2} - \frac{\upsilon_{21}^2}{E_1}\right) \tag{3.40}$$

The in-situ shear strength is given by the Equation (3.32) is valid for thin ply case, but the expression for ϕ is given as;

$$\phi = \frac{24G_{IIC}}{\pi t} \tag{3.41}$$

G_{IIC} is mode II fracture toughness.

For the in-situ strength of out-of-plane shear and transverse compression, Equations (3.35) and (3.36) are applicable.

Thin Outer Ply

A slit crack in a thin outer ply is shown in Figure 3-20. This is a special version of thin embedded case with a lack of second embedded surface causing energy release rate to be magnified.

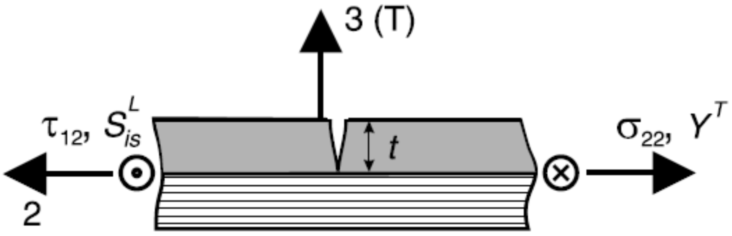

Figure 3-20 Thin outer ply [96]

The transverse tensile in-situ strength is in the form of;

$$Y_T^{is,thin,o} = \sqrt{\frac{4G_{IC}}{\pi t \mathring{\Lambda}_{22}}} \tag{3.42}$$

The in-situ shear strength is given by Equation (3.32) is valid for thin outer ply case, but the expression for ϕ is given as;

$$\phi = \frac{48G_{IIC}}{\pi t} \tag{3.43}$$

For the in-situ strength of out-of-plane shear and transverse compression, Equations (3.35) and (3.36) are applicable.

3.2.4 LaRC05 Failure Criteria

There are several approaches determining the failure of composite materials. These approaches' capability to encounter several objectives is investigated with the World Wide Failure Exercise series. The first WWFE was started in 1996 to review existing criteria on composite materials under a 2D stress state and ended in 2004 with the results published in [80]. By considering the weakness of existing criteria, Davila, Camanho, and Rose proposed new criteria for a 2D stress state called LaRC03, revising Puck’s matrix fracture model in [83] and [84]. Pinho et al. [67] revised existing criteria and developed them called LaRC04 criteria, including 3D stress state and shear nonlinearity. The latest version of the NASA Langley Research Center (LaRC) family of failure criteria is LaRC05, which has shown a good correlation with the experimental results of WWFE-II [81], [82]. LaRC05 criteria are the revised matrix failure version of LaRC04 by Pinho et. al.[94], [95] during WWFE-II. Due to boundary conditions and thickness, it accounts for in-situ strength effects in the cross-ply laminates. Since micro-cracks formed during manufacturing are accounted for in the in-situ strength calculations, the criteria are physically based and show better predictions. LaRC05 considers four types of failure criteria: matrix failure, fiber kinking, fiber splitting, and fiber tension.

3.2.4.1 Matrix Failure

Predicting the matrix failure by accounting stresses on the fracture plane is first proposed by Puck and co-workers [83] [84] with modifications on Mohr-Coulomb criterion. The matrix failure index in LaRC05 criteria is an extension of Puck’s model regarding in-situ strengths of the plies and friction effects.

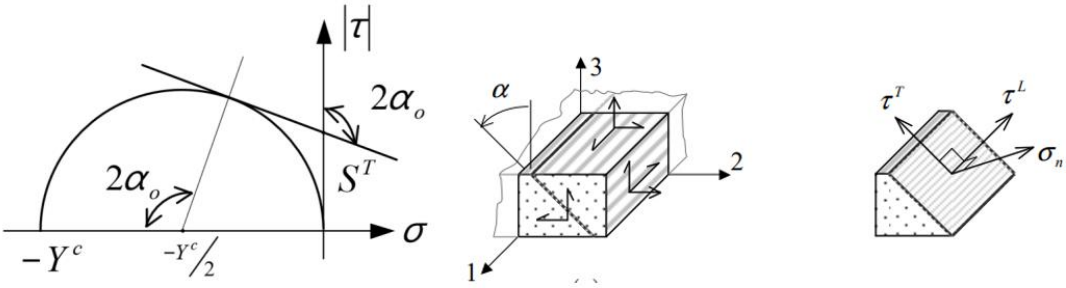

Figure 3-21 Representation of a) Mohr's circle for pure transverse compression b) fracture plane in through the thickness c) stress components acting on 3D fracture plane adapted from [67]

Mohr-Coulomb criterion states that under biaxial stresses in the normal direction, fracture occurs tangent to the fracture line. For pure compression, the fracture plane angle, α_0 is a material property measured experimentally. For carbon and glass composites, the typical range for α_0 ranges from 51° to 55° [67], [83]. For general loading, fracture plane angle α depends on the stress state, as shown in Figure 3-21 b). It is selected numerically, which maximizes the matrix failure index in the range $0° \leq \alpha \leq 180°$.

The matrix failure index is determined as;

$$FI_M = \left(\frac{\tau_T}{S_T^{is} - \eta_T \sigma_N}\right)^2 + \left(\frac{\tau_L}{S_L^{is} - \eta_L \sigma_N}\right)^2 + \left(\frac{\langle \sigma_N \rangle_+}{Y_T^{is}}\right)^2 \tag{3.44}$$

where τ_T, τ_L, σ_N are stress components acting on the fracture plane as represented in Figure 3-21 c) and are calculated by the stress transformation as below;

$$\sigma_N = \frac{\sigma_2 + \sigma_3}{2} + \frac{\sigma_2 - \sigma_3}{2} \cos(2\alpha) + \tau_{23} \sin(2\alpha) \tag{3.45}$$

$$\tau_T = -\frac{\sigma_2 - \sigma_3}{2} \sin(2\alpha) + \tau_{23} \cos(2\alpha) \tag{3.46}$$

$$\tau_L = \tau_{12} \cos(\alpha) + \tau_{31} \sin(\alpha) \tag{3.47}$$

To account friction effect on the fracture plane, friction coefficients $\eta_L \ and \ \eta_T$ are used to increase shear strengths in the case of compressive traction and to decrease shear strengths under tensile traction. η_T is obtained experimentally from pure compression test as

$$\eta_T = -\frac{1}{\tan(2\alpha_0)} \tag{3.48}$$

η_L is also a material property, but it can be calculated from Equation (3.38) placed in in-situ strength section. The McCauley bracket in failure index calculation means that $\langle x \rangle_+ = max\{0, x\}$.

3.2.4.2 Fiber Kinking and Splitting

Failure of fibers under compression results from shear-dominated matrix failure in a misaligned frame. Observations from experiments under combined longitudinal compression and in plane shear [100] proposed that if longitudinal compressive stresses are greater than half of the strength ($\frac{X_C}{2}$), fiber kinking occurs. On the other hand, if longitudinal compression is less than the half strength, then fiber kinking does not occur according to the tests under longitudinal compression and transverse tension combined case in [101]. Based on these observations, two different failure criteria are discussed in this section which are fiber kinking and splitting.

The same criterion is applied to both failure types according to the magnitude of longitudinal compression. If $\sigma_1 \leq -\frac{X_C}{2}$, FI is for fiber kinking. Otherwise $\sigma_1 \geq -\frac{X_C}{2}$, FI is for fiber splitting.

The failure index for fiber kinking and splitting is then;

$$FI_{KINK} = FI_{SPLIT} = \left(\frac{\tau_{23}^{m}}{S_T^{is} - \eta_T \sigma_2^{m}}\right)^2 + \left(\frac{\tau_{12}^{m}}{S_L^{is} - \eta_L \sigma_2^{m}}\right)^2 + \left(\frac{\langle \sigma_2^{m} \rangle_+}{Y_T^{is}}\right)^2 \tag{3.49}$$

where $\tau_{23}^{m}, \tau_{12}^{m}, \sigma_2^{m}$ are the stresses in the kink band coordinates shown in Figure 3-22 a). The stress components are rotated twice to the fiber misalignment frame. The first stress rotations to the kink-band plane ψ are expressed as;

$$\sigma_2^{\psi} = \cos^2\psi \sigma_2 + \sin^2\psi \sigma_3 + 2 sin\psi cos\psi \tau_{23} \tag{3.50}$$

$$\tau_{12}^{\psi} = \tau_{12} cos\psi + \tau_{31} \sin\psi \tag{3.51}$$

$$\tau_{23}^{\psi} = -sin\psi cos\psi \sigma_2 + sin\psi cos\psi \sigma_3 + (\cos^2\psi - \sin^2\psi)\tau_{23} \tag{3.52}$$

$$\tau_{31}^{\psi} = \tau_{31} cos\psi - \tau_{12} sin\psi \tag{3.53}$$

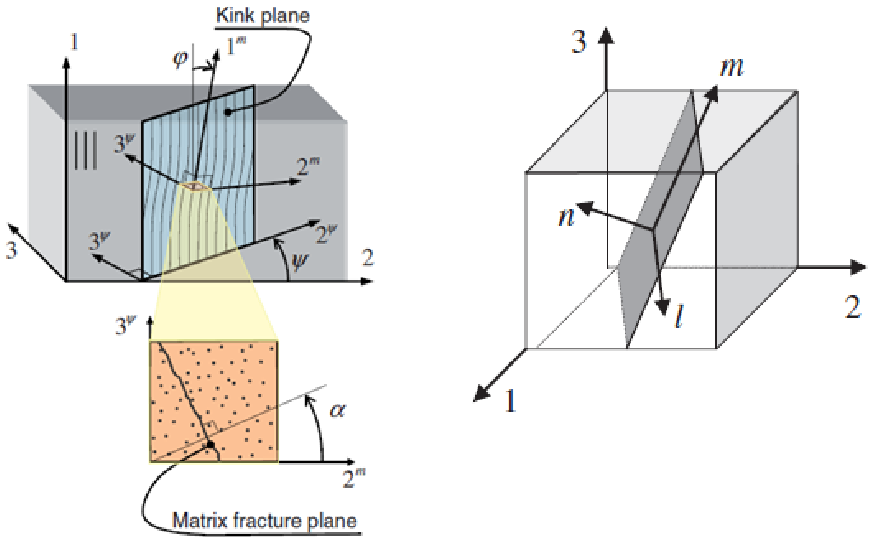

Figure 3-22 a) Kink-band formation model b) coordinate system aligned with the defect adapted from [94]

The angle of the kink band, ψ is determined numerically similar to matrix fracture plane angle in order to maximize the fiber compression failure index. The second transformation is to the fiber misalignment frame,

$$\sigma_2^m = \sin^2\varphi\ \sigma_1 + \cos^2\varphi\, \sigma_2^\psi - 2 sin\varphi cos\varphi \tau_{12}^\psi \tag{3.54}$$

$$\tau_{12}^m = -sin\varphi cos\varphi \sigma_1 + sin\varphi cos\varphi \sigma_2^\psi + (\cos^2\varphi - \sin^2\varphi)\, \tau_{12}^\psi \tag{3.55}$$

$$\tau_{23}^\psi = \tau_{23}^\psi cos\varphi - \tau_{31}^\psi sin\varphi \tag{3.56}$$

where φ is the fiber misalignment angle the sum of the initial misalignment angle φ^0 produced by manufacturing defect and shear strain γ_{m^0} aligned with the manufacturing defect coordinate represented in Figure 3-22 b). γ_{m^0} is expressed as a function of corresponding shear stress in same plane.

$$\varphi = sign\left(\tau_{12}^\psi\right)\varphi^0 + \gamma_{m^0} \tag{3.57}$$

$$\gamma_{m^0} = \gamma(\tau_{m^0}) \tag{3.58}$$

The material property $\varphi^0$is found by solving iterative equation given below;

$$\varphi^0 = \varphi^c - \gamma(\tfrac{1}{2}\sin(2\varphi^0)\, X_C) \tag{3.59}$$

where φ^c is expressed as [67],

$$\varphi^c = arctan\left(\frac{1-\sqrt{1-4\left(\frac{S_L}{X_C}+\eta_L\right)\frac{S_L}{X_C}}}{2\left(\frac{S_L}{X_C}+\eta_L\right)}\right) \tag{3.60}$$

3.2.4.3 Fiber Tension

The maximum stress criterion on fiber tensile failure is well correlated with the experiments during WWFE-I [80]. Hence, maximum allowable stress criterion is adapted for fiber tensile failure as;

$$FI_{FT} = \frac{\langle\sigma_1\rangle_+}{X_T} \tag{3.61}$$

3.2.4.4 Finite Element Implementation of LaRC05 Criteria

The LaRC05 built-in subroutine is used combined with the XFEM feature of ABAQUS 2020. For the used version, it has not yet been integrated into the user interface, that is why material names located within the region of interest must begin with the initial string ‘ABQ_LARC05_DMGINI’to invoke the DMGINI routine for damage initiation for XFEM enriched elements. Since there is no user interface, 15 material parameters should be given to the input file, as referenced in [22]. For the regions which are interested in the failure, the propagating crack should be defined from the interaction-special-XFEM path in ABAQUS. To prevent penetration of crack surfaces, there should be defined an interaction property.

CHAPTER 4

FAILURE ANALYSIS OF L-BEAM STRUCTURES

In this part of the thesis, unidirectional and cross-ply thick L-beam specimens investigated experimentally by Taşdemir and Çöker [106] will be analyzed using ABAQUS/Standard dynamic-implicit solver. Two different approaches which are: CZM and XFEM coupled with LaRC05 failure criteria will be used. Since the numerical study on a unidirectional specimen was performed by Ata and Çöker [103] and experimental results were available, the numerical methods will be validated first using the unidirectional case. Then detailed numerical modeling of cross-ply thick laminate will be performed. The complete list of the studies is shown in Table 1. The study aims to determine the capability of the physically based failure criterion and XFEM on matrix crack-induced failure prediction compared to the pure delamination modeling approach CZM in the curved specimens.

Table 1 Breakdown of the studies performed at Chapter 4

Laminate	**Model**		**Study**
Unidirectional $[0_3]$	3D	CZM	Intact Strengths
		XFEM-LaRC05	
	3D-slice	CZM	
		XFEM-LaRC05	
Cross Ply $[0_3/90_3/0_3/90_3/0_3]_s$	3D-slice	CZM	Intact Strengths
			Study 1 - Interlaminar strength reduction in 1st and 2nd cohesive layers
			Study 2 - Interlaminar strength reduction in all cohesive layers
		XFEM-LaRC05	Intact Strengths
			Study 1 - Intralaminar strength reduction in 1st $[90_3]$ plies
			Study 2 - Reduction in 1st and 2nd $[90_3]$ plies

4.1 Numerical Modeling

4.1.1 Geometry and Boundary Conditions

Since experimental studies of Taşdemir & Çöker [106] on thick curved composite beams are taken as a reference for the scope of this chapter, geometric dimensions and boundary conditions corresponding to the experimental procedure are implemented. L-beam is composed of the lower arm, upper arm, and curved regions.

The illustration of the geometry is shown in Figure 4-1, and the dimensions are listed in Table 2.

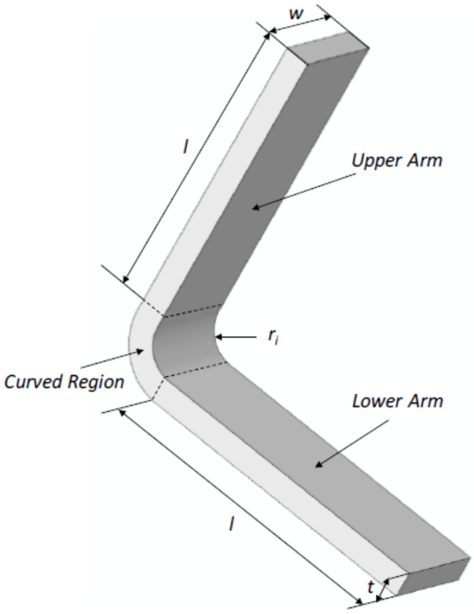

Figure 4-1 Geometric dimensions of the curved beam specimen taken from [103]

Table 2 Geometrical dimensions used in the analyses are from [105]

t_{ply} [mm]	*l* [mm]	r_i [mm]	*Width* [mm]
0.188	76.36	8	25.0

The experimental setup is shown in Figure 4-2. The test fixture designed to produce mixed loading at the curved region and specimen are shown in Figure 4-2 a). The specimen is attached to the fixture via freely rotating pins with bolts. The freely rotating pin is gripped to the servo-hydraulic 250kN testing machine, and loading is applied in the y direction as displacement-controlled manner. The details of the loading condition are depicted in Figure 4-2 b). To represent actual loading and boundary conditions, a freely rotating pin is idealized as a reference point with free rotation in the z direction while constrained in the x and y directions. Vertical displacement is only applied to the upper reference point as 10 mm, varying over time with smooth step amplitude. Kinematic coupling is applied from pin midpoints to specimen upper and lower faces to transfer load correctly. The resulting finite element boundary conditions for 3D and 3D-slice FEMs are shown in Figure 4-3.

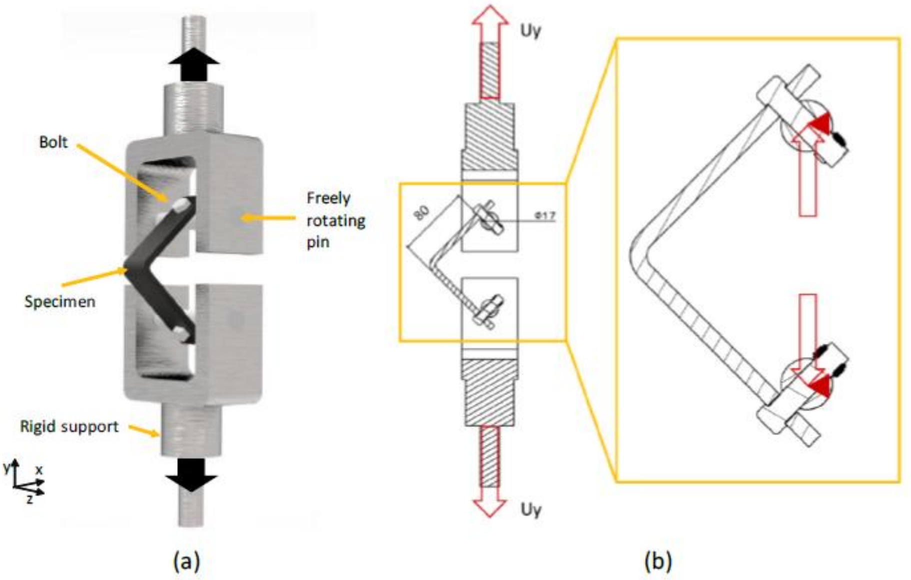

Figure 4-2 Illustration of a) experimental setup and b) details of the loading [103]

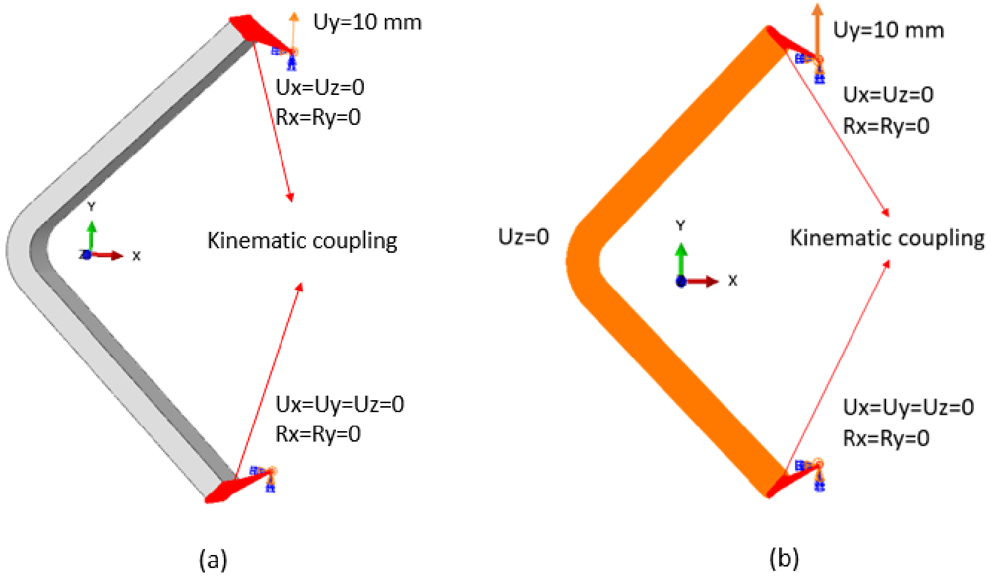

Figure 4-3 Boundary conditions applied on (a) 3D and (b) 3D-slice FEMs

Although the actual width of the specimen is 25 mm, as in the 3D, the 3D-slice model having 0.1 mm along the z direction is also used in finite element idealization. Therefore, plane strain condition (Uz=0) is applied to both faces in the width direction.

3D-Slice Modeling

Wisnom investigated the anticlastic bending of the curved beam in 1996 [107] using a 3D and 2D plane strain models. The 3D model showed variations in the stress fields through width caused by restraint on anticlastic bending due to curvature. However, as width increases, the 3D model approaches the 2D plane strain case in the study. Therefore, if the width is relatively greater than the thickness, then Wisnom states that plane strain boundary conditions are applicable. Since the width dimension is 25 mm in both L-beam and T-joint specimens, the plane strain condition is said to be appropriate.

Although 2D plane strain modeling is used commonly, the 3D-slice model with plane strain conditions is less in the literature. There are several studies available using this assumption. For example, Hélénon, Wisnom, Hallet, and Trask [26] utilized slice modeling for the investigation of T-joint failure. Similarly Xu et al. [37] compared half width, full width and slice models and stated that the slice model is efficient in terms of computation and accuracy. Another advantage of slice modeling over 3D is dismissing the free edge effect and mesh refinement necessity around edges. Also, this technique is advantageous over full width modeling because of its much lower computational cost and allowing more refined mesh through the thickness direction, which is important for intralaminar failure prediction. However, stress variations and failure through the width direction cannot be investigated by this method. The reason behind the selection of this modeling instead of 2D plane strain in the thesis is that it allows 3D stress components needed for 3D failure criteria and XFEM.

4.1.2 Material Properties

AS4/8552 UD prepreg is used for composite laminates with a cured ply thickness of 0.188mm and density of 1580 kg/m^3. Elastic material properties and strength values are taken from Lopes et al. [102] and listed in Table 3. The in-situ strength values are calculated for cross-ply laminate according to formulas given in section 3.2.3. For unidirectional case, UD strengths are used as is.

Table 3 Material properties of AS4/8552 used in the analyses

Elastic Properties	**E_{11} [GPa]**	**E_{22} [GPa]**	**E_{33} [GPa]**	**G_{12} [GPa]**	**G_{13} [GPa]**	**G_{23} [GPa]**	**ν_{12}**	**ν_{13}**	**ν_{23}**
	135	9.6	9.6	5.3	5.3	3.4	0.32	0.32	0.487
LaRC05 material properties	**G_{IC} [N/mm]**	**G_{IIC} [N/mm]**	**G_{IIIC} [N/mm]**	**G_{FT} [N/mm]**	**G_{KINK}/G_{SPLIT} [N/mm]**	**α_0 [94]**	**β [29]**	**n_L**	**n_T**
	0.28	0.79	0.79	80	100/50	53°	2.1 E-08	0.261	0.287
Strengths	**X_T [MPa]**	**X_C [MPa]**	**Y_T [MPa]**	**Y_C [MPa]**	**S_L [MPa]**	**S_T [MPa]**			
UD	2207	1531	80.7	199.8	114	80			
Thin Embedded	2207	1531	77.9	261.7	89.7	98.6			
Thick Embedded	2207	1531	127.8	406.3	139.3	153.1			
Thin Outer	2207	1531	55.1	208.3	71.4	78.5			

For properties between layers of composite laminate, AS4/8552 interface properties are used in Table 4. Note that interface strength values are taken from the unidirectional curved beam and short beam test results of Ata and Çöker [103], while other interface properties are from [102].

Table 4 Interface properties of AS4/8552 UD prepreg

k_I^0 [MPa/mm]	**k_{II}^0 [MPa/mm]**	**k_{III}^0 [MPa/mm]**	**t_I^0 [MPa]**	**t_{II}^0 [MPa]**	**t_{III}^0 [MPa]**	**G_{Ic} [N/mm]**	**G_{IIc} [N/mm]**	**G_{IIIc} [N/mm]**	**η**
2.6e6	2.6e6	2.6e6	79.07	106.4	106.4	0.28	0.79	0.79	1.45

Stacking sequences are taken same with the reference study as $[0_{30}]$ and $[0_3/90_3/0_3/90_3/0_3]_s$ for unidirectional and cross ply laminates, respectively. 90° ply lies through the Z direction shown in Figure 4-3.

4.1.3 Finite Element Modeling

4.1.3.1 Mesh Sensitivity

A mesh sensitivity study is conducted for a 3D-slice model by considering cross-ply laminate due to a more complex stress state. Since the 3D model used by Ata and Çöker [103] is taken as a reference for unidirectional specimens and mesh sensitivity was done before, the same mesh density is used in this study.

For the cohesive zone model, the element length is calculated using Equations (3.13), (3.14) and (3.15) and the calculated element length is 0.1 mm in the case of 5 elements across cohesive zone length. No further mesh refinement is made since it is sufficiently fine.

Although it is stated in ABAQUS documentation [22] that there is almost no mesh dependence of XFEM if the mesh is sufficiently refined, the stress mapping in the element ahead of the crack tip is important for the initiation criterion LaRC05. Therefore, a detailed mesh sensitivity study is performed for XFEM-LaRC05 models to eliminate the effect of mesh on the results. Firstly, different element sizes of 0.284 mm, 0.2 mm, and 0.1 mm are analyzed. It is figured out from the results regarding stress components that greater changes happen for the maximum values of stress component of σ_{13} (S13) on the curved region. Hence the stress component of S13 in the curved region is selected for comparisons. The stress values are captured at 1312 N to see unaffected stresses resulting from failure initiation. Figure 4-4 (a) shows that a 14.4 % improvement in the maximum S13 stress component is achieved from 0.284 mm to 0.2 mm. Although further refinement to 0.1 mm does not affect significantly the results, which are 2 %, accounting through the thickness mesh refinement element size is selected as 0.1 mm to preserve the aspect ratio of the elements within acceptable limits.

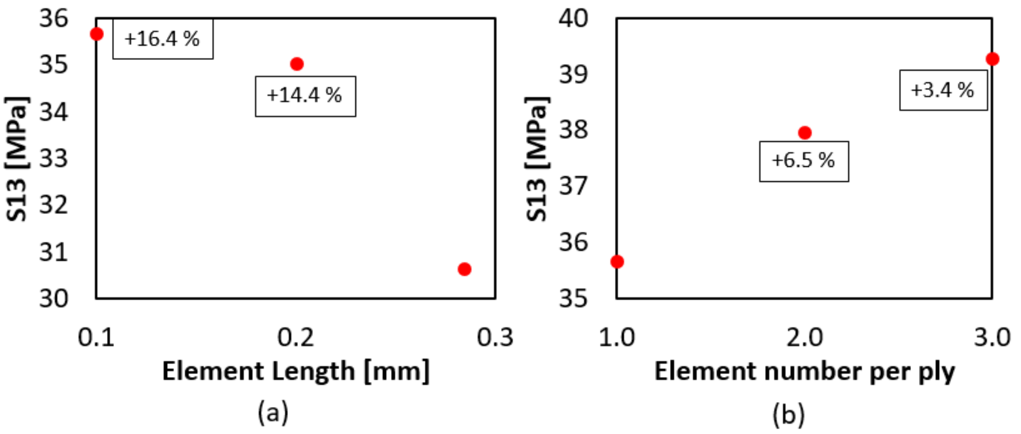

Figure 4-4 Mesh sensitivity study of XFEM on S13 stress accounting a) effect of element length, b) effect of element number per ply for 0.1 mm element length

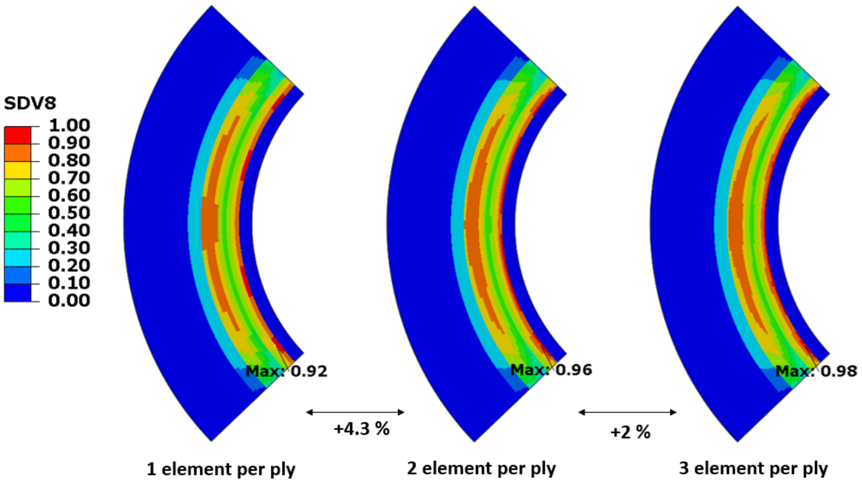

Figure 4-5 Matrix failure index SDV8 comparison for different number of plies across ply thickness

Further study is made on the thickness refinement of the mesh to better capture intralaminar failures within plies for XFEM model. That is to see which side of the ply failure initiates and propagates. It is observed that 6.5 % increase in the stress level is captured using two elements per ply as shown in Figure 4-4 (b). However, further refinement only contributes to the stress less than 5%. As matrix failure indices are compared at 1312N as shown in Figure 4-5, same as the stress sensitivity, it is observed that the SDV8 value which is matrix failure index increases with an increasing number of plies in through the thickness. However, 2 % increase between 2-3 elements per ply is insignificant. As a result, two elements per ply is selected as the final mesh with a 0.1 mm element size.

4.1.3.2 Unidirectional [0_{30}] Laminate

Final mesh details of unidirectional laminate are shown in Figure 4-6 and Figure 4-7 for 3D and 3D-slice models, respectively. In 3D model, the number of first-order elements is 925760 in total, whereas it is just 92520 for 3D-slice model. The element type of C3D8R with enhanced hourglass control is chosen to prevent shear locking. Incompatible mode elements are also a good choice regarding shear locking; however, using this type in XFEM is not recommended because the stress level at the cracked element may not return to the unloaded state due to the discarding of contributions from incompatible modes by ABAQUS/Standard [22]. As explained in the geometry and boundary conditions subsection, the element number across the width is one for the slice model since a 0.1 mm slice is used.

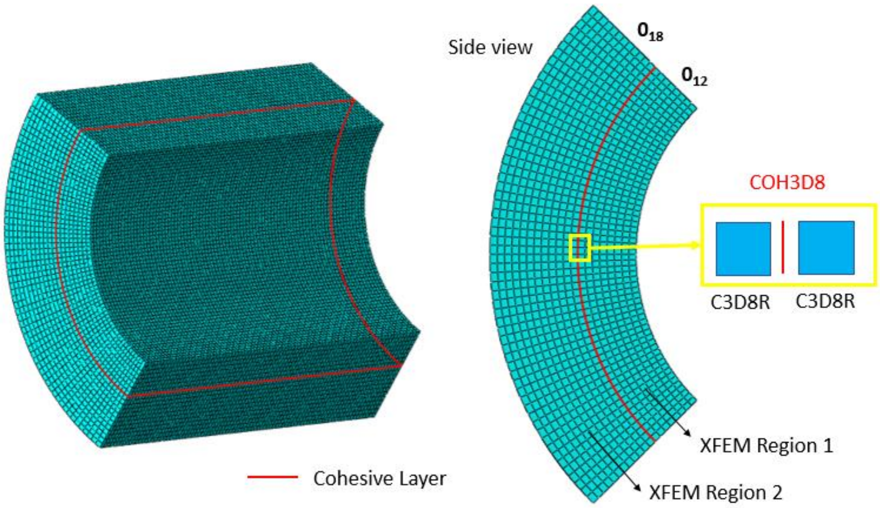

Figure 4-6 3D FEM detailed representation of mesh, location of cohesive layer and XFEM regions for UD laminate

For the sake of computation time, cohesive elements are placed between the 12th and 13th plies from the inner radius, as shown in Figure 4-6 and Figure 4-7 for 3D and 3D-slice cohesive models. There are 1542 and 46288 COH3D8 type cohesive elements for 3D-slice and 3D models respectively. The viscosity parameter is used as 10^{-5} for the cohesive elements to ease convergence.

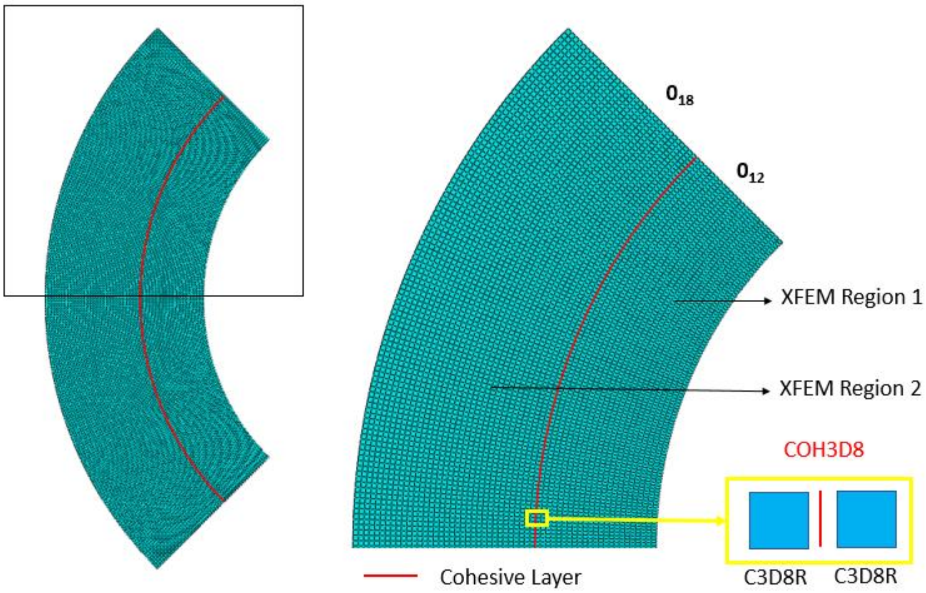

Figure 4-7 3D-slice FEM detailed representation of mesh, location of cohesive layer and XFEM regions for UD laminate

For the XFEM model, enrichment is defined only in the curved region. There exist two regions, as shown in Figure 4-7. The damage stabilization parameter is used as $1e^{-5}$ for enriched elements to ease convergence.

4.1.3.3 Cross Ply $[0_3/90_3/0_3/90_3/0_3]_s$ Laminate

The final mesh details of cross ply laminate are shown in Figure 4-8 and Figure 4-9 for CZM and XFEM models. There are 92520 first-order elements for this configuration for the bulk material. The element type is 3D stress type C3D8R with enhanced hourglass control to prevent shear locking. Incompatible mode elements are also a good choice regarding shear locking; however, using this type in XFEM is not recommended because the stress level at cracked element may not return into unloaded state due to discarding of contributions from incompatible modes by ABAQUS/Standard [22]. The element number across the width is one since a 0.1 mm slice is used, as explained in the geometry and boundary conditions subsection.

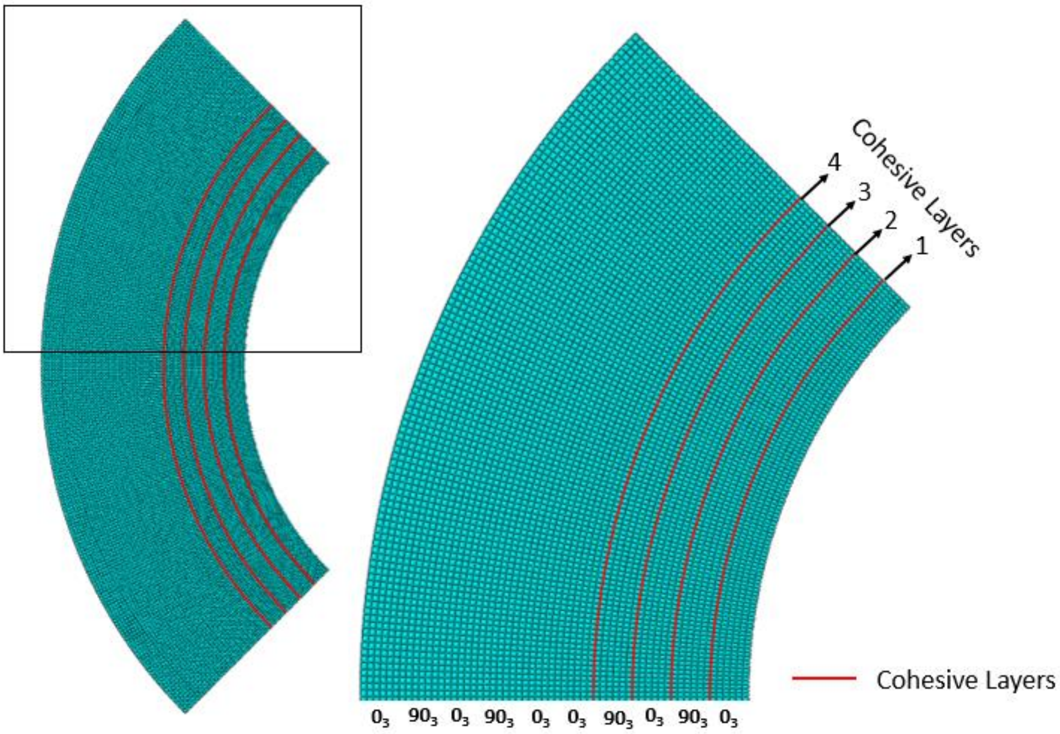

Figure 4-8 Mesh details for CZM model on the curved region of cross-ply L-beam

For the sake of computation time, cohesive elements are placed into the outer interfaces of the 1st and 2nd 90-degree group, as shown in Figure 4-8 for the cohesive model. There are 6168 COH3D8 type cohesive elements in part. The viscosity parameter is used as 1e^{-5} for the cohesive elements to ease convergence.

For the XFEM model, enrichment is defined only to the region of interest in the curved region starting from the first ply group to the end of the 3rd 0 degree group of plies illustrated in Figure 4-9. There exists a single region for each three ply group since these groups exhibit unified behavior. The damage stabilization parameter is used as 1e^{-5} for enriched elements, to ease convergence.

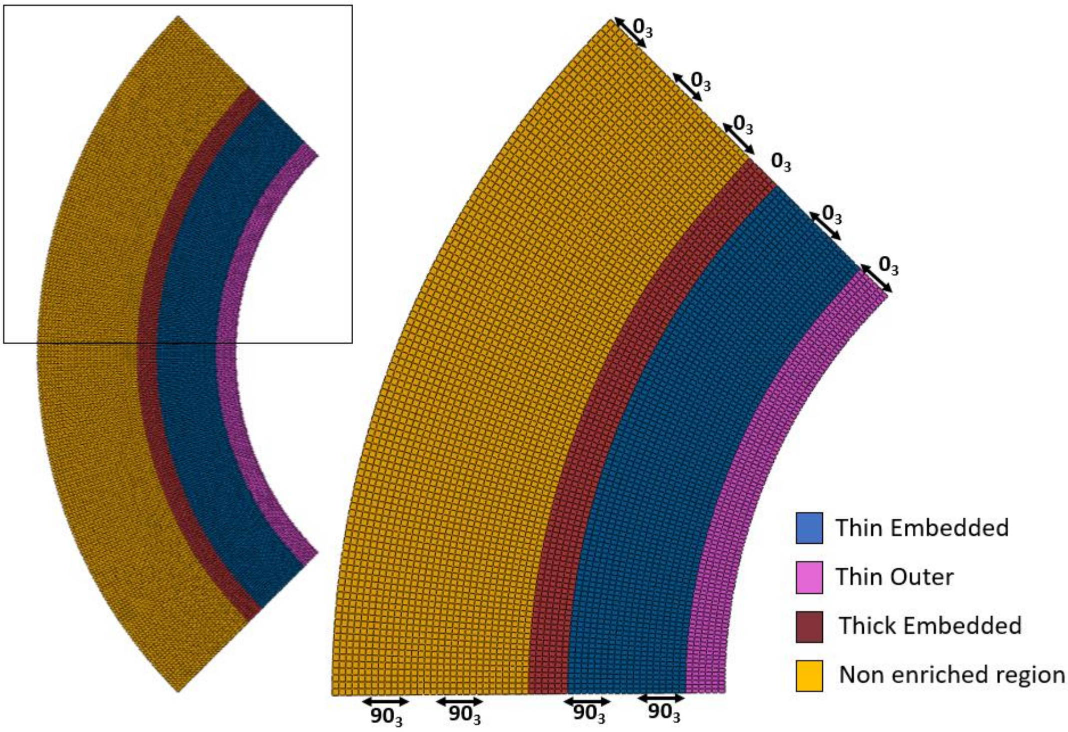

Figure 4-9 Details of mesh and sections assigned to XFEM enriched regions for cross-ply L-beam

4.2 Unidirectional [0_{30}] Laminate Results

4.2.1 CZM

4.2.1.1 3D

Internal energy (ALLIE) vs. artificial strain energy (ALLAE) is checked to determine whether artificial strain energy given to the system during enhanced hourglass control exceeds the limit of 5% defined in the ABAQUS manual [22] for reliable analysis. 5% of the internal energy, internal energy, and artificial strain energy history are plotted in Figure 4-10. It is shown that the artificial energy with the blue line does not exceed 5% of the internal energy shown with the green line throughout the analysis. Therefore, enhanced hourglass control is applied successfully.

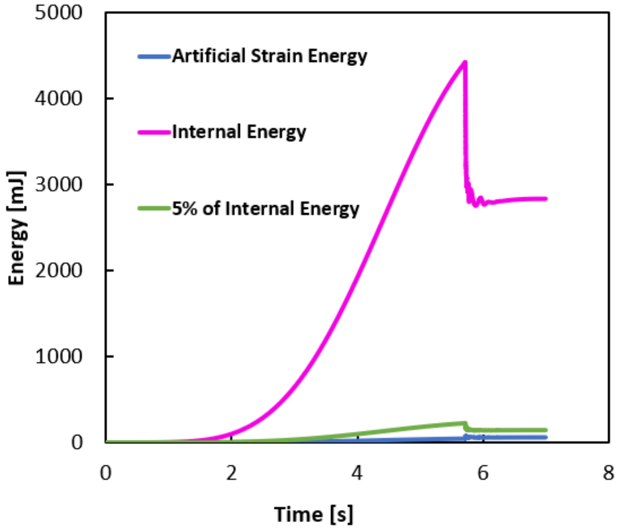

Figure 4-10 Artificial strain energy check for 3D CZM model

To check whether quasi-static loading is applied correctly, the history of kinetic vs. internal energy is examined. It is seen in Figure 4-11 that KE shown with yellow color is small enough during the analysis with respect to internal energy with pink color. Therefore, quasi-static loading is said to be successfully applied.

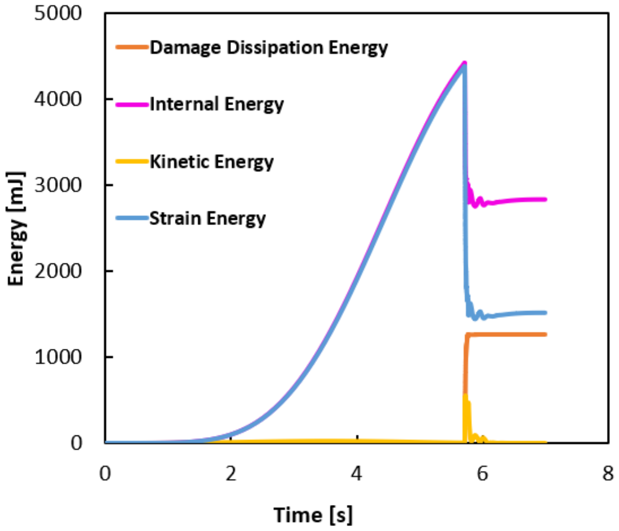

Figure 4-11 Energy histories throughout the analysis for 3D CZM model

Further examination of the energy histories revealed that damage dissipation energy with orange color increases while strain energy with blue color decreases instantaneously due to the failure of interface elements. After small oscillations due to delamination propagation through the arms, all energy components stabilize. The investigation of energy outputs revealed that the numerical model was successfully generated.

The load-displacement response of curved unidirectional thick laminate from 3D modeling coupled with the CZM method is shown in Figure 4-12 with blue color. The grey curves represent the experimental results, while the dashed black curve is from the explicit analysis of the 3D model by Ata and Çöker [103]. The stiffness in the linear elastic region demonstrates good agreement with the experimental results and reference numerical solution. Also, the main load drop takes place similar to load levels observed in the experiment.

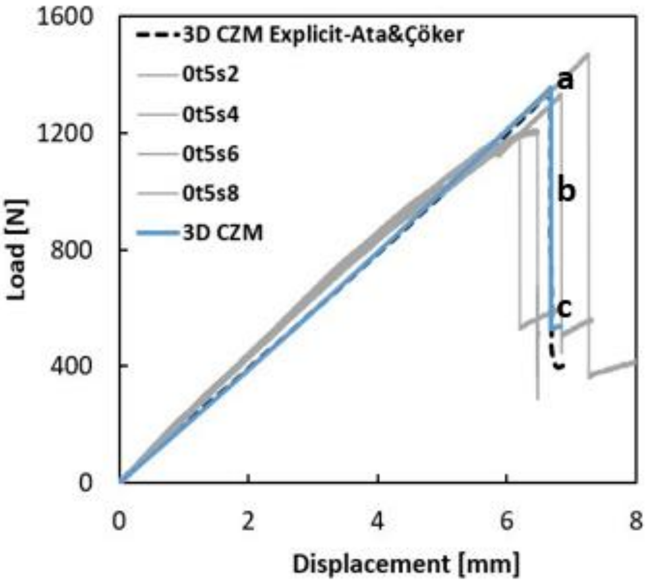

Figure 4-12 Load-displacement response of unidirectional L-beam for 3D CZM model

Figure 4-13 shows the damage sequence at corresponding point a-c in the load-displacement plot Figure 4-12. The failure starts at the 12th and 13th ply interface in the mid of the curved region and grows through the width and tangential directions, as in Figure 4-13. At point b, the damage reaches the arms and then grows through the arms until point c.

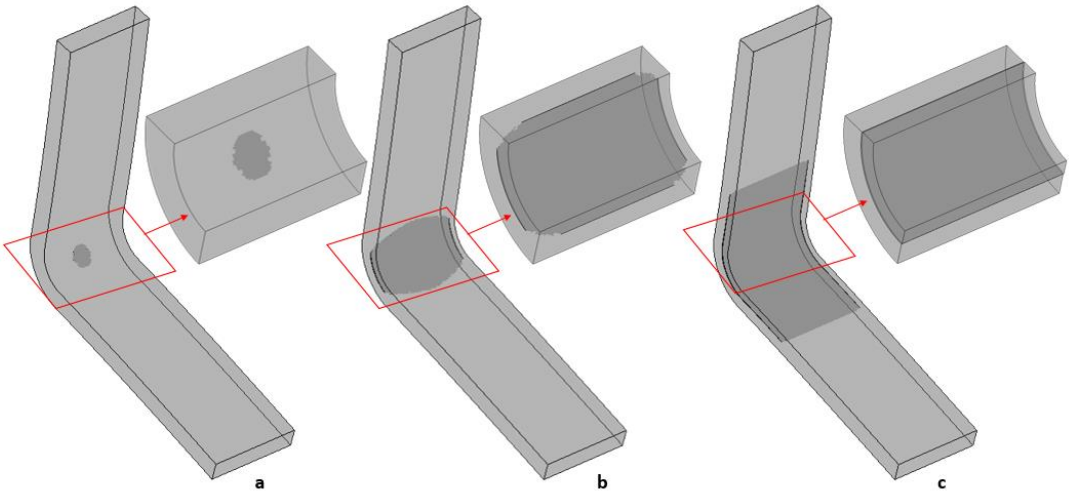

Figure 4-13 Damage propagation at the critical points on load-displacement curve for 3D CZM model

Figure 4-14 illustrates radial stresses through the width direction and on the edge and mid sections of the curved region at the points located in the load-displacement graph shown at the left.

Figure 4-14 (a) illustrates the state just before the initiation of the delamination. The radial stresses before failure are maximum at 0.33R from the inner radius, consistent with the DIC and analytical results shared by Taşdemir and Çöker [106]. Additionally, the stresses at the mid-section are more significant than the edge section stresses. This causes delamination to initiate and diffuse from mid-width to the edges. Although cohesive elements were not deleted before complete degradation, the damage variable changed the stress state in Figure 4-14 (b). Figure 4-14 (c) shows crack formation after the complete degradation of cohesive elements at the center of mid-width. Crack faces are under almost zero stress state at this point. The load started decreasing after (c), and delamination grew to the arms.

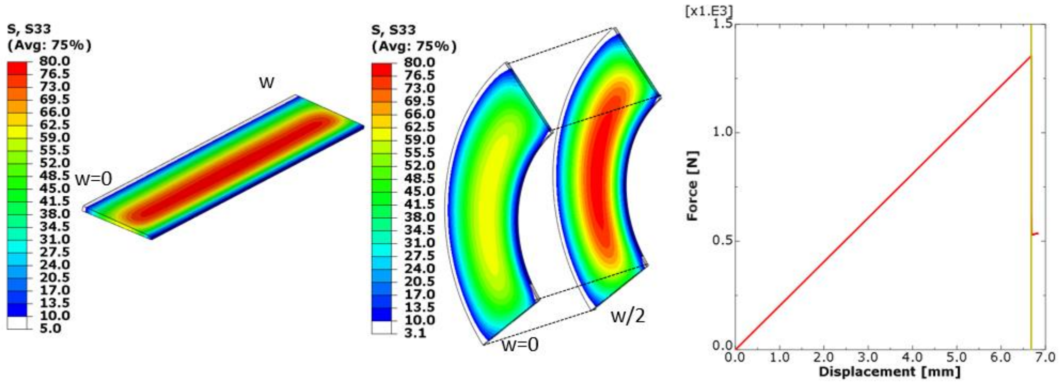

(a) 1353 N @6.67 mm

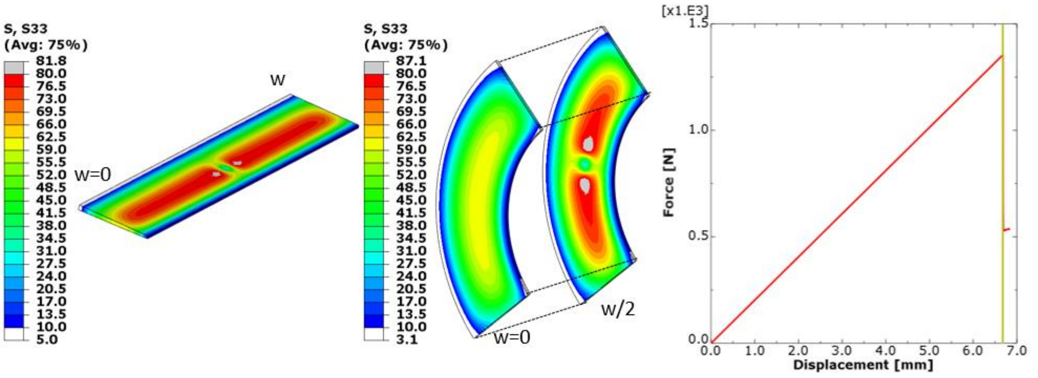

(b) 1354 N @6.68 mm

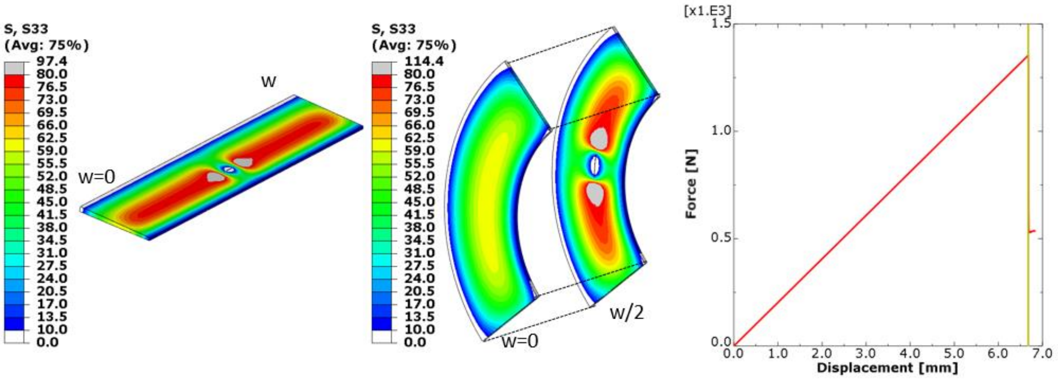

(c) 1354 N @6.68 mm

Figure 4-14 Stress contours through the width (left figure), on the edge and mid sections of the curved beam (mid figure) and load-displacement graph at corresponding points a-f (right figure) for 3D CZM model

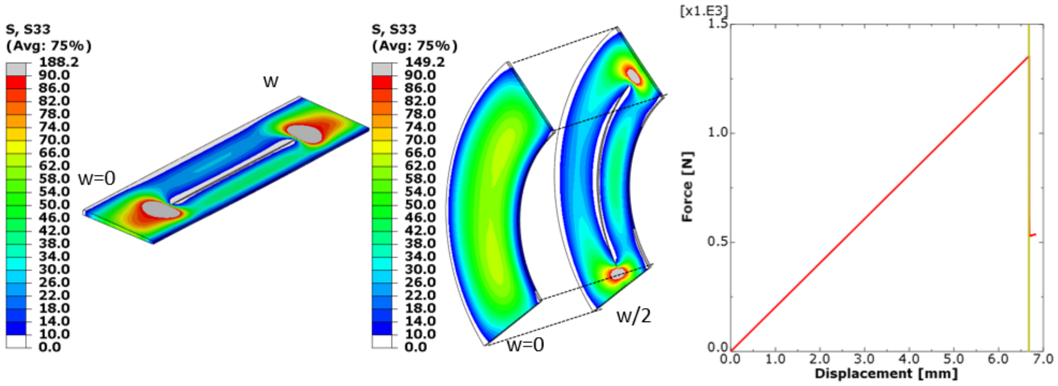

(d) 1224 N @6.68 mm

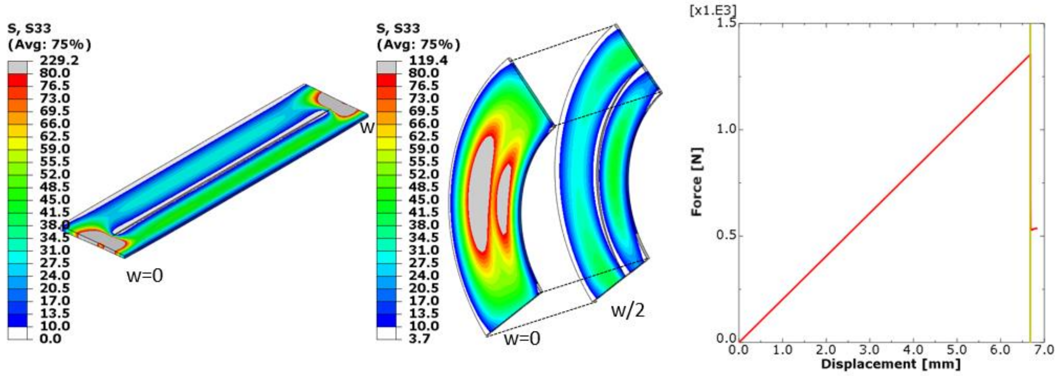

(e) 1046 N @6.68 mm

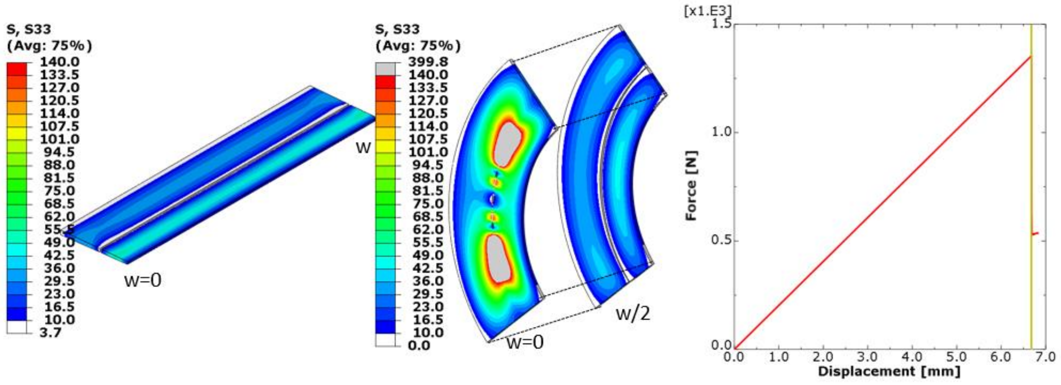

(f) 926 N @6.68 mm

Figure 4-14 (continued)

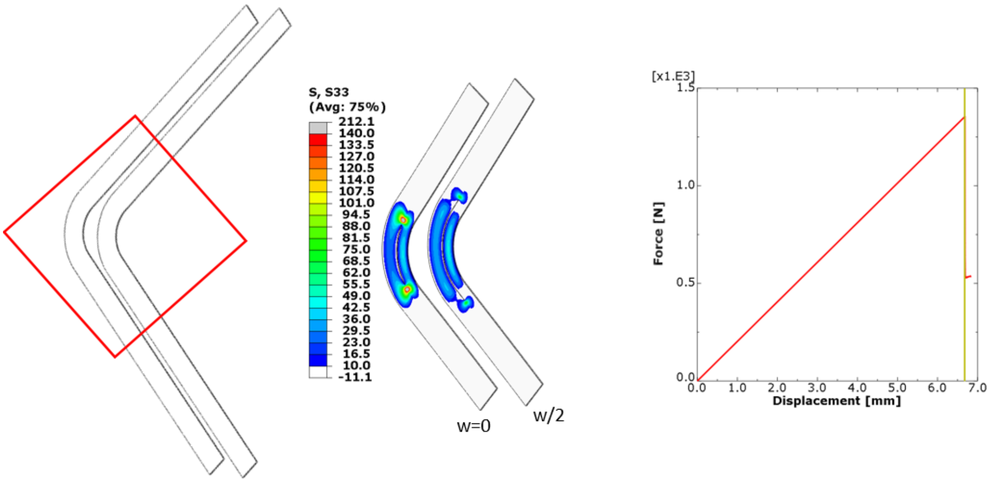

(g) 842 N @6.68 mm

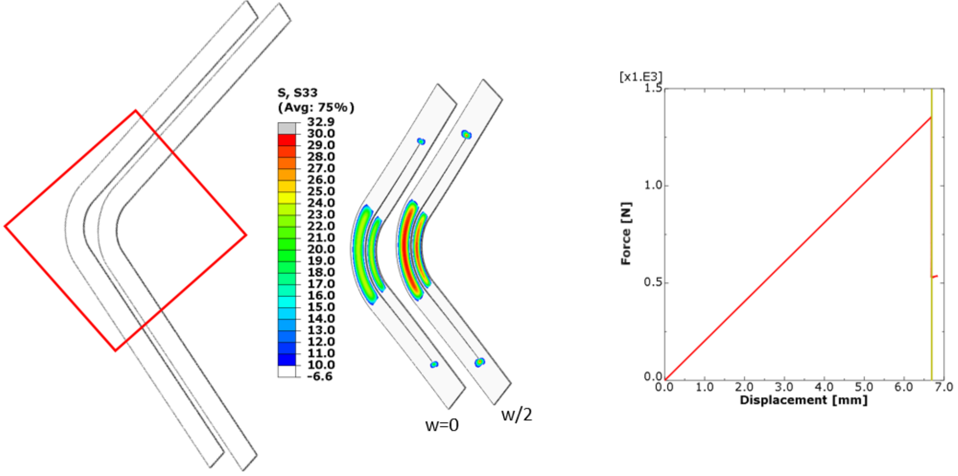

(h) 529 N @6.69 mm

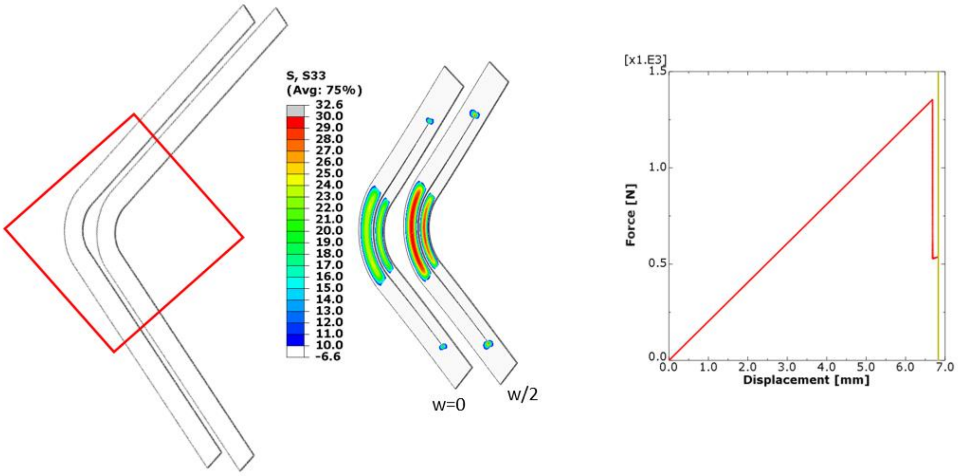

(i) 536 N @6.83 mm

Figure 4-15 Stress contours on the edge and mid sections of the curved beam and load-displacement graph at corresponding points a-c for 3D CZM model

Figure 4-14 (d) represents the state at 1224 N load and 6.68 mm displacement. It is seen that radial stress at the edge is not uniformly distributed along the curve rather, two dominant contours exist near the arms. The delamination front in the width direction is very close to the edge and, the singularity field at the crack tips is the main cause of this unexpected field. As loading continues to (e), this field is changed to the two separate fields lying tangentially. This is the consequence of the inside crack very close to the edge. The stress field around the left tip of the inside crack at this section is seen at the edge. The delamination front reaches the edge at Figure 4-14 (f) and cohesive elements were deleted, and the stress field also changed at this point. The propagation of the edge crack towards the arms is shown in Figure 4-15 (g). Thereafter, the crack at the edge continued through the arms at (h) and (i).

4.2.1.2 3D-Slice

Internal energy (ALLIE) vs. artificial strain energy (ALLAE) is checked to determine whether artificial strain energy given to the system during enhanced hourglass control exceeds the limit 5% defined in the ABAQUS manual [22] reliable analysis. 5% of the internal energy, internal energy, and artificial strain energy history are plotted in Figure 4-16. Certainly, the artificial energy with the blue line does not exceed 5% of the internal energy shown with the green line throughout the analysis. Therefore, enhanced hourglass control is applied successfully.

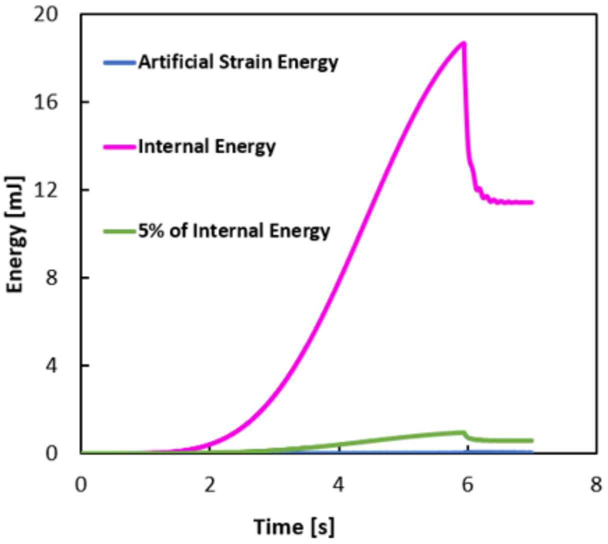

Figure 4-16 Artificial strain energy check

To check whether quasi-static loading is applied properly, kinetic vs. total strain energy (internal energy) history is examined. It is seen in Figure 4-17 that KE shown with yellow color is small enough during the analysis with respect to internal energy with pink color. Therefore, quasi-static loading is said to be successfully applied.

Further examination of the energy histories revealed that damage dissipation energy with orange color increases while strain energy with blue color decreases instantaneously due to the failure of interface elements. There are small oscillations in the slice model compared to 3D while delamination propagation through the arms. Energy components get stabilized after some time and remain almost constant, as in the 3D. The magnitude of the energies gets much smaller due to slice modeling but, the trends of the curves are almost identical. The investigation of energy outputs and comparison with the 3D CZM model revealed that the numerical 3D-slice model is successfully generated and analysis results are reliable. Hence further investigations will not be performed for the other 3D-slice CZM models throughout this chapter.

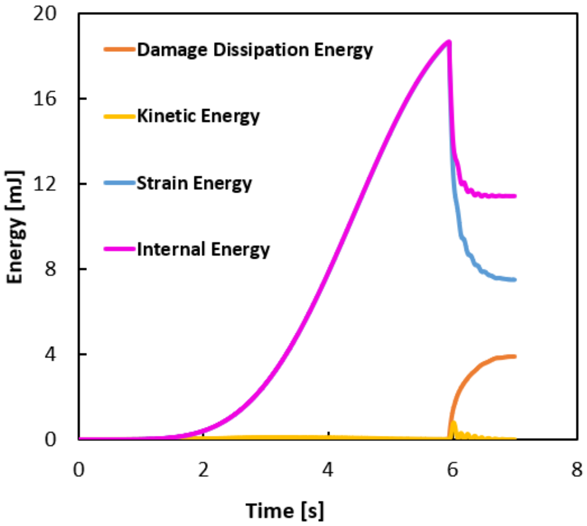

Figure 4-17 Energy histories throughout the analysis

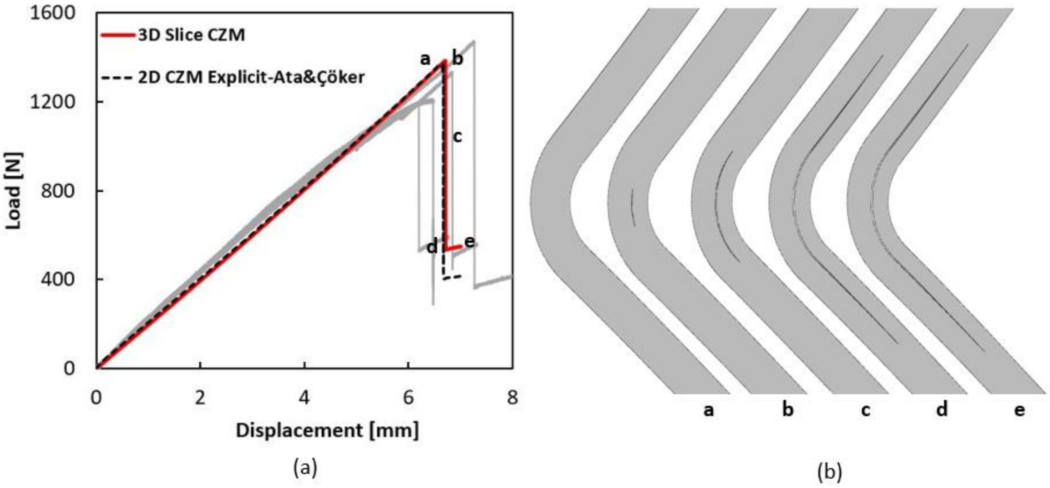

(a)

(b)

Figure 4-18 Load-displacement response of unidirectional L-beam from 3D-slice CZM model and crack locations on load-displacement curve for critical points

The load-displacement response of curved unidirectional thick laminate from 3D-slice modeling coupled with the CZM method is shown in Figure 4-18 (a) with red color. The grey curves represent the experimental results, while the dashed black curve is from the explicit analysis of the 2D plain strain model by Ata and Çöker [103]. The stiffness in the linear elastic region demonstrates good agreement with the experimental results and reference numerical solution. Moreover, the main load drop takes place inside the scatter of experiments.

Figure 4-18 (b) shows the damage sequence at corresponding points a-e in the load-displacement plot Figure 4-18 (a). These represent the damage sequence from failure initiation to the final prescribed displacement of 7 mm. Failure starts at the predefined interface between the 12th and 13th ply (point b) at the load of 1383 N and grows through the arms until point d. After point d, load drop is stopped, and propagation becomes stable. Afterward, load-carrying capacity increases with reduced stiffness to point e. The simulation is successfully completed at the prescribed displacement of 7 mm.

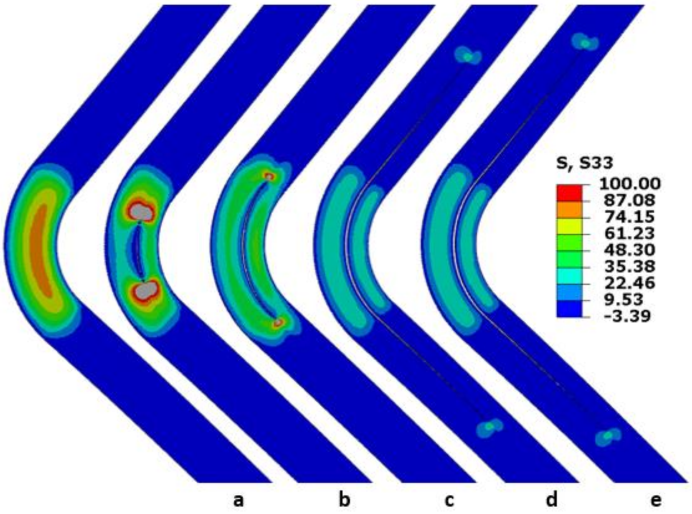

Figure 4-19 Stress contours on the deformed curved beam at critical points on the load-displacement curve for 3D-slice CZM model

Figure 4-19 illustrates radial stresses in the curved region at points a-e. The radial stresses are maximum at the middle, around 0.33R, consistent with the DIC and analytical results shared by Taşdemir and Çöker [106]. The delamination in the interface at 0.33R grows, and the stress field is affected by this damage, and tip fields were formed at point b in Figure 4-19. After delamination reaches the ends of the curved region, radial stresses became significant in the middle of the left and right sides separately as loading increases. The delamination stabilized in the half length of the arms, and load carrying capacity started to increase. The simulation was completed successfully, but if further loading was applied, delamination might grow at the ends of the arms, or new delamination may occur.

4.2.2 XFEM-LaRC05

4.2.2.1 3D

Internal energy (ALLIE) vs. artificial strain energy (ALLAE) is checked to determine whether artificial strain energy given to the system during enhanced hourglass control exceeds the limit of 5% defined in the ABAQUS manual [22] for reliable analysis. 5% of the internal energy, internal energy, and artificial strain energy history are plotted in Figure 4-20. Although the artificial energy with the blue line does not exceed 5 % of the internal energy shown with the green line, they become almost equal at the end of the analysis. Enhanced hourglass control is applied successfully.

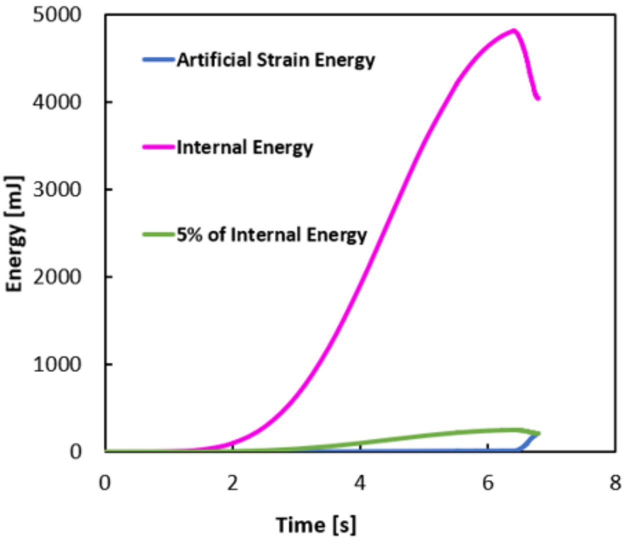

Figure 4-20 Artificial strain energy check of 3D XFEM-LaRC05 model

To check whether quasi-static loading is applied properly, kinetic vs. total strain energy (internal energy) history is examined. It is seen in Figure 4-21 that KE shown with yellow color is small enough during the analysis with respect to internal energy with pink color. Therefore quasi-static loading is said to be successfully applied.

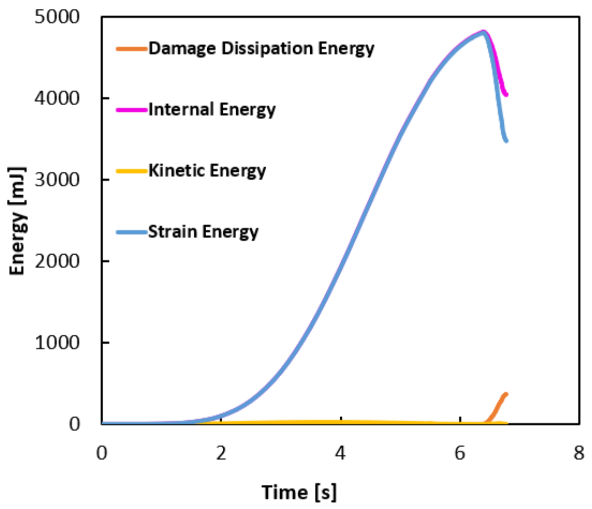

Figure 4-21 Energy histories throughout the analysis for 3D XFEM-LaRC05 model

Further examination of the energy histories revealed that damage dissipation energy with orange color increases, while strain energy with blue color decreases instantaneously due to the failure initiation in the enriched elements. Since simulation is stopped after all curved region was delaminated, further changes cannot be captured. However, the investigation of energy outputs revealed that the numerical model was successfully generated.

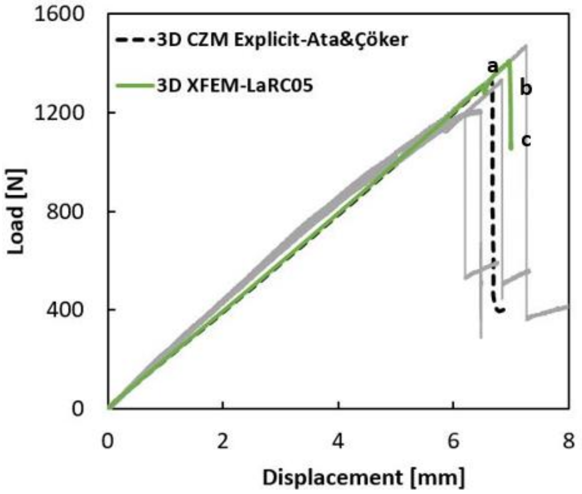

Figure 4-22 Load-displacement graph of UD L-beam for 3D XFEM-LaRC05 model

The load-displacement response of curved unidirectional thick laminate from 3D modeling coupled with the XFEM method is shown in Figure 4-22 with blue color. The grey curves represent the experimental results, while the dashed black curve is from the explicit analysis of the 3D model by Ata and Çöker [103]. The stiffness in the linear elastic region demonstrates good agreement with the experimental results and reference numerical solution. Also, the main load drop takes place inside the scatter of experiments. But there is a small load drop in the elastic part before the failure index reaches 1. Certainly, there exists, no damage initiation at that load level, and this minor disruption was ignored. Figure 4-23 shows the damage sequence at corresponding points a-c in the load-displacement plot Figure 4-23 . The failure starts at the prescribed displacement and location (12th and 13th ply interface) as in the 3D CZM and reference. However, the further load is observed until damage variable d reaches one at the cracked enriched elements. Initiation occurs in the curved region's mid and grows through the width and tangential directions, as in Figure 4-23. At point d, the damage reaches to arms, and simulation is stopped by hand since the XFEM region is only applied to the curved part, and further loading cannot simulate the propagation within the arms.

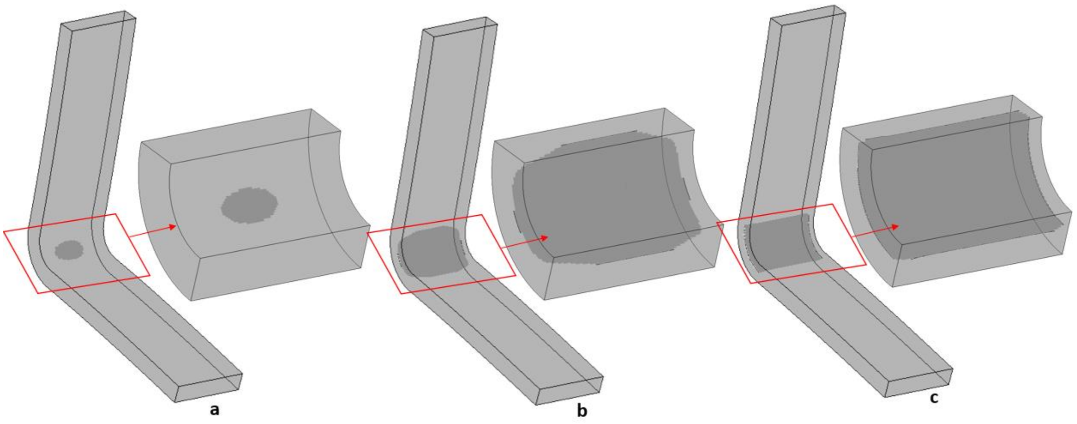

Figure 4-23 Damage propagation at the critical points on load-displacement curve for 3D XFEM model

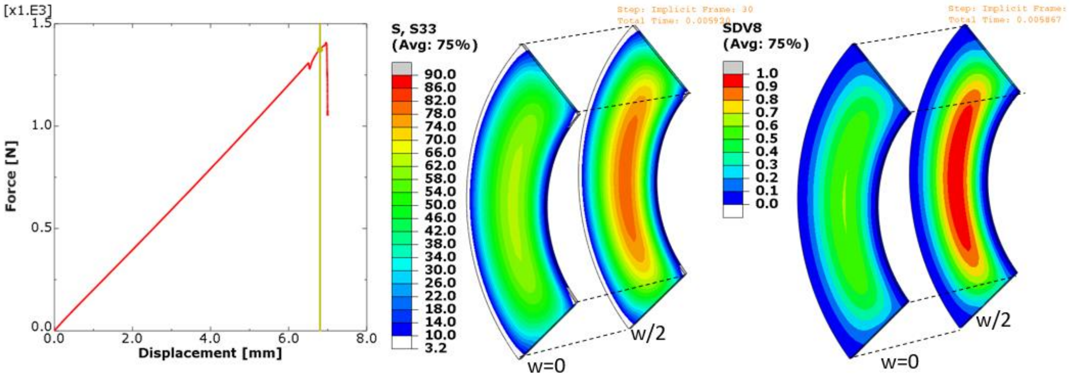

(a) 1370 N @ 6.77 mm

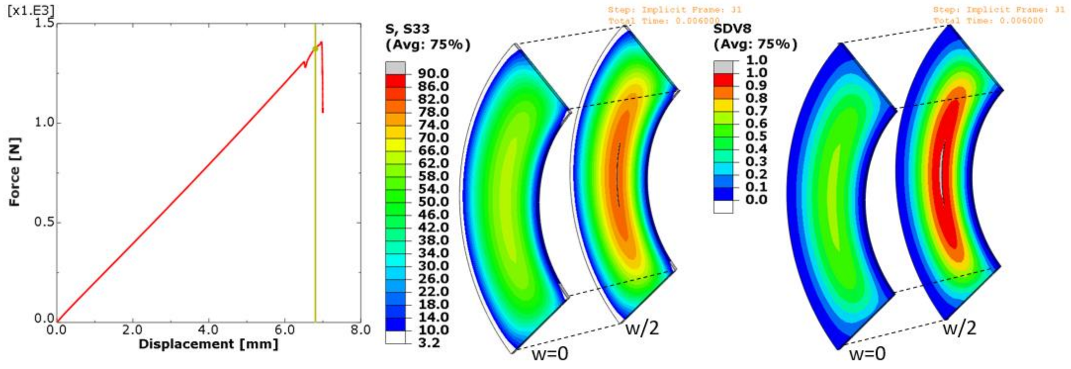

(b) 1375 N @ 6.79 mm

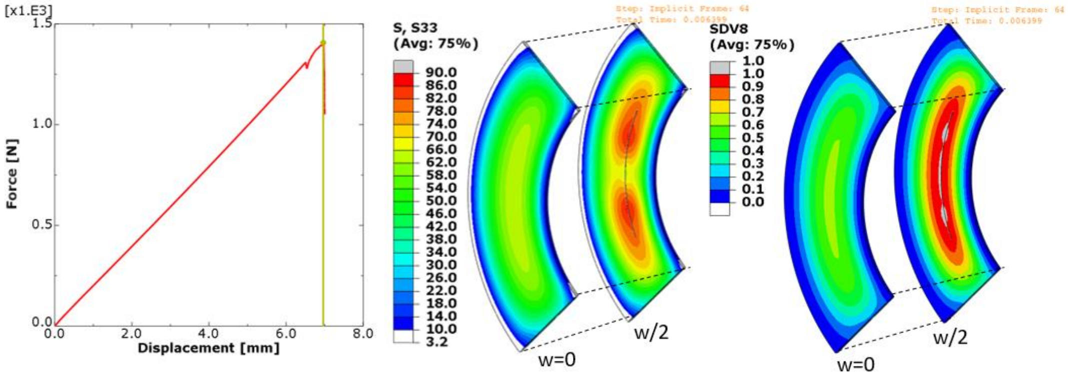

(c) 1406 N @ 6.96 mm

Figure 4-24 Stress contours and SDV8 matrix failure criterion on the edge and mid sections of the curved beam at critical points for 3D XFEM-LaRC05 model

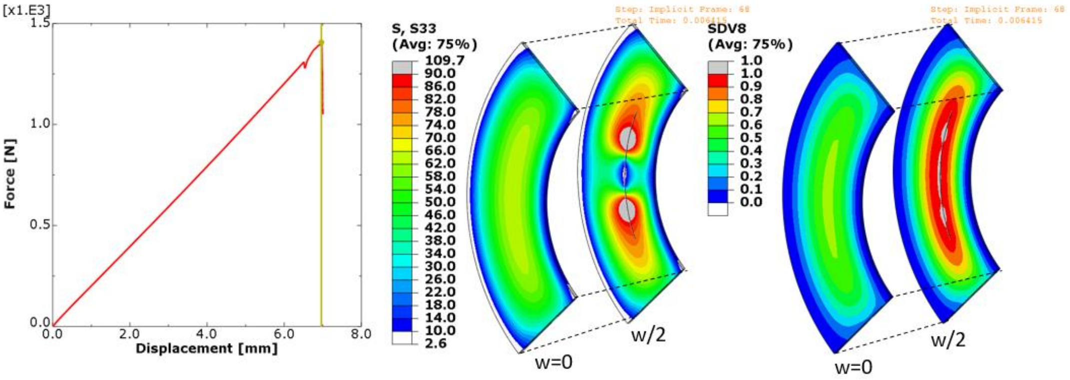

(d) 1406 N @ 6.96 mm

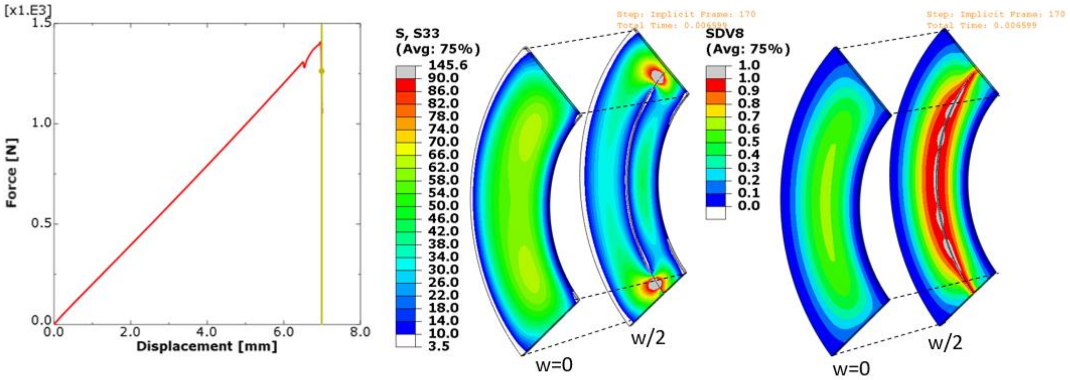

(e) 1262 N @ 6.98 mm

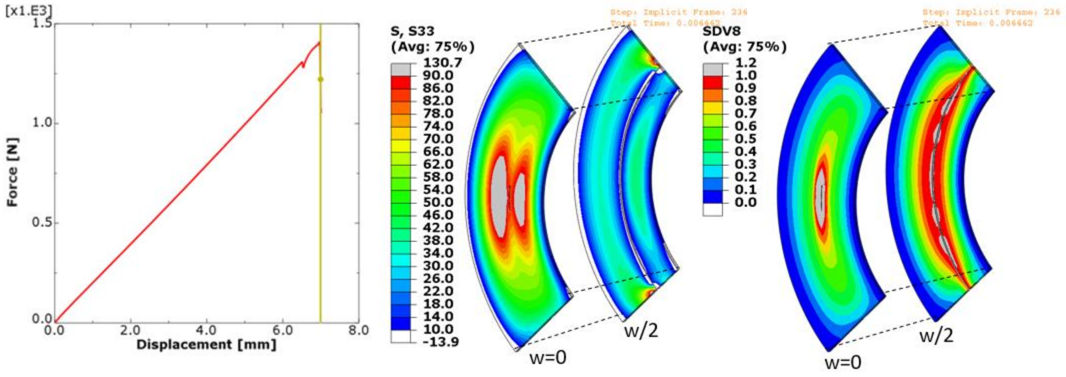

(f) 1222 N @ 6.99 mm

Figure 4 24 (continued)

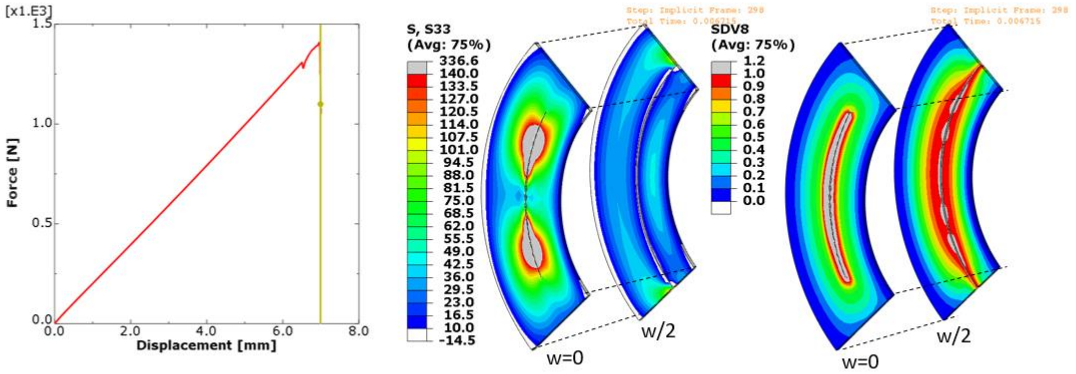

(g) 1102 N @ 6.99 mm

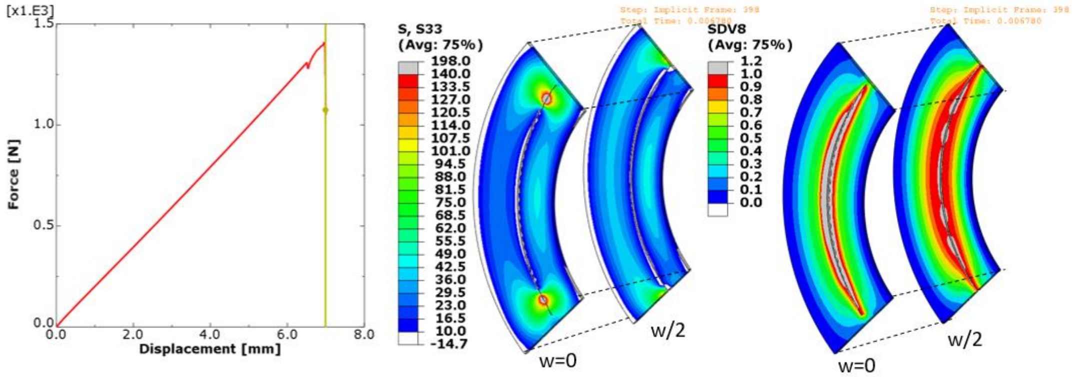

(h) 1073 N @ 7 mm

Figure 4 24 (continued)

Figure 4-24 illustrates radial stresses, failure indices on the edge and mid-sections of the curved region at the points located in the load-displacement graph shown at the left. The radial stresses are maximum at 0.33R from the inner radius, consistent with the DIC and analytical results shared by Taşdemir and Çöker [106]. Additionally, the stresses at the mid-section are more significant than the edge section stresses. This causes delamination to initiate and diffuse from mid-width to the edges.

Figure 4-24 (a) illustrates the state just before the delamination initiation. The matrix failure criterion is in line with the radial stress distribution with localization at 0.33R from the inner radius, and damage onset is likely to occur at the midsection. Although enriched elements were separated by a crack in Figure 4-24 (b), the stress state did not change by this visual crack and, load continued to increase up to (c). At (c), stress release started at the middle of the visual crack, and singularity fields formed at both crack tip. Singularity fields are obvious in (d) of Figure 4-24, and the SDV8 value exceeds one at the cracked elements. The load started decreasing after (d), and delamination grew to the arms, as seen in (e) of Figure 4-24. The delamination reached the free edge of the L-beam, but the S33 stress field at the edge is quite different, as seen in Figure 4-24 (f). Two distinct fields were observed at both sides of the visual crack, but it is not the outcome of the edge crack but rather the influence of the stress field around the crack coming from inside. This phenomenon will be explained in detail in the upcoming paragraphs. As softening of the cracked elements takes place, stresses at the edge get affected, and crack tip singularities occur clearly. Finally edge crack reached the arms in a tangential direction at (h) and the analysis stopped.

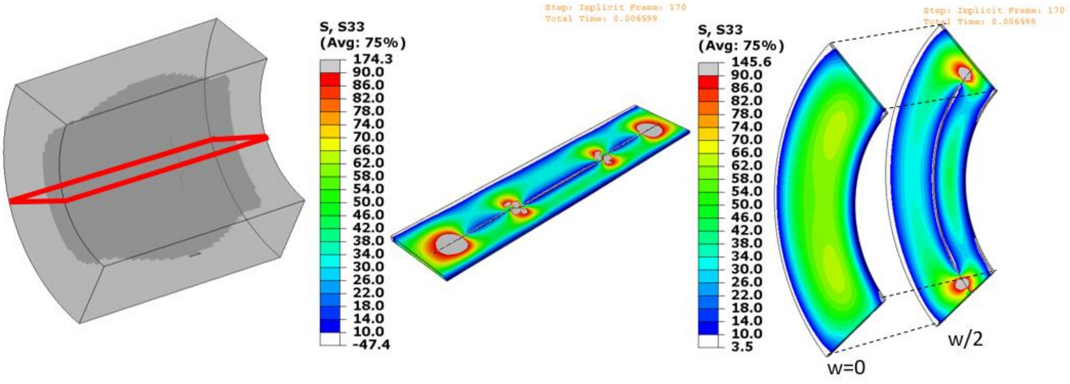

(a) 1406 N @ 6.96 mm

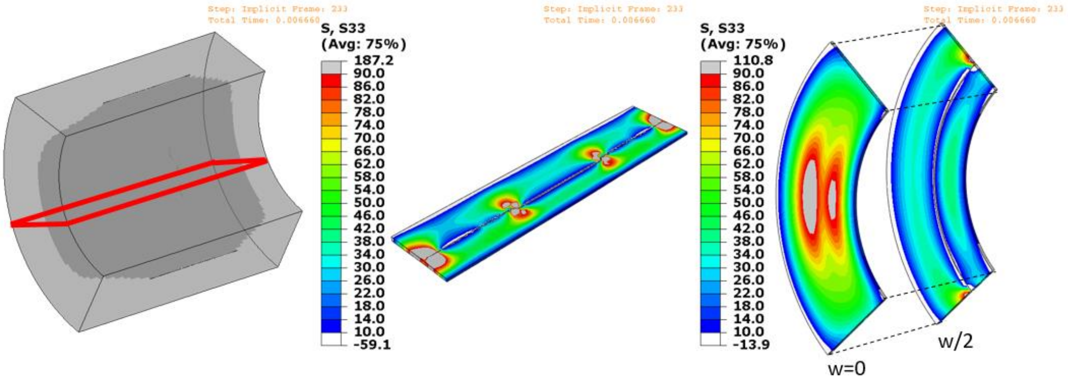

(b) 1225 N @ 6.99 mm

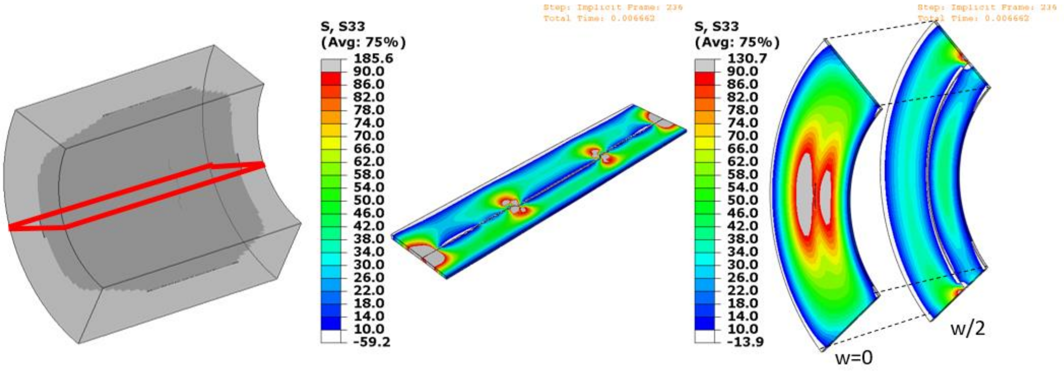

c) 1222 N @ 6.99 mm

Figure 4-25 Detailed examination of the stress contours for 3D XFEM-LaRC05 model

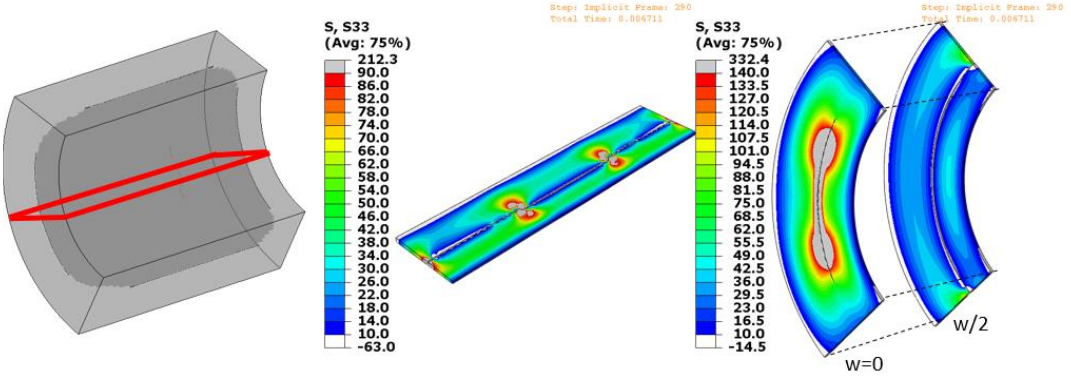

(d) 1112 N @ 6.99 mm

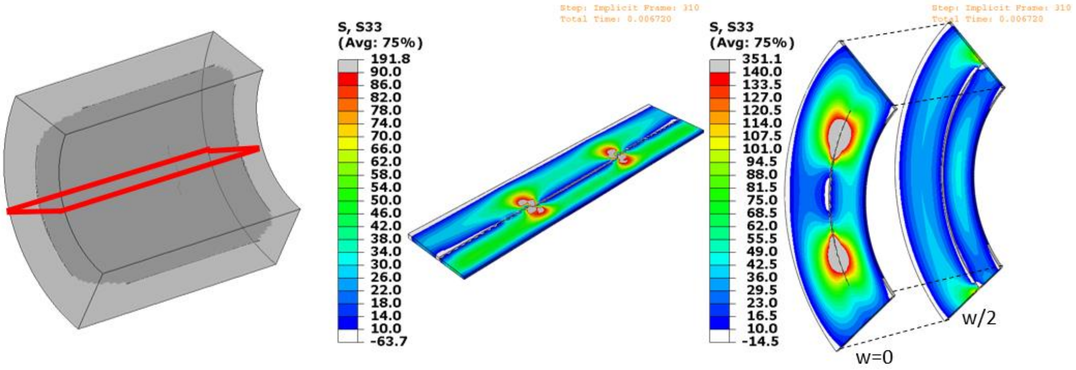

(e) 1089 N @ 6.99 mm

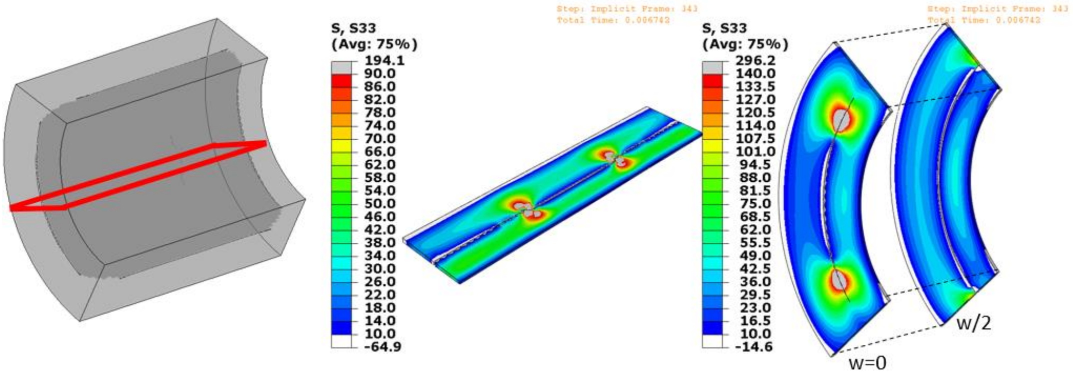

(f) 1053 N @ 6.99 mm

Figure 4-26 (continued)

Figure 4-25 illustrates matrix failure propagation and radial stresses on the edge, mid, and through the width sections of the curved region at the selected load levels

(a) to (f). This figure explains the stress distribution at the edge influenced by the inside damage moving to the sides. Figure 4-25 (a) represents the state at 1406 N load and 6.96 mm displacement. It is seen that radial stress at the edge is not uniformly distributed along the curve rather, two dominant contours exist near the arms. The delamination front in the width direction is very close to the edge, and singularity fields at the crack tips leads to this unexpected stress field. As displacement increased to 6.99 mm at (b), this field is changed to the two separate fields lying tangentially. This is the consequence of the inside crack very close to the edge at the mid-section, shown by red lines. The stress field around the left tip of the inside crack at this section is seen at the edge. The delamination front reaches the edge at Figure 4-25 (c), and a crack separates enriched elements, but the stress field did not change at this point. When softening happened at the cracked elements lying on through the width, stresses at the cracked surfaces were reduced, and crack tips started to form at the edge, as seen in (d). Complete separation led edge crack to move in the tangential direction, and tip stress fields are obvious at this time in Figure 4-25 (e). After that crack at the edge continued to the arms at (f). The concentrations at the through the width section is due to the small inclination of the crack at those locations and not notable since do not jump to the other interfaces.

4.2.2.2 3D-Slice

Internal energy (ALLIE) vs. artificial strain energy (ALLAE) is checked to determine whether artificial strain energy given to the system during enhanced hourglass control exceeds the limit of 5% defined in the ABAQUS manual [22] for reliable analysis. 5% of the internal energy, internal energy, and artificial strain energy history are plotted in Figure 4-27. It is shown that the artificial energy with the blue line does not exceed 5% of the internal energy shown with the green line throughout the analysis. Therefore, enhanced hourglass control is applied successfully.

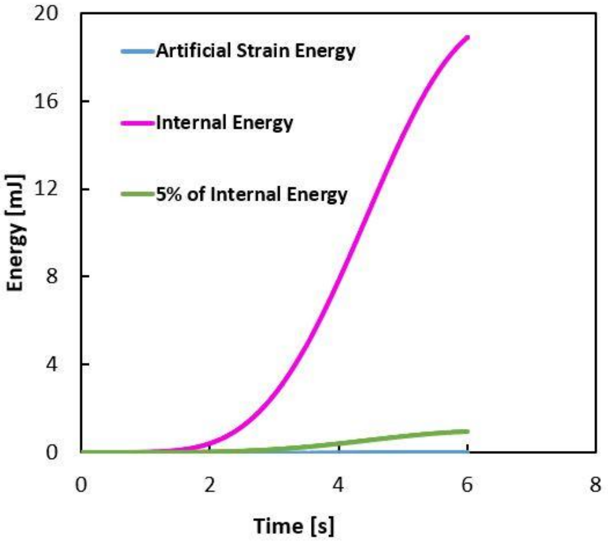

Figure 4-27 Artificial strain energy check of 3D-slice XFEM-LaRC05 model

To check whether quasi-static loading is applied correctly, kinetic vs. total strain energy (internal energy) history is examined. It is seen in Figure 4-28 that KE shown with yellow color is small enough during the analysis with respect to internal energy with pink color. Therefore, quasi-static loading is said to be successfully applied.

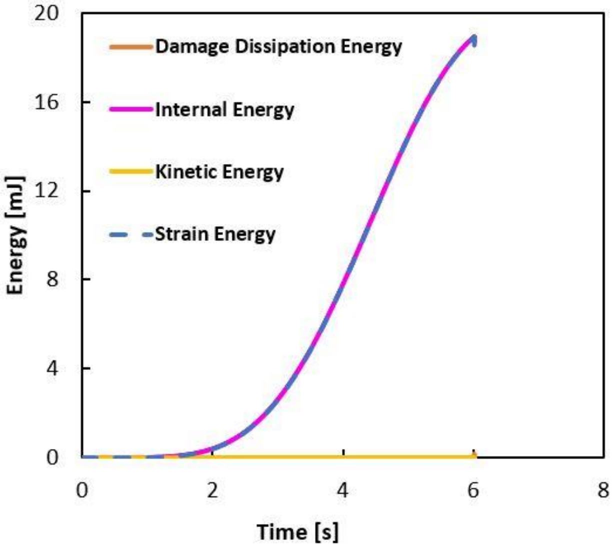

Figure 4-28 Energy histories throughout the analysis for 3D-slice XFEM-LaRC05 model

Further examination of the energy histories revealed that damage dissipation energy with orange color starts increasing, while strain energy with blue color decreases only slightly due to the failure initiation in the enriched elements. Since simulation is stopped due to contact of the crack surfaces, further changes cannot be captured.

The load-displacement response of curved unidirectional thick laminate from 3D-slice modeling coupled with the XFEM-LaRC05 method is shown in Figure 4-29 with yellow color. The grey curves represent the experimental results, while the dashed black curve is from the explicit analysis of a 2D plain strain model by Ata and Çöker [103]. The stiffness in the linear elastic region demonstrates good agreement with the experimental results and reference numerical solution. However, softening of the enriched elements and resulting load drop was not captured. The simulation ended at the very beginning of the delamination.

The major load drop takes place inside the scatter of experiments. Failure starts at exactly the same location (12th and 13th ply interface) as in the 3D CZM and references numerical solution. The initiation begins in the mid of the curved region and grows through tangential directions.

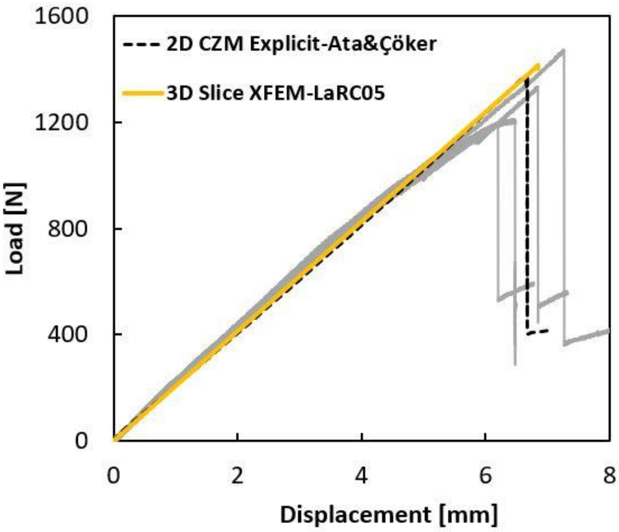

Figure 4-29 Load-displacement response of unidirectional L-beam from 3D-slice XFEM-LaRC05 model

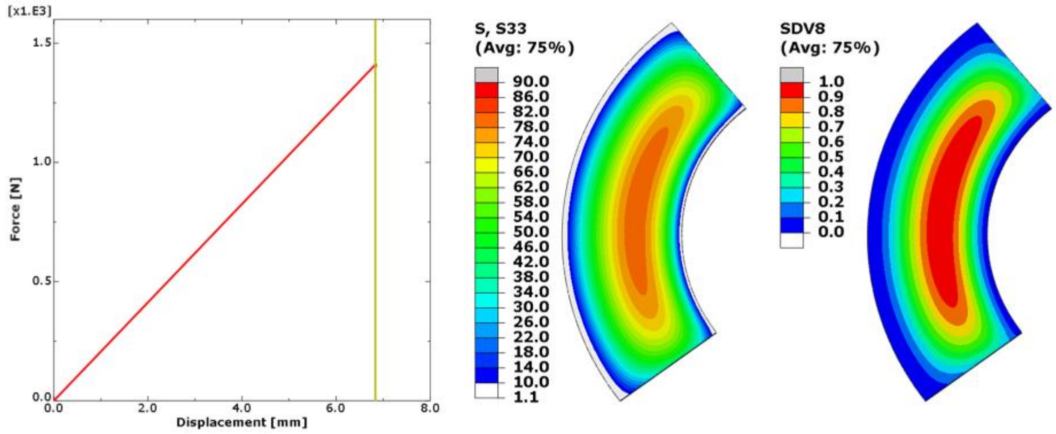

(a) 1411 N @ 6.83 mm

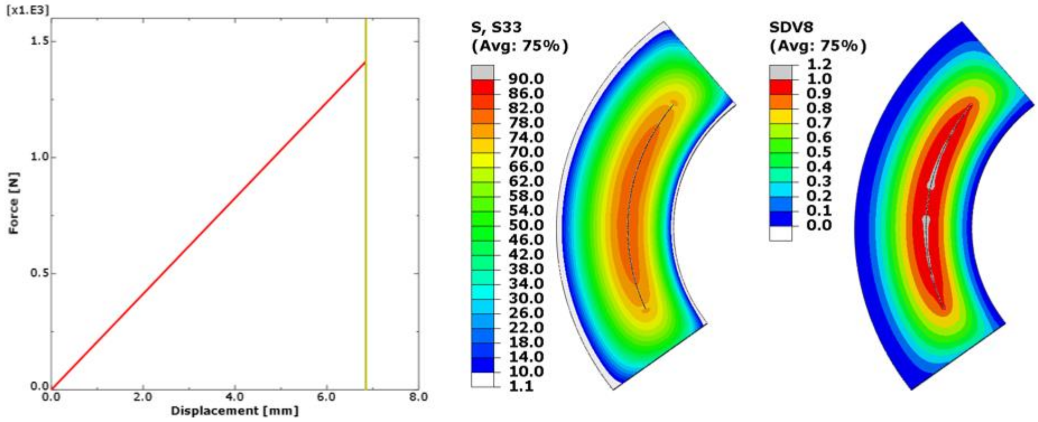

(b) 1412 N @ 6.84 mm

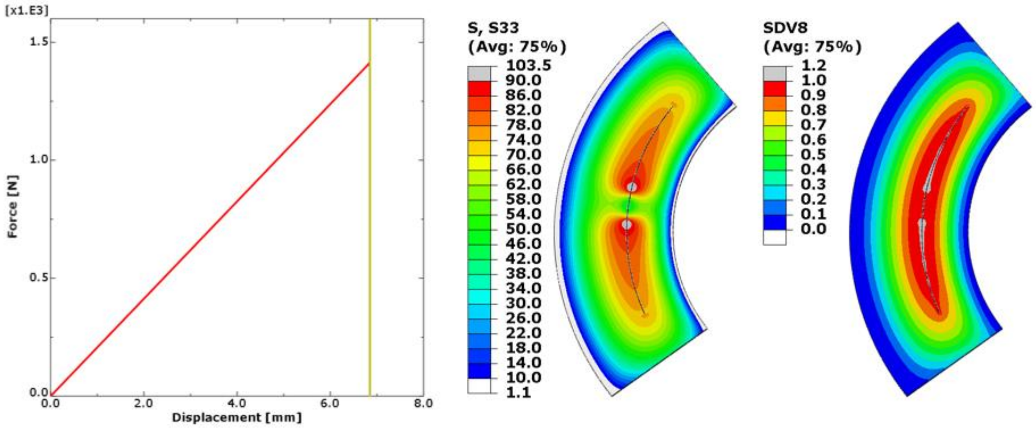

(c) 1410 N @ 6.84 mm

Figure 4-30 Radial stress contours and SDV8 matrix failure criterion of the curved beam slice at critical points for 3D-slice XFEM-LaRC05 model

(d)

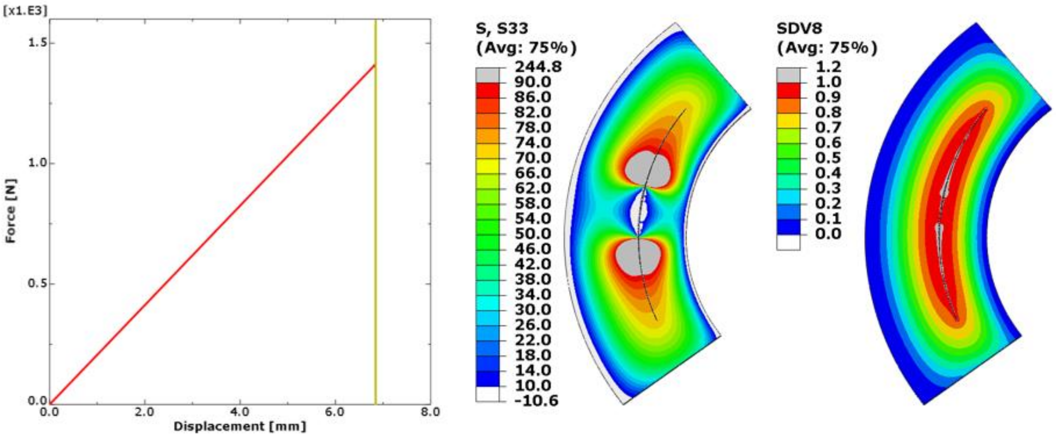

(e) 1400 N @ 6.84 mm

Figure 4-31 (continued)

Figure 4-30 illustrates radial stresses and failure indices on the slice of the curved region at points a-d. The radial stresses are maximum at 0.33R from the inner radius, consistent with the DIC and analytical results shared by Taşdemir and Çöker [106]. Moreover, comparison of the 3D XFEM model revealed that stress state at the slice model just before failure initiation is strictly identical to the mid-section stresses of the 3D model. That is 3D-slice model is representative of the mid-section of the 3D model through the width.

Figure 4-30 (a) illustrates the state just before the initiation of the matrix failure. The matrix failure criterion is in line with the radial stress distribution with localization at 0.33R from the inner radius, and damage onset is likely to occur at this localized region. Although enriched elements were separated by a crack in Figure 4-30 (b), the stress state did not change by this visible crack, and the load continued to increase up to (c). At (c), stress release started at the middle of the visual crack and singularity fields formed at both crack tips. The load started decreasing after (c), and delamination grew towards the arms, as seen in (d) in the same figure. Singularity fields are more evident in the (d) in Figure 4-30, and the SDV8 value exceeds the value of 1 at the cracked elements. However, excessive distortion at the crack surface led to the interaction of the surfaces, and further steps were unreliable.

4.2.3 Discussions

Figure 4-32 shows the post-mortem pictures of specimens after failure. Failure locations are the same for all numerical models in agreement with the experimental results, as seen in Figure 4-32. The load-displacement curves of numerical studies performed for unidirectional specimens are combined in Figure 4-33 for better comparison. Failure loads are within the scatter of experiments shown with grey lines.

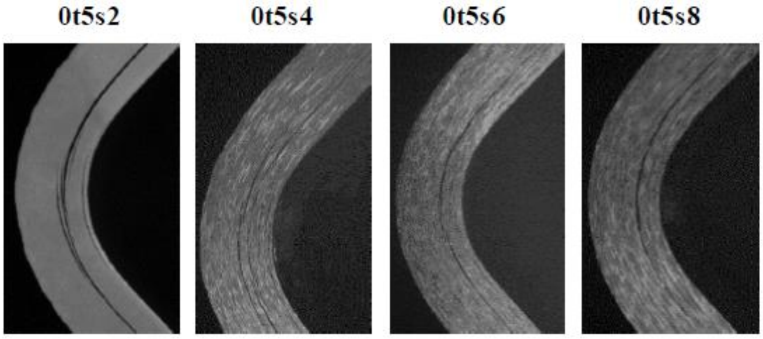

Figure 4-32 Post-mortem pictures of specimens after failure adapted from [106]

3D CZM and XFEM-LaRC05 models predict delamination initiation at 1355 N @ 6.68 mm and 1375 N @ 6.79 mm respectively. That is, LaRC05 failure criteria successfully predict the matrix failure-driven delamination at the same location and with a 1% higher load compared to 3D CZM with unidirectional strength values. Therefore XFEM combined with the LaRC05 matrix failure criterion was successful in the numerical simulation of the delamination for the 3D case. Nevertheless, the 3D-slice model encounters stability issues and distortions at the crack faces which affects the progression using XFEM. It also gives insight into the failure location and initiation load but is poor in softening phase.

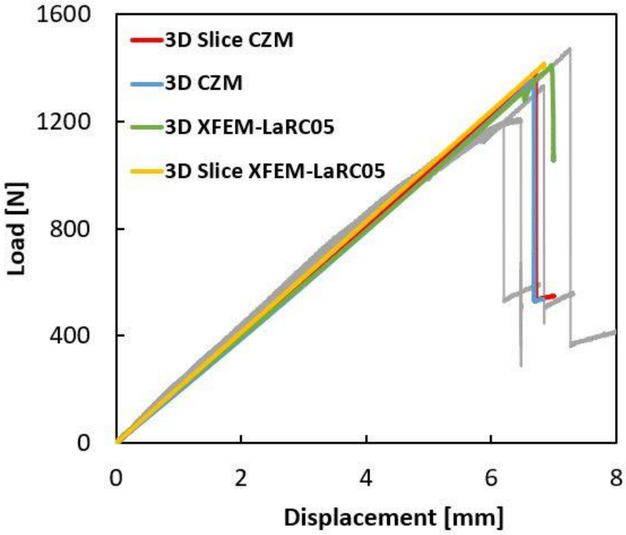

Figure 4-33 Load-displacement response of unidirectional L-beam for different numerical models and experiments

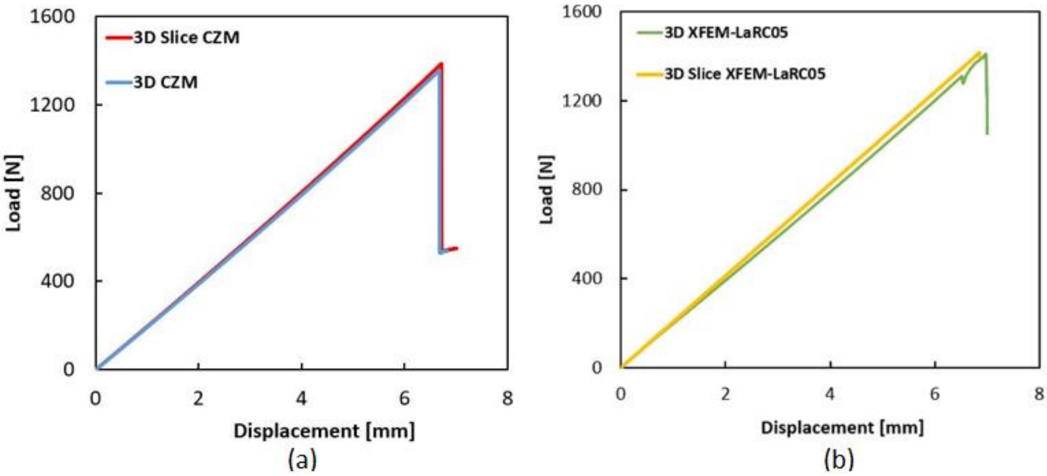

Figure 4-34 Load-displacement graphs using a) CZM and b) XFEM-LaRC05 method showing differences between 3D and 3D-slice models

3D-slice and 3D model with CZM have same load-displacement behavior as seen in Figure 4-34, and similar failure sequence are observed in these models. However 3D slice model have less computational cost. 3D-slice model with CZM is the best model among others in terms of accuracy and stability in the propagation phase. Both slice models of CZM and XFEM show a slight stiffer response in the elastic region than the 3D model due to plane strain constraints applied, as seen in Figure 4-34.

4.3 Cross Ply $[0_3/90_3/0_3/90_3/0_3]_s$ Laminate Results

4.3.1 3D-Slice CZM

The load-displacement response of curved cross-ply thick laminate from 3D-slice modeling coupled with the CZM method is shown in Figure 4-35 (a) with blue color. The stiffness in the linear elastic region demonstrates good agreement with the experimental results shown with dashed black lines. Failure in the simulations takes place at a higher load of 1460 N, which is much higher than the experimental average failure load of 860 N.

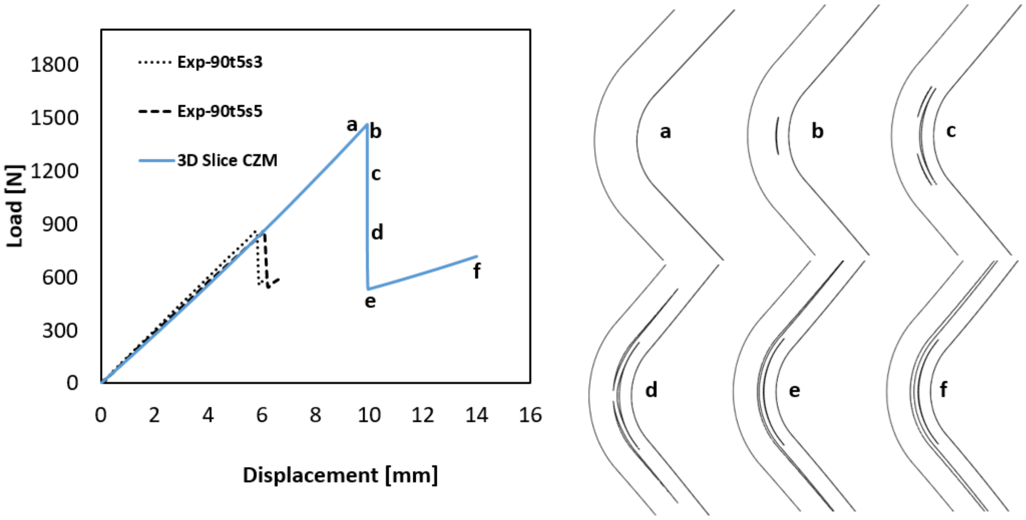

Figure 4-35 Load-displacement response of cross ply L-beam from 3D-slice CZM model and crack locations on load-displacement curve for critical points

Figure 4-35 (b) shows the damage sequence at corresponding points a-f in the load-displacement plot Figure 4-35 (a). These represent the damage sequence from failure initiation to the final prescribed displacement of 14mm. Failure starts at the interface between the second 0 degree and third 90 degree grouped plies (point b) and grows to the arms, but two other delamination appear at the fourth interface nearly 45° from midline grow inside the arms (point d). When delamination on the fourth interface is unified, load drop is stopped, and load increases with reduced stiffness to point f. The simulation is successfully completed at the prescribed displacement of 14mm.

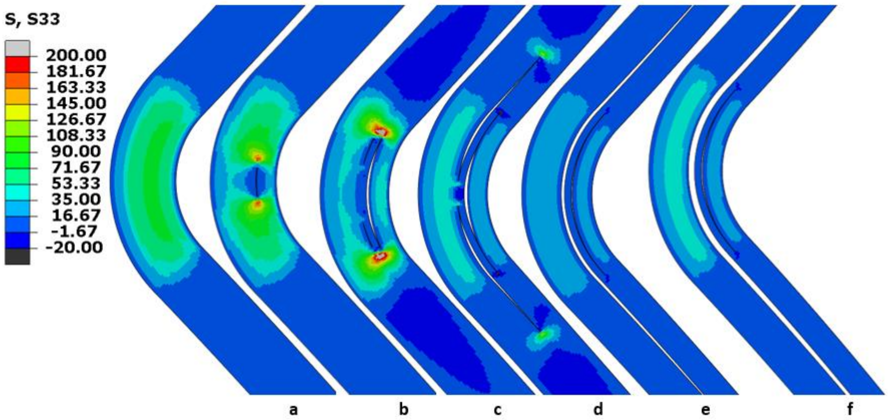

Figure 4-36 Stress contours on the deformed curved beam at critical points on the load-displacement curve

Figure 4-36 illustrates radial stresses in the curved region at points a-f. The radial stresses are maximum at the second 90_3 group, consistent with the analytical results [105]. The delamination in the third interface grows, and the stress field is affected by this damage as shown in Figure 4-36-b. After delamination is combined at the fourth interface, radial stresses become significant in the middle of the left side as loading increases. The main load-carrying member is this left-hand side part. The simulation is completed successfully, but if further loading is applied, delamination may grow at the ends of the arms, or new delamination may take place in the left load-bearing member.

4.3.2 3D-Slice XFEM-LaRC05

The load-displacement response of curved cross-ply thick laminate from 3D-slice modeling coupled with the XFEM-LaRC05 method is shown in Figure 4-37 with blue color. The stiffness in the linear elastic region demonstrates good agreement with the experimental results shown with dashed black lines. Points a-d represent damages in the curved region from failure initiation to final converged increment. Failure in the simulations takes place at a load of 1443 N much higher than the experimental average failure load of 860 N. A magnified view of the load-displacement graph is shown in the right of Figure 4-37. Severe convergence problems led the simulation to stop at the beginning of the load drop.

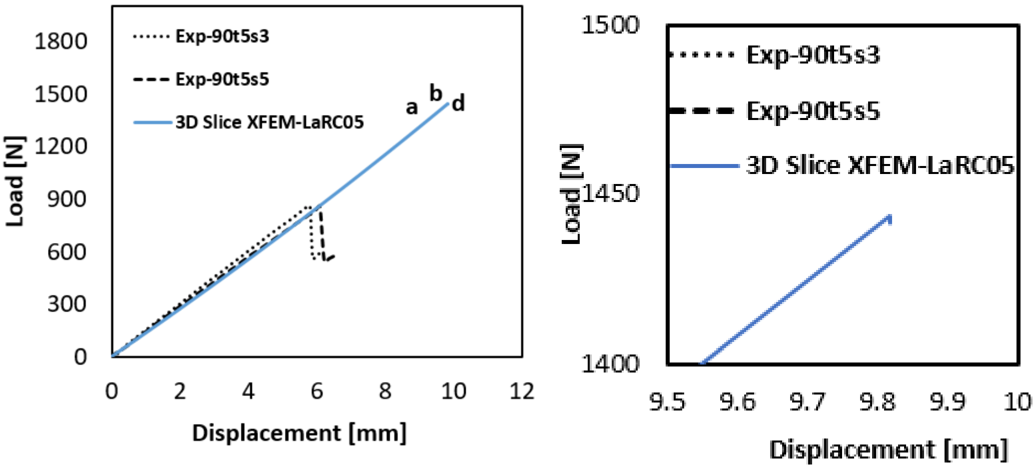

Figure 4-37 Load-displacement response of cross ply L-beam from XFEM-LaRC05 model

Figure 4-38 shows the damage sequence at corresponding points a-d in the load-displacement plot Figure 4-37. These represent the damage sequence from failure initiation to final converged increment. Damage starts nearly 1380 N under 9.4 mm displacement as a matrix failure in both the upper and lower part of the first 90° ply group, as displayed in Figure 4-38 point a, although it does not cause a load drop. This shear cracks remain stable throughout the simulation. The load drop starts with the delamination at the beginning of the second 90_3 group of plies after the load increased to 1440 N. Delamination occurs at the location where the radial stress is maximum through the thickness direction. This delamination grows up to the arms, as shown in Figure 4-38 point c resulting in a sudden load drop, and there exists another shear crack in the first 90-degree grouped plies close to the midline. The simulation stopped at point d due to convergence problems.

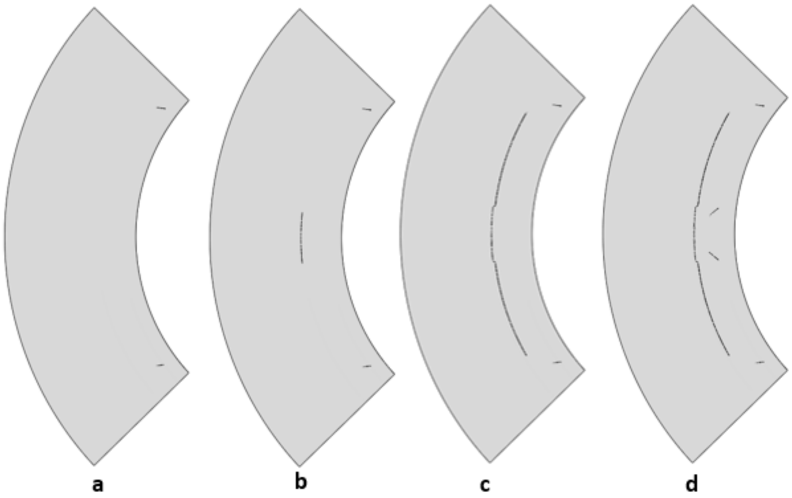

Figure 4-38 Damage evolution on the curved region at points a, b, c, d on the load-displacement curve respectively

The SDV8 contours at points on the load-displacement curve are represented in Figure 4-39. At point a, the first 90_3 group is critical, but as load increases to point b, SDV8 reaches 1 throughout the second 90_3 group, and delamination begins at the mid portion of the curve very close to the interface between ninth and tenth plies and evolves to the arms at the same interface. As a last event new set of shear cracks occurs at the first 90_3 group close to the center of arc length prior to SDV8 value reaches 1.

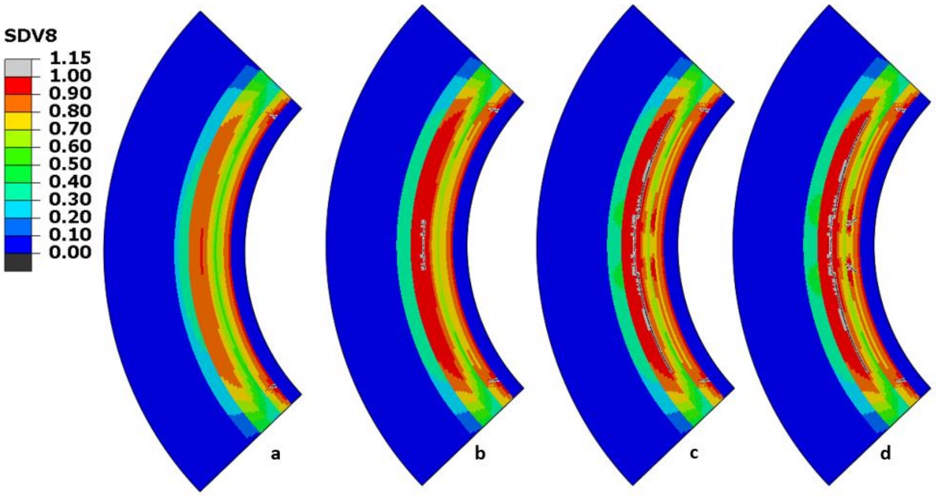

Figure 4-39 SDV8 Matrix failure index for the points a, b, c and d respectively

Figure 4-40 illustrates radial stresses in the curved region at the points a-d located in the load-displacement graph Figure 4-37. Radial stress is located mainly in the second 90_3 group. While the first matrix crack does not cause any change in the stress field, as delamination grows and softening occurs at the second 90° plies, the stress field is affected by this damage. Crack surfaces after softening are under almost zero stress state.

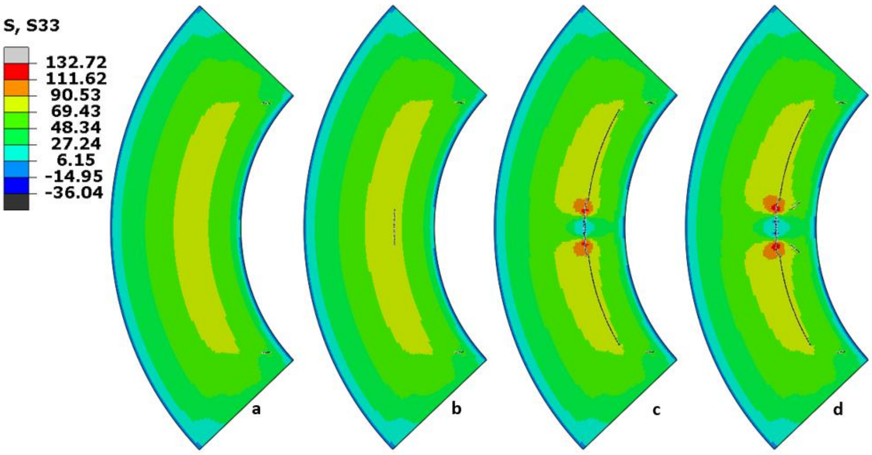

Figure 4-40 Stress contours at points a, b, c and d on load-displacement curve

4.3.3 Results using Reduced Strengths

In the previous section, both CZM and XFEM-LaRC05 models, in which the strength values stated by [102] and Taşdemir and Çöker [105] used, predicted the failure initiation load to be nearly two times that of the experimental results. Also, failure location does not conform to the experimental observations. Experimental results cover two thick specimens, both fail due to delamination in the first 90_3 ply group shown in Figure 4-41, which is not predicted by both numerical simulation methods. The cracks initiate as a matrix crack at the location shown by yellow arrows and propagate parallel to the interface, and jump to the upper interface with a 40-50° shear crack close to the arms. Load bearing capacity increases as delamination evolves within arms at the upper interface of the first 90_3 ply group.

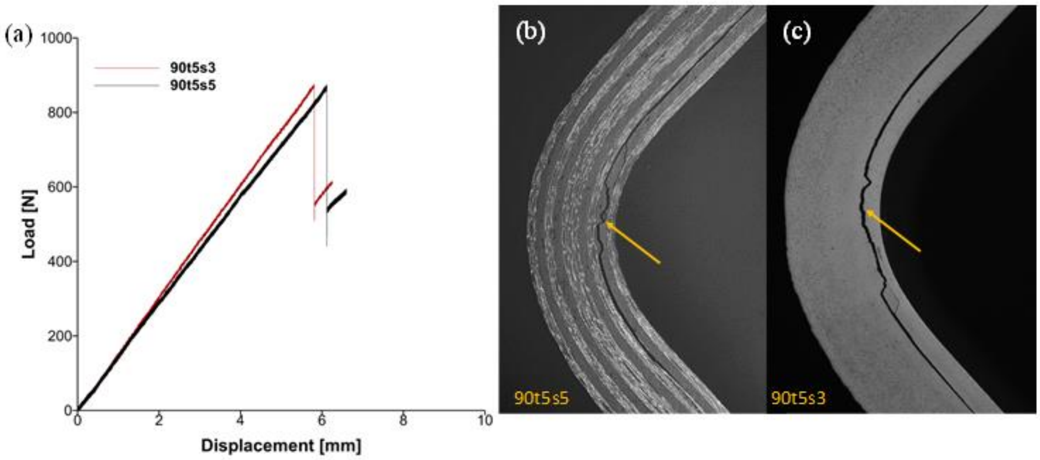

Figure 4-41 a) Load-displacement graph and post-mortem pictures of failure in b) specimen 90t5s3, c) specimen 90t5s5 taken from [105]

Taşdemir and Çöker [105] stated that visible voids exist in thick specimens due to inadequate vacuuming of the specimens, as shown in Figure 4-42. The voids cause stress concentration related to their geometry, location, and density and promote intralaminar crack initiation and propagation. There are many references in the literature studying the effect of void on mechanical properties and delamination of composites [108]-[111]. However, void content and density should be identified to determine the reduction levels of mechanical properties. Since experimental specimens were not inspected before tests, it is impossible to detect void content and possible effects directly in our case. However, studies on the effects of defects on the mechanical performances of composite laminates point out that mostly interlaminar properties are degraded, and excess matrix or voids cause matrix dominated properties to be reduced. The other possible reason for earlier failure initiation might be process induced residual stresses. To encounter this effect, thermal step should be added to simulations of curved beams.

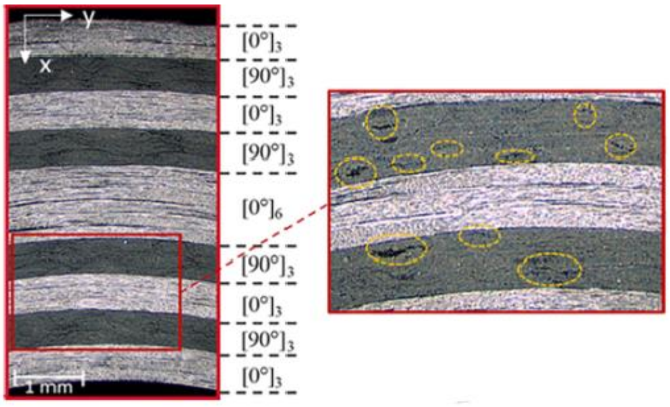

Figure 4-42 Manufacturing defects and voids in the specimens [105]

The study conducted by Liu, Tay, Ng, and Tan states that interlaminar shear strength ILSS decreases with mismatch angle according to multidirectional laminate short beam strength tests [112]. They suggested that it is crucial to use true interlaminar properties for the better prediction of load-displacement curve and damage sequences. Moreover, a study on interlaminar tensile strengths of cross-ply laminates by Yavuz, Parnas, and Çöker [113] demonstrated that cross-ply interfaces have lower ILTS than unidirectional laminates, as shown in Figure 4-43. The value of ILTS for 45/-45 interface with a 90° mismatch angle is nearly 50% lower than 0/0 interface. This significant difference is attributed to the excess resin between angled interfaces.

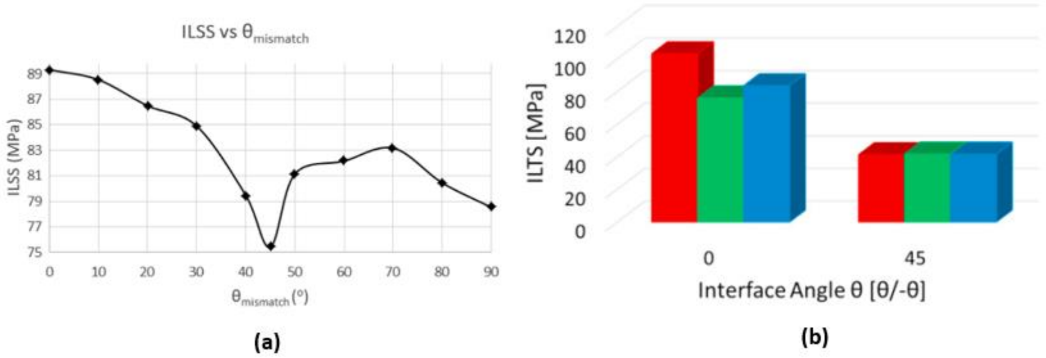

Figure 4-43 (a) ILSS variation with mismatch angle taken from [112] and (b) ILTS variation with interface angle taken from [113]

Therefore, matrix-dominated properties and interlaminar properties are significantly reduced (50 %) in different manners, as tabulated in Table 5, to observe change in the failure loads and mechanisms.

Table 5 Strength reduction studies on cross ply laminates

Model	**Study**
3D-slice CZM	Study 1 – Interlaminar strength reduction in 1st and 2nd cohesive layers
	Study 2 - Interlaminar strength reduction in all cohesive layers
3D-slice XFEM-LaRC05	Study 1 - Intralaminar strength reduction in 1st 90_3 plies
	Study 2 - Intralaminar strength reduction in 1st and 2nd 90_3 plies

The updated material strengths and interface properties used in these studies are given in red color in Table 6 and Table 7, respectively.

Table 6 Material strengths of AS4/8552 used in the reduction study

Strengths	**X_T [MPa]**	**X_C [MPa]**	**Y_T [MPa]**	**Y_C [MPa]**	**S_L [MPa]**	**S_T [MPa]**
Thin Embedded	2207	1531	38.95	130.89	44.89	49.32

Table 7 Interface properties of AS4/8552 UD prepreg used in the reduction study

k_I^0 [MPa/mm]	**k_{II}^0 [MPa/mm]**	**k_{III}^0 [MPa/mm]**	**t_I^0 [MPa]**	**t_{II}^0 [MPa]**	**t_{III}^0 [MPa]**	**G_{Ic} [N/mm]**	**G_{IIc} [N/mm]**	**G_{IIIc} [N/mm]**	**η**
2.6e6	2.6e6	2.6e6	39.5	53.2	53.2	0.28	0.79	0.79	1.45

4.3.3.1 3D-Slice CZM

Study 1- Interlaminar strength reduction in 1st and 2nd cohesive layers

To trigger failure in the first 90 group, interlaminar strengths of the first and second cohesive layers shown in Figure 4-44 a) are reduced by 50 %. The load-displacement response of curved cross-ply thick laminate for study 1 is shown in Figure 4-44 (b) with red color. Points a-f represents damages at specific points from failure initiation to the final increment of the simulation.

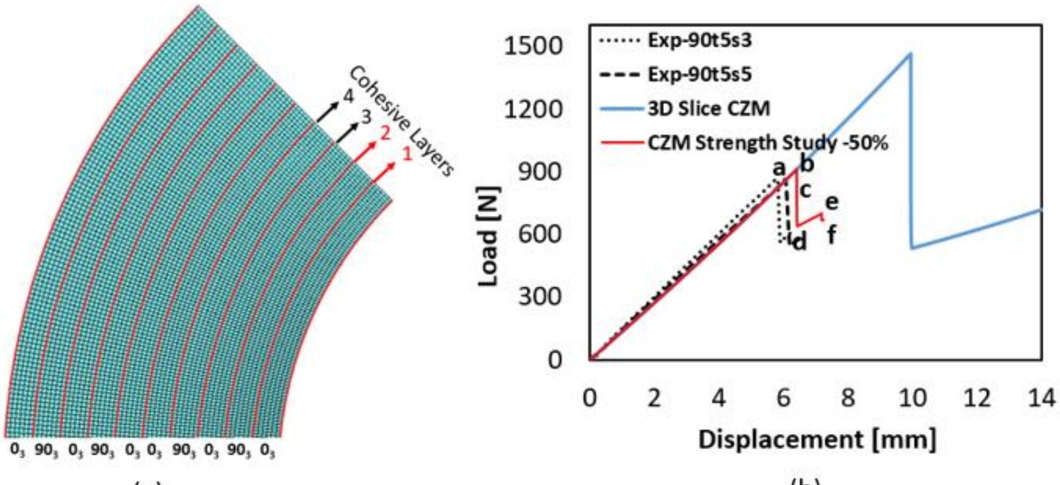

(a) (b)

Figure 4-44 Representation of a) reduction regions (1 and 2) and b) resulting load-displacement curve

The ultimate load decreased to almost half of the entire case as expected, and the load-displacement response is very close to the experiments. The damage sequence corresponding to points a-f are illustrated in Figure 4-45. Failure starts at the cohesive layer 1, and grows to the arms, but two other delamination appear at the second interface close to the tips of first crack. At point d, load drop is stopped, and load carrying capacity increases with reduced stiffness. As delamination on the second interface is unified, a small load drop is observed, and simulation was completed at the 7 mm prescribed displacement.

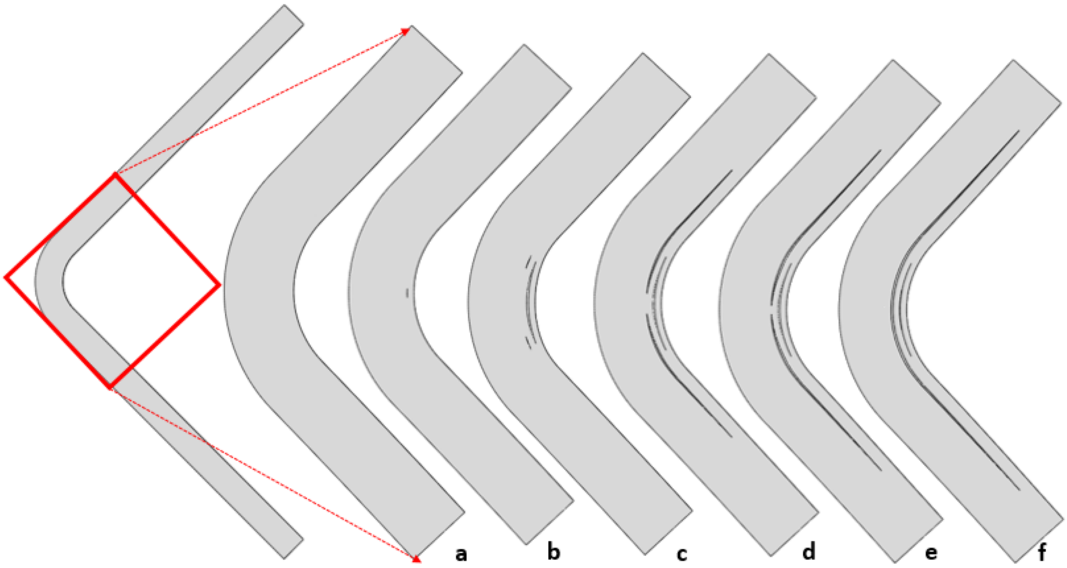

Figure 4-45 Damage evolution on the curved region at points a-f on the load-displacement curve respectively

Through-the-thickness stress contours corresponding the points a-f are represented particularly in Figure 4-46. Stress concentration is seen around second 90° group of plies before failure initiation at point a, but delamination takes place at the lower interface of first 90° group as seen in point b. When the crack appeared, stress concentration fields were formed and localized at the upper interface of these groups at the tips. Then two new cracks originated at localized regions of the S33 stresses at point c and moved to the arms. When delamination growth through the arms stabilized (point d), the beam started to carry loading with a stiffness lower than the initial one up to point e. At point e, delamination at the upper interface was unified, and a small load drop was observed. Subsequently, loading started to increase with the new load-carrying member above the delamination region, and the S33 field was maximized at third 90° group as seen in Figure 4-46f.

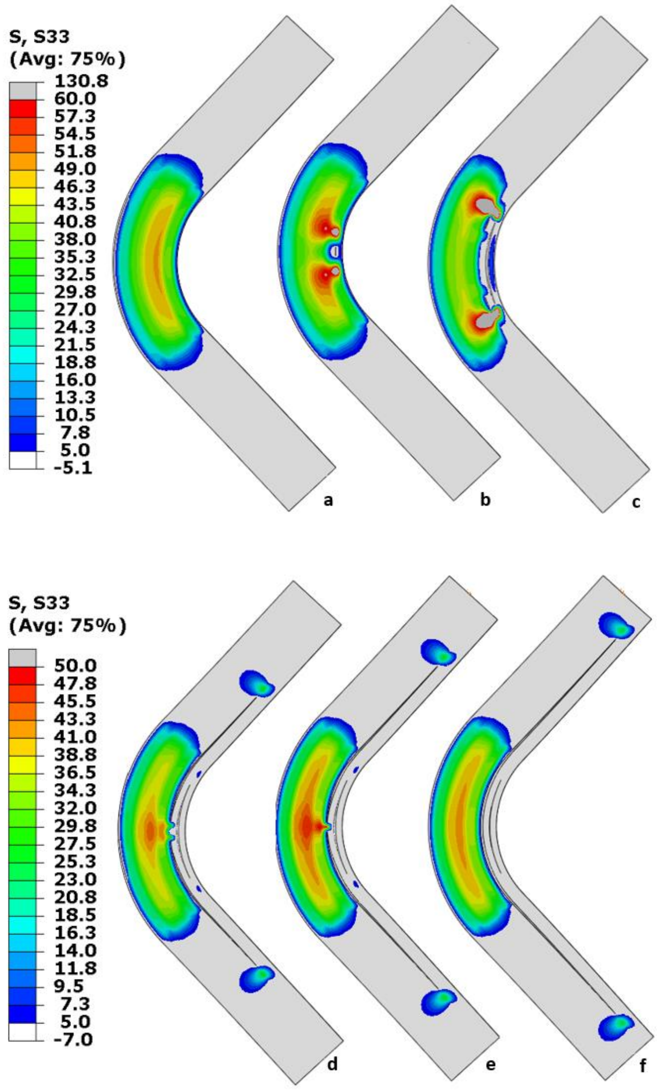

Figure 4-46 S33 stress contours on the deformed curved beam at critical points of the reduction study 1 for CZM model

Study 2- Interlaminar strength reduction in all cohesive layers

The load-displacement response of curved cross-ply thick laminate is shown in Figure 4-47 (a) with purple color for 50 % strength reduction in all cohesive layers. The points a-d represents damages in the curved region. The damage sequence corresponding to the critical points is illustrated in Figure 4-47 (b). The section is the same as shown in Figure 4-45.

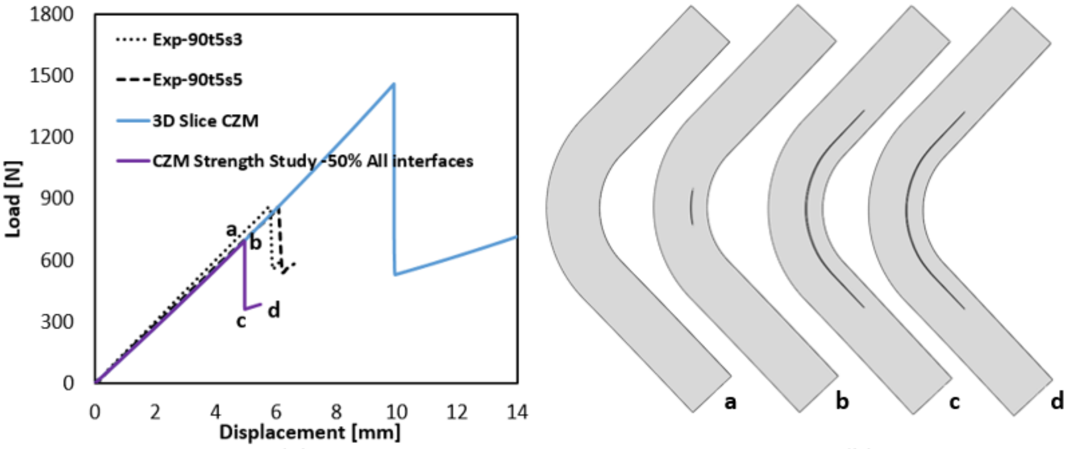

(a) (b)

Figure 4-47 Load-displacement response of CZM with 50% reduction at all interfaces and damage illustration for critical points

Failure starts at the cohesive layer 3 at a load of 693 which is lower than the experimental failure load and grows to the arms. At point c, load drop is stopped, and the load increases with reduced stiffness. After point c, the damage is stabilized, and only small propagation is seen between c and d.

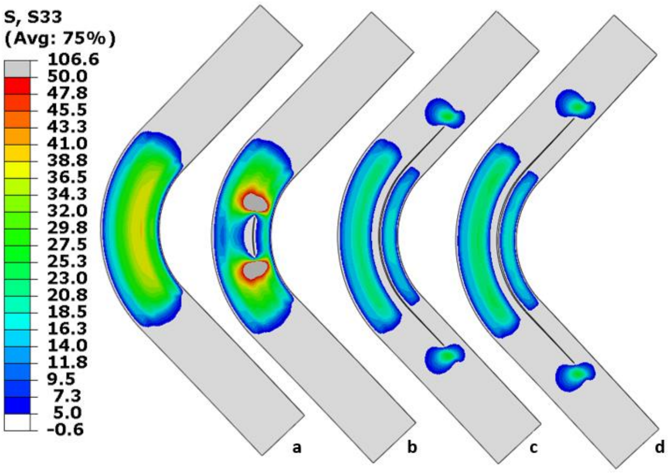

Figure 4-48 S33 stress contours on the deformed curved beam at critical points of the reduction study 2 for CZM model

Corresponding through the thickness stress contours of critical points are given particularly in Figure 4-48. Stress concentration is around second 90° group of plies before failure initiation at point a, and failure initiates exactly at the location where radial stresses is high. When the crack appeared, stress concentration fields were formed at the tips. Then delamination moved to the arms. When delamination growth through the arms stabilized (point c), the beam started to carry loading with loss of initial stiffness up to point d. The main load-carrying member is the part above the delamination region, and the S33 field was maximized at third 90° group.

4.3.3.2 3D-Slice XFEM-LaRC05

Study 1- Intralaminar strength reduction only in 1st 903 plies

XFEM regions are defined in Figure 4-49 (a), in which the green is for the reduced strength region. The load-displacement response of curved cross-ply thick laminate with 50 % strength reduction is shown in Figure 4-49 (b) with red color. Points a-f represents damages in the curved region from the first failure initiation to the final converged increment.

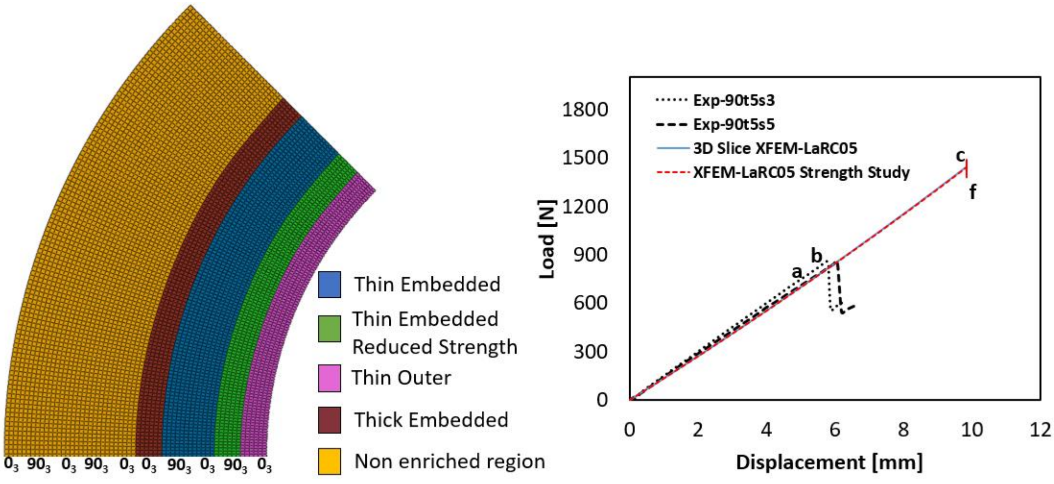

(a) (b)

Figure 4-49 Representation of a) reduction regions (green) and b) resulting load-displacement curve

The damage sequence at the critical points is represented in Figure 4-50. The first failure starts at the first 90° group as a matrix crack even before the experiments and grows to the upper interface of this ply group up to point b in Figure 4-50.

Nevertheless, these cracks do not trigger delamination or cause load drop. The initiation of the delamination occurs at the lower interface of second 90 degree group plies at the same load level without a load drop as seen in Figure 4-50 and grows to the arms. Lastly, new delamination starts at the upper interface of this group Figure 4-50 e) and severe convergence problems led the simulation to stop after a small load drop.

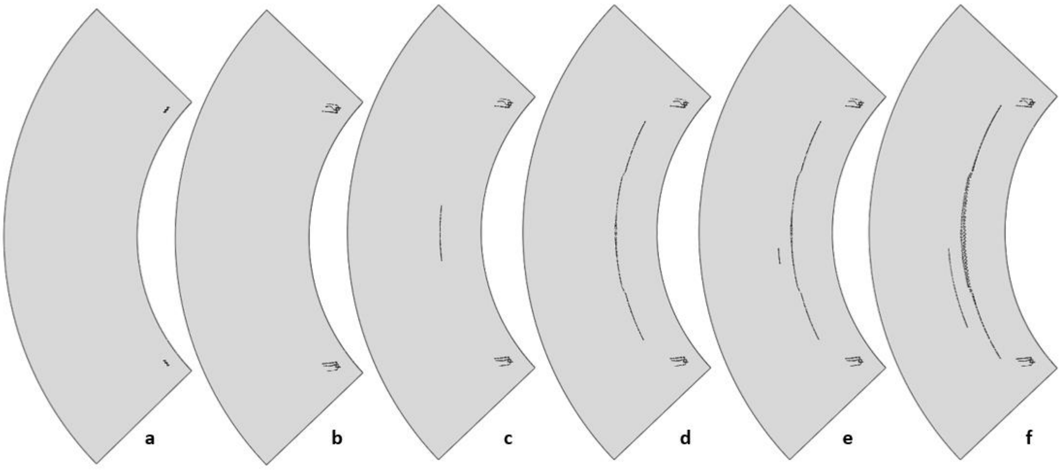

Figure 4-50 Damage evolution on the curved region at critical points on the load-displacement curve respectively

Radial stress distributions and corresponding points on the load-displacement graph are shown in Figure 4-51. The first damage starts nearly 672 N under 4.8 mm displacement as a shear crack in both the upper and lower parts of the first 90° ply group, as displayed in Figure 4-51 point a, although it does not cause load drop. These shear cracks remain stable throughout the simulation. Load drop starts with the delamination at the beginning of second 90_3 group of plies after the load is increased to 1444 N. It is seen from stress contours that the location of delamination lies on the maximum through the thickness stresses at point c. This delamination grows to the arms, as shown in Figure 4-51 point d resulting in load drop. A new matrix crack initiates at the upper interface of second 90° ply group, but the stress field was not affected by this crack since the damage variable is small. The simulation stopped at point f due to convergence problems. At the last point, it was seen that there is no stress at the crack surfaces as expected.

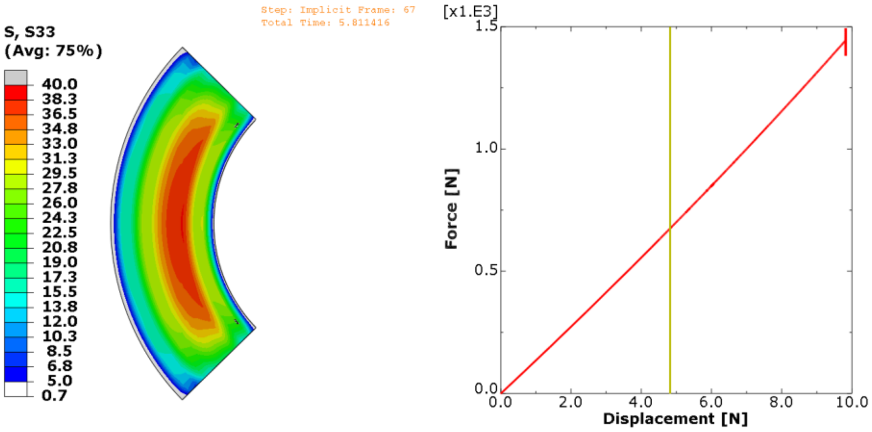

(a) 672 N @ 4.8 mm

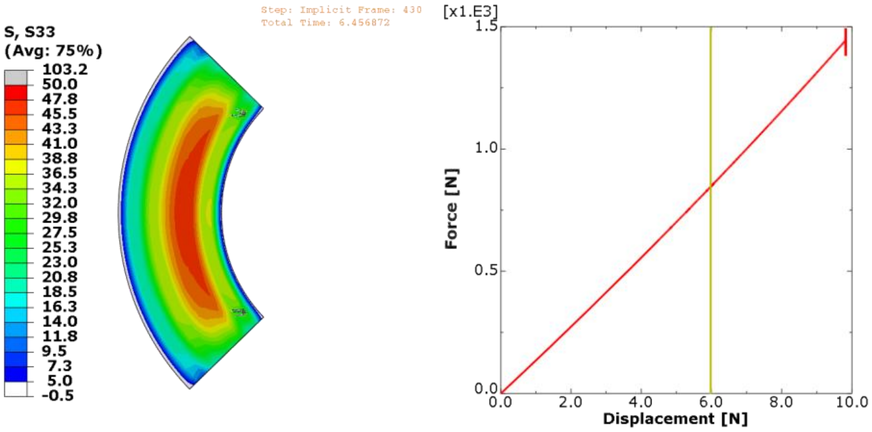

(b) 846 N @ 5.98 mm

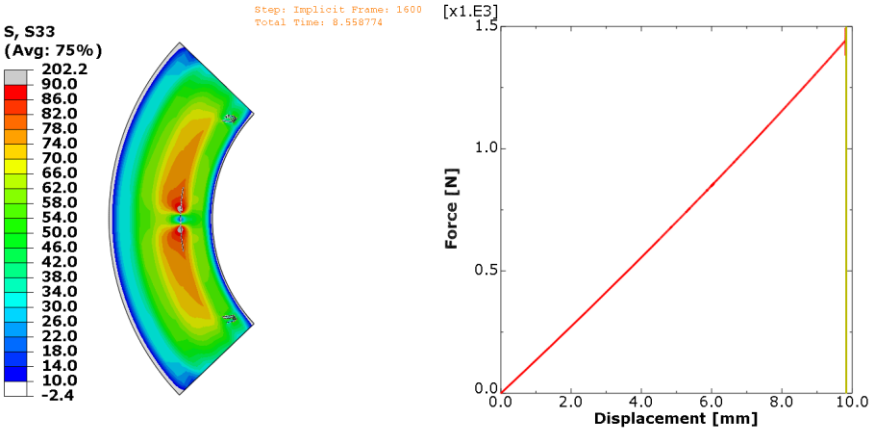

(c) 1444 N @ 9.82 mm

Figure 4-51 S33 stress contours on the deformed curved beam at critical points of the reduction study 1 for XFEM model

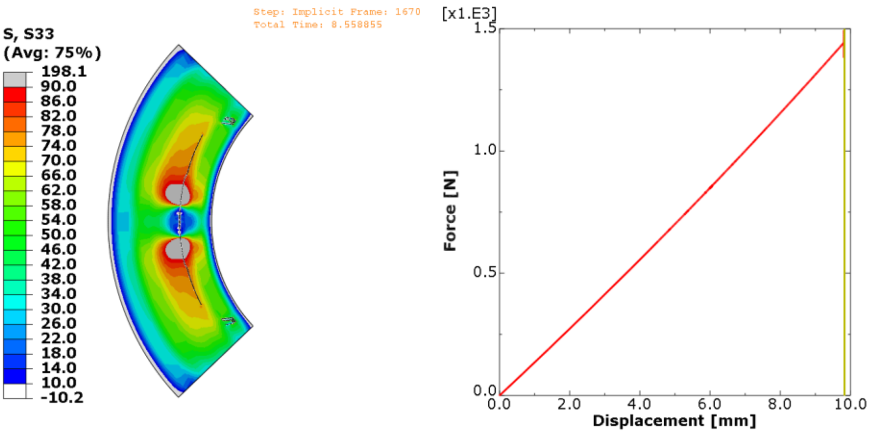

(d) 1440 N @ 9.82 mm

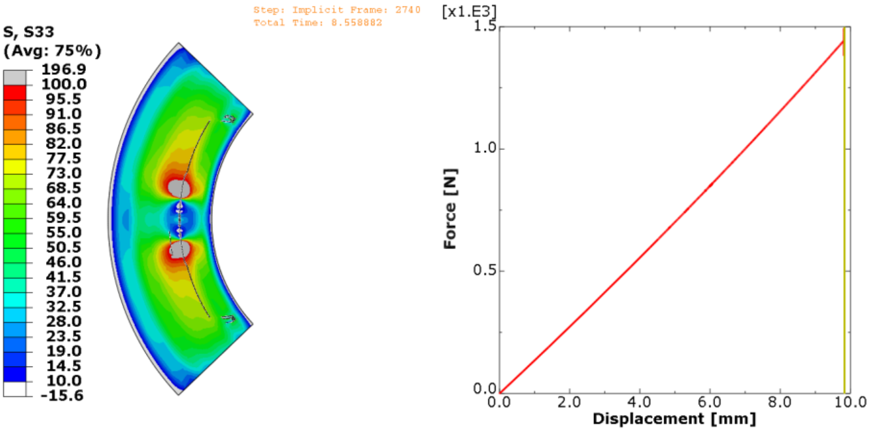

(e) 1436 N @ 9.82 mm

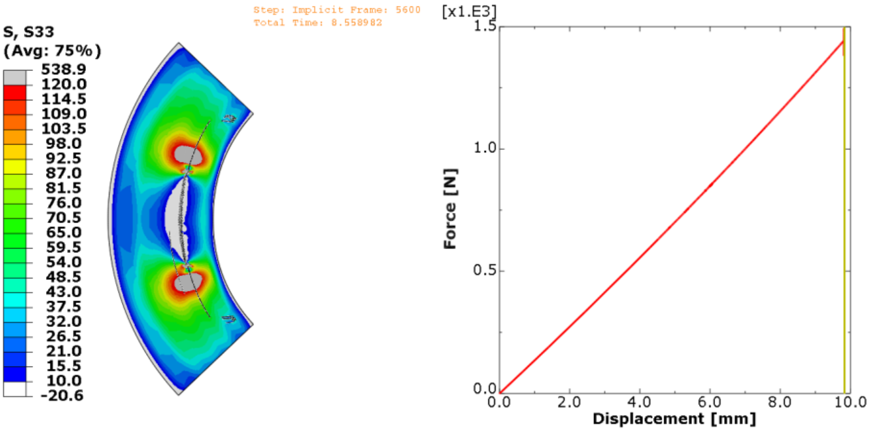

(f) 1382 N @ 9.82 mm

Figure 4-52 (continued)

Study 2- Intralaminar strength reduction 1st and 2nd 90_3 plies

For the second study, the strength of both 1st and 2nd 90_3 plies, shown as green regions in Figure 4-53, are reduced. The load-displacement response of this model is shown in Figure 4-54 with red color. Points a-c represent damages in the curved region from the first failure initiation to the final converged increment.

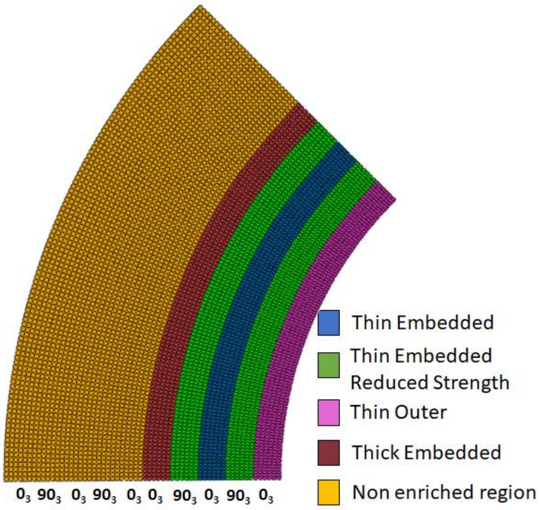

Figure 4-53 Representation of reduction regions (green)

The first failure starts at the first 90° group as a matrix crack before the experiments and grows to the upper interface of this ply group up to point b in Figure 4-54. Nevertheless, these cracks do not trigger delamination or cause load drop. Delamination at the 2nd 90° lower interface begins at exactly the same load level without reduction at point b in Figure 4-54 and grows to the arms. Severe convergence problems led the simulation to stop after a small load drop.

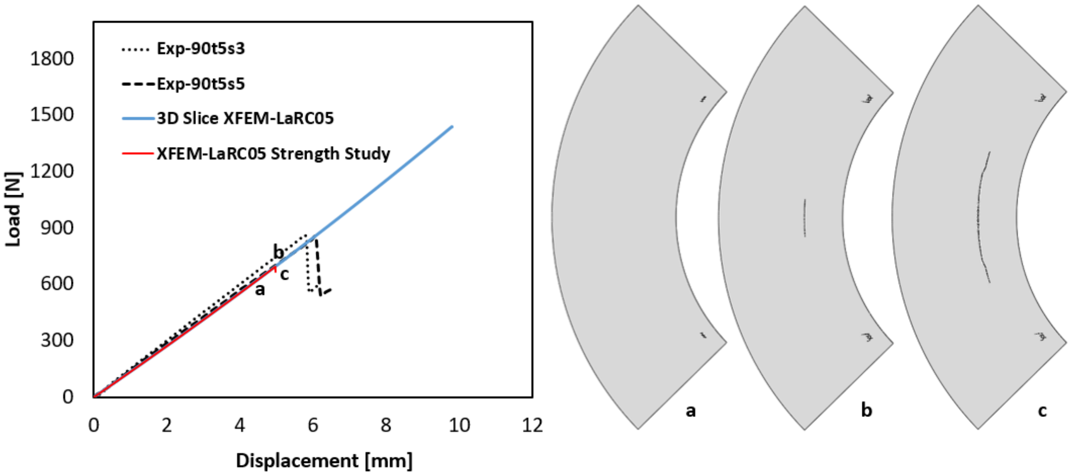

Figure 4-54 Load-displacement curve with reduced strengths (red) and damage evolution at critical points

Radial stress distributions and corresponding points on the load-displacement graph are shown in Figure 4-55. Damage starts nearly 683 N under 4.87 mm displacement as a matrix failure in both the upper and lower part of the first 90° ply group, as displayed in Figure 4-55 point a, although it does not cause load drop. These shear cracks remain stable throughout the simulation. Load drop starts with the delamination at the beginning of second 90° group of plies after the load increased to 695 N. It is seen from stress contours that the location of delamination lies on the maximum through the thickness stresses at point b. This delamination grows to the arms insignificantly, as shown in Figure 4-55 point c resulting in load drop. Simulation stopped after point c due to convergence problems. At the last point, it is seen that there was no stress at the crack surfaces as expected.

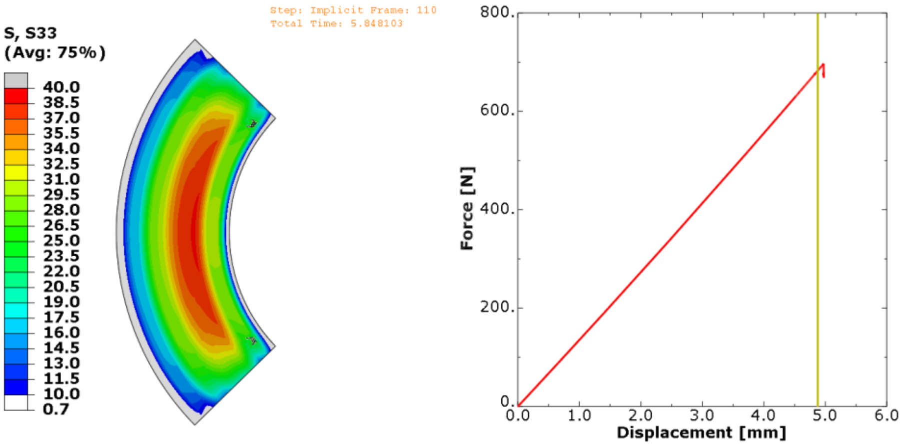

(a) 683 N @ 4.87 mm

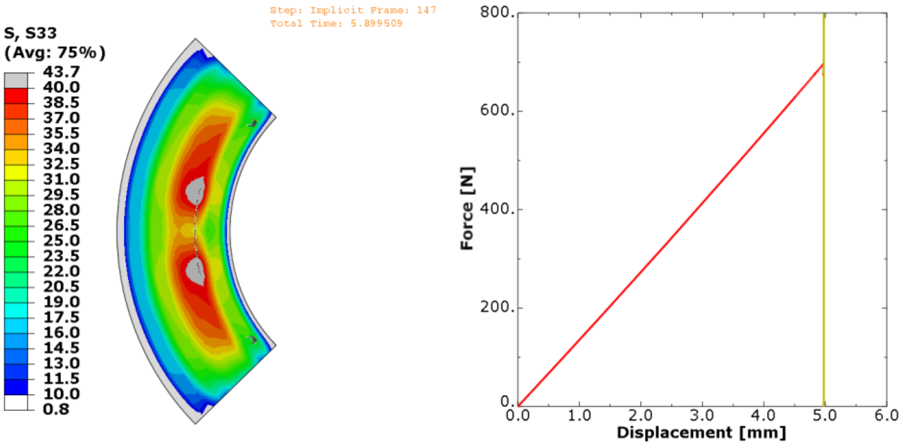

(b) 695 N @ 4.97 mm

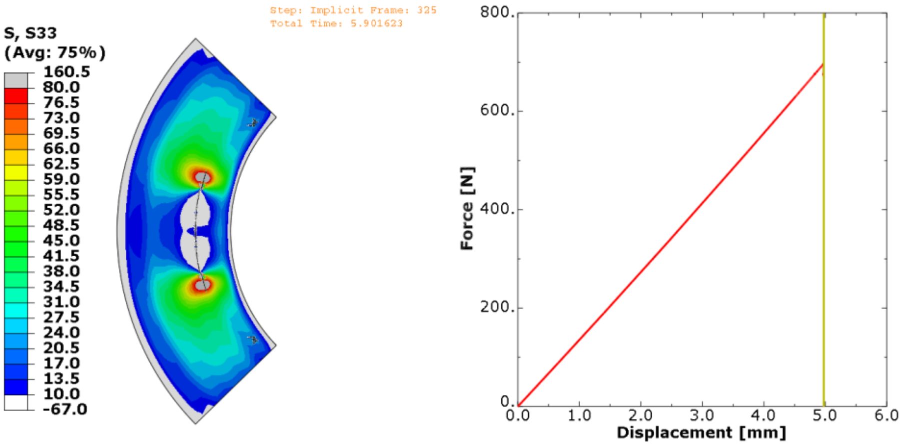

(c) 668 N @ 4.97 mm

Figure 4-55 S33 stress contours on the deformed curved beam at critical points of the reduction study 2 for XFEM model

4.3.4 Discussions

When interlaminar strengths were taken from unidirectional specimen tests and intralaminar strengths were taken for standard intact laminates without voids, both CZM and XFEM-LaRC05 models predict delamination nearly at 1450N, 9.8 mm, as shown in Figure 4-56. Failure locations of CZM and XFEM-LaRC05 models are in agreement, as well as the load which is due to delamination at the lower interface of 2nd 90_3 plies represented in Figure 4-35 and Figure 4-38. Different from CZM, the XFEM-LaRC05 model estimated a matrix shear crack nearly at the 1350N, 9.4mm located symmetrically on the first 90_3 plies making 22.5° angle with the horizontal midline, Figure 4-38. It is common in the literature that shear matrix cracks induce delamination when they come to the interface [15].

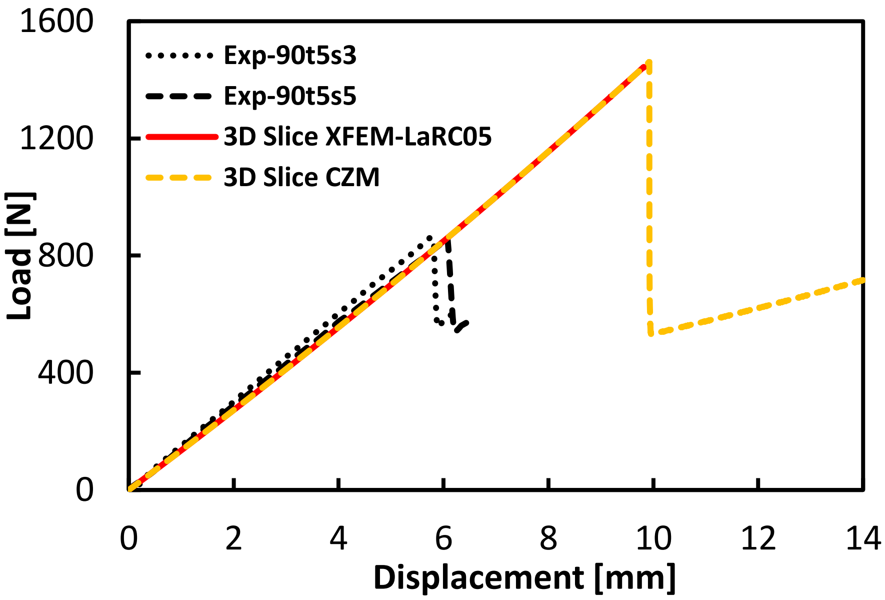

Figure 4-56 Load-displacement comparisons of CZM and XFEM-LaRC05 models for intact case

In the intact case comparison using standard strength values, LaRC05 failure criteria successfully predict the matrix failure-driven delamination at the same location and load with CZM. If convergence issues of XFEM would be solved or another stable damage propagation feature is utilized, LaRC05 failure criteria well estimates intralaminar cracks and delamination caused by matrix cracking.

The entire cases failed to simulate the experiments in terms of failure load and behavior. The numerical models were updated considering voids in the test specimens and the effects of cross-ply on interface strengths. The load-displacement graphs regarding updated strength values in the first 90_3 group and their outer interfaces are illustrated in Figure 4-57. The load of the first damage is reduced in the XFEM model, as shown with point a in Figure 4-54, but it is still unable to predict delamination in first 90_3 group, rather the damage is in the form of a shear crack. After the first damage, the XFEM model predicts delamination at the lower interface of the second 90 group at the same load because strength reduction is applied only to the first 90 group. However CZM model with reduced strengths at the first two interfaces accomplished the similar behavior with tests in Figure 4-45 despite the deficiency of delamination jump through plies.

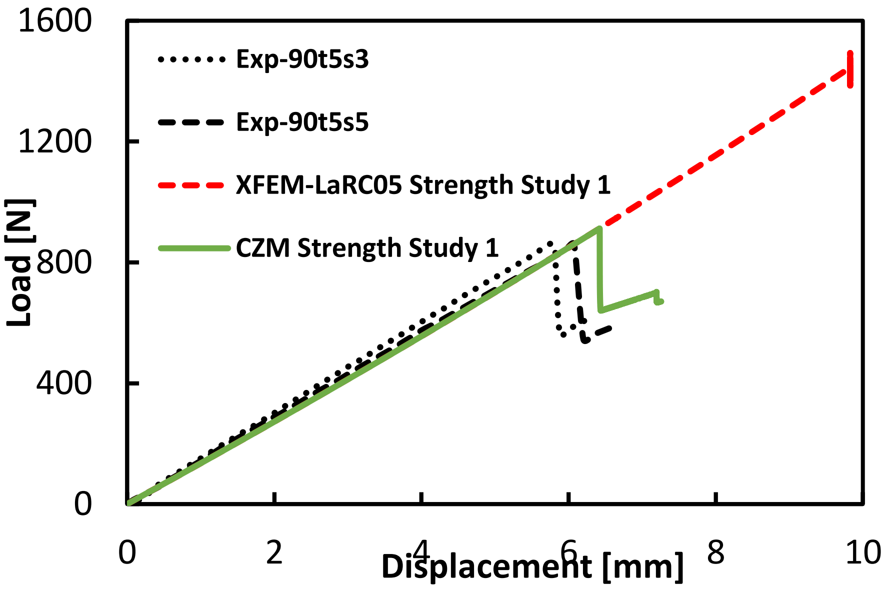

Figure 4-57 Load-displacement comparisons of CZM and XFEM-LaRC05 models with reduced strength study 1

The load-displacement graphs for the second study are illustrated in Figure 4-58. The load of the first damage is reduced in the XFEM model, as shown with point a in

Figure 4-54, but it is still unable to predict delamination at the first 90_3 group, rather the damage is in the form of a shear crack. After the first damage, the XFEM model predicts delamination at the lower interface of the second 90 group before the experiments. CZM model with reduced strengths at all interfaces accomplished the same failure load with XFEM-LaRC05 Study 2, as shown in Figure 4-58. Besides delamination location is also at 0.33R from the inner radius.

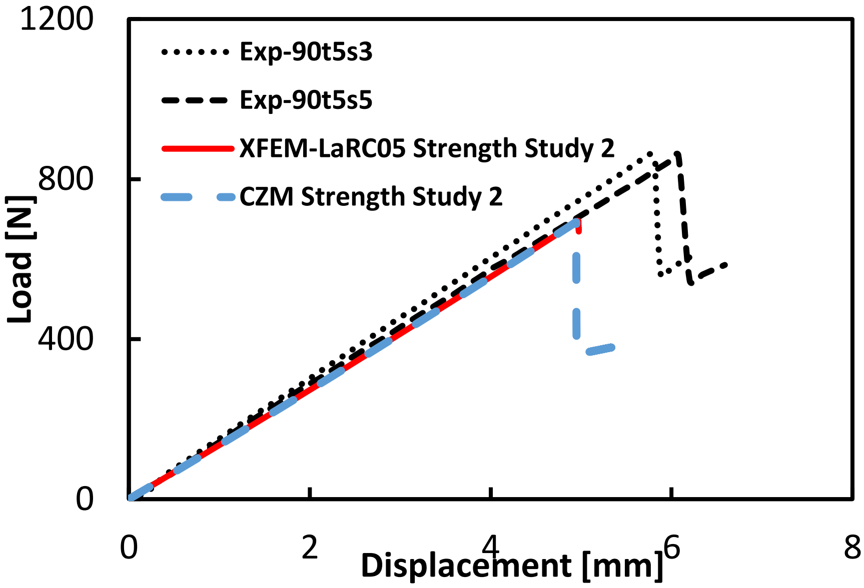

Figure 4-58 Load-displacement comparisons of CZM and XFEM-LaRC05 models with reduced strength study 2

XFEM model is found to be ineffective during the dynamic crack propagation phase because of convergence issues, although damage stabilization is applied to enriched elements. CZM successfully handled the dynamic crack growth and completed the simulations without convergence difficulty. CZM is more stable in the dynamic crack growth for the complete failure investigation. However, jumps between interfaces cannot be captured without damage initiation and evolution accounting intralaminar failures.

If intralaminar damage is included combined with CZM, after the first delamination at the first cohesive interface, matrix crack may lead to a jump to the next interface, which is the case in the experiments. But it is quite obvious that the interlaminar strengths of the specimens used in the experiments were less than the measured values for the unidirectional case by Ata and Çöker [103]. It is essential to use actual material properties affected by manufacturing and interface mismatch angles.

4.3.4.1 Convergence Issue

XFEM model encounters severe convergence difficulties at the very beginning of load drop due to softening of the enriched elements. It is found in the literature that XFEM has stability problems arising from the linear dependence of the global stiffness matrix caused by the partition of unity approximation and inconsistent energy transfer between neighboring time steps in dynamic simulations [115], [116]. The first problem becomes troubled when the mesh is defined in the enriched domain resulting in increasing matrix conditioning. Convergence with implicit solver is even slower or fails. Since the second issue cannot be solved for dynamic crack growth analysis, decreasing nodal dofs may improve convergence by decreasing the effect of linear dependence of the stiffness matrix. However, the coarse mesh is not appropriate for composite laminates because of small ply thicknesses. Each ply should be modeled with at least one element to give correct orientations for cross-ply laminates. Nevertheless, in our case, each three sets of plies have the same orientation and can be modeled with coarse meshes. Therefore, 3D-slice model with a coarser mesh is studied to take forward the simulation for the XFEM-LaRC05 model. A further load drop is achieved, but it still encounters severe convergence problems. The failure behaviors and ultimate loads are the same for both fine-coarse meshes meaning that coarse mesh is better by taking into account computational times.

4.4 Conclusions

Numerical simulations of unidirectional and cross-ply curved CFRP laminates were performed in this chapter using two different damage modeling approaches: CZM and XFEM-LaRC05 using ABAQUS dynamic-implicit solver. The following conclusions are drawn;

Unidirectional Laminate

- 3D CZM and 3D XFEM models successfully simulated failure in UD laminates.
- 3D slice CZM model was successful also whereas 3D-Slice XFEM model has convergence difficulty.
- LaRC05 failure initiation criteria successfully model matrix failure close to the interface.
- XFEM based models have convergence difficulties when used with 3D-slice modeling. A 3D model with XFEM is better at capturing damage propagation ahead than 3D-slice modeling assumption.
- The 3D model is better for capturing the width variation of stresses and resulting delamination growth. However, since the most significant stresses exist in the mid-width, 3D-slice modeling gives adequate insight for unidirectional curved laminates. Cost saving is significant using slice models over 3D models.

Cross Ply Laminate

- XFEM-LaRC05 model and CZM model predicted failure load 2 times the experimental failure load using UD strengths.
- Reduced interlaminar strength values at the first two interfaces give closer results to the experimental observations in terms of both failure load and failure location for the CZM model. While for XFEM based model, only the initiation load of the matrix crack is reduced significantly without causing any load drop.

- Interlaminar properties are dependent on the interface angle, and this effect cannot be discarded for simulations of cross-ply laminates.

General

- LaRC05 failure initiation criteria successfully estimate matrix crack-driven delamination and shear cracks, but it can be used combined with a more stable damage propagation feature rather than XFEM in ABAQUS. User element implementation works better with improved stability in most of the studies.
- Dynamic crack growth simulations using XFEM suffer from stability issues arising from both linear dependences of stiffness matrices and energy mismatch between neighboring increments.
- To ease convergence difficulties of XFEM, the coarse mesh may be used to decrease ill-conditioning in the global stiffness matrix due to the partition of the unity concept. However, it will neither help energy mismatch between increments for dynamic events.
- Standard material strengths and properties can lead to inaccurate simulations by dismissing manufacturing knockdown factors. Especially for physically based failure criteria, material properties should be determined for the utilized manufacturing case.
- The use of intralaminar failure criterion is important for the determination of matrix cracks in the structure, but initiation criteria are not enough to predict the type of damage. The calculated values of the failure index do not mean that load drop or failure will be achieved. Damage evolution should be investigated to realize the type of damage.

4.5 Future Work

Future work for composite L-beam structures based on current study can be performed by below suggestions.

- UMAT/VUMAT can be written and used for the implementation of LaRC05 failure criteria combined with interface elements.
- Stable user elements can be utilized instead of ABAQUS library for the XFEM propagation.
- Cross-ply analyses can be repeated after obtaining true material strengths by eliminating manufacturing effects.
- 3D modelling of cross-ply L-beam is essential to observe stresses and failure behavior through the width by accounting free edge effects.
- Residual stresses can be accounted for better prediction of the failure load.

CHAPTER 5

FAILURE ANALYSIS OF T-JOINT STRUCTURES

In this part of the thesis, the T-joint specimen used by Gülaşık and Çöker [1], [2] is analyzed using CZM of ABAQUS/Standard dynamic-implicit solver under different loading conditions in terms of failure mechanisms and stress fields. In addition to 2D models of T-joints under axial loading, 3D modeling under axial loading and detailed investigations of transverse and oblique loading cases by 2D modeling. The complete list of the studies is shown in Table 8. For oblique and transverse loadings, 2D plane strain CZM is utilized. 3D numerical modeling of the T-joint specimen is performed only for the axial loading case due to its high computational cost.

Table 8 Breakdown of the studies performed at Chapter 5

Loading	**Model**
0° - Axial	3D CZM
45° - Oblique	2D CZM
90° - Transverse	

5.1 Numerical Modeling

5.1.1 Geometry and Boundary Conditions

Since the study of Gülaşık & Çöker [1], [2] is taken as a reference for the scope of this chapter, geometric dimensions, and boundary conditions are taken the same for the T-joint consisting of stringer/over laminate, skin, and filler regions. The illustration of the geometry is in Figure 5-1 and dimensions are listed in Table 9.

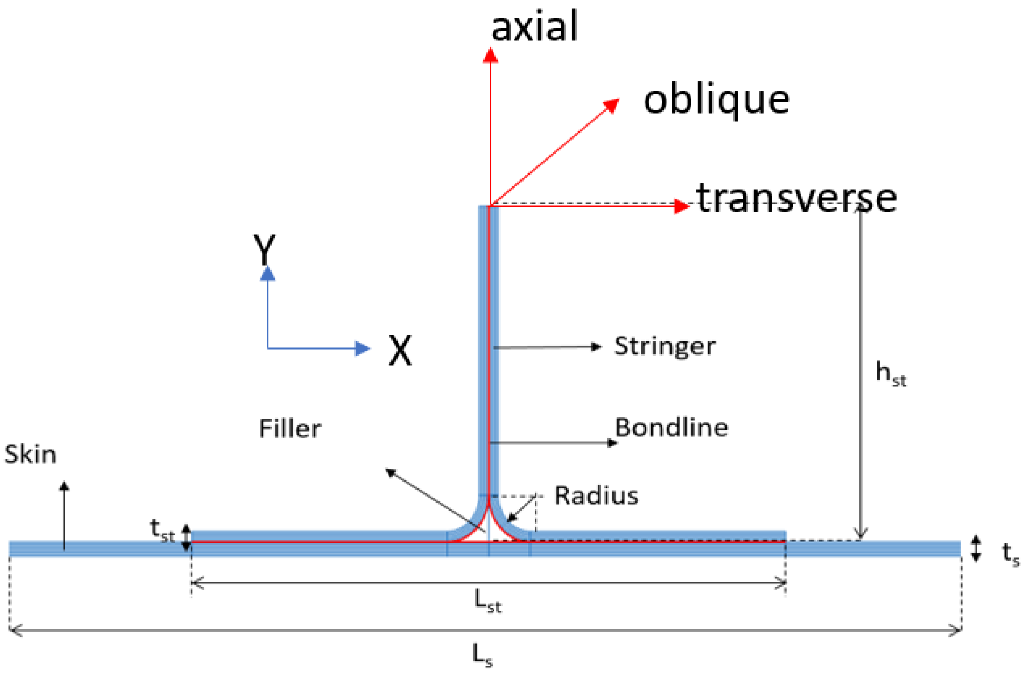

Figure 5-1 T-joint specimen definitions [1]

Table 9 Geometrical dimensions used in the analyses are from [1], [21] and [24]

t_{ply} [mm]	h_{st} [mm]	t_{st} [mm]	t_s [mm]	L_{st} [mm]	L_s [mm]	*Radius* [mm]	*Width* [mm]
0.15	28.0	0.9	1.2	56.0	156.0	3.0	25.0

The boundary conditions for 2D and 3D FEMs are shown in Figure 5-2 (a) and (b), respectively. Left and right sides of the skin are fixed. Loading is applied to upper surface FOR 3D model or edge for 2D model in a quasi-statically increasing until failure. Kinematic coupling is applied to the 3D model at the left and right surfaces of the skin and top surface of the web for simplicity in reading displacement data and reaction forces.

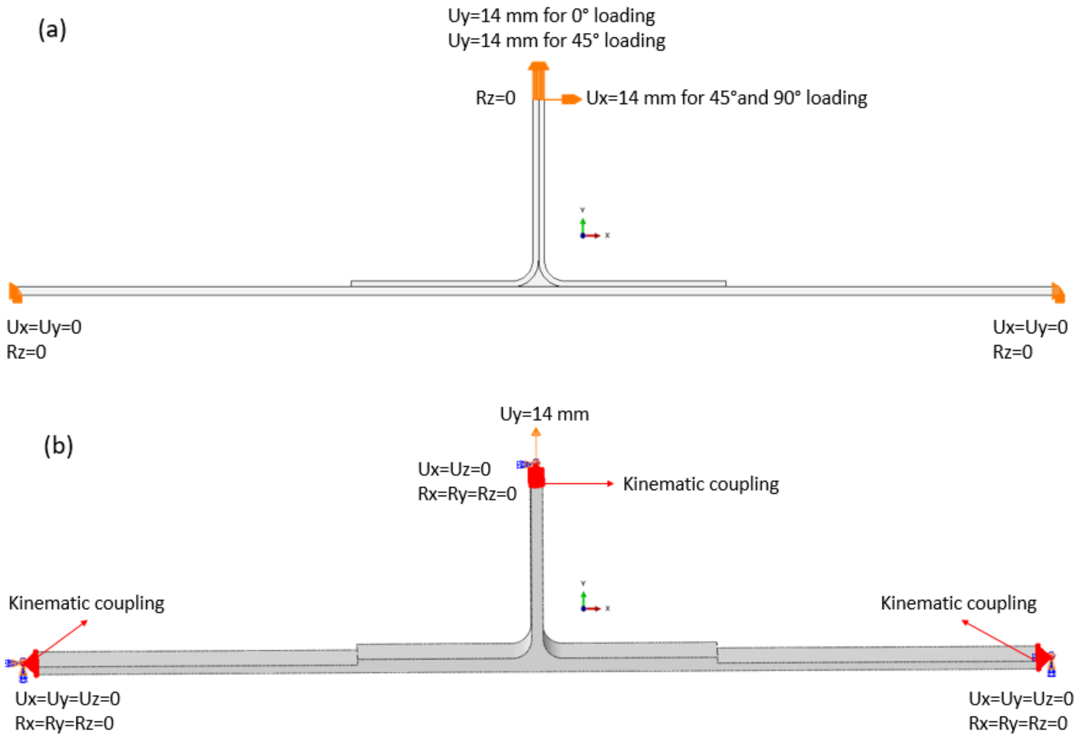

Figure 5-2 Boundary conditions applied on (a) 2D and (b) 3D finite element models for T-joint

5.1.2 Material Properties

IM7/8552 UD prepreg is used for composite laminate manufacturing, and FM300 adhesive is used for isotropic filler and bonding interfaces. Layer interfaces inside laminates are composed of interfacial properties of IM7/8552 material. Elastic material properties are taken from [1], [21] and [23], and listed in Table 10.

Table 10 Elastic properties of IM7/8552 UD and FM300 adhesive from [1], [21],[23]

	E_{11} [GPa]	**E_{22} [GPa]**	**E_{33} [GPa]**	**G_{12} [GPa]**	**G_{13} [GPa]**	**G_{23} [GPa]**	**ν_{12}**	**ν_{13}**	**ν_{23}**
IM7/8552	147	11.8	11.8	6.0	6.0	4.0	0.3	0.3	0.475
FM300 (isotropic)	2.38	-	-	0.68	-	-	-	-	-

For the interface elements between layers of composite laminate, IM78552 properties are used, while for bonding lines specified in Figure 5-1, FM300 properties are used from Table 11.

Table 11 Interface properties of IM7/8552 and FM300 are from [1], [21] and [23]

	k_I^0 [MPa/mm]	k_{II}^0 [MPa/mm]	k_{III}^0 [MPa/mm]	t_I^0 [MPa]	t_{II}^0 [MPa]	t_{III}^0 [MPa]	G_{Ic} [N/mm]	G_{IIc} [N/mm]	G_{IIIc} [N/mm]	η
IM7/8552	1e6	1e6	1e6	60	90	90	0.243	0.514	0.514	4.6
FM300	1e6	1e6	1e6	50	100	100	0.9	2.5	2.5	8

Stacking sequences are shown in Figure 5-5. The 0° ply is laid down in the out of plane direction, namely the width direction of the specimen, while 90 degree plies are along layer directions shown in Figure 5-3. 45° plies are symmetrical on the web while skin has the same 45° directions on left and right sides of the joint at the vertical wall. This induces unequal stacking in the left and right flange-skin co-bonded sections.

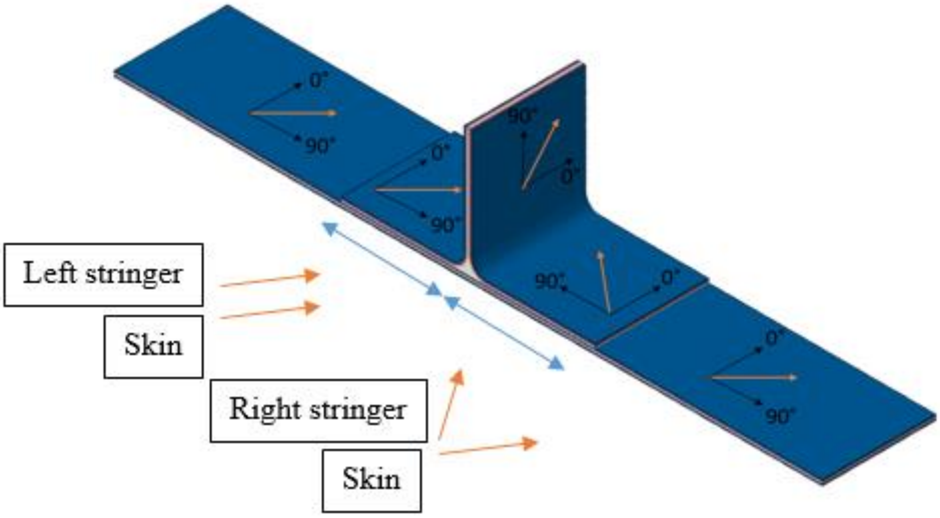

Figure 5-3 Stacking orientations on skin, stringer flange and stringer web

5.1.3 Finite Element Modeling

Material properties are defined as engineering constants in predefined material orientations shown in Figure 5-4 in both 2D and 3D models. In this case, elastic property transformation is performed since material coordinates of the finite element model are different than problem orientations shown in Figure 5-3. Stress contours in upcoming sections are plotted according to the local material directions unless otherwise stated. While material orientations for left hand side of the filler from web midline are assigned in line with the left stringer radius, other side of the filler, material orientations are in-line with the right stringer radius. As a result, stress fields in the filler region are discontinuous due to different orientations on sides.

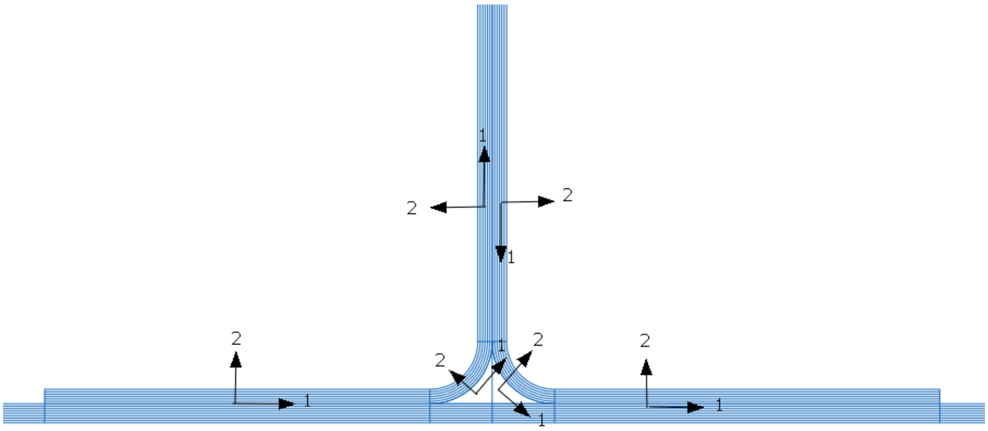

Figure 5-4 Material directions for each component for 2D and 3D models

Approximate mesh size is selected as the same with the Gülaşık’s work as 0.2 mm. Since mesh convergence study almost do not change the load-displacement curve and stress field in the structure in [1], 2 element per ply thickness is maintained for 2D model. However, [29] proposes at least 3-4 elements in ply thickness to capture stress contours within plies accurately in plain strain problems. Due to computational limitations, one element per ply thickness is used in ply thickness for the 3D model.

5.1.3.1 2D Plane Strain CZM

Element selection is important to conduct reliable finite element models and analyses. Elements should be carefully selected according to the nature of the problem and modeling choices. Due to interlaminar evaluation of T-joint and high out of plane stresses generated around radius, plane strain modelling is preferred for the scope of 45° and 90° load cases. Plane strain modelling allows fully integrated, reduced integration and incompatible mode elements. Fully integrated elements are not recommended in order to avoid shear locking in the case of bending dominated problems [78]. Reduced integration elements suffer from hourglass effect and need extra attention [58]. Although element shape highly affects the performance of incompatible mode type under shear locking, they are the most suitable type of element for our modelling. Therefore CPE4I elements for quads and CPE3 for triangular elements are used for 2D plane strain modeling. Due to their stiff response, triangular elements are used as least as possible in the filler region. Zero thickness cohesive elements are placed in the bond-line and all the ply interfaces as shown in Figure 5-5 (a) for the 2D plane strain model of T-joint. The stacking orientations are defined from the tool surface. The tool surfaces are the inner radius of the stringers and the lower surface of the skin. Stacking orientation directions are shown with arrow directions in Figure 5-5 (b) and are well defined in FEM using the sweep meshing technique with adjusted sweep paths.

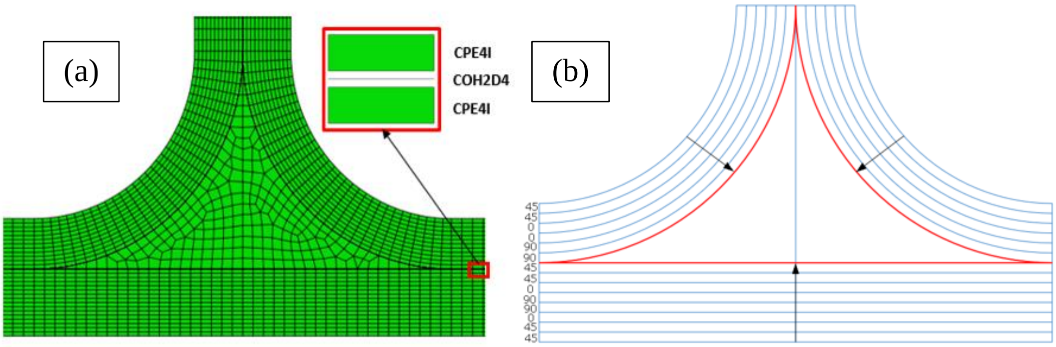

Figure 5-5 T-joint filler area showing (a) the 2D meshing with zero thickness cohesive elements, (b) stacking orientations

Figure 5-6 shows the 2D FEM mesh and the stacking details. There are 19272 linear quadrilateral elements of type CPE4I, 10 linear triangular elements of type CPE3 and 8669 linear quadrilateral elements of type COH2D4 in 2D model. To ease convergence, viscosity parameter is used as 10^{-5} for the cohesive elements.

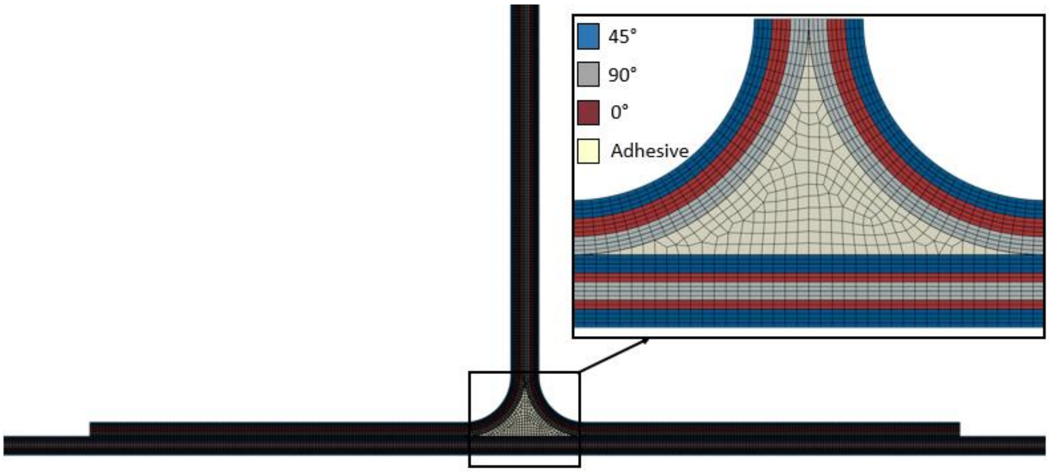

Figure 5-6 2D FEM mesh and the stacking details

5.1.3.2 3D CZM

The mesh details for the 3D model is shown in Figure 5-7. There are 1214750 elements of type C3D8I, 1250 elements of type C3D6 and 58125 elements of type COH3D8 in the model. One element is used in the thickness direction of a ply. For the sake of computation time cohesive elements are placed only on the bond-line in the 3D model since the main mode of failure is debonding under 0° loading. To ease the convergence, viscosity parameter is used as 10^{-5} for the cohesive elements.

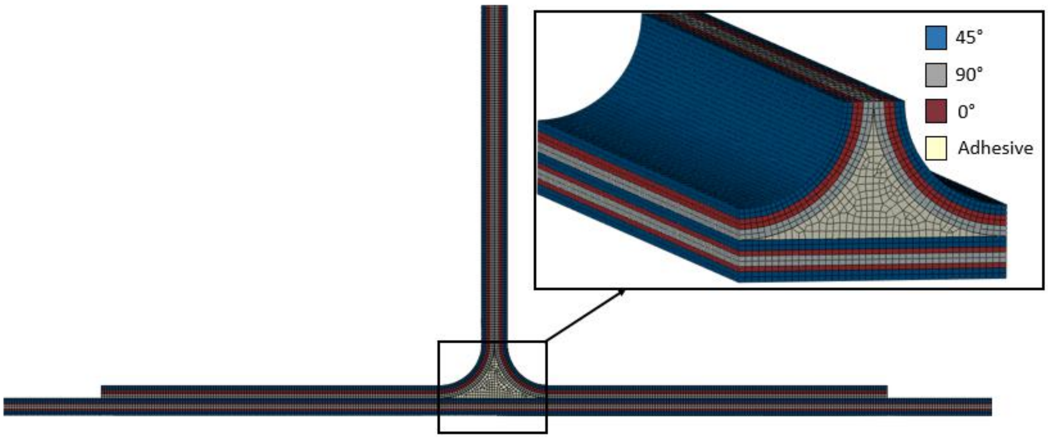

Figure 5-7 3D FEM mesh and stacking details

5.2 Numerical Studies on T-Joint Failure Investigation

5.2.1 Comparative Study on Cohesive Behavior Modeling under 0° Loading

This study aims to give an idea about the interface modeling technique selection and performance of different solver types on T-joint structure debonding analysis. The study of Gülaşık & Çöker [1] is taken as a reference T-joint configuration, and results were compared with it. The main failure modes of this type of structure are delamination and debonding caused by mixed mode bending, as seen from the literature [1], [30]. Different cohesive zone modeling techniques (cohesive element and cohesive surface) and different solvers (static and dynamic implicit- quasi static) are used to analyze delamination and debonding with 2D plane strain modeling in ABAQUS/Standard 2020. There are four numerical solutions constructed as combinations of two types of cohesive modeling and two types of the solver.

5.2.1.1 Interface Modeling

First, the non-cohesive model is created according to the given dimensions and materials. The load-displacement curve is compared with the reference study [1] in §5.2.1.3. After validating model stiffness and response for this model, cohesive interfaces were added to investigate delamination and de-bonding behaviors. Unlike the reference, there are no cohesive interfaces inside the stringer, and skin layups. Because major load-carrying capacity is lost after complete filler de-bonding occurs and skin delamination has almost no effect on failure propagation [1]. The effect of large displacements complicates the stability of the solution and increases the run time in an immeasurable manner at that stage. By considering the pros and cons, modeling interface layers between layups are not preferred in this comparative part of the study.

ABAQUS offers two options to model the interface; one is cohesive surface interaction, and the other is cohesive elements [22]. Detailed explanation is available in Section §3.2.1.3.

Cohesive Surface

Surface-to-surface contact with cohesive property is used in the bonding interfaces shown in red lines in Figure 5-5.

Cohesive Element

The bond-line shown in Figure 5-5 is created as a separate part with 0.1 mm thickness and meshed with an element length of 0.2 mm compatible with the surrounding structures. Tie constraint combines the bonding part to the adjacent surfaces with zero thickness. Cohesive property is given by cohesive section assignment using default thickness value 1.0 to eliminate the geometric thickness effect since there is no available feature for surface-based interfaces to define thickness as mentioned in Section §3.2.1.3.

5.2.1.2 Solution Procedure and Parameters

Cohesive element-based and cohesive surface-based modeling are used in separate models to figure out their response and capability. Moreover, two types of solvers: static general and dynamic-implicit with quasi-static loading are used for all cohesive models to see their effects on convergence and accuracy. The numerical simulation matrix is shown in Table 12. The viscosity parameter of $1e^{-5}$ is used in both models to stabilize the solution by giving energy dissipation. For all the numerical models and solutions in this thesis, ABAQUS/Standard version 2020 is utilized.

Table 12 Numerical simulation matrix

Solver	**Interface Modeling**
Dynamic-Implicit	Cohesive Surface
	Cohesive Element
Static-Implicit	No interface
	Cohesive Surface
	Cohesive Element

5.2.1.3 Results and Discussion

Loads corresponding to 12 mm displacement for non-cohesive models seen in Figure 5-8 are within 0.8 % accuracy; the finite element model is created per the reference. Compatibility of the load-displacement curves of cohesive models with the non-cohesive model before failure initiation demonstrates model stiffness is correct, meaning that cohesive layers are adapted to the model successfully. Moreover, cohesive surface and cohesive element-based models show similar behavior, and they also correlate with each other.

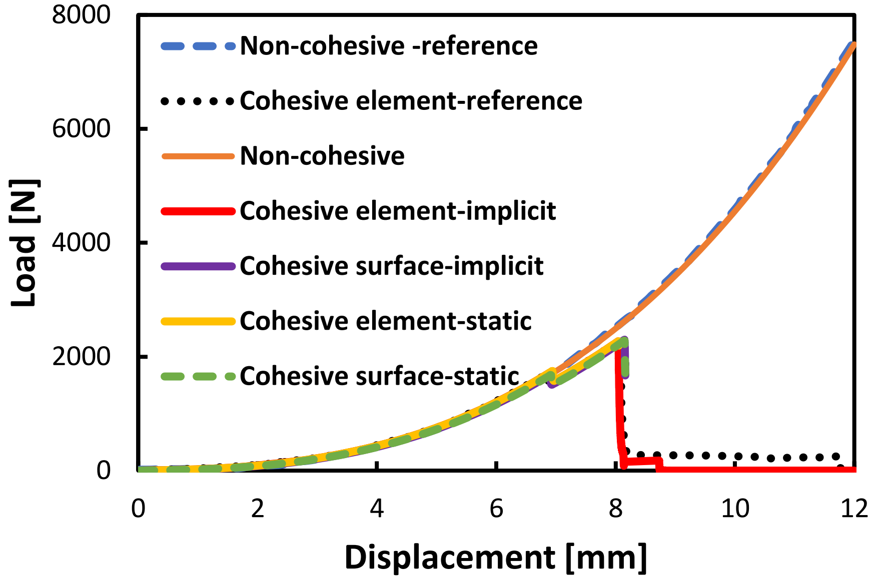

Figure 5-8 Load-displacement curve comparison of the models

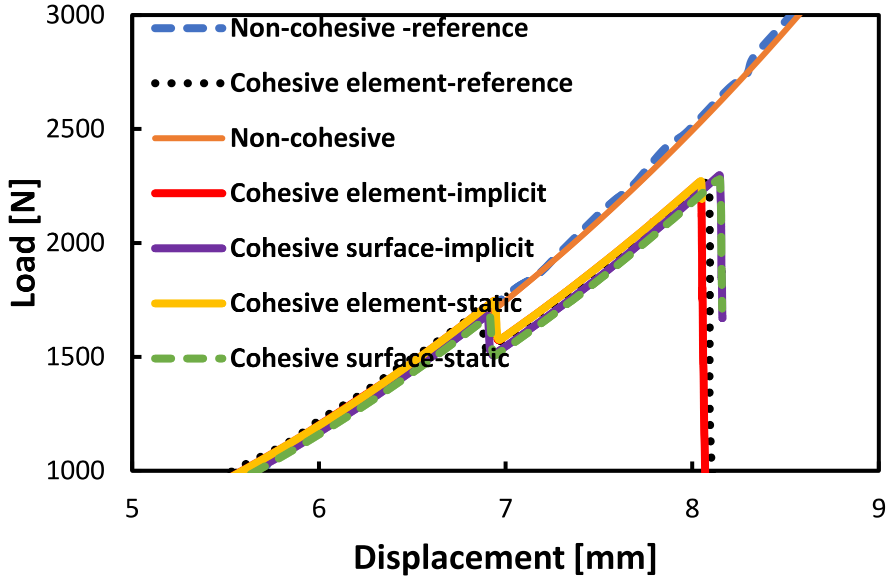

Figure 5-9 Load-displacement curve comparison zoomed in version

For a general understanding of the failure behavior, debonding sequence is given in the below figure. The failure initiates close to the upper-end point of the filler under the mixed mode of opening and shear stresses. It propagates through the web and stabilizes in second capture. Afterward, a new debond appears almost at the symmetric location to the first damage, and filler debonds completely from the stringers at fourth capture. Debonding of stringer legs from the skin results in complete loss of the loading capacity, as shown in sixth image in Figure 5-10.

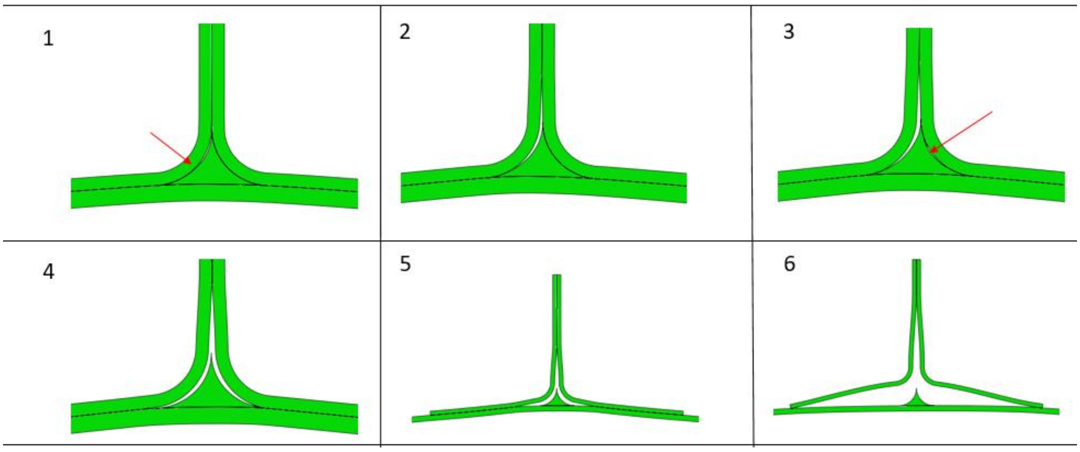

Figure 5-10 Failure sequence under 0° loading

Table 13 Failure investigation for different cohesive interface-solver combinations

Solver	**Interface**	**Load @ First Drop [N]**	**δ @ First Drop [mm]**	**Load @ Second Drop [N]**	**δ @ Second Drop [mm]**	**Max Load [N]**	**Max δ [mm]**	**Failure Investigation**
Dynamic-Implicit Quasi-Static	Cohesive Element **Reference**	1675	6.91	2256	8.08	2256	15	Debond initiates at filler-right stringer interface and propagates through stringer web. Second debond initiates at filler-left stringer interface and propagates through stringer web. After complete filler debonding occurs, stringer legs are separated completely from the skin gradually.
	Cohesive Surface	1681	6.90	2291	8.13	2291	8.16	Debond initiates at filler-right stringer interface and propagates through stringer web. Second debond initiates at filler-left stringer interface and propagates through stringer web. After complete filler debonding occurs, stringer legs are debonded from the skin gradually up to last converged increment.

Table 13 (continued)

Solver	**Interface**	**Load @ First Drop [N]**	**δ @ First Drop [mm]**	**Load @ Second Drop [N]**	**δ @ Second Drop [mm]**	**Max Load [N]**	**Max δ [mm]**	**Failure Investigation**
	Cohesive Element	1746	6.94	2269	8.04	2269	12	Debond initiates at filler-left stringer interface and propagates through stringer web. Second debond initiates at filler-right stringer interface and propagates through stringer web. After complete filler debonding occurs, stringer legs are separated completely from the skin gradually.
Static-Implicit	Non-cohesive **Reference**	-	-	-	-	7544	12	No failure
	Non-cohesive	-	-	-	-	7483	12	No failure
	Cohesive Surface	1678	6.91	2279	8.14	2279	8.16	Debond initiates at filler-right stringer interface and propagates through stringer web. Second debond initiates at filler-left stringer interface and propagates through stringer web. After complete filler debonding occurs, stringer legs are debonded from the skin gradually up to last converged increment.
	Cohesive Element	1746	6.94	2271	8.04	2271	8.05	Debond initiates at filler-left stringer interface and propagates through stringer web. Second debond initiates at filler-right stringer interface and propagates but complete filler debonding does not occur due to convergence difficulties.

The detailed explanations of failure and critical points on the load-displacement curve corresponding to load drop initiation were tabulated in Table 13.The initiation occurs at the left interface of the filler for cohesive element-based models while at the right interface for cohesive surface-based models, as stated in Table 13. This is unimportant because the joint and stresses are symmetrically the same for both interfaces, and only slight differences induce this variation. Static-implicit and dynamic-implicit solution results are examined the below sections separately in detail.

Static-Implicit

As shown in Figure 5-11, both models have non-converged solutions considering applied 12mm displacement, while cohesive contact is better than a cohesive element-based interface. Cohesive element-based solutions suffer from minimum increment size, although it is tiny (1e-15). Hence, the cohesive element-based interface is not favorable with static general solution procedure after failure initiation occurs. If the failure propagation is not significant for the user, it gives a very performant even the same result compared to the implicit solution for the initiation load and displacement without excessive run times. However, a cohesive surface-based interface works better than a cohesive element does. Failure propagation at a point where high nonlinearity and large displacements, namely dynamic behavior, occur due to integrity loss is achieved successfully even with a static solver. Compared to the reference cohesive solution, the surface-based interface estimates almost the same initiation load, whilst the cohesive element-based model is just 4 % away. The cohesive element predicts failure initiation 0.03mm beyond the cohesive surface, which is exactly the same for the reference cohesive model as 6.91mm.

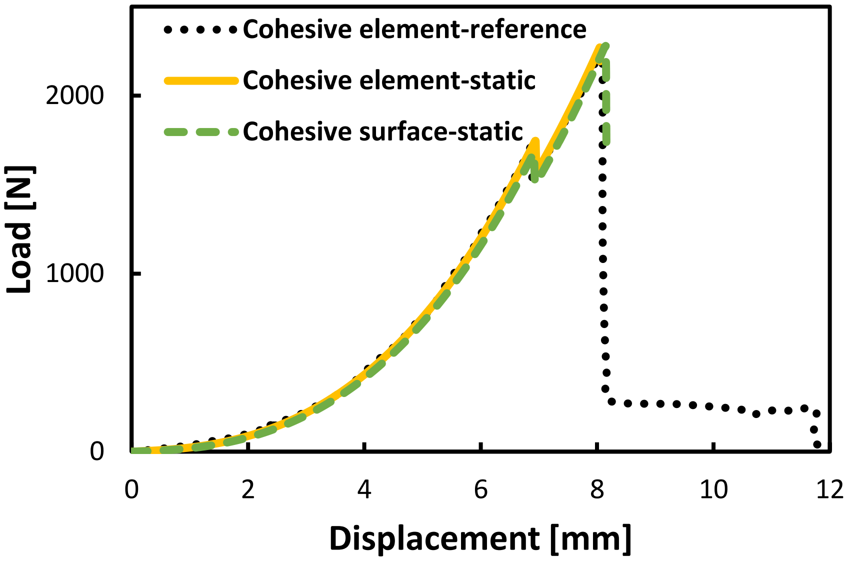

Figure 5-11 Cohesive and non-cohesive model load-displacement curve comparison (Static-Implicit)

Dynamic Implicit (Quasi-Static)

The cohesive contact model has a non-convergent solution as in the static solver. However, cohesive element model completes the analysis up to 12mm by the dynamic implicit solver. Cohesive surface-based solutions suffer from maximum increment size, although it is tiny (10^{-12}). Hence, the cohesive surface-based interface is not favorable even with the dynamic implicit solution procedure after filler integrity is lost. If the failure propagation is not significant for the user, then it gives a very performant even the same result for the initiation load and displacement without excessive run times seen in Figure 5-12.

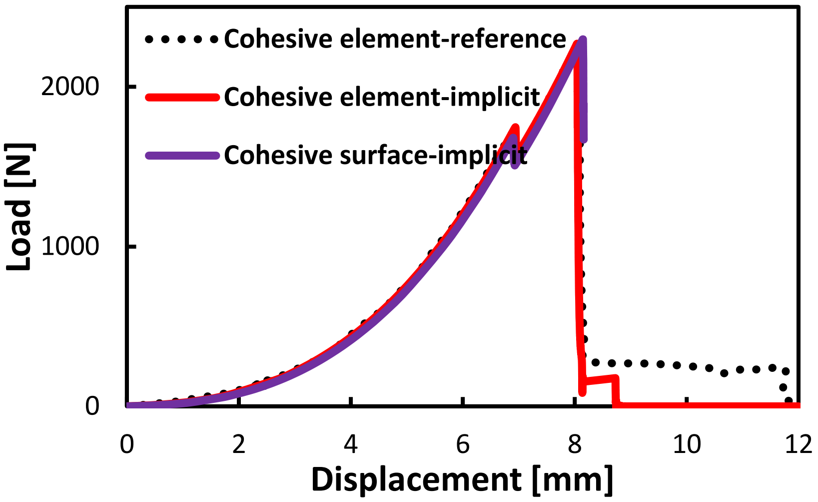

Figure 5-12 Cohesive and non-cohesive model load-displacement curve comparison (Dynamic Implicit-Quasi Static)

Failure propagation at a point where high nonlinearity and large displacements occur due to integrity loss is achieved successfully only with the cohesive element-based model using a dynamic implicit solver. Compared to the reference cohesive solution, estimates the initiation load within 4 % accuracy with reference cohesive model.

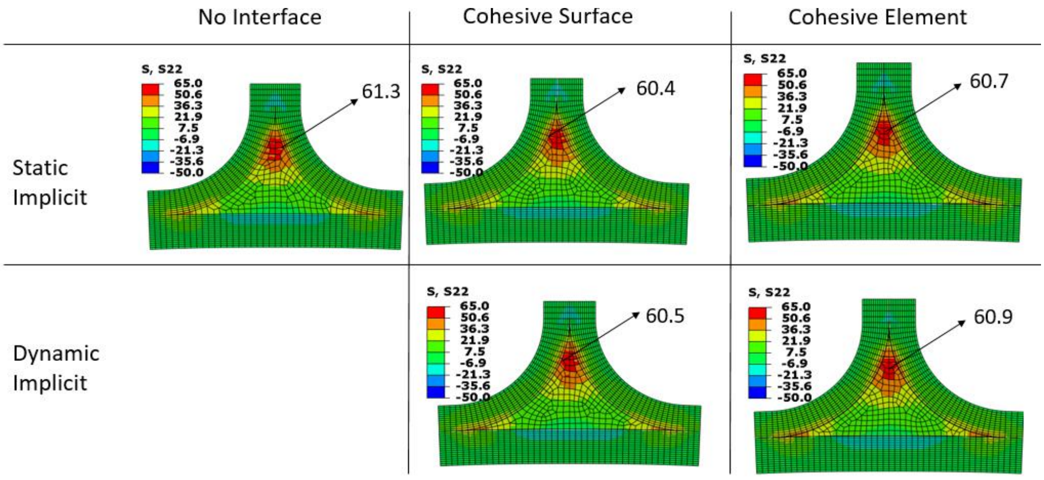

Figure 5-13 S22 stress for various interface models with static and dynamic solvers at 6.6 mm

Stress contour gives more about the understanding of failure than the load-displacement curve does. Most critical stress components, S22 out-of-plane and S12 interlaminar shear for t-joint structure, are compared at the prescribed displacement of 6.6 mm before failure initiation.

Maximum stress values and locations agree with the reference study and each other for all the models (S22_max=60 MPa in filler top corner, S12_max=70 MPa in 57° from the horizontal axis for left and right filler-stringer interfaces [1]). Compared to no interface case, stress values are within the range of 1.5 %; hence the differences are negligible. For the cohesive surface and cohesive element model, the maximum S12 stress component occurs in the stringer radius, making an angle of 55° and 52°, respectively, with the skin-bottom filler interface. It is nearly the exact location where maximum S12 takes place in the study of Gülaşık & Çöker [1]. The reason for a small difference in location is the meshing.

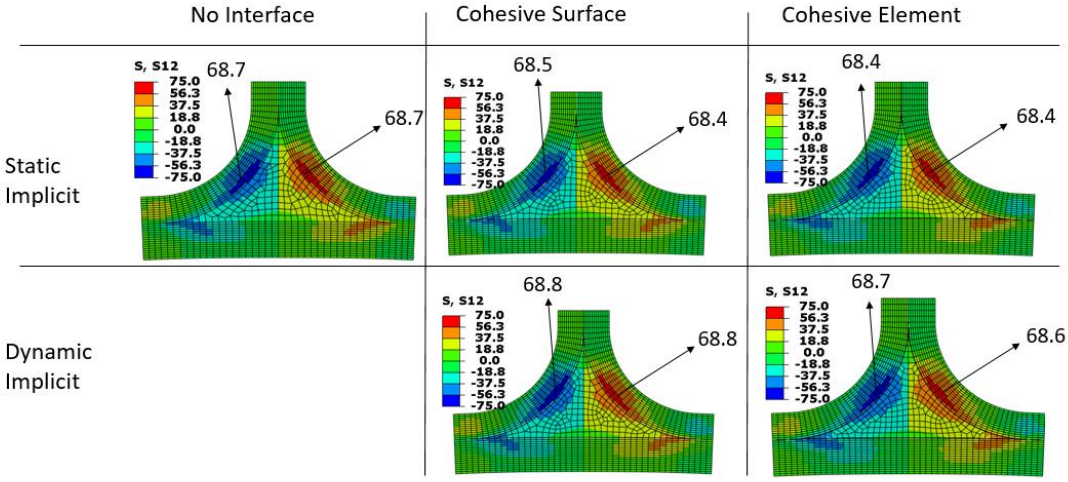

Figure 5-14 S12 stress components for various interface models with static and dynamic solvers at 6.6 mm

5.2.1.4 Conclusion

The only difference between the static and implicit cohesive element-based models is the convergence, as shown in Figure 5-15. In other words, the solutions follow the same load-displacement curve up to the loss of filler integrity, but the static solver cannot handle the large deformations beyond that second load drop in the structure. If the main concern is failure initiation in the composite structures for the user, as in most of the industrial structural analysis teams, then the static solver will useful to determine the failure behavior and the load-carrying capacity of the joint.

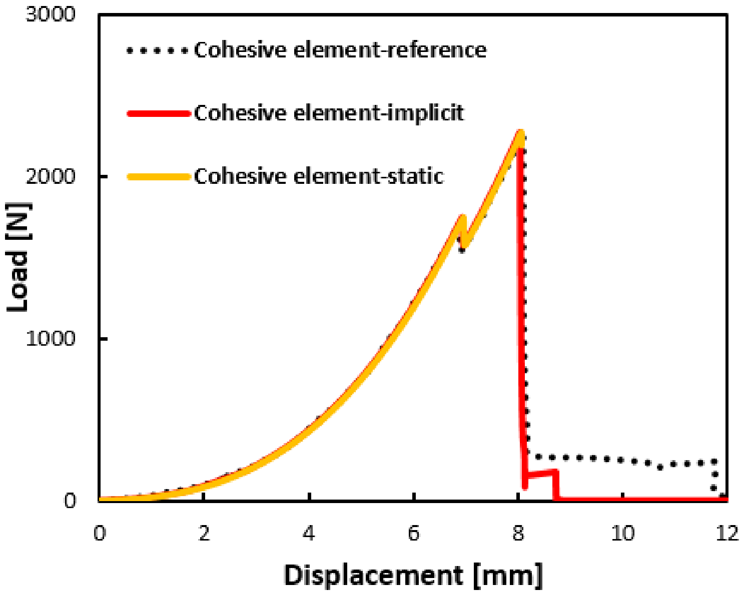

Figure 5-15 Load-displacement graph for cohesive element-based models with different solvers

For the cohesive surface-based model, both solver types failed to achieve convergence up to 12 mm displacement Figure 5-16. However, they both predicted the load drops very close to each other. The solution steps for cohesive surface-based models are nearly two times that of the cohesive element-based models for both static and implicit solvers. The selection of the interface modeling is a trade-off because a cohesive surface-based interface saves time in the construction of the FEM but needs more time than the others in the solution phase.

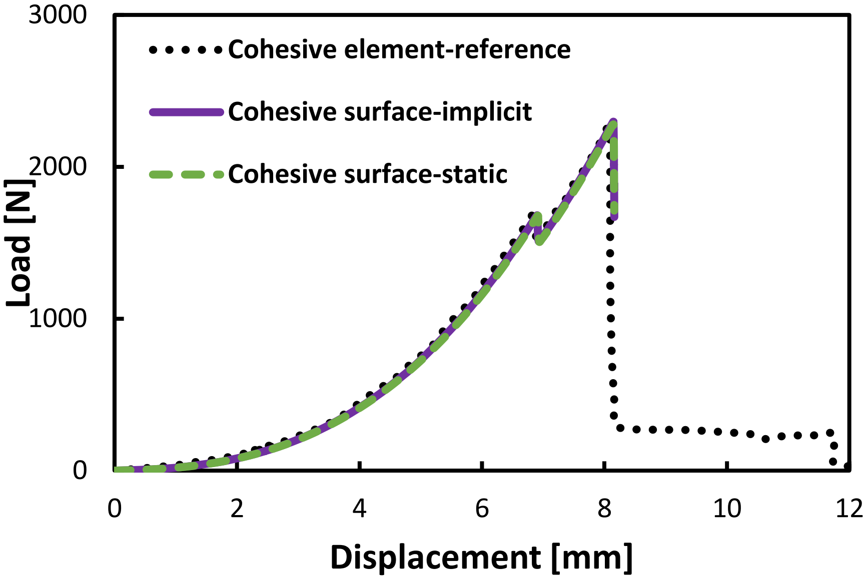

Figure 5-16 Load-displacement graph for cohesive surface-based models with different solvers

Finally, in this chapter, the effects of interface modeling and solver selection in ABAQUS were investigated on the debonding failure analysis of T-joint structures. The findings are as follows;

- While the surface-based interface saves time during modeling, it spends more time in the solution phase than the other.
- Although the static solvent cannot handle large deformations in the structure beyond the second load drop, it has been observed that the ultimate load can be obtained for similar structures in industrial applications.
- If it is desired to see the behavior under large deformations, the element-based implicit solution is the most suitable option in terms of convergence.

5.2.2 Failure Investigation of T- Joint under Different Loadings

Figure 5-17 is a load-displacement graph consists of the study performed by Gülaşık et al. [1] and newly generated numerical results under different loadings for 2D and 3D models. Black dotted line is used for the analysis of Gülaşık while blue and red lines represent current 2D CZM and 3D CZM analyses under 0° axial loading respectively. Also in the figure, 45° loading response is shown by purple color while green color is used for 90° transverse loading. The response of newly generated 2D numerical model was first analyzed under 0°-axial loading for verification with the originally constructed simulation by Gülaşık et al. [1], and a good correlation is achieved, as seen in the graph. The final failure of complete debonding of the stringer from the skin occurred just 1mm before Gülaşık's work because of the unsymmetrical debonding of the left and right stringer legs from the skin. The deformation is large at that stage and can lead to unsymmetrical propagation due to larger increments used in the simulation.

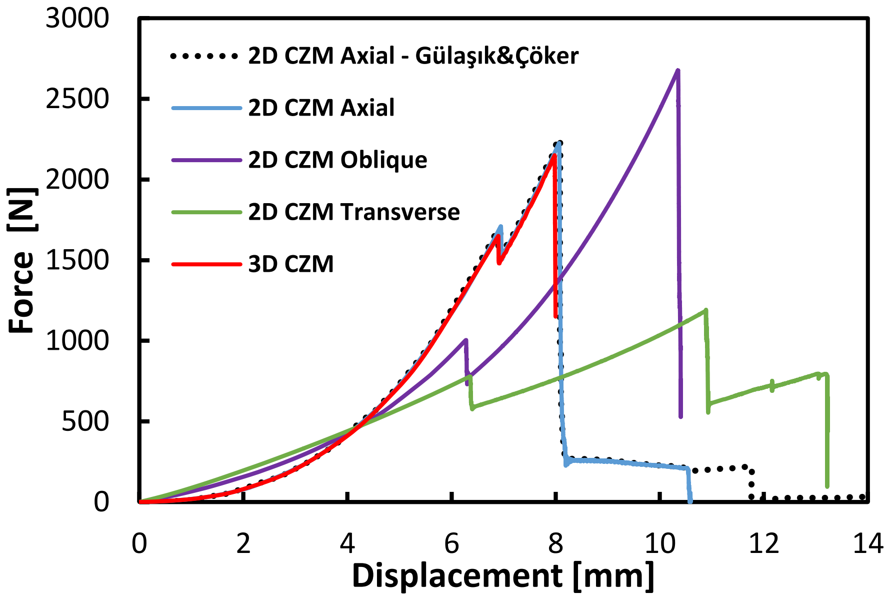

Figure 5-17 Load-Displacement graph under 0°, 45° and 90° loadings

Table 14 Computational cost comparison of 2D and 3D models under axial loading

	Time Passed	Processor
2D	20 hours	10
3D	10 days	28

Also, seen in the figure, 3D CZM model under axial loading agrees well with the Gülaşık and current 2D CZM model till the end of first load drop. There is a slight difference between the stiffness values of 2D and 3D models. This is because of additional plane strain constraints of the 2D model. Computational cost of 3D model is excessive as seen from Table 14, therefore, further loadings are simulated using 2D modelling.

After the finite element model is verified above, the load-displacement curve, stress distributions, and delamination/debond behaviors under axial, oblique and transverse loadings were investigated in detail in the next sections.

5.2.2.1 0°-Axial Loading

Axial loading is best representative of out-of-plane joints. This is because box structures such as wing, aileron or turbine blades are subjected to bending which is simulated by axial loading at top of the web. Understanding the joint response under such a loading scenario is essential for the designers to avoid unexpected scenarios.

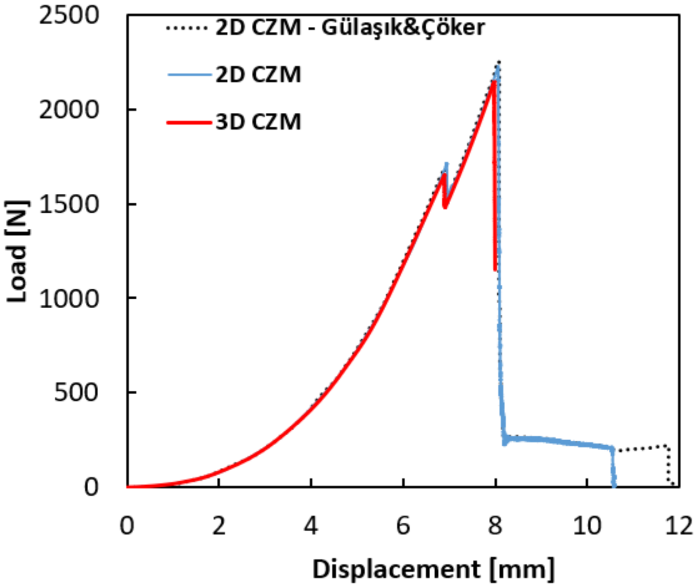

Figure 5-18 Load-displacement graph for 0° loading in detailed

Figure 5-18 shows load-displacement graph of T-joint structure under axial loading. The results of Gülaşık and Çöker is shown with black dotted line. Load-displacement responses of the current study with 2D and 3D models are plotted with blue and red color, respectively.

Compared to the transverse and oblique loading cases, the structure's maximum load carrying capacity is intermediate under axial loading, as seen in Figure 5-17. Three load drops happened during axial loading, as seen in Figure 5-18. The first load drop represents debonding of the filler/left stringer interface for 2D model while filler/right stringer interface for 3D model. The second load drop initiates due to the debonding of the other interface of the filler with stringer. The last drop is the structure's collapse by completely separation of stringer legs from the skin.

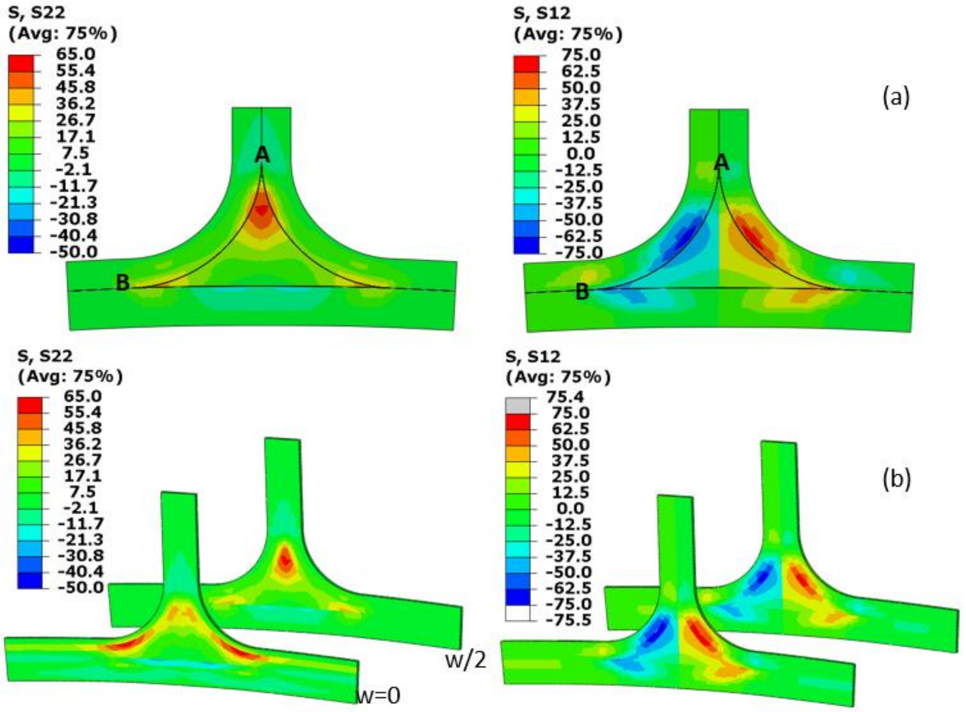

Figure 5-19 S22 and S12 stress contours at 6.6 mm for (a) 2D model and (b) 3D model at the edge and mid sections

Figure 5-19 illustrates the S22 and S12 stress fields for (a) 2D model and (b) 3D model as in the directions shown in Figure 5-4 . 3D model shows stresses at the edge and mid-section through the width. The stress fields were captured at 6.6 mm displacement before failure initiation nearly at the load of 1500N. Stress fields revealed that 2D model represents the mid portion of 3D model through the width direction. The S22 stress state at the edge is totally different than the mid-section. While filler edges are under high S22 stress in the mid-width, field is concentrated on 0° plies lying on the width direction close to the lower end of stringer bend at the edge. This is because of the free-edge effect since the row of elements adjacent to the edge shows similar stress distribution to mid-section concentrated on the filler edges. Shear stress distribution can be said to be uniform despite stresses at the edge are slightly higher than the mid-section. The stress levels of 2D and 3D models are close to each other implying that the 3D model was constructed appropriately.

To understand the stress components on the left filler interface, the out-of-plane and shear stresses on the left filler interface are taken from path A-B which is shown in Figure 5-19 (a) before the initiation of crack. Figure 5-20 is generated using this path. The stresses along path A-B reveal that at point A, the tip of the filler, both stress components are zero but, S12 and S22 magnitude increases along the radius. At the crack initiation location specified with the vertical red dashed line, both stress components have almost the same magnitude (~40-45 MPa), confirming the mixed mode crack initiation as stated by Gülaşık et al. [1].

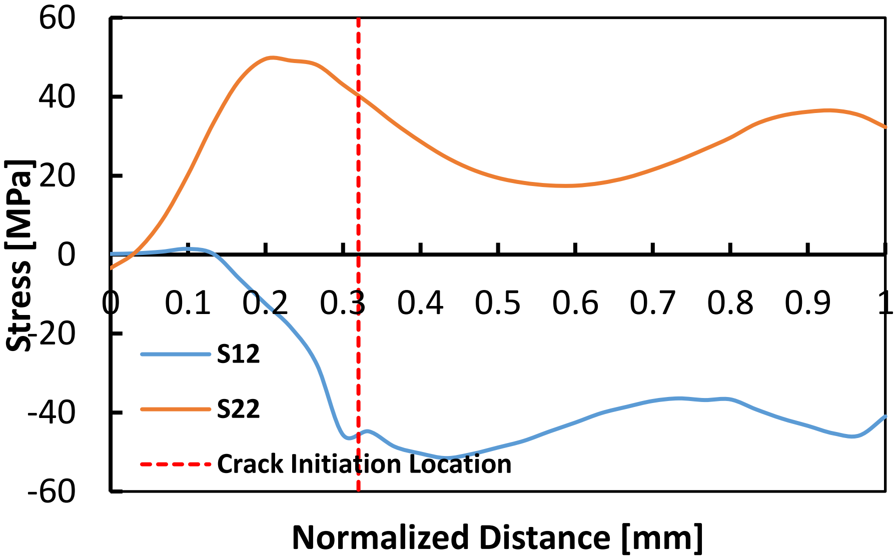

Figure 5-20 Stress distributions along path A-B at 1500 N under axial loading for 2D model

2D CZM

Firstly, delamination/debond behavior under 2D model is shown in Figure 5-21 for the understanding of the study of Gülaşık. The left portion represents damage and right portion shows the corresponding point on load-displacement curve.

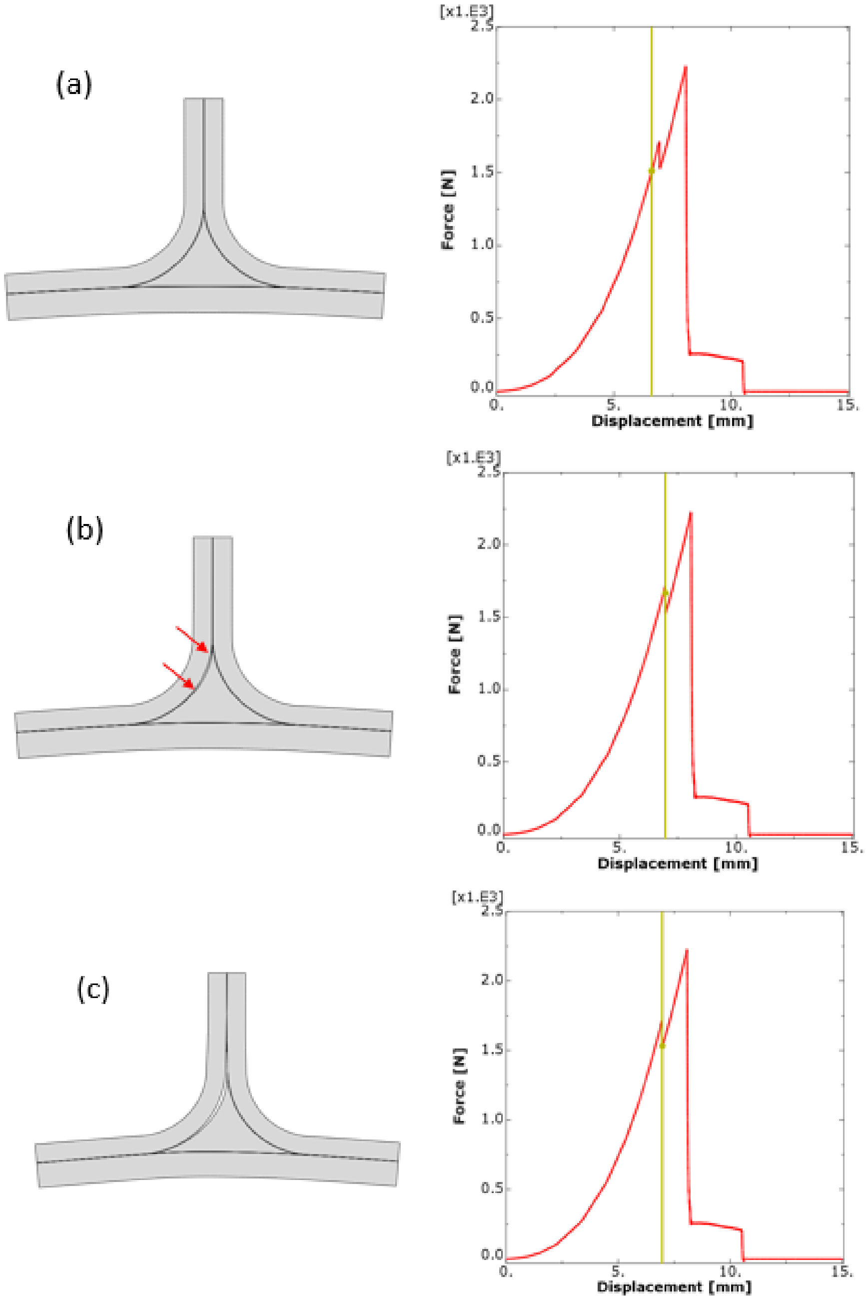

Figure 5-21 Failure sequence and corresponding load-displacement graphs through (a)-(h) for 2D model

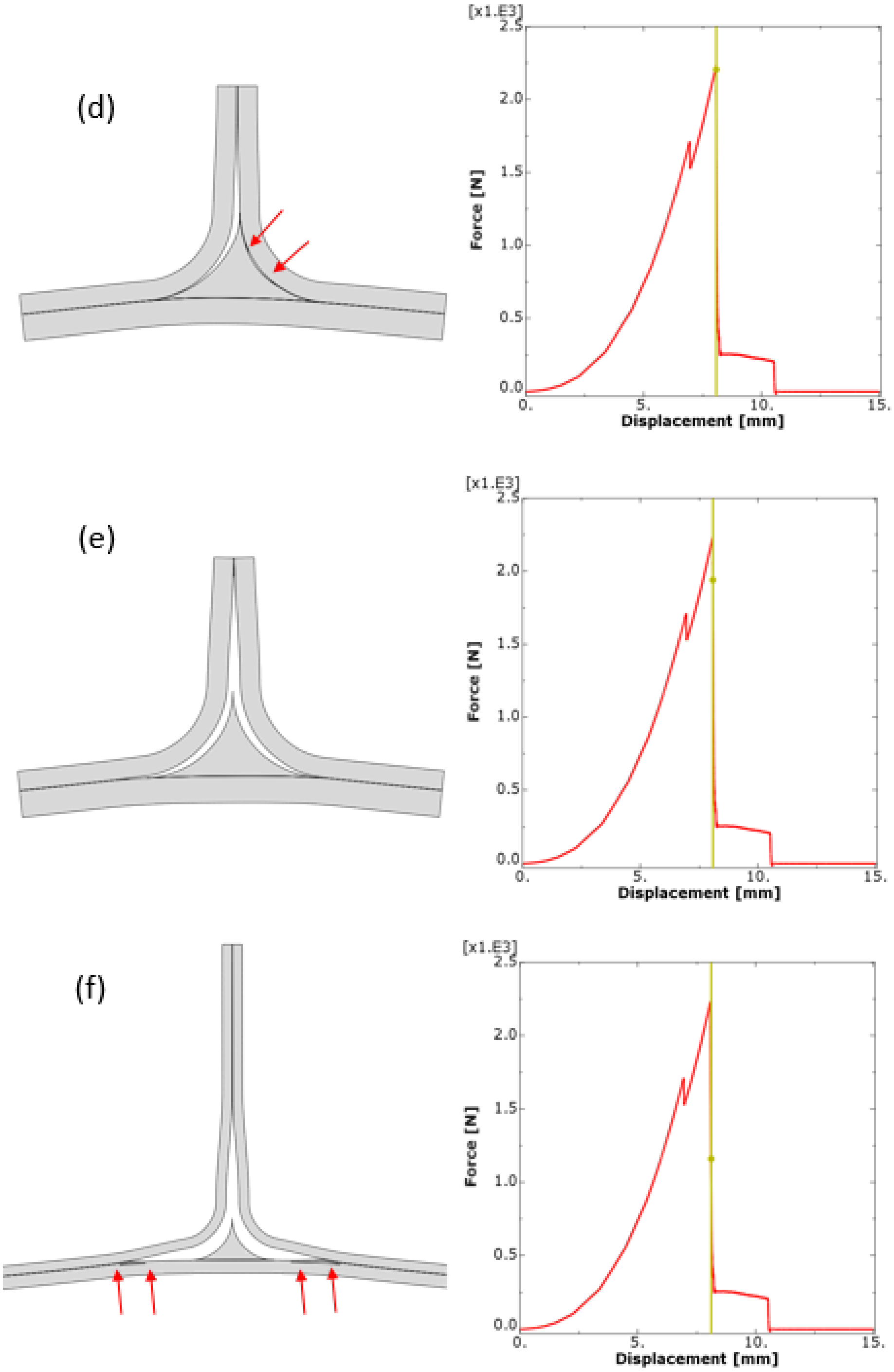

Figure 5 21 (continued)

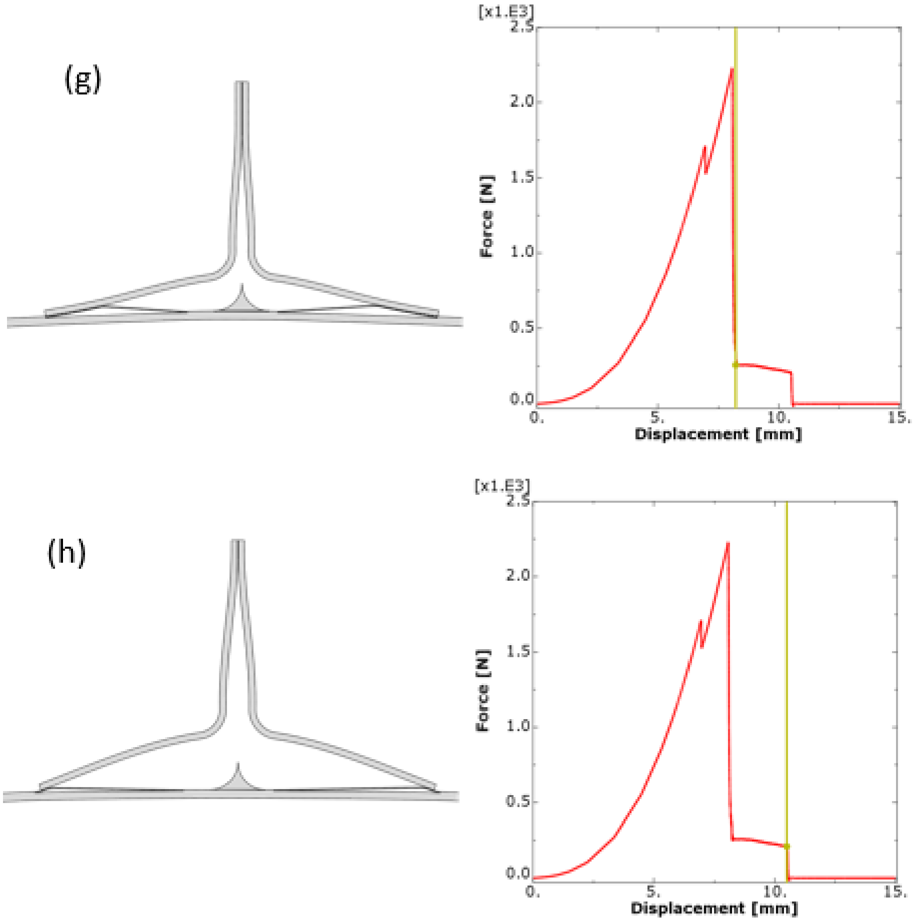

Figure 5 21 (continued)

Figure 5-21-(a) represents the state before failure initiation at 6.6 mm. Failure begins at the 1709 N at 6.94 mm tensile loading as shown in Figure 5-21-(b) with the red arrows at the tip of crack. Upper tip of crack propagates through web up to Figure 5-21-(c). Then crack is stabilized and load-carrying capacity started to increase. After initiation of the second crack at the filler-right interface in Figure 5-21-(d), load-carrying capacity started decreasing. Complete debonding of the filler from stringer is achieved in Figure 5-21-(e) and stringer legs started to separate from skin. Two new cracks appeared during this separation in Figure 5-21-(f). Debonding of stringer from skin and delamination between skin plies continued to (g) at an instant. At this point cracks stabilized and only slight decreasing is seen up to Figure 5-21-(h). Finally, stringer legs debonded from skin with total loss of load-bearing.

3D CZM

The load-displacement response of T-joint structure under axial loading for 3D CZM is shown in Figure 5-22 with red color. The dashed black curve is from the implicit analysis of the 2D model by Gülaşık and Çöker [1][103]. Points a-j represent critical points in terms of damage in the deltoid region before initiation of debonding to the end of simulation.

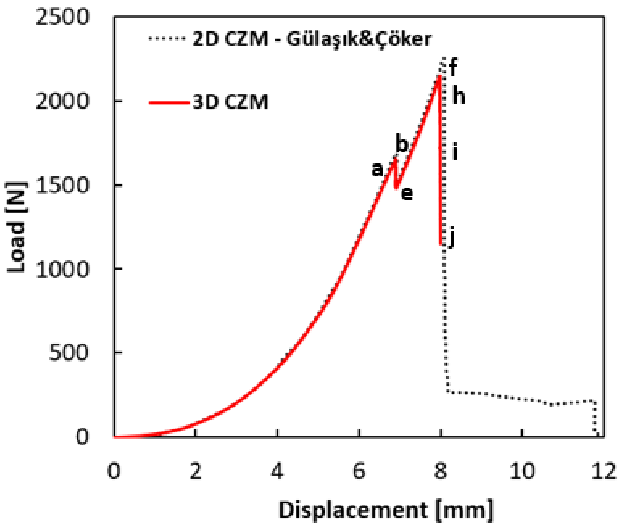

Figure 5-22 Load-displacement graph for 3D CZM under axial loading

It is observed that failure load of 3D model is 3.3% lower than the 2D model. The reason is attributed to the fact that debonding of the second interface initiates in two zones as shown in Figure 5-23-f and reaches the middle later in 3D model while 2D plane strain model represents only the mid-section and assumes same behavior through the width.

Figure 5-23 shows the damage sequence at corresponding b-j in the load-displacement plot Figure 5-22. Damage initiates at the filler/right stringer interface at the mid-width section in point b of Figure 5-23 as an ellipsoid. Propagation takes place through the width to point d and then crack at the edge grows tangentially through the web in Figure 5-23-e. After a significant increase in the load carrying capacity, debonding takes place in the filler/left stringer interface symmetrically in regard to mid-plane of the width as shown in Figure 5-23-f. These debonding zones connected and reached the edges in Figure 5-23-h. After complete debonding of the filler from stringers at point i, failure of skin/stringer interface and web continues. Final failure was not captured due to excessive run times of the 3D model.

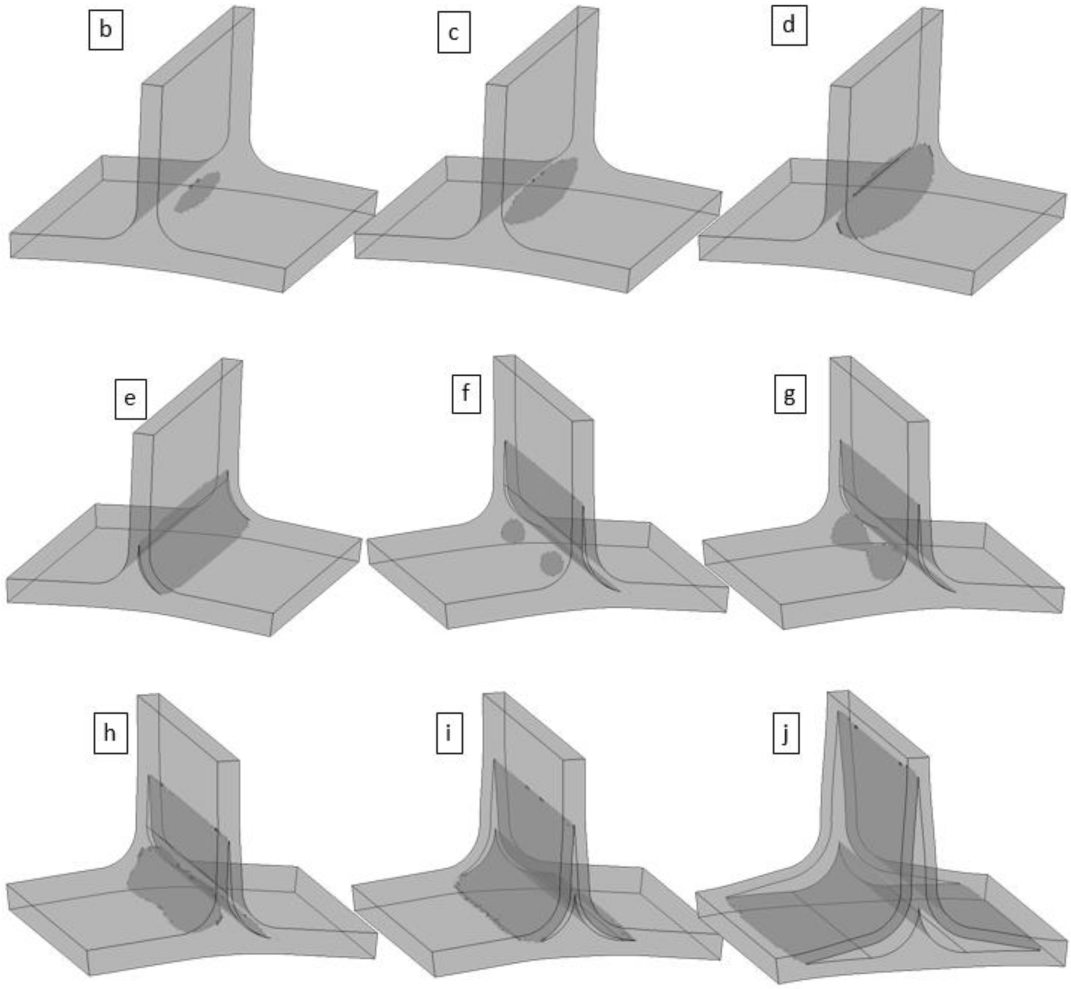

Figure 5-23 Damage sequence through the points b-j

Stress fields and delamination/debond behavior at the edge and mid-section through the width are investigated at the points b-f in detail. Figure 5-24 illustrates the S22 and S12 stress fields for 3D model as in the directions shown in Figure 5-4. After the initiation of the crack at the mid-width, stress distributions at point b are shown in Figure 5-24-b. Filler stress is reduced remarkably after the crack, and a new stress state is established at the middle. The upper and lower crack fronts are under high peel and shear stresses, revealing propagation may occur on both sides of the crack under mixed mode. The stress field at the edge almost did not change. Figure 5-24-c shows the state at which debonding is very close to the edge and affects stress field at the edge. S22 field is localized on the filler right corner and shear stress magnitudes gets higher. The crack at the mid propagated through upper and lower tips and still has stress concentrations at the tips. Debonding reached to the edge in Figure 5-24-d. Both upper and lower crack tips at the edge are under high peel and shear stresses showing mixed mode propagation will take place.

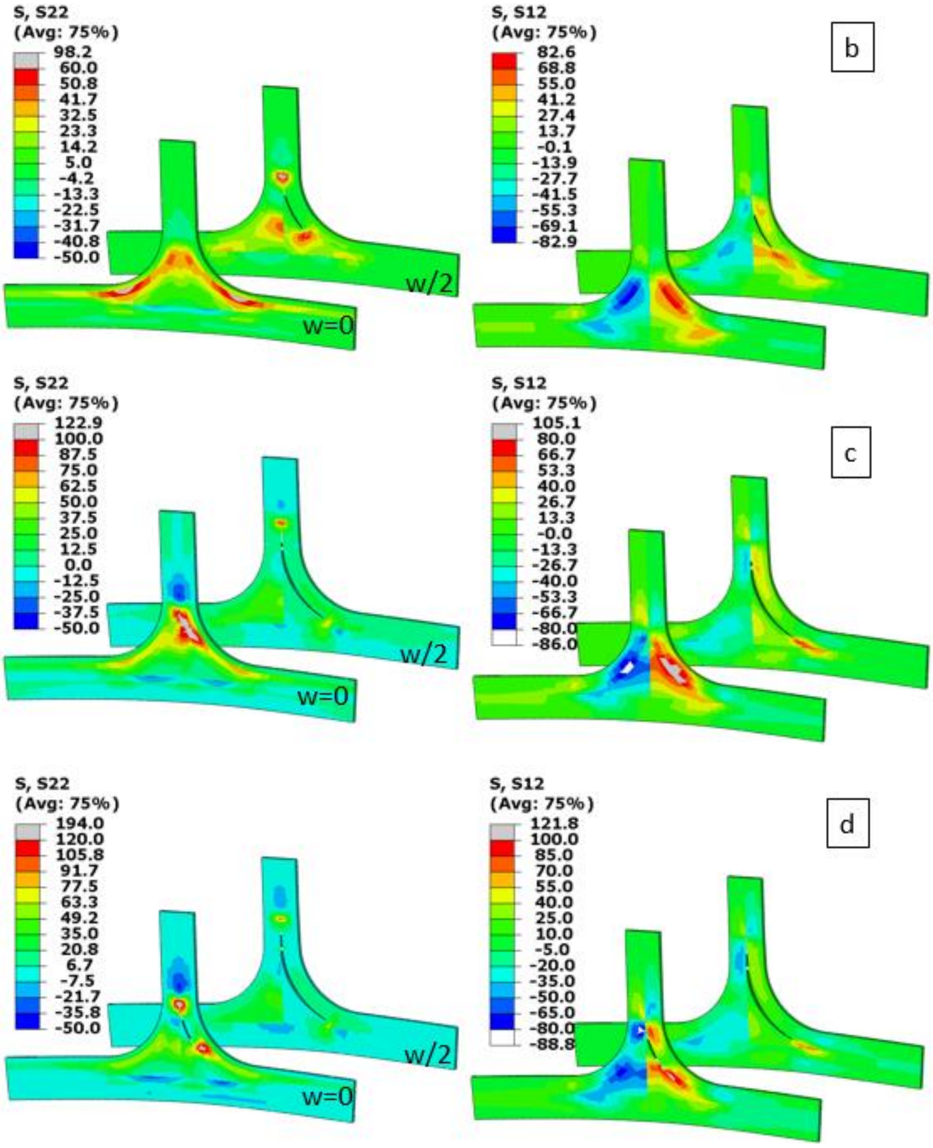

Figure 5-24 S22 and S12 stress fields for the points b-d at the edge and mid-width sections of deltoid for 3D CZM

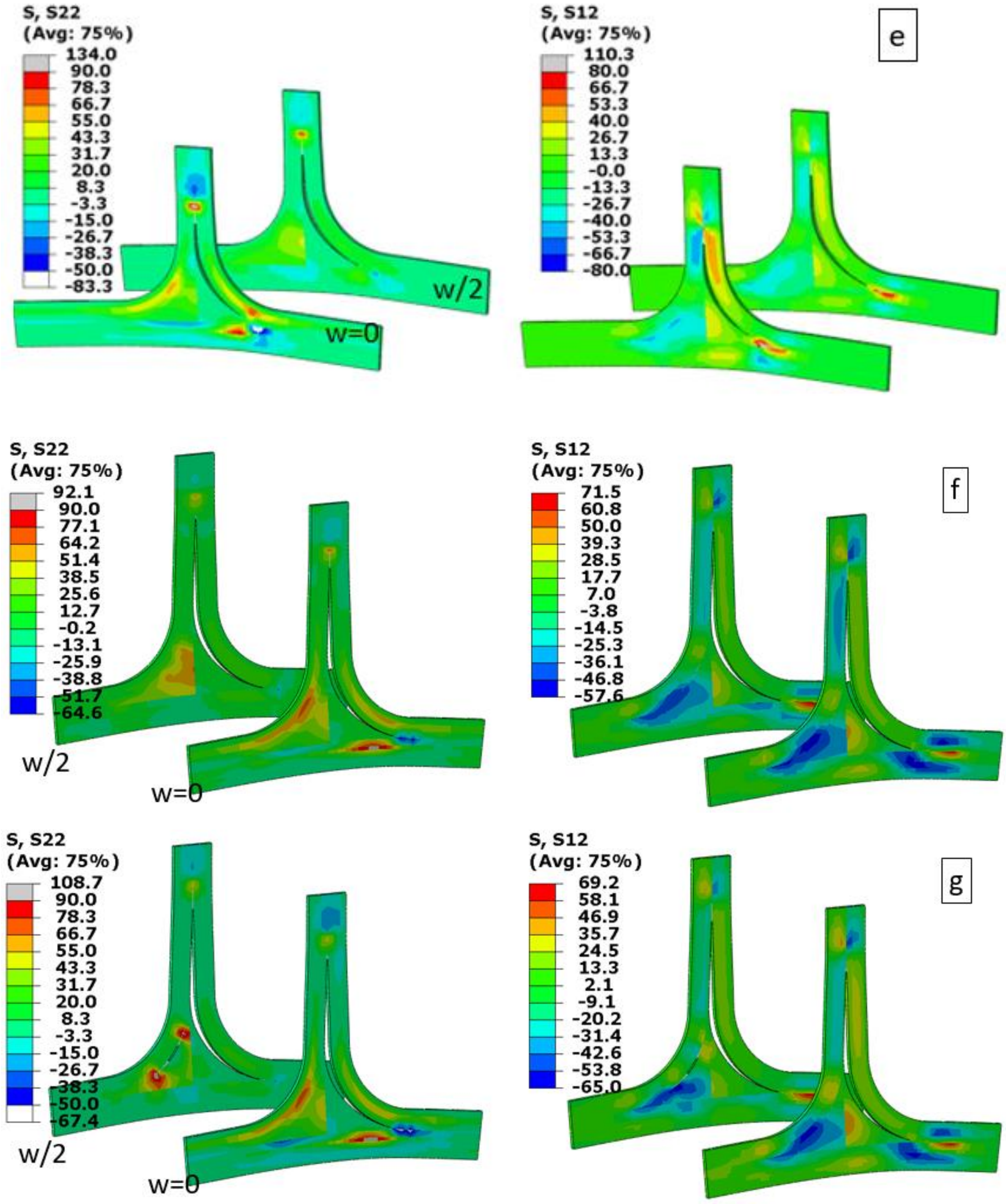

Figure 5-25 S22 and S12 stress fields for the points e-g at the edge and mid-width sections of deltoid for 3D CZM

Figure 5-25-e represents both edge and mid cracks which are almost at the same level through the web. The magnitudes of peak stresses at the edge section are reduced compared to point d, and stable crack propagation is achieved after this point. From points e to f, the loading on the structure is increasing as in Figure 5-22 while the first crack continues upwards in a stable manner. Figure 5-25-f shows stress state after debonding initiation at the filler/left stringer interface in two zones. Since only mid and edge sections are shown in this figure, crack itself is not captured. The left stringer carries the main load; therefore, stresses are higher on the filler/left stringer interface as seen in Figure 5-25-f. The crack at the right interface only propagated towards upwards between e-f, because there exist compressive S22 stresses at the lower crack tip in Figure 5-25-f since left portion sustain structural integrity and resistance. The debonded zones combined at the mid-section at point g as shown in Figure 5-23. The crack at the middle is seen near the top corner in Figure 5-25-g. Both upper and lower crack tips are under high peel stresses indicating that mode-I dominated crack propagation will take place. Stress field at the edge is almost the same at the point f.

As shown in Figure 5-26-h, crack at the mid-section extended in both upper and lower directions through the left interface of the filler. Moreover, debonding reached to the edges of the structure. The lower crack tip at the edge is under both S22 and S12 stresses, thus, downwards crack propagation will be under mixed mode. Figure 5-26-i illustrates complete debonding of filler from the stringer. All the crack tips are under excessive stress concentration indicating that propagation will take place suddenly. The compressive S22 field on the lower tip of the right interface debonding does not exist after loss of filler/stringer integrity. The simulation is stopped at point j when almost half of the ultimate load is achieved in Figure 5-22 which means collapse of the structure. The crack tips at this point is still under high stresses and debonding will propagate under mixed mode through the web, and skin/stiffener interfaces as shown in Figure 5-26-j.

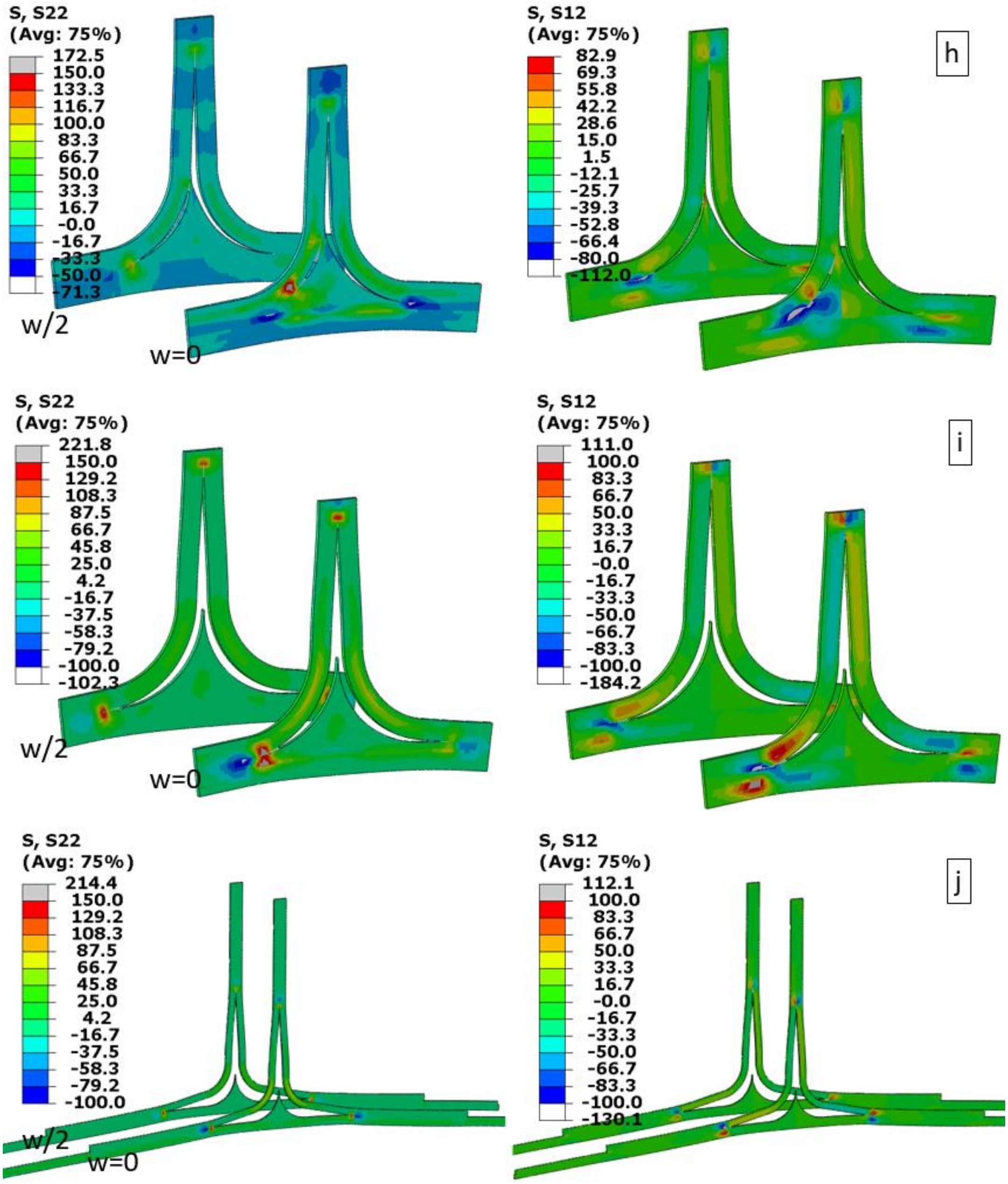

Figure 5-26 S22 and S12 stress fields for the points h-j at the edge and mid-width sections of deltoid for 3D CZM

5.2.2.2 45°-Oblique Loading

Oblique loading is one of the major types of out-of-plane loading of joints. This is because box structures such as wing, aileron or turbine blades are subjected to both tensile and bending forces in a combined way. Understanding the joint response under such a loading scenario is essential for the designers to avoid unexpected problems.

Firstly, compared to 0° and 90° pure loading cases, the structure's maximum load-carrying capacity is the highest under 45° loading, as seen in Figure 5-17. The reason behind this increase in the ultimate load is deducted by Chen et al. [32] as the deformation of the joint under oblique loading is less compared to pure tensile and bending loadings due to their opposite nature. That is, while the stringer left flange is in the opening mode after the first crack in the left stringer/filler interface under tensile loading, the bending component leads to closing and therefore resisted crack opening. As a result, the initiating second crack leading to a major decrease in load bearing capacity is postponed by opposed forces.

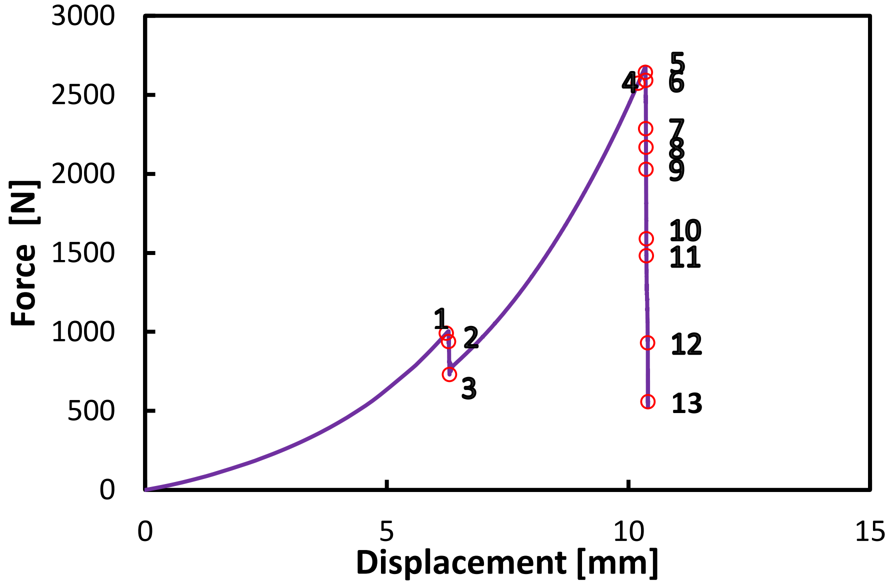

Figure 5-27 Load-displacement graph for 45° loading in detailed

Figure 5-27 shows load-displacement graph of T-joint structure under oblique loading. Two load drops happened during 45° loading, as seen in Figure 5-27. The first represents debonding of the filler/left stringer, while the second initiates due to the filler/right stringer debonding and go downwards with other cracks. Stress components and delamination/debond behavior are investigated at the points 1-13 shown in Figure 5-27 in detail. Critical points are selected before and after the crack formations, as seen in the below table.

Table 15 Failure investigation points and crack data for oblique loading

Point	**Displacement [mm]**	**Force [N]**	**Explanation**
1	6.235	992	
	6.282	968	1st crack initiates at left stringer/filler interface
2	6.283	938	
3	6.299	730	End of the 1st load drop due to complete debonding of filler from left stringer. Crack continue extending down but stabilized in upper region.
4	10.201	2572	
	10.352	2677	2nd crack initiates at right stringer/filler interface
5	10.356	2641	
6	10.358	2590	2nd crack stabilizes at the bottom right corner of the deltoid
7	10.363	2285	
	10.364	2216	3rd crack initiates between 5th -6th right stringer plies
8	10.365	2167	
	10.365	2117	4th crack initiates between 7th -8th skin plies
9	10.366	2028	
	10.370	1741	5th crack initiates between 6th -7th skin plies
10	10.371	1588	
	10.372	1487	6th crack initiates between 5th -6th right stringer plies in web
11	10.373	1481	

Table 14 (continued)

Point	Displacement [mm]	Force [N]	Explanation
	10.400	955	7th crack initiates between 7th -8th skin plies and 8th crack initiates between 5th -6th left stringer plies at the left flange tip
12	10.402	930	
13	10.407	557	Left stringer flanges separated from skin

Figure 5-28 shows the out-of-plane normal stress, S22, and the shear stress, S12 distributions around the filler region under oblique loading at point 1 on the load-displacement plot. The ply interface lines are used to better visualize debond/delamination until a ply interface fails. Understanding the stress distribution on the T-joint structure just before losing structural integrity is important because it gives many key points for the designers. Firstly, the S22 component is positive on the left side of the filler while it is negative on the other side, meaning that the opening side will be the left side while the right side is under compression. In contrast, the S12 is dominant on the right radius but also has a significant magnitude on the left bottom part of the radius.

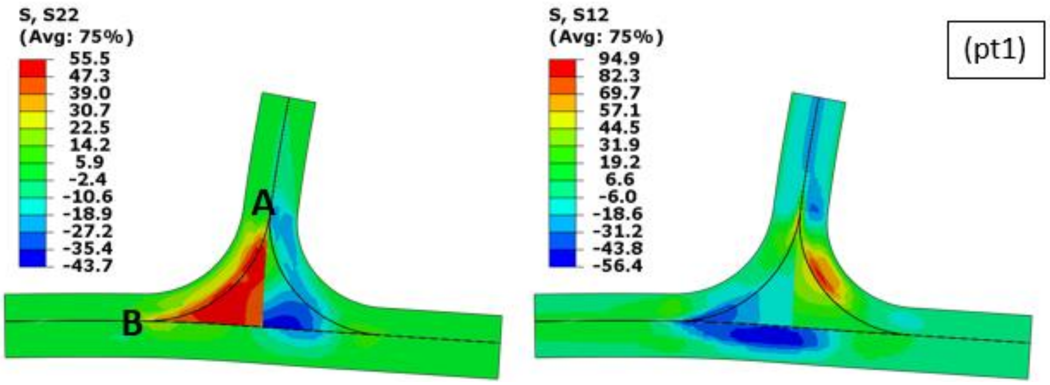

Figure 5-28 Stress distributions on deltoid region at point 1 in the load-displacement plot

The stress components on the critical left filler interface, the out-of-plane and shear stresses on the path A-B shown in Figure 5-28 before the first crack initiation are shown in Figure 5-29. The stresses along path A-B reveal that at point A, the tip of the filler, almost all the stress is shear stress with a small compressive out-of-plane stress. Along the path out-of-plane component increases and the shear stress decreases. At the crack initiation location specified with the vertical red dashed line in Figure 5-29, both stress components have almost the same magnitude (~40-45 MPa), confirming the mixed mode crack initiation similar to the 0° tensile case (45MPa) stated by Gülaşık et al. [1]. Although the S12 component is higher than the shear allowable at the right side of the filler, debond initiates near the left bottom side of the filler/stringer interface (nearly 22° from the filler bottom) due to compressive S22 component prevents crack formation on the right interface.

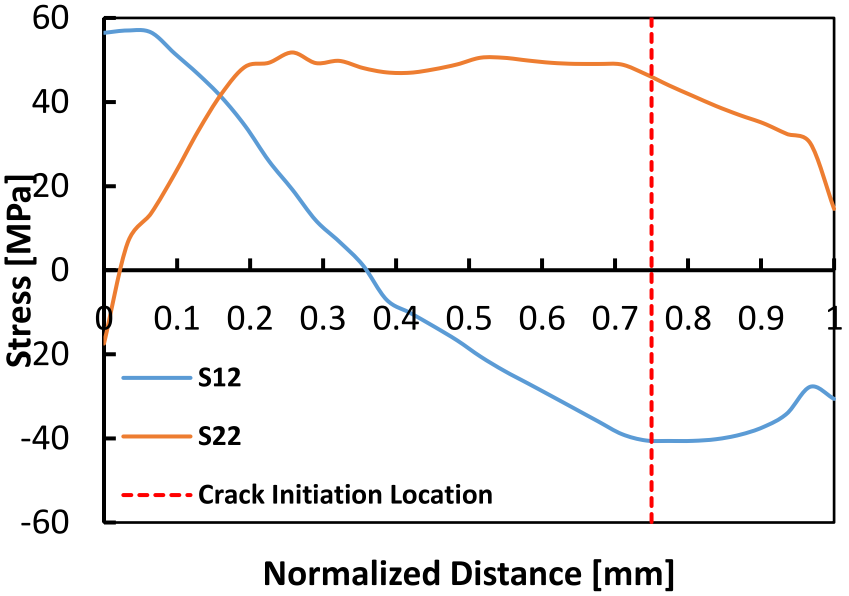

Figure 5-29 Stress distributions along path A-B at point 1 under 45° loading

After the initiation of the crack, contours corresponding to point 2 on the load-displacement plot are shown in Figure 5-30. Filler stress is reduced significantly after the crack, and a new stress state is established, revealing propagation may occur on both sides of the crack. The upper crack front is under high peel stress, but lower crack front is exposed to both high peel and shear stresses.

At point 3 on the load-displacement plot, the stresses around the deltoid are reduced during the load drop, and there are no critical regions in terms of high stresses except the crack fronts. The load drop caused by the first debond shown in Figure 5-27 is about to end, and Figure 5-30 (pt3) show that both crack tips will propagate under mixed mode behavior because of the high shear and out-of-plane stresses around the crack tips. However, magnitudes of the peak stresses are also reduced, and stable crack propagation is achieved after this point.

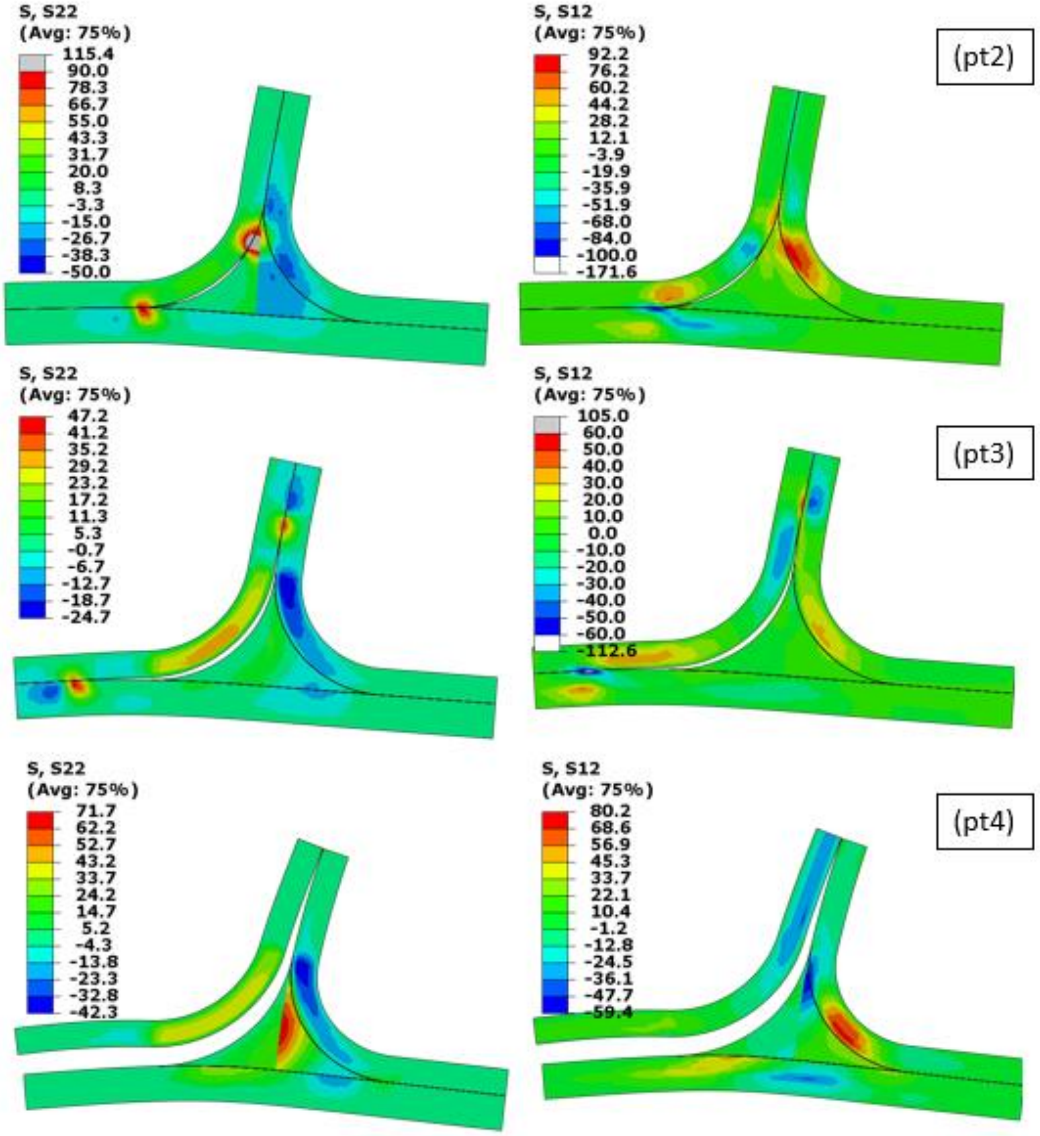

Figure 5-30 Stress distributions at selected points on the T-joint structure at point 2 to point 4

Before the second load drop, stress distributions at point 4 are captured in Figure 5-30 (pt4). From points 3 to 4, the load monotonically increase while the first crack propagates upwards and downwards in a stable manner. The right stringer carries the main load; therefore, stresses are higher on the filler/right stringer interface. Due to the bending component of the applied displacement, compressive S22 stresses exist in the right stringer plies, but the filler interface is still under interlaminar tensile stresses. Shear stresses are localized in the right flange radius and filler top corner. The crack initiates near the top corner as seen in Figure 5-31 (pt5). After the initiation of crack, the stress concentration of the S22 component at the lower tip is seen from the contour indicating further propagation may occur. As shown in Figure 5-31 (pt6) crack extends in both the upper and lower directions through the interface. Although the upper tip reached the filler tip, the compressive S22 component in the right corner of the filler stopped the propagation in the lower tip, as seen in Figure 5-31 (pt7). After debonding a large part of the filler/right stringer flange interface, the crack tip reached the bottom corner of the filler where through the thickness stresses are extremely high due to geometry and crack tip singularity. Also, shear stresses concentrated on the right stringer flange bend region move downward with the crack and concentrated on the junction point, Figure 5-31 (pt7).

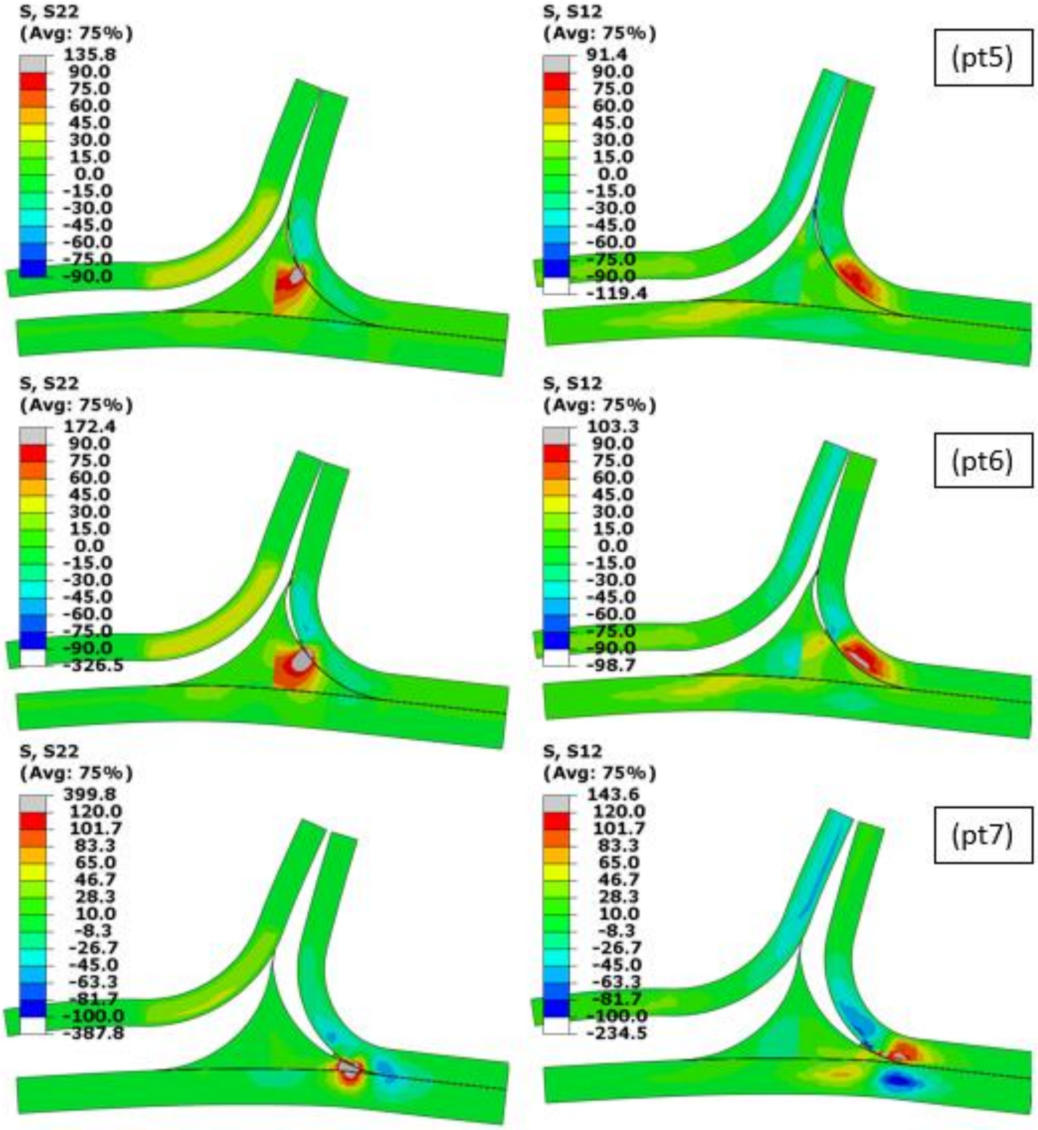

Figure 5-31 Stress distributions at selected points on the T-joint structure at point 5 to point 7

After stabilization of the second crack tip, third crack initiates in the stringer right flange 5-6th ply interfaces near the right junction point of the components due to high interlaminar tensile and shear stresses, Figure 5-32 (pt8). After this crack formation, the filler/stringer interface continues separating, and a new crack is seen at the 7th - 8th ply interface of the skin, Figure 5-32 (pt9). As the separation of stringer from the skin is growing, delamination between 7th-8th plies of the skin under 5th crack occurs as in Figure 5-32 (pt10). A significant loss in the load carrying capability is obvious after the pre-mentioned cracks looking to point 10 in Figure 5-27, but the structure still has some load bearing.

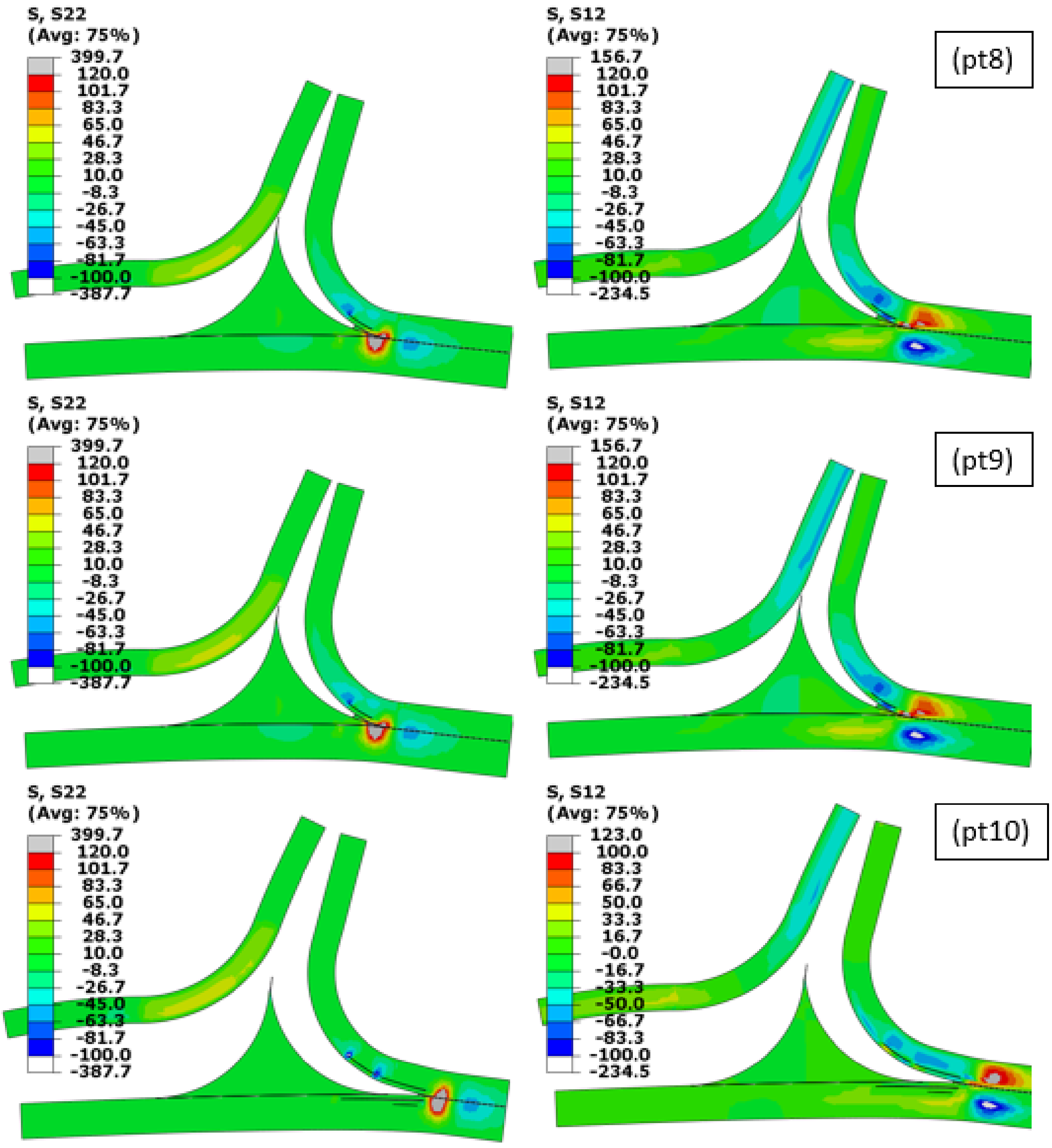

Figure 5-32 Stress distributions at selected points on the T-joint structure at point 8 to point 10

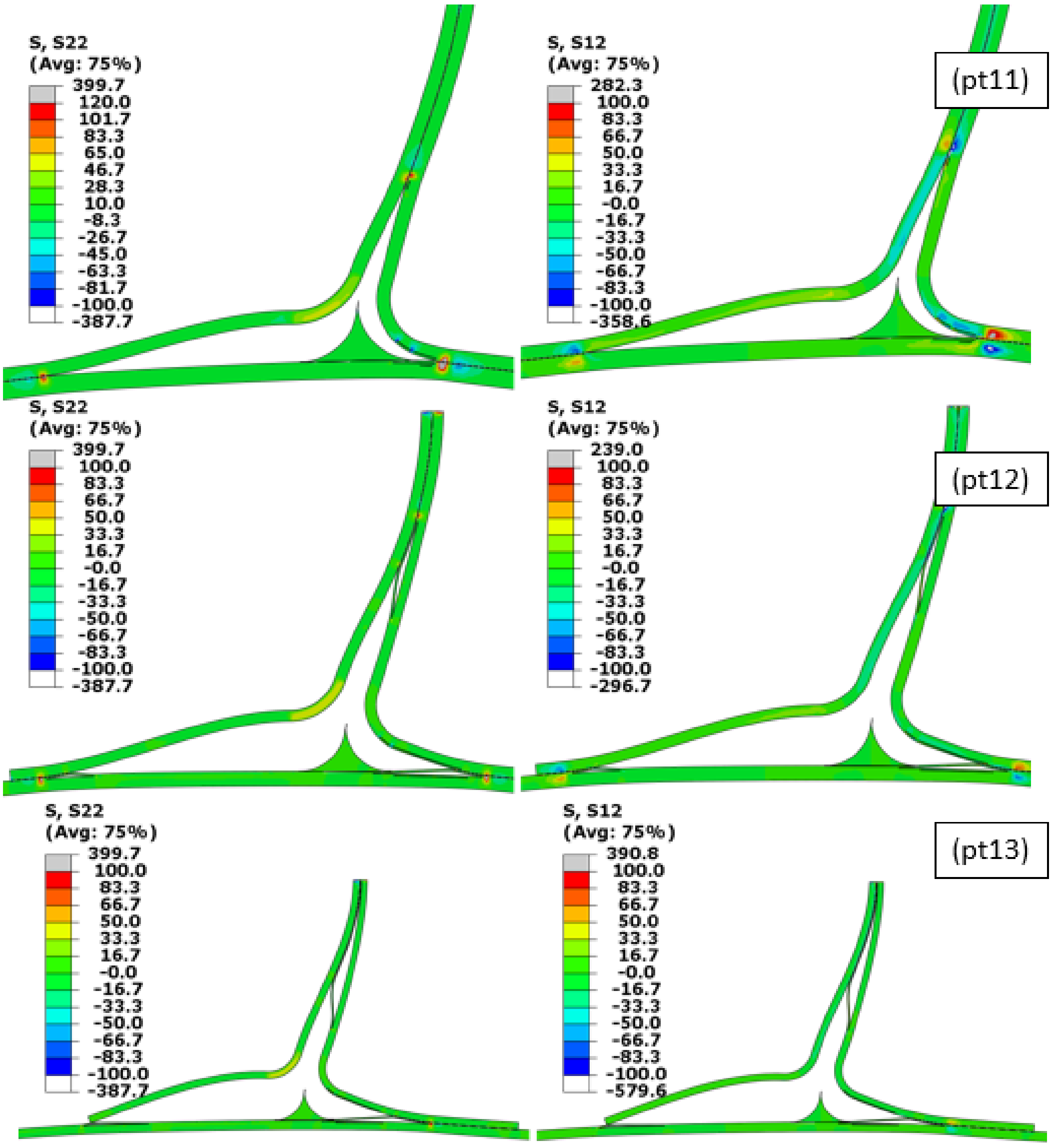

Figure 5-33 Stress distributions at selected points on the T-joint structure at point 11 to point 13

After complete debonding of filler from the stringer, the left and right flanges undergo large deformation, and a new crack appears between 5th and 6th plies on the right side of the web and grows rapidly to the top, as shown in Figure 5-33 (pt11) and (pt12). Before the final failure, the last delaminations are seen in the left flange tip between both in stringer 5th -6th and skin 7th-8th ply from Figure 5-33 (pt12). After the complete separation of the left stringer leg from the skin, Figure 5-33 (pt13), the simulation is aborted due to convergence difficulties.

5.2.2.3 90°-Transverse Loading

Transverse loading is one of the significant loading types of out-of-plane loading of joints. This is because box structures such as wing, aileron or turbine blades are subjected to high bending loads transferred in the shear form in the skin. Understanding the joint response under such a loading scenario is important for the designers to avoid unexpected problems.

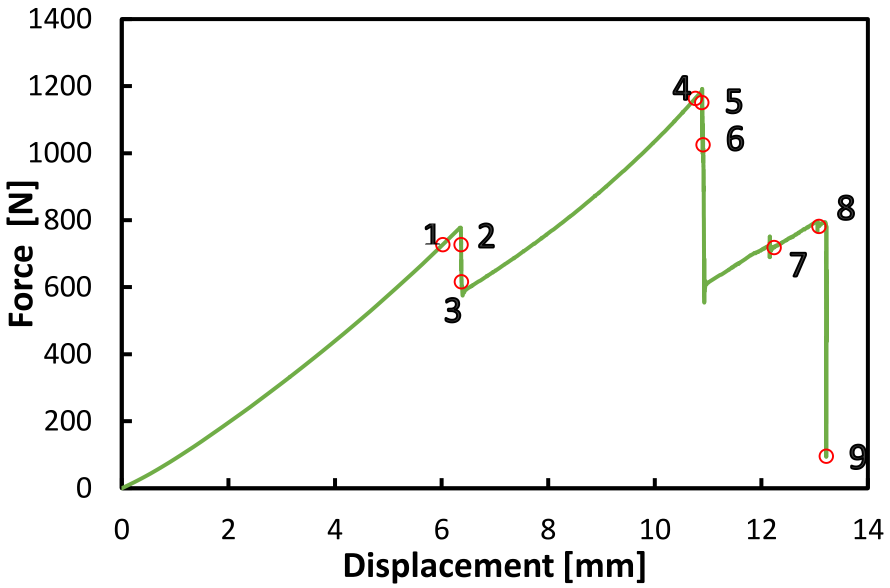

Figure 5-34 Load-displacement graph for 90° loading in detailed

Figure 5-34 shows load-displacement graph of T-joint structure under transverse loading. The points 1 to 9 are critical points for the understanding of failure. These points are selected before and after the crack formations, as seen in Table 16. Stress components and delamination/debond behavior are investigated at the points shown in Figure 5-34 in detail.

Firstly, compared to 0° and 45° pure loading cases, the structure's maximum load carrying capacity is the lowest under 90° loading, as seen in Figure 5-17. Three load drops happened during 90° loading, as seen in Figure 5-34. The first represents debonding of the filler/left stringer and the unfolding of the left stringer at the 5th and 6th ply interfaces, while the second initiates due to the filler/right stringer interface debonding and skin delamination close to the filler right corner. The last drop is the structure's collapse by completely separating the left stringer leg from the skin.

Table 16 Failure investigation points and crack data for transverse loading

Point	**Displacement [mm]**	**Force [N]**	**Explanation**
1	6.026	728	
	6.356	778	1st crack initiates at left str filler interface
2	6.366	727	
	6.369	675	2nd crack initiates at left str 5-6th ply interface
3	6.374	617	
4	10.764	1164	
	10.879	1184	3rd crack initiates at right str filler interface
5	10.888	1151	
	10.905	1026	4rd crack initiates at filler right corner skin interface
6	10.907	1026	
7	12.243	719	
8	13.083	782	
9	13.219	96	Left stringer flanges separated from skin

Figure 5-36 (pt1) shows the out-of-plane normal stress, S22, and the shear stress, S12 distributions around the filler region under oblique loading at point 1 on the load-displacement plot. The ply interface lines are used for a better visualization of debond/delamination. Understanding the stress distribution on the T-joint structure just before losing structural integrity is important because it gives many key points for the designers. Firstly, the S22 component is positive on the left side of the filler while negative on the other side, meaning that the opening side will be the left side while the right side is under compression. In contrast, S12 is dominant on the right radius but also has significant magnitude on the top and bottom left parts of the filler.

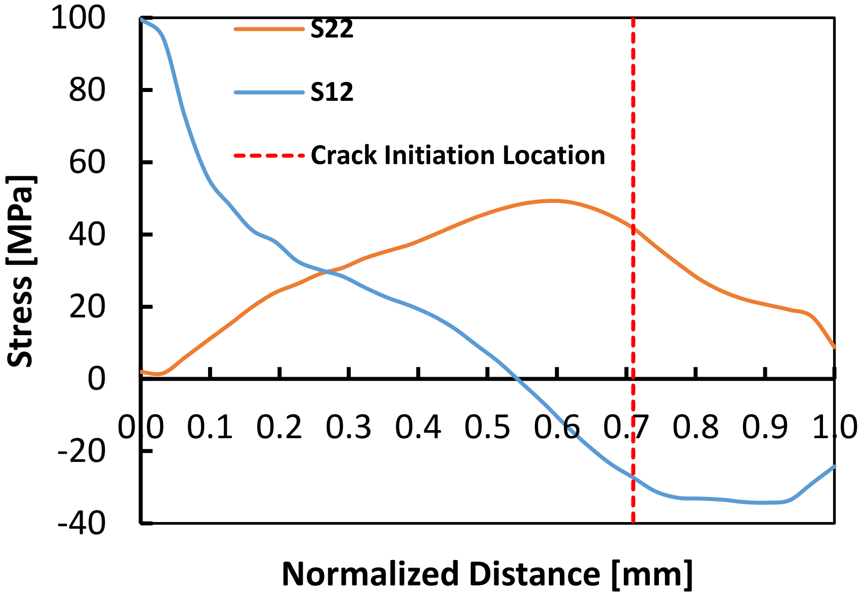

Figure 5-35 Stress distributions along path A-B at point 1 under 90° loading

The stress components on the critical left interface, the out-of-plane normal and shear stresses on the path A-B shown in Figure 5-36 before the first crack initiation are shown in Figure 5-35 . The stresses along path A-B reveal that at point A, the tip of the filler, almost all the stress is shear stress with a small compressive out-of-plane stress. Along the path out-of-plane component increases and the shear stress decreases. At the crack initiation location specified with the vertical red dashed line, both stress components have almost the same magnitude (~30-40 MPa), confirming the mixed mode crack initiation similar to the 0° tensile case (45MPa) stated by Gülaşık et al. [1]. Although the S12 component is higher than the shear allowable at the right side of the filler, debond initiates near the left bottom side of the filler/stringer interface (nearly 22° from the filler bottom) due to compressive S22 component prevents crack formation on the right interface.

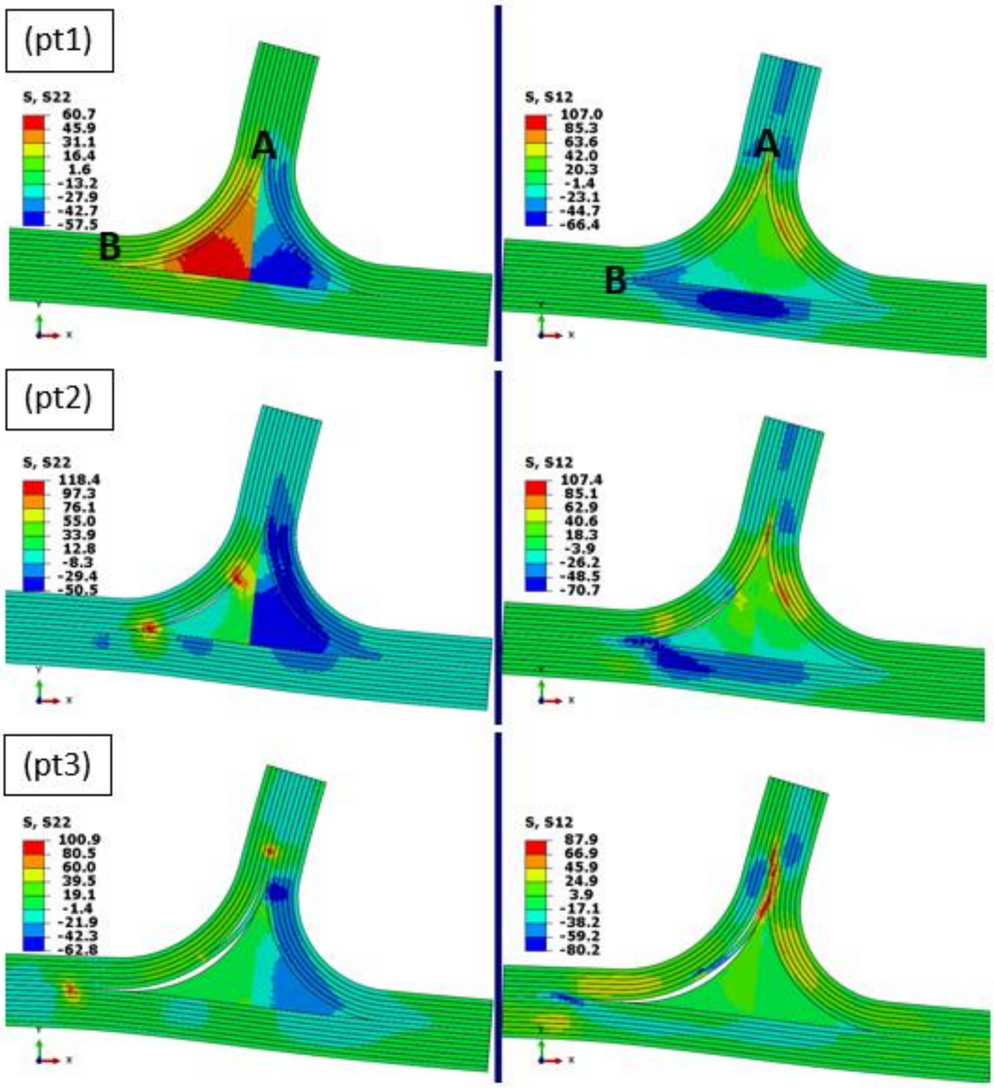

Figure 5-36 Stress distributions at selected points on the T-joint structure at point 1 to point 3 in the load-displacement plot

After initiation of the crack, stress contours corresponding to point 2 on the load-displacement plot are shown in Figure 5-36. Filler stress is reduced significantly after the crack, and a new stress state is established. The crack tips are under both high shear and peel stresses.

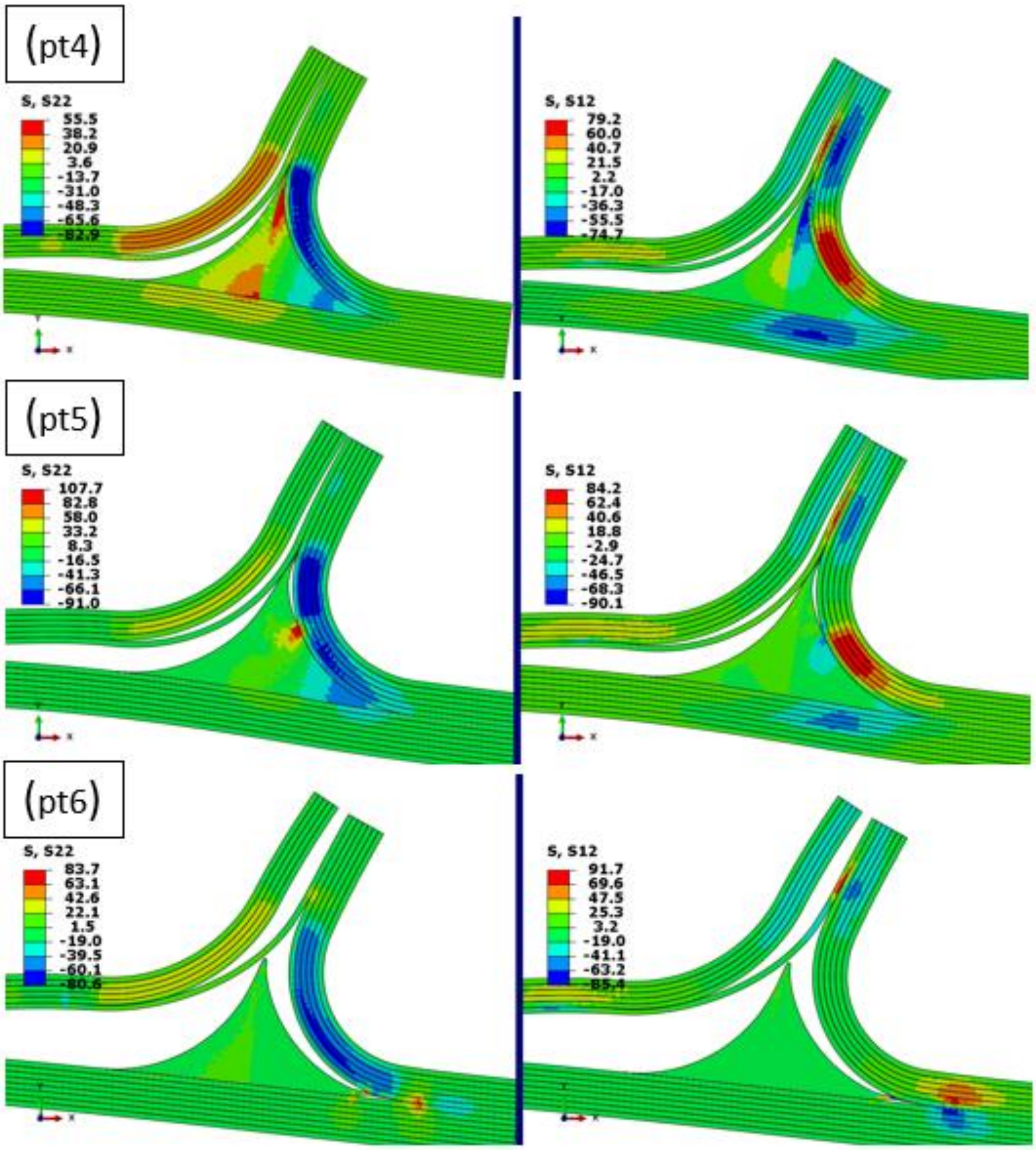

Figure 5-37 Stress distributions at selected points on the T-joint structure at point 4 to point 6

At point 3 on the load-displacement plot, after delamination at the 5th-6th ply interfaces of the left stringer, the upper crack tip is under both high peel and shear stresses. The debonding crack tip at the lower-level experiences high peel stresses, and propagation is expected to occur through this front since second crack reduced the stress level significantly at the upper crack tip. The load drop caused by these two cracks is shown in Figure 5-34 finished, and Figure 5-37 (pt4) shows that both cracks propagated significantly in a stable manner with the increase of load bearing.

Before the second load drop, stress distributions at point 4 are captured in Figure 5-37 (pt4). From points 3 to 4, the load monotonically increase while the first crack propagates downwards, and second crack propagates upwards suddenly. The right stringer carries the main load; therefore, stresses are higher on the filler/right stringer interface. Due to bending, compressive S22 stresses exist in the right stringer plies, but the filler interface is still under interlaminar tensile stresses. The shear stresses are more significant in the middle of right stringer radius and filler top corner. The crack initiates near the top corner, as seen in Figure 5-37 (pt5). After the crack initiation, the stress concentration of S22 component at lower tip is seen from the contour indicating further propagation may occur. As shown in Figure 5-37 (pt6) crack extends in both upper and lower directions through the interface.

After debonding a large part of the filler/right stringer flange interface, the crack tip reached the bottom corner of the filler where through-thickness stresses are extremely high due to geometry and crack tip singularity. Also, shear stresses concentrated on the right stringer flange bend region move downward with the crack. Geometric singularity combined with the crack tip stress field induces a new crack at the skin/filler interface near the right corner of the filler. This crack is stable since the compressive S22 field exists at the crack tip due to bending. After this crack formation, represented by Figure 5-37 (pt6), filler/stringer interface separation stopped and stabilized till the collapse of the left flange. Load carrying capacity is reduced to half of it after filler integrity loss which also induces debonding of the web looking to Figure 5-34. Only a small portion of the web is bonded and transferred loading separately to the stringers. It is obvious that the structure had collapsed already at this point, but the simulation was continued to see complete debonding of the left flange.

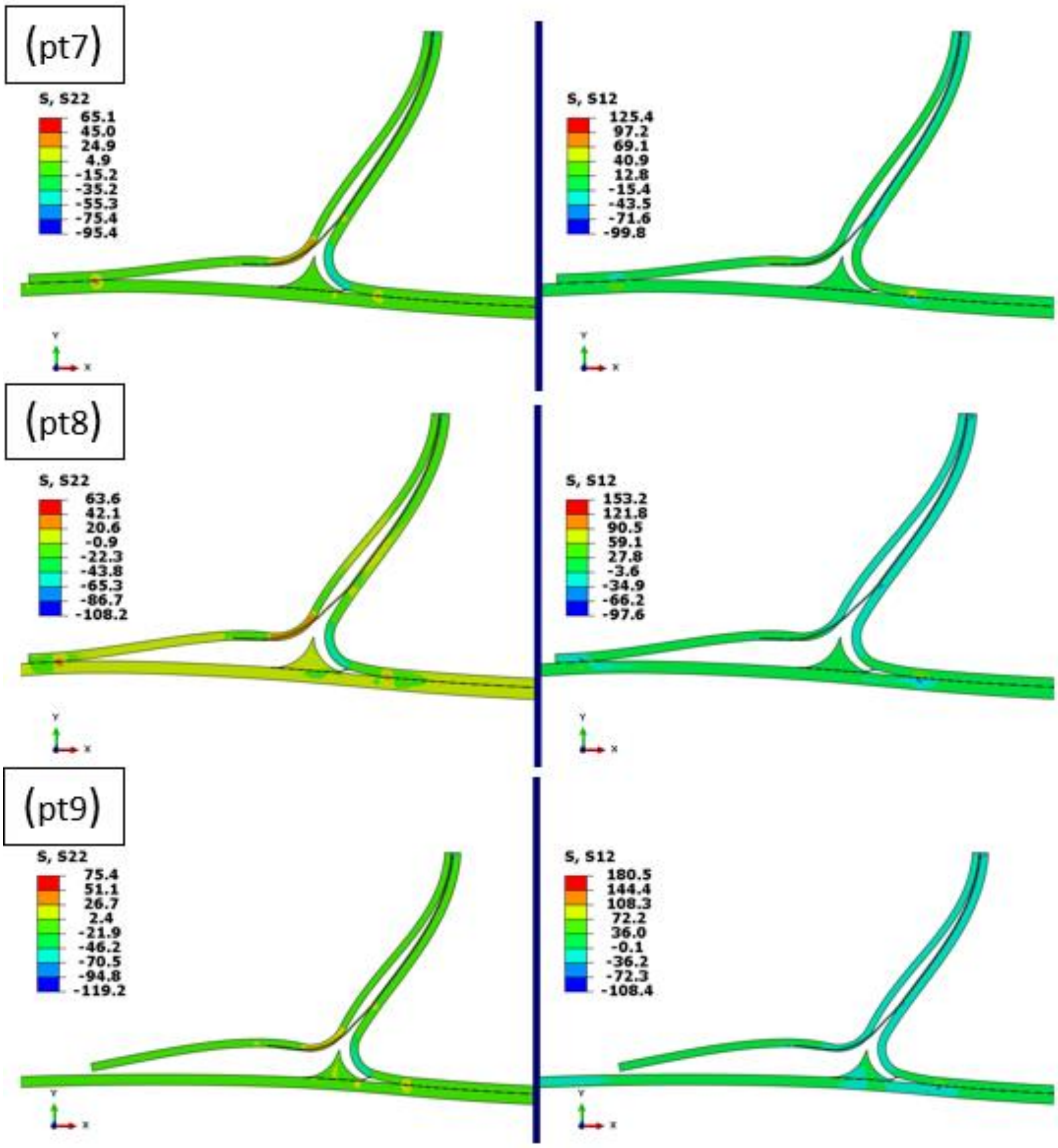

Figure 5-38 Stress distributions at selected points on the T-joint structure at point 7 to point 9

After debonding of the filler from the stringer, the left flanges undergo large deformation, and debonding grows to the end under the concentration of peel and shear stresses at the tips through points 7 and 8 in Figure 5-38. After the complete separation of the left stringer leg from the skin, Figure 5-38, the simulation is aborted due to the loss of load-carrying capacity.

5.3 Conclusion

Numerical simulations of CFRP T-joint was performed in this chapter using CZM with dynamic-implicit solver of ABAQUS. Axial, oblique and transverse loadings were analyzed and stress fields, load-displacement graphs were examined in detail. The following conclusions are drawn;

- Initiation of the debonding is under mixed mode for axial, oblique and transverse loadings at filler/stringer interface.
- For all the loading types, failure initiates as interface failure of adhesive. Although, delamination between skin plies was also seen at the later stages of simulation for 0° loading, cohesive elements in the adhesive regions are sufficient for 3D modelling under tensile loading to reduce computational cost. Transverse loading component in 45° and 90° loading led delamination between stringer ply interfaces at opening side of the joint. As a result, modelling of ply interfaces is crucial under transverse and oblique loadings.
- Ultimate load under oblique loading is the highest among others due to opposing mechanisms driven by axial and transverse components.
- 3D implicit FEM with CZM was used successfully for axial loading. Failure initiates at the center through the width direction in 3D model under axial loading. Through the thickness stress field at the edge of deltoid region is different than mid-section due to free-edge-effect. The mesh refinement at the free-edge should be taken into account for 3D models.
- For all the loadings it is observed that there is a small load drop after the debonding of the filler on one side. Then the structure loses its main load bearing capability after complete debonding of the filler from stringer on both sides. It demonstrates that filler is the critical part of such joint structures as proven before for 0° loading by Gülaşık et al. [1]. In mentioned study of Gülaşık [1], updated numerical model for 0° loading with empty filler area was resulted in more than 50% decrease in the ultimate load and totally changed the failure pattern.

- For axial loaded T-joint 3D CZM model, damage initiates at the stringer flange tip due to discontinuity, but deletion of cohesive elements happens in the filler interface. Stringer flange tips are the high concentration of the peel and shear stresses due to geometric discontinuity. Design changes should be made to reduce stresses in these regions using tapered or bio-inspired ply embedment or drop-off in the run-outs.

5.4 Future Work

Future work for composite T-joint structures based on current study can be listed as below.

- Intralaminar failure criteria can be included in the laminates combined with interface elements at the bond-line for better prediction of failure.
- Compressive matrix and fiber failure criteria should be implemented especially for transverse and oblique loadings.
- Transverse and oblique load cases can be applied to 3D model to observe through the width variation under unsymmetrical loadings.
- T-joint structure can be analyzed under fatigue loading with tensile-compressive loading cycles.
- Explicit analyses can be carried out to examine crack tip speeds and nature of the propagation.
- Discrete damage modelling can be applied to the filler region to determine whether crack at the adhesive interface propagates inside the filler.
- Residual stresses can be accounted by simulating thermal expansion during manufacturing as a separate step.
- Since main failure mode is complete debonding of the filler from surrounding laminates, strengthening studies on filler interfaces can be investigated to increase load bearing. Special attention should be given to increase filler and its interface strength.

REFERENCES

[1] Gülasik, H., & Coker, D. (2014). Delamination-debond behaviour of composite t-joints in wind turbine blades. In *Journal of Physics: Conference Series* (Vol. 524, No. 1, p. 012043). IOP Publishing.

[2] Gülaşık, H. (2014). *Modeling of Mixed Mode Delamination in Composite T-Joints* (Master's thesis, Middle East Technical University).

[3] Lekhnitskii, S. G. (1968). Anisotropic plates. NY: Gordon & Breach.

[4] Kedward, K. T., Wilson, R. S., & McLean, S. K. (1989). Flexure of simply curved composite shapes. *Composites, 20* (6), 527 - 536.

[5] Ko, W. L., & Jackson, R. H. (1989). Multilayer theory for delamination analysis of a composite curved bar subjected to end forces and end moments. In *Composite Structures 5* (pp.173 – 198). Springer, Dordrecht.

[6] Gonzalez-Cantero, J. M., Graciani, E., Blazquez, A., & París, F. (2016) A new analytical model for evaluating interlaminar stresses in the unfolding failure of composite laminates. *Composite Structures, 147,* 260-273.

[7] Kim, R. Y., & Soni, S. R. (1986). Failure of composite laminates due to combined interlaminar normal and shear stresses. *Composites, 86,* 341-350.

[8] Brewer, J. C., & Lagace, P.A. (1988). Quadratic stress criterion for initiation of delamination. *Journal of composite materials,* 22(12), 1141-1155.

[9] Wisnom, M. R., Hill, G. F., & Jones, M. I. (2001). Through thickness failure prediction of composite structural element. In *13th International Conference on Composite Materials, Beijing, China, paper* (No. 1623).

[10] Martin, R. H. (1992). Delamination failure in a unidirectional curved composite laminate. *Composite materials: Testing and design., 10,* 365 - 383.

[11] Martin, R. H., & Jackson, W. C. (1993). Damage prediction in cross-plied curved composite laminates. *Composite materials: Fatigue and fracture, 4,* 105 - 126.

[12] Chang, F. K., & Springer, G. S. (1986). The strength of fiber reinforced composite bends. *Journal of Composite Materials, 20*(1), 30 - 45.

[13] Sun, C. T., & Kelly, S. R. (1988). Failure in composite angle structures Part I: Initial failure. *Journal of Reinforced Plastics and Composites, 7*(3), 220 - 232.

[14] Sun, C. T., & Kelly, S. R. (1988). Failure in composite angle structures Part II: Onset of delamination. *Journal of Reinforced Plastics and Composites, 7*(3), 233-244.

[15] González-Cantero, J. M., Graciani, E., López-Romano, B., & París, F. (2018). Competing mechanisms in the unfolding failure in composite laminates. *Composites Science and Technology, 156,* 223-230.

[16] Gözlüklü, B., & Coker, D. (2012). Modeling of the dynamic delamination of L - shaped unidirectional laminated composites. *Composite Structures, 94* (4), 1430-1442.

[17] Gözlüklü, B., Uyar, I., & Coker, D. (2015). Intersonic delamination in curved thick composite laminates under quasi - static loading. *Mechanics of Materials, 80*, 163-182.

[18] Albiol, D. (2010). Buckling analyses of composite laminated panels with delamination.

[19] Turon, A., Dávila, C. G., Camanho, P. P., & Costa, J. An engineering solution for solving mesh size effects in the simulation of delamination with cohesive zone models. *Engineering Fracture Mechanics.*

[20] Alfano, M., Furgiuele, F., Leonardi, L., Maletta, C., & Paulino, G. H. (2007). Fracture analysis of adhesive joints using intrinsic cohesive zone models. *Key Eng Mater, 348,* 13-16.

[21] Orifici, A. C., Thomson, R. S, Degenhardt, R., Bisagni, C., & Bayandor, J. (2009). A finite element methodology for analysing degradation and collapse in postbuckling composite aerospace structures. *Journal of composite materials, 43*(26), 3239-3263.

[22] ABAQUS (2022). ABAQUS/CAE user’s guide. Dassault Systèmes, Providence, RI, USA.

[23] Psarras, S., Pinho, S. T., & Falzon, B. G. (2012). Damage-tolerant design of stiffener run-outs: A finite element approach. *Finite Element Analysis-New trends and developments, InTech,* 277-300.

[24] Orifici, A. C., Shah, S. A., Herszberg, I., Kotler, A., & Weller, T. (2008). Failure analysis in postbuckled composite T-sections. *Composite Structures, 86*(1-3), 146-153.

[25] Jun, L., Liu, X. Y., Nan, Y. Y., & Xuefeng, Y. (2016). Numerical and experimental analysis of delamination in the T-stiffener integrated composite structure. *Mechanics of Advanced Materials and Structures, 23*(10), 1188-1196.

[26] Hélénon, F., Wisnom, M. R., Hallett, S. R., & Trask, R. S. (2012). Numerical investigation into failure of laminated composite T-piece specimens under tensile loading. *Composites Part A: Applied Science and Manufacturing, 43*(7), 1017-1027.

[27] Hélénon, F., Wisnom, M. R., Hallett, S. R., & Trask, R. S. (2013). Investigation into failure of laminated composite T-piece specimens under bending loading. *Composites Part A: Applied Science and Manufacturing, 54*, 182-189.

[28] Sápi, Z., Butler, R., & Rhead, A. T. (2018). Numerical prediction of failure in composite t-joints using progressive damage modelling. In *2018 AIAA/ASCE/AHS/ASC Structures, Structural Dynamics, and Materials Conference* (p. 0221).

[29] Sapi, Z., Butler, R., & Rhead, A. (2019). High fidelity analysis to predict failure in T-joints. *Composite Structures, 225*, 111143.

[30] Chen, J., Ravey, E., Hallett, S., Wisnom, M., & Grassi, M. (2009). Prediction of delamination in braided composite T-piece specimens. *Composites Science and Technology, 69*(14), 2363-2367.

[31] Chen, J. (2012). A numerical investigation of thermal-related matrix shrinkage crack and delamination in composite T-piece specimens using a modified interface cohesive model. *Journal of Thermoplastic Composite Materials, 25*(3), 267-282.

[32] Chen, J., & Fox, D. (2012). Numerical investigation into multi-delamination failure of composite T-piece specimens under mixed mode loading using a modified cohesive model. *Composite Structures, 94*(6), 2010-2016.

[33] Li, X., & Chen, J. (2016). The implementation of the extended cohesive damage model for multicrack evolution in laminated composites. *Composite Structures, 139*, 68-76.

[34] Wang, Y., & Soutis, C. (2018). A finite element and experimental analysis of composite T-joints used in wind turbine blades. *Applied Composite Materials, 25*(4), 953-964.

[35] Tan, Y., Li, Y., Huan, D., Zhang, X., & Chu, Q. (2017). Failure analysis and strengthening mechanism of Z-pinned composite T-joints under tensile loading. *Science and Engineering of Composite Materials, 24*(5), 783-790.

[36] Kumari, S., & Sinha, P. K. (2002). Finite element analysis of composite wing T-joints. *Journal of reinforced plastics and composites, 21*(17), 1561-1585.

[37] Xu, X., Wisnom, M. R., Hallett, S. R., Holden, G., & Gordon, B. (2016). Predicting debonding and delamination in adhesively bonded T-joints. In *17th European Conference on Composite Materials* (pp. 26-30).

[38] Cui, H., Li, Y., Koussios, S., & Beukers, A. (2010). Parametric evaluation on the curved part of composite T-joints based on numerical simulation. In *27th International Congress of the Aeronautical Sciences, Nice-France.*

[39] Wu, H., Xiao, J., Xing, S., Wen, S., Yang, F., & Yang, J. (2015). Numerical and experimental investigation into failure of T700/bismaleimide composite T-joints under tensile loading. *Composite Structures, 130,* 63-74.

[40] Bruyneel, M., Delsemme, J. P., Jetteur, P., & Germain, F. (2009). Modeling inter-laminar failure in composite structures: illustration on an industrial case study. *Applied Composite Materials, 16*(3), 149-162.

[41] Pham, D. C., Cui, X., Lua, J., & Goyal, V. (2021). High-fidelity Progressive Damage Predictions of Composite T-joints using Advanced Continuum Damage Model and B-Spline Analysis Method. In *AIAA Scitech 2021 Forum* (p. 0703).

[42] Shenoi, R. A., & Hawkins, G. L. (1992). Influence of material and geometry variations on the behaviour of bonded tee connections in FRP ships. *Composites, 23*(5), 335-345.

[43] Phillips, H. J., & Shenoi, R. A. (1998). Damage tolerance of laminated tee joints in FRP structures. *Composites Part A: Applied Science and Manufacturing, 29*(4), 465-478.

[44] Dharmawan, F., Thomson, R. S., Li, H., Herszberg, I., & Gellert, E. (2004). Geometry and damage effects in a composite marine T-joint. *Composite Structures, 66*(1-4), 181-187.

[45] Di Bella, G., Borsellino, C., Pollicino, E., & Ruisi, V. F. (2010). Experimental and numerical study of composite T-joints for marine application. *International Journal of Adhesion and Adhesives, 30*(5), 347-358.

[46] Trask, R. S., Hallett, S. R., Helenon, F. M. M., & Wisnom, M. R. (2012). Influence of process induced defects on the failure of composite T-joint specimens. *Composites Part A: Applied Science and Manufacturing, 43*(4), 748-757.

[47] Thawre, M. M., Pandey, K. N., Dubey, A., Verma, K. K., Peshwe, D. R., Paretkar, R. K., ... & Manjunatha, C. M. (2015). Fatigue life of a carbon fiber composite T-joint under a standard fighter aircraft spectrum load sequence. *Composite Structures, 127,* 260-266.

[48] Li, H. C. H., Dharmawan, F., Herszberg, I., & John, S. (2006). Fracture behaviour of composite maritime T-joints. *Composite Structures, 75*(1-4), 339-350.

[49] Wang, Y., & Soutis, C. (2016). Modelling the effect of tufted yarns in composite T-joints. *Proceedings of the Institution of Civil Engineers-Engineering and Computational Mechanics, 169*(4), 158-170.

[50] Burns, L. A., Mouritz, A. P., Pook, D., & Feih, S. (2012). Bio-inspired design of aerospace composite joints for improved damage tolerance. *Composite Structures, 94*(3), 995-1004.

[51] Burns, L. A., Mouritz, A. P., Pook, D., & Feih, S. (2012). Strength improvement to composite T-joints under bending through bio-inspired design. *Composites Part A: Applied Science and Manufacturing, 43*(11), 1971-1980.

[52] Burns, L., Mouritz, A. P., Pook, D., & Feih, S. (2015). Bio-inspired hierarchical design of composite T-joints with improved structural properties. *Composites Part B: Engineering, 69,* 222-231.

[53] Burns, L., Mouritz, A. P., Pook, D., & Feih, S. (2016). Strengthening of composite T-joints using novel ply design approaches. *Composites Part B: Engineering, 88,* 73-84.

[54] Roy, A. (2008). Adhesive bonding for structural marine applications. In *Proceedings of the International Conference Innovation in High Performance Sailing Yachts, 29-30 May 2008, Lorient, France, ISBN: 978-1-905040-46-9, Organized by: the Royal Institution of Naval Architects, RINA, Paper: P2008-3 Proceedings.*

[55] Camanho, P. P., Dávila, C. G., Pinho, S. T., Iannucci, L., & Robinson, P. (2006). Prediction of in situ strengths and matrix cracking in composites under transverse tension and in-plane shear. *Composites Part A: Applied Science and Manufacturing, 37*(2), 165-176.

[56] Catalanotti, G. (2019). Prediction of in situ strengths in composites: some considerations. *Composite Structures, 207,* 889-893.

[57] Camanho, P. M. (2008). *Progressive failure analysis of advanced composites*. PORTO UNIV (PORTUGAL) DEPT OF MECHANICAL ENGINEERING.

[58] ABAQUS (2022). ABAQUS elements guide. Dassault Systèmes, Providence, RI, USA.

[59] Camanho, P. P., & Dávila, C. G. (2002). *Mixed-mode decohesion finite elements for the simulation of delamination in composite materials* (No. NAS 1.15: 211737).

[60] Kenane, M., & Benzeggagh, M. L. (1997). Mixed-mode delamination fracture toughness of unidirectional glass/epoxy composites under fatigue loading. *Composites Science and Technology, 57*(5), 597-605.

[61] Belytschko, T., & Black, T. (1999). Elastic crack growth in finite elements with minimal remeshing. *International journal for numerical methods in engineering, 45*(5), 601-620.

[62] Benzley, S. E. (1974). Representation of singularities with isoparametric finite elements. *International journal for numerical methods in engineering, 8*(3), 537-545.

[63] Melenk, J. M., & Babuška, I. (1996). The partition of unity finite element method: basic theory and applications. *Computer methods in applied mechanics and engineering, 139*(1-4), 289-314.

[64] Gigliotti, L. (2012). Assessment of the applicability of XFEM in Abaqus for modeling crack growth in rubber.

[65] Sápi, Z., Butler, R., & Rhead, A. (2019). Filler materials in composite out-of-plane joints–A review. *Composite Structures, 207,* 787-800.

[66] Sapi, Z., Hutchins, S., Butler, R., & Rhead, A. (2019). Novel filler materials for composite out-of-plane joints. *Composite Structures, 229,* 111382.

[67] Pinho, S. T., Dávila, C. G., Camanho, P. P., Iannucci, L., & Robinson, P. (2005). *Failure models and criteria for FRP under in-plane or three-dimensional stress states including shear non-linearity* (No. NASA/TM-2005-213530).

[68] Novak, J. K., & Selvarathinam, A. S. (2021). A Comparison of Discrete Damage Modeling Methods: the Effect of Stacking Sequence on Progressive Failure of the Skin Laminate in a Composite Pi-joint Subject to Pull-off Load. In *AIAA Scitech 2021 Forum* (p. 0571).

[69] Bru, T. (2018). *Material characterisation for crash modelling of composites.* Chalmers Tekniska Hogskola (Sweden).

[70] Zhao, L., Qin, T., Zhang, J., & Shenoi, R. A. (2013). Modified maximum stress failure criterion for composite π joints. *Journal of composite materials, 47*(23), 2995-3008.

[71] Baran, I., Warnet, L. L., & Akkerman, R. (2018). Assessment of failure and cohesive zone length in co-consolidated hybrid C/PEKK butt joint. *Engineering Structures, 168,* 420-430.

[72] Radaj, D. (1990). *Design and analysis of fatigue resistant welded structures.* Woodhead Publishing.

[73] Ma, X., Bian, K., Liu, H., Wang, Y., & Xiong, K. (2020). Numerical and experimental investigation of the interface properties and failure strength of CFRP T-Stiffeners subjected to pull-off load. *Materials & Design, 185,* 108231.

[74] Panigrahi, S. K., & Pradhan, B. (2009). Development of load coupler profiles of spar wingskin joints with improved performance for integral structural construction of aircraft wings. *Journal of reinforced plastics and composites, 28*(6), 657-673.

[75] Hannig, A., Nolte, F., & Horst, P. (2017). Experimental investigation of integral composite T-joints under mixed mode loading. *In 21st International Conference on Composite Materials.*

[76] Zhao, L., Gong, Y., Qin, T., Mehmood, S., & Zhang, J. (2013). Failure prediction of out-of-plane woven composite joints using cohesive element. *Composite Structures, 106,* 407-416.

[77] Cui, H. (2014). Delamination and debonding failure of laminated composite T-joints.

[78] Bathe, K. J. (2006). *Finite element procedures.* Klaus-Jurgen Bathe.

[79] Reeder, J. R. (2000). Refinements to the mixed-mode bending test for delamination toughness.

[80] Hinton, M. J. K. A., Soden, P. D., & Kaddour, A. S. (Eds.). (2004). *Failure criteria in fibre reinforced polymer composites: the world-wide failure exercise.* Elsevier.

[81] Hinton, M. J., & Kaddour, A. S. (2012). The background to Part A of the Second World-Wide Failure Exercise: Evaluation of theories for predicting failure in polymer composite laminates under three-dimensional states of stress. *Journal of Composite Materials, 46*(19-20), 2283-2294.

[82] Hinton, M. J., & Kaddour, A. S. (2013). The background to Part B of the Second World-Wide Failure Exercise: Evaluation of theories for predicting failure in polymer composite laminates under three-dimensional states of stress. *Journal of Composite Materials, 47*(6-7), 643-652.

[83] Puck, A., & Schürmann, H. (1998). Failure analysis of FRP laminates by means of physically based phenomenological models. Composites Science and Technology, 7(58), 1045-1067.

[84] Puck, A., & Schürmann, H. (2002). Failure analysis of FRP laminates by means of physically based phenomenological models. *Composites science and technology, 62*(12-13), 1633-1662.

[85] Parvizi, A., Garrett, K. W., & Bailey, J. E. (1978). Constrained cracking in glass fibre-reinforced epoxy cross-ply laminates. *Journal of Materials Science, 13*(1), 195-201.

[86] Wang, A. S. D., & Crossman, F. W. (1980). Initiation and growth of transverse cracks and edge delamination in composite laminates Part 1. An energy method. *Journal of Composite Materials, 14*(1), 71-87.

[87] Chang, F. K., & Chen, M. H. (1987). The in situ ply shear strength distributions in graphite/epoxy laminated composites. *Journal of Composite Materials, 21*(8), 708-733.

[88] Flaggs, D. L., & Kural, M. H. (1982). Experimental determination of the in situ transverse lamina strength in graphite/epoxy laminates. *Journal of composite materials, 16*(2), 103-116.

[89] Wang, A. S. D. (1983). *Fracture Mechanics of Sublaminate Cracks in Composite Laminates.* DREXEL UNIV PHILADELPHIA PA DEPT OF MECHANICAL ENGINEERING AND MECHANICS.

[90] Dvorak, G. J., & Laws, N. (1987). Analysis of progressive matrix cracking in composite laminates II. First ply failure. *Journal of Composite Materials*, *21*(4), 309-329.

[91] Laws, N., & Dvorak, G. J. (1988). Progressive transverse cracking in composite laminates. *Journal of composite materials*, *22*(10), 900-916.

[92] Tan, S. C., & Nuismer, R. J. (1989). A theory for progressive matrix cracking in composite laminates. *Journal of Composite Materials*, *23*(10), 1029-1047.

[93] Davila, C. G., Camanho, P. P., & Rose, C. A. (2005). Failure criteria for FRP laminates. *Journal of Composite materials*, *39*(4), 323-345.

[94] Pinho, S. T., Darvizeh, R., Robinson, P., Schuecker, C., & Camanho, P. P. (2012). Material and structural response of polymer-matrix fibre-reinforced composites. *Journal of Composite Materials*, *46*(19-20), 2313-2341.

[95] Pinho, S. T., Vyas, G. M., & Robinson, P. (2013). Material and structural response of polymer-matrix fibre-reinforced composites: Part B. *Journal of Composite Materials*, *47*(6-7), 679-696.

[96] Camanho, P. P., Dávila, C. G., Pinho, S. T., Iannucci, L., & Robinson, P. (2006). Prediction of in situ strengths and matrix cracking in composites under transverse tension and in-plane shear. *Composites Part A: Applied Science and Manufacturing*, *37*(2), 165-176.

[97] Hahn, H. T., & Tsai, S. W. (1973). Nonlinear elastic behavior of unidirectional composite laminae. *Journal of Composite Materials*, *7*(1), 102-118.

[98] Catalanotti, G., Camanho, P. P., & Marques, A. T. (2013). Three-dimensional failure criteria for fiber-reinforced laminates. *Composite Structures*, *95*, 63-79.

[99] Catalanotti, G. (2019). Prediction of in situ strengths in composites: some considerations. *Composite Structures*, *207*, 889-893.

[100] Mannigel, M. (2007). *Influence of shear stresses on the fibre failure behaviour in carbon fibre reinforced plastics (CFRP)* (Doctoral dissertation, PhD Thesis, Institut für Kunststoffverarbeitung (IKV), RWTH Aachen, 2007 [German]).

[101] Li X. (2007). *Comparative study on the failure behaviour of advanced carbon-epoxy composites.* (Master's Thesis, Department of Aeronautics, Imperial College London)

[102] Lopes, C. S., Camanho, P. P., Gürdal, Z., Maimí, P., & González, E. V. (2009). Low-velocity impact damage on dispersed stacking sequence laminates. Part II: Numerical simulations. *Composites Science and Technology*, *69*(7-8), 937-947.

[103] Ata, T. T., & Coker, D. (2021). 2D and 3D simulations of dynamic delamination in curved unidirectional CFRP laminates subjected to moment/axial combined loading. *Composite Structures*, *268*, 113899.

[104] Ata, T. T. (2019). *2D and 3D finite element analyses of dynamic delamination in curved CFRP laminates*. (Master's thesis, Middle East Technical University).

[105] Tasdemir, B., & Coker, D. (2019). Comparison of damage mechanisms in curved composite laminates under static and fatigue loading. *Composite Structures*, *213*, 190-203.

[106] Taşdemir, B. (2018). *Fatigue and static behavior of curved composite laminates*. (Master's thesis, Middle East Technical University).

[107] Wisnom, M. R. (1996). 3-D finite element analysis of curved beams in bending. *Journal of composite materials*, *30*(11), 1178-1190.

[108] de Almeida, S. F. M., & Neto, Z. D. S. N. (1994). Effect of void content on the strength of composite laminates. *Composite structures*, *28*(2), 139-148.

[109] Zhu, H. Y., Li, D. H., Zhang, D. X., Wu, B. C., & Chen, Y. Y. (2009). Influence of voids on interlaminar shear strength of carbon/epoxy fabric laminates. *Transactions of Nonferrous Metals Society of China*, *19*, s470-s475.

[110] McMillan, A. J. (2012). Material strength knock-down resulting from multiple randomly positioned voids. *Journal of Reinforced Plastics and Composites*, *31*(1), 13-28.

[111] Zhuang L.Q. (2012) *Effects of voids on delamination growth in composite laminates under compression.* (Master's thesis, Texas A&M University).

[112] Liu, J. L., Tay, T. E., Ng, S. W., & Tan, V. B. C. (2022). Effects of inter-ply mismatch angle on interlaminar properties and their influence in numerical simulations. *Composites Part A: Applied Science and Manufacturing*, *154*, 106795.

[113] Yavuz, B. O., Parnas, L., & Coker, D. (2019). Interlaminar tensile strength of different angle-ply CFRP composites. *Procedia Structural Integrity*, *21*, 198-205.

[114] González Cantero, J. M. (2017). Study of the unfolding failure of curved composite laminates.

[115] Wen, L., & Tian, R. (2016). Improved XFEM: Accurate and robust dynamic crack growth simulation. *Computer Methods in Applied Mechanics and Engineering*, *308*, 256-285.

[116] Tian, R., Wen, L., & Wang, L. (2019). Three-dimensional improved XFEM (IXFEM) for static crack problems. *Computer Methods in Applied Mechanics and Engineering*, *343*, 339-367.